Self-Sensing Shape Memory Alloy Wire Actuators using Kalman Filters

By

Hema Gurung

DEPARTMENT OF MECHANICAL ENGINEERING

INDIAN INSTITUTE OF TECHNOLOGY GUWAHATI

GUWAHATI - 781039, ASSAM, INDIA.

November 2017

Self-Sensing Shape Memory Alloy Wire Actuators using Kalman Filters

A thesis submitted

In partial fulfillment of the requirements

for the degree of

Doctor of Philosophy

By

Hema Gurung

To the

DEPARTMENT OF MECHANICAL ENGINEERING

INDIAN INSTITUTE OF TECHNOLOGY GUWAHATI

GUWAHATI - 781039, ASSAM, INDIA.

November 2017

TH-1636_10610313

Certificate

This is to certify that the work contained in the Thesis entitled "**Self-Sensing Shape Memory Alloy Wire Actuators using Kalman Filters**" submitted by *Hema Gurung*, Roll No. 10610313, has been carried out under my supervision for the partial fulfillment of degree of Doctor of Philosophy in department of Mechanical Engineering, Indian Institute of Technology Guwahati and this work has not been submitted elsewhere for the award of any other degree.

Dr. Atanu Banerjee

Associate Professor

Department of Mechanical Engineering

Indian Institute of Technology Guwahati

Guwahati - 781039, Assam, India

November, 2017

TH-1636_10610313

Abstract

Shape Memory Alloys (SMA) are known to undergo large deformation at low temperature and can recover the same while subjected to high temperature. This ability offers SMA as a potential candidate for actuation. They offer large displacement, typically 4-5% of the length in case of wire, and considerable force, equivalent to 300-400 MPa, at low operating speed, in the range of 0.1-10 Hz. The SMA based actuators are found to be very promising in case of miniature applications, where, size, weight and smooth operating conditions are important. Out of all the forms available, SMA wire based actuators are mostly used, because these can easily be activated through resistive heating. In addition, the SMA materials exhibit nonlinear and hysteretic behavior; offering challenges in terms of controlling the actuators for practical applications.

In literature, sophisticated control algorithms have been proposed, requiring one or more feedback sensors. The introduction of feedback sensors makes system bulky and costly. To obviate this situation, the variation in electrical resistance of the SMA material has been explored as a measure of the level of actuation. In this way, the SMA actuator can simultaneously be used as a sensor. This is what is known as *self-sensing actuator* application of SMA. For this purpose, empirical relations are derived between the change in electrical resistance of the SMA wire actuator and the system response and are being used to obtain the system response for a given measured change in electrical resistance of the same. This works well in cases, where the pre-tension in the wire is sufficient enough to make the hysteresis gap negligible. Moreover, the derived relations are only applicable for that particular system, as system parameters, as well as the loading conditions, significantly affect this relationship. To circumvent this, in this thesis, different variants of Kalman Filter have been explored;

TH-1636_10610313

to estimate the system response for a given change in electrical resistance of the SMA wire actuator.

Firstly, Extended Kalman Filter models of SMA wire actuated linear spring and a cantilever beam undergoing large displacement are developed. Here, the objective is to estimate the systems response from the variation in electrical resistance of the SMA wire, while it is being heated following resistive heating. The system response imply, the change in length of the linear spring in the first case and the displacement of the free end of the cantilever beam for the latter system. The state equations of the system's model are derived using heat balance equation, constitutive relation of the SMA wire, phase kinetics, force equilibrium, and the relation between electrical resistance and strain at different phases. The time update step of a Kalman Filter has been implemented using both implicit and explicit numerical schemes. Following a convergence study, the time steps are decided. From the simulation, it has been found that the implicit scheme requires less computational time as compared to that of the explicit scheme. The estimated stress and temperature are verified using an established model for different input voltage signals.

To verify the performance of the developed EKF models, an experimental set-up is designed and fabricated. The set-up consists of a real-time control hardware DS1006 from dSPACE, a laser displacement sensor, a voltage divider circuit and a programmable power supply. Two systems are being fabricated. The first one is basically a linear spring biased SMA wire actuator; while the other one comprises of the a flexible beam with discretely attached SMA wire at a given offset. Here, the DS1006 is used as DAQ, to acquire the voltage signals from the divider circuit as well as the displacement sensor. The voltage divider circuit is developed to determine the electrical resistance of the SMA wire during actuation. The displacement sensor is used to measure the actual displacement of the system which has only been used to verify the estimation. The temperature of the SMA wire is varied by

TH-1636_10610313

applying time varying voltage signal, which has been simulated in Simulink©Mathworks. A programmable power supply is used to amplify the voltage signal before being applied to the SMA wire actuator. Using this set-up, the electrical resistance of the SMA wire is measured for a given voltage signal and is being used offline in the EKF models to estimate the stress and temperature of the SMA wire. Then the system response is estimated and is compared with respect to the same, measured using the displacement sensor. A qualitative agreement between the estimated and measured displacements are observed for both the systems.

To get rid of the requirement of linearizing the state equations in EKF model, an Unscented Kalman Filter (UKF) has been explored for the linear spring biased SMA wire actuator. Here, the UKF model has been developed from the system model to estimate the displacement of the spring from the electrical resistance variation of the SMA wire actuator. The same set-up is used to measure the electrical resistance variation of the SMA wire actuator and the corresponding change in length of the spring for a given voltage signal. These are then used offline to estimate the displacement of the spring using the developed UKF model. The estimated displacement obtained using UKF model are compared with that of the EKF model, as well as the measured displacements. It has been observed, that the estimation obtained using the UKF model is quantitatively almost same as that of the EKF model. However, the computational time taken by the UKF model is almost 50% as that of the EKF model. This is a very important findings, particularly for real-time applications of these algorithms in low-end hardware.

The quantitative discrepancies, between the estimation and the actual displacements, are found to be quite significant and do not allow the estimator to be a replacement of the feedback sensor. To improve the quantitative accuracy, different approaches are explored. Firstly, the phase transformation temperature of SMA wire is determined following DSC. It is observed that there is an overlap between the forward and reverse transformation zones and

TH-1636_10610313

require a different approach for the phase kinetics to implement. Next, an Artificial Neural Network (ANN) model trained based on the estimation of the EKF model is developed and its performance is tested against another ANN model which has been trained solely using the measured data. It has been observed, that for the same number of neurons and same training data, EKF based ANN model yields better result in comparison to ANN based on experimental data, even at higher frequencies. In another approach, a time varying process noise covariance is derived for the system in hand, to take care of the uncertainties involved in the model as well as in the SMA behavior. However, in this approach, no significant improvement in the estimation is observed. In a different approach, the electrical resistivity model of the SMA has been modified to simulate the experimentally observed nature of the same. In addition, two unknown constants are incorporated in the model of the coefficient of convective heat transfer coefficient and specific heat of SMA. These constants are then estimated along with the state of the system. In this approach, significant quantitative accuracy is achieved, even for partial transformation cases. Finally, the effectiveness of the algorithm has been demonstrated by implementing the same in a less resourceful hardware, named Arduino UNO.

TH-1636_10610313

Acknowledgement

I shall forever remain obliged to my supervisor Dr. Atanu Banerjee, Assistant Professor in the Department of Mechanical Engineering, for providing me a noble opportunity to work with him in the interesting field of Shape Memory Alloy. His enthusiasm and zest to adopt and appreciate the latest trends in this research area and his eagerness to discuss and offer important suggestions have been a constant source of inspiration and encouragement. Each discussion carried out with him gave me confidence and clear direction of thought for my research work. I am especially thankful to him for critically reviewing the reports and research papers despite his busy schedule of academic and other administrative works. I owe him a lot for the valuable advice he has given whenever I needed.

I would like to acknowledge Vibration and Acoustic Laboratory, Mechatronics and Robotics Laboratory, Strength of Material Laboratory and Central Workshop of Indian Institute of Technology Guwahati for providing instruments to carry out the research work. I am sincerely thankful to Prof. S. K. Dwivedy, Prof. R. Tiwari and Dr. I. Kar, Doctoral Committee members, for giving important suggestions and ideas to improve the quality of the work and the thesis report.

I am thankful to Prof. Anoop K. Dass, Prof. Pinakeswar Mahanta and Prof. Debabrata Chakraborty, present and former Heads, Department of Mechanical Engineering, Indian Institute of Technology Guwahati, for providing various laboratory facilities and sanctioning funds without which completion of the work would not have been possible. Their co-operation had paved the way to my research work.

I am grateful to Dr. D. J. Bordoloi, Mr. Jiten Basumatary, Mr. M. Dowarah, Mr. N. Borah and Mr. Sanjib Sarma, technical staff in the Department of Mechanical Engineering for their valued support, time and patience to carry out my experimental studies without any

TH-1636_10610313

hindrance. I am also thankful to Mr. Nabajyoti Dutta, Mr. Raju Talukdar, Mr. Narayan Kalita and Mrs. Trishna Choudhury for their support in administrative works.

My sincere gratitude to my family members for their immense support during the course of my PhD work. Their patience, goodwill, caring nature and encouraging words kept me driving, and helped me to focus on my work. I dedicate this thesis to all of them. I express my heartfelt gratitude to all my friends and colleagues Mr. Saptarishi Karmarkar, Chinmay kr. Tarai, Nripen Kalita, Swaroop Kalita and Animesh Kundu, of IIT Guwahati for their timely help and moral support.

Last, but not the least, I shall always be grateful to god Ganesha for providing me such an awesome aura for research work.

TH-1636_10610313

Dedicated

To

My Parents

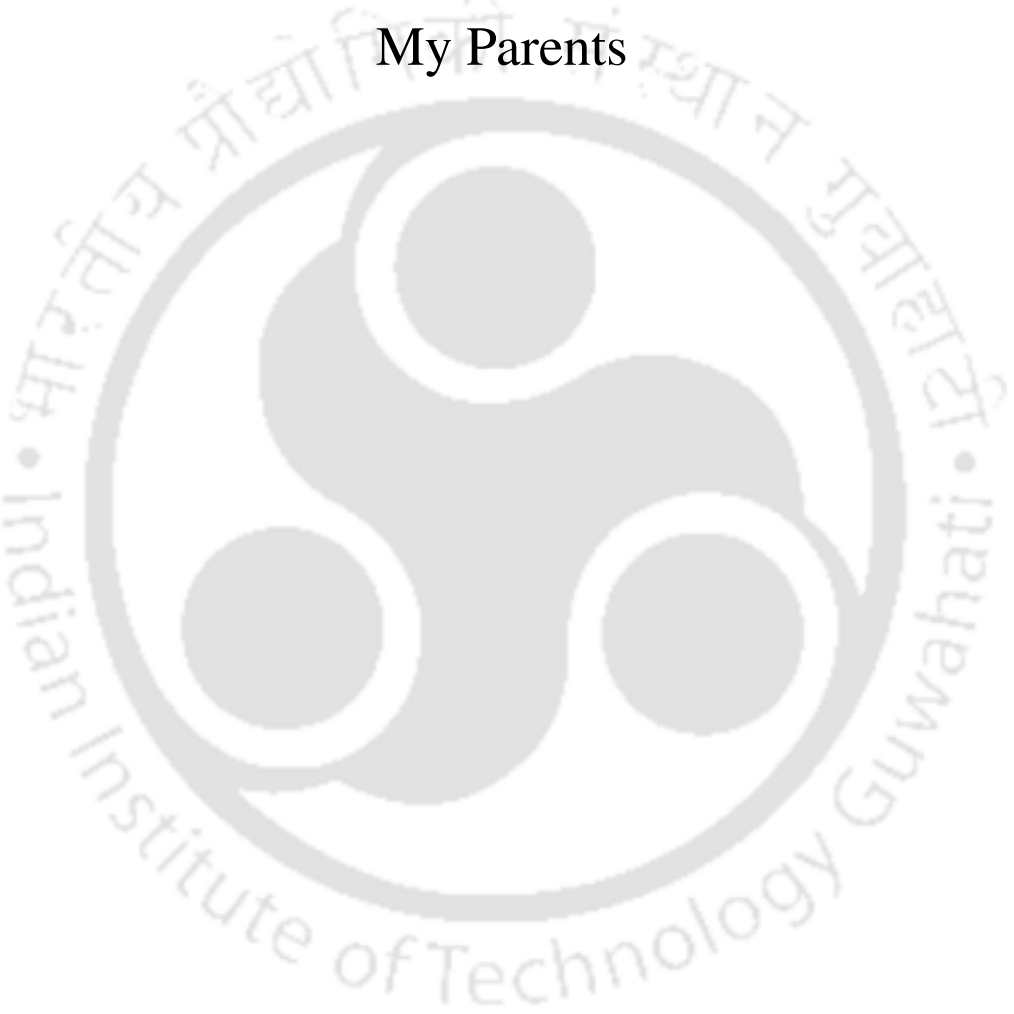

TH-1636_10610313

Contents

1 Introduction **1**

1.1 Introduction 1

1.2 Literature Review 6

1.2.1 History and Application of SMA 6

1.2.2 Modeling of SMA Behavior 9

1.2.3 Feedback Control 13

1.2.4 SMA as Self-sensing Actuator 15

1.2.5 Kalman Filter (KF) 19

1.3 Motivation and Objective 21

1.3.1 Organization of the Present Work 23

2 Modelling of Shape Memory Alloy (SMA) Wire Behavior **26**

2.1 Introduction 26

2.2 Constituent phases in SMA materials 27

2.2.1 Martensite Phase 27

2.2.2 Austenite Phase 28

2.3 SMA Wire Behavior 29

2.3.1 Shape Memory Effect (SME) 29

TH-1636_10610313

2.3.2 Pseudo-elasticity 30
2.4 Phase Diagram 31
2.5 SMA Actuators 35
2.6 Modeling of SMA 36
2.6.1 One-Dimensional Constitutive Behavior of SMA 37
2.6.2 Phase Kinetics 39
2.6.2.1 Simple Loading 39
2.6.2.1.1 Forward Transformation : 40
2.6.2.1.2 Reverse Transformation : 42
2.6.2.2 Arbitrary Thermo-mechanical Loading 43
2.6.2.2.1 Forward Transformation : 44
2.6.2.2.2 Reverse Transformation : 45
2.6.2.2.3 Passive Transformation : 46
2.7 Implementation of Phase Kinetics 47
2.7.1 Algorithm for Zone Selection 48
2.7.2 Algorithm for Updating the Memory Parameters 49
2.8 Heat Balance Equation 50
2.9 Summary 52

3 Development of Extended Kalman Filter for Self-sensing Application of Shape Memory Wire Actuator 53

3.1 Introduction 53
3.2 Self-sensing SMA Wire Actuator 54
3.3 SMA Wire Actuated Systems 55
3.4 Extended Kalman Filter (EKF) 58
3.5 Modeling 64

TH-1636_10610313

3.5.1 Force Equilibrium and Kinematic Constraint 65
3.5.1.1 Linear system 66
3.5.1.2 Nonlinear system 67
3.5.2 Relation between Electrical Resistance and Strain 71
3.6 EKF for SMA Actuated System 72
3.6.1 Linear System 73
3.6.1.1 Implicit Method 73
3.6.1.2 Explicit Method 76
3.6.1.3 Comparison between the EKF Models 79
3.6.1.4 Validation of EKF Model 82
3.6.1.5 Comparison between EKF Estimation and SMA Model for SMA Actuated Cantilever Beam 87
3.7 Summary 89

4 Experimental Validation of EKF Model for Self-sensing Application of SMA Wire Actuator 90

4.1 Introduction 90
4.2 Experimental Set-up and Procedure 91
4.2.1 Experimental Procedure 96
4.3 EKF Model for Linear Spring Biased Wire Actuator 98
4.3.1 Linear Spring biased SMA Wire Actuator 98
4.3.2 Determination of Spring Stiffness 99
4.3.3 Determination of Process and Measurement Noise Covariance . . . 100
4.3.4 Results and Discussion 103
4.4 EKF for SMA Actuated Cantilever Beam 104
4.4.1 SMA Actuated Nonlinear System 106

TH-1636_10610313

4.4.2 Modulus of Elasticity . . . 107
4.4.3 Determination of Process and Measurement Noise Covariance . . . 109
4.4.4 Determination of Convective Heat Transfer Coefficient . . . 111
4.4.5 Results and Discussion . . . 113
4.5 Summary . . . 116

5 Unscented Kalman Filter for Self-sensing SMA Wire Actuator 117
5.1 Introduction . . . 117
5.2 Unscented Kalman Filter (UKF) . . . 118
5.2.1 The Unscented Kalman Filter . . . 119
5.3 System Description . . . 124
5.4 UKF for SMA Actuated System . . . 125
5.4.1 Validation of the UKF Model . . . 128
5.5 Results and Discussion . . . 129
5.6 Summary . . . 134

6 Modified Kalman Filters 135
6.1 Introduction . . . 135
6.2 Differential Scanning Calorimetry (DSC) . . . 136
6.2.1 Determination of Transformation Current Zone . . . 138
6.3 Artificial Neural Network (ANN) . . . 139
6.3.1 Description of the System . . . 140
6.3.2 EKF based Artificial Neural Network (ANN) . . . 140
6.3.3 Experimental Details . . . 142
6.3.4 Results and Discussion . . . 142
6.4 EKF model with Varying Process Noise . . . 144

TH-1636_10610313

6.4.1 Modified Extended Kalman Filter (EKF) . . . 145
6.4.2 Varying Process Noise Covariance . . . 147
6.4.3 Determination of Process Noise Covariance **Q** . . . 148
6.4.4 Results and Discussion . . . 151
6.5 Parameter Estimation . . . 152
6.5.1 Modified Extended Kalman Filter . . . 153
6.5.1.1 Modified System Model . . . 154
6.5.2 Modified EKF model for linear spring biased SMA wire . . . 156
6.5.3 Results and Discussion . . . 158
6.6 Summary . . . 161

7 EKF Implementation using Microcontroller 162
7.1 Arduino UN0 328 . . . 163
7.2 Experimental Set-up . . . 164
7.3 Results and Discussion . . . 172
7.4 Summary . . . 174

8 Conclusions and Future Work 175
8.1 Contributions . . . 175
8.2 List-of-Publications . . . 178
8.3 Scope of Future Works . . . 179

Appendices 180

A Arbitary Thermomechanical Loading 181

B Derivation of the State Equations 187

TH-1636_10610313

Bibliography **192**

TH-1636_10610313

List of Figures

1.1 Phase transformation in SMA materials. 2

1.2 Available forms of SMA materials. 3

1.3 SMA wire as an actuator. 3

2.1 (a) Twinned martensite and (b) Detwinned martensite [1]. 28

2.2 Reverse phase transformation in SMA [1]. 29

2.3 (a) Typical phase diagram of SMA, and (b) Stress-Strain response in SMA during Shape Memory Effect. 33

2.4 Stress-Strain response in SMA during Pseudo-elasticity. 34

2.5 Phase diagram of SMA. 34

2.6 (a) Spring biased SMA actuator for linear motion, (b) spring biased SMA actuator for rotational motion, (c) antagonistically placed SMA actuators for linear motion, and (d) antagonistically placed SMA actuators for rotational motion. 35

2.7 Simplified phase diagram of SMA. 40

2.8 Arbitrary thermo-mechanical loading path in (a) forward transformation zone, and (b) reverse transformation zone of phase diagram. 44

2.9 Phase transformation zone of SMA. 48

TH-1636_10610313

3.1 (a) Variation of stress with temperature in SMA wire, and (b) corresponding change in electrical resistance of SMA with temperature. 54

3.2 Schematic of a linear spring biased SMA wire actuator. 56

3.3 Schematic of a SMA wire actuated cantilever beam. 57

3.4 Flow diagram of the EKF model. 63

3.5 (a) A cantilever beam actuated by a discretely placed SMA wire actuator, and (b) forces and moment applied by the SMA wire on the free end of the beam. 68

3.6 (a) Voltage applied across the SMA wire, (b) variation of electrical resistance of SMA as obtained from the model, (c) estimated stress with that of temperature of SMA, and (d) estimated displacement of the SMA actuated system. 80

3.7 Comparison of system responses obtained using SMA model [2] and EKF for the (a) input voltage, (b) electrical resistance variation in SMA, (c) temperature of the SMA wire, (d) stress variation with temperature, (e) martensite volume fractions with temperature, and (f) spring displacement. 83

3.8 Comparison of system responses obtained using SMA model [2] and EKF during partial transformation for (a) input voltage across SMA, (b) electrical resistance variation in SMA (c) temperature of the SMA wire, (d) stress with temperature, (e) martensite volume fractions with temperature, and (f) spring displacement 84

3.9 (a) Voltage applied across SMA, (b) electrical resistance of SMA, (c) temperature of the SMA, (d) stress variation with temperature, (e) martensite volume fractions, and (f) end-displacement of the link, as obtained from the SMA model [2] and EKF model. 88

4.1 Experimental set-up. 91

4.2 (a) dSPACE with DS1006 processor and I/O board and (b) schematic of the working principle of dSPACE. 93

TH-1636_10610313

4.3 (a) Front and (b) back panel of the DC programmable power supply. 94

4.4 Laser displacement sensor (opto NCDT-1402-100). 95

4.5 Schematic of the voltage divider circuit. 96

4.6 (a) Schematic of experimental set-up. 97

4.7 Flow diagram of the experiment. 98

4.8 (a) Top and (b) isometric view of linear spring biased SMA wire actuator. . 99

4.9 (a) Set-up for spring stiffness measurement and (b) force-displacement response of the spring. 101

4.10 Experimentally determined electrical resistance of R_1 for $V_T = 0.1$ V. . . . 102

4.11 (a) Applied voltage across the SMA wire, (b) estimated and measured displacement of the system, (c) estimation error with time for different process noise covariance ($\mathbf{Q}$), and (d) RMSE for different ($\mathbf{Q}$). 103

4.12 (a) Applied voltage across SMA wire, (b) measured electrical resistance of SMA, (c) variation of measured displacement with applied voltage, (d) change in measured displacement with electrical resistance of SMA, and (e) comparison between measured and estimated displacement of the system. . 105

4.13 Comparison between EKF estimated and experimental responses for continuous periodic input voltage having time period of (a) 10 sec and (b) 5 sec. . 106

4.14 Comparison between EKF estimated and experimental responses for step input voltage for time period of (a) 10 sec and (b) 5 sec. 106

4.15 (a) Undeformed and (b) deformed shape of the SMA wire actuated cantilever beam. 108

4.16 (a) Specimens of the tensile test and (b) experimental stress-strain curve of the beam material. 108

4.17 (a) Voltage applied across the SMA wire, (b) estimated and measured displacement of the system, (c) effect of process noise covariance ($\mathbf{Q}$) on estimation error, and (d) effect of $\mathbf{Q}$ on RMSE. 110

TH-1636_10610313

4.18 Comparison between EKF estimated and experimental responses before optimization. 111

4.19 a) Change in objective function with number of iteration, (b) comparison between the EKF estimated and experimentally measured displacement with optimized h. 113

4.20 Comparison between EKF estimated and experimental responses for continuous periodic voltage having frequency, (a) 0.1 Hz, (b) 0.2 Hz, and (c) 0.5 Hz. 114

4.21 Comparison between EKF estimated and experimental responses for step voltage having time period, (a) 10 sec, (b) 5 sec, and (c) 2 sec. 115

5.1 Steps in Unscented Kalman Filter. 123

5.2 Schematic of the SMA actuated system. 124

5.3 Comparison between experimental response and UKF estimation for continuous periodic signal of time period, (a) 10 sec, and (b) 5sec. 130

5.4 Comparison between experimental response and UKF estimation for step input of time period, (a) 10 sec, and (b) 5sec. 131

5.5 Comparison between Experimental Response, EKF and UKF estimation for a continuous decreasing periodic signal of time period 10 sec. 132

6.1 Results obtained from the DSC test conducted for two cycles at a rate of 5 °C. 137

6.2 Phase diagram of the SMA wire with transformation temperatures, (a) obtained from DSC test, and (b) obtained from literature [2]. 137

6.3 (a) Comparison between EKF estimated and experimental response, (b) schematic of the ANN models, (c) details of ANN-I and (d) details of ANN-II. 141

6.4 Comparison between EKF estimated and experimental responses for continuous periodic input voltage signal of (a) amplitude = 6.4 V and frequency = 0.1 Hz, and (b) amplitude = 6.4 V and frequency = 0.2 Hz. 143

TH-1636_10610313

6.5 Comparison between EKF estimated and experimental responses for continuous periodic input voltage signal of (a) amplitude = 4.5 V and frequency = 0.1 Hz, and (b) amplitude = 4.5 V and frequency = 0.2 Hz. 143

6.6 Comparison between EKF estimation and experimental response for different process noise covariance ($\mathbf{Q}$). 152

6.7 (a) Comparison between estimated and measured electrical resistance of SMA wire (b) before and (c) after modification. 155

6.8 Comparison between EKF-I, EKF-III and experimental response for continuous decreasing periodic input voltage of amplitude = 6.2 V and time period = 25 sec. 158

6.9 Comparison between EKF-I, EKF-III and experimental response for continuous input voltage (a) amplitude = 6.2 V and time period =10 sec (b) amplitude = 6.2 V, time period = 5 sec and (c) amplitude = 4 V, time period = 10 sec. 159

6.10 Comparison between EKF-I, EKF-III and experimental response for step input voltage (a) amplitude = 6.2 V, time period = 10 sec and (b) amplitude = 6.2 V, time period = 5 sec. 160

7.1 Arduino UNO development board. 163

7.2 (a) Flow diagram of the experimental set-up and (b) actual experimental set-up. 165

7.3 Schematic of (a) low pass filter, and (b) connection between Arduino and low pass filter. 167

7.4 (a) Pin configuration of 741 op-amp, (b) inverting amplifier of unity gain, and (c) signal flow diagram using inverting amplifier. 168

7.5 Voltage signal acquired from Arduino UNO for measuring the actual displacement of the system, and electrical resistance of SMA. 170

7.6 Schematic of (a) voltage divider circuit and (b) connection between voltage divider circuit with Arduino UNO. 171

TH-1636_10610313

7.7 Comparison between EKF estimated and experimental response for (a) step and (b) continuous voltage signal 173

A.1 Arbitrary thermo-mechanical loading path in forward transformation zone. . 182

A.2 Arbitrary thermo-mechanical loading path in reverse transformation zone. . 184

TH-1636_10610313

List of Tables

3.1 Properties assumed for the linear spring biased SMA wire actuated system [3]. 79

3.2 Computational time of the explicit and implicit methods based EKF models. 81

3.3 Properties of the cantilever beam. 87

4.1 Initial and final values of the co-efficient of convective heat transfer. 112

5.1 Computational time of the EKF and UKF models. 133

6.1 Properties assumed for the linear spring biased SMA wire actuated system [3]. 151

7.1 Arduino UNO development board technical specifications. 164

TH-1636_10610313

Nomenclature

A_s = Austenite start transformation temperature.

A_f = Austenite finish transformation Temperature.

M_s = Martensite start transformation temperature.

M_f = Martensite finish transformation Temperature.

C_{vA} = Heat capacity of austenite phase.

C_{vM} = Heat capacity of martensite phase.

C_A = Stress influence slope of an SMA in the austenite zone.

C_M = Stress influence Slope of an SMA in the martensite zone.

d = Diameter of the SMA wire.

D = Elastic modulus.

D_A = Modulus of elasticity of austenite zone.

D_M = Modulus of elasticity of martensite zone.

ρ = Electrical resistivity of SMA wire.

ρ_A = Electrical resistivity of SMA in austenite zone.

ρ_M = Electrical resistivity of SMA in martensite zone.

h = Convective heat transfer coefficient.

L_0 = Initial or unstretched length of SMA.

$\overline{n}^A$ = Transformation direction in austenite transformation zone.

$\overline{n}^M$ = Transformation direction in martensite transformation zone.

P_j^i = Perpendicular distance along the transformation direction in the j^{th} segment of i^{th} transformation zone.

A_{surf} = Total surface area of the SMA wire.

T = Temperature of the SMA wire in degree Celsius.

σ = Stress within the wire in MPa.

TH-1636_10610313

ξ = Total martensite volume fraction of the phase transformation.

ξ_S = Stress induced martensite volume fraction of the phase transformation.

ξ_T = Temperature induced martensite volume fraction of the phase transformation.

δ = Estimated Displacement of the system.

δ_m = Measured displacement of the system.

Θ = Coefficient of thermal expansion of SMA.

ϕ^A = Slope of austenite zone.

ϕ^M = Slope of martensite zone.

V_m = Total volume of the SMA wire

Δt = Sampling time.

K_s = Spring stiffness.

A = Cross-sectional area of the SMA wire.

R = Calculated electrical resistance of SMA.

R_{SMA} = Measured electrical resistance of SMA.

ϵ = Strain within the SMA wire.

ϵ_l = Maximum strain capacity of SMA wire.

$\overline{\tau}$ = Direction of loading along any thermomechanical path.

λ = Latent heat of phase transformation.

$\boldsymbol{\eta}$ = Process nonlinear vector function.

$\mathbf{\Gamma}$ = Observation nonlinear vector function.

$\mathbf{X}$ = State vector of the system.

$\mathbf{u}$ = Input vector of the system.

$\mathbf{P}$ = Sate error covariance matrix.

$\mathbf{J}$ = Jacobian of the process nonlinear vector function.

$\mathbf{Q}$ = Process noise covariance matrix.

TH-1636_10610313

$\mathbf{G}$ = Kalman gain.

$\mathbf{Y}$ = Output vector of the system.

$\mathbf{H}$ = Jacobian of the observation vector function.

$\mathbf{M}_n$ = Measurement noise covariance matrix.

t_k = Current time instant.

t_{k-1} = Previous time instant.

$(.)_{t_k}$ = Represent the corresponding value of the variable present within the parenthesis at current time instant t_k.

$(.)_{t_{k-1}}$ = Denote the corresponding value of the variable present within the parenthesis at previous time instant t_{k-1}.

$\hat{(.)}_{t_k}^{-}$ = a-priori estimation of the variable present within the parenthesis, at time instant t_k.

$\hat{(.)}_{t_k}^{+}$ = a-posteriori estimation of the variable present within the parenthesis, at current time instant t_k.

$\hat{(.)}_{t_{k-1}}^{+}$ = Represent the a-posteriori estimation of the variable present within the parenthesis, at previous time instant t_{k-1}.

$(.)_0$ = Corresponds to the initial state of the variable present within the parenthesis.

TH-1636_10610313

Chapter 1

Introduction

1.1 Introduction

The need of miniaturization in various medical and robotic systems requires a decrease in size and weight of their components. One of the important elements of these systems is the actuator. Actuators impart motion to some of the parts of a system with respect to the other. These require various energy sources like electric current, fluid, pressure etc. Thus actuators are basically transducers, converting one form of energy into the other.

Some of the examples of conventional actuators are motors, hydraulic and pneumatic actuators, etc. These actuators are bulky and mainly adopted for very high to medium load manipulation and for large systems; having dimension above few hundred millimeter. As the dimension of a system drops below few millimeter, smart material based actuators become a superior choice. These group of materials include piezoelectric, electro-active polymers, magnetostrictive, thermally and magnetically activated shape memory alloys, etc. The range of actuation stress over strain and energy density over actuation frequency are illustrated

TH-1636_10610313

in Fig. 1.1 and Fig. 1.2 of [1]. It is evident from the figures, that thermally activated shape memory alloys are capable of offering both large force and displacement at low actuation frequency. Thermally activated shape memory alloys are basically a group of metallic alloys, that can memorize its high temperature shape. This capability is known as shape memory effect. Figure 1.1 illustrates a complete loading cycle, demonstrating the shape memory effect. As the alloy is cooled down from high temperature, it's internal microstructure changes

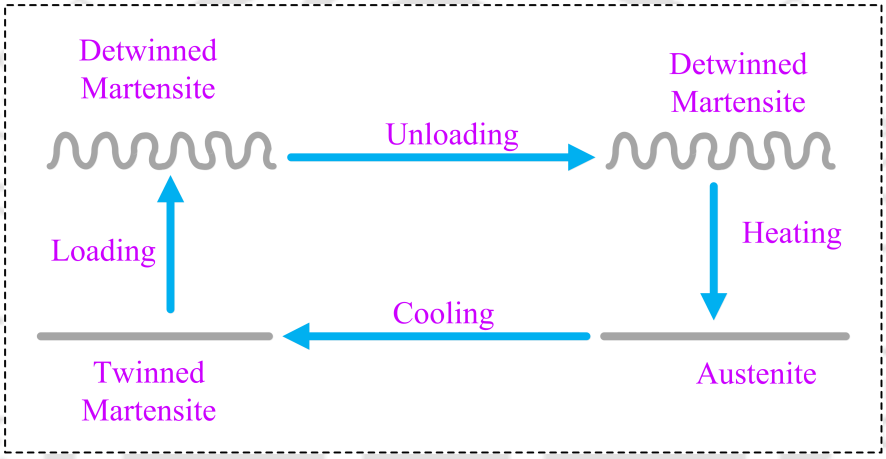

Figure 1.1: Phase transformation in SMA materials.

without any significant macroscopic change. At low temperature, upon loading beyond a critical point, a permanent deformation sets in. If the load is withdrawn, deformed shape of the object can be observed, i.e., in absence of any load the element will remain in the deformed configuration. This deformation can be completely recovered, if the element is again heated at high temperature. Again upon subsequent cooling, the initial undeformed configuration of the element will be obtained. This phenomenon is exploited in developing SMA based actuators, couplings, fittings etc. Nowadays, SMA's are available commercially in different forms, e.g., wires, tubes, thin film, spring, plate, sheet etc. A pictorial view of the available shapes are presented in Fig. 1.2.

The working principle of using SMA wire as actuator is demonstrated in Fig. 1.3.

TH-1636_10610313

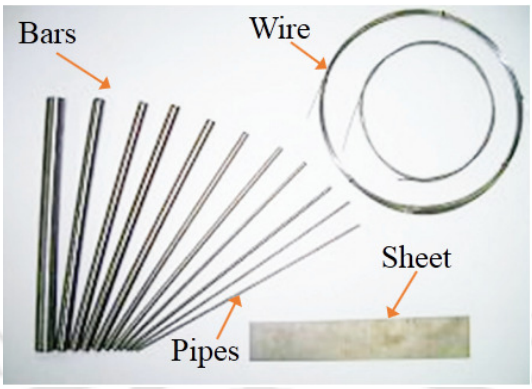

Figure 1.2: Available forms of SMA materials.

Initially, at low temperature, the wire is deformed beyond the critical point to impart a permanent strain. The load is removed and the wire is then fixed to the system to be actuated. To move the system the temperature of the SMA is increased above a certain temperature, due to which the SMA wire contracts, pulling the load (refer Fig. 1.3).

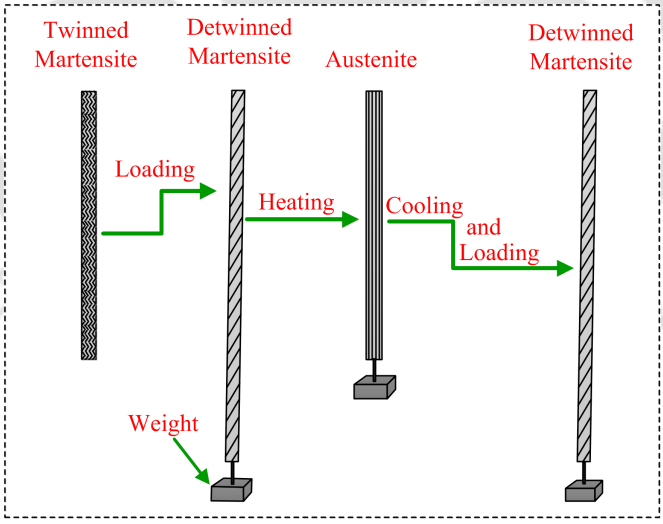

Figure 1.3: SMA wire as an actuator.

There are two modes of actuation, namely, one-way and two-way shape memory effect. In former case, the system's stiffness or inertia stretches the SMA wire back to its initial deformed size, ensuring actuation in the subsequent heating. Whereas, in the latter case, the

TH-1636_10610313

SMA wire is trained in such a way, that during cooling it automatically stretches back to its initial deformed length and no external force is required. Another interesting feature that the SMA offers is known as super-elasticity or pseudo-elasticity. Above a particular temperature, SMA can undergo large deformation due to external load and can subsequently recover the deformation upon unloading. In other words, at constant temperature, it undergoes strain beyond elastic limit and can recover completely during loading and unloading, respectively. This is exploited in biomedical devices, e.g., stent, where the member has to undergo large deformation associated with little increment in stiffness and recover the deformation completely once the external load is withdrawn. In this process, SMA exhibits large hysteresis, allowing dissipation of energy and damping of unwanted vibration in structures.

Along with all these advantages, SMA offers the challenges in terms of low operating frequency, nonlinear, and hysteretic response; making it difficult to be controlled in engineering applications. In case of SMA actuators, advanced feedback controllers are being adopted in literature to tame its behavior. This makes the feedback sensors unavoidable, in presence of which the system becomes bulky as well as costly. To obviate this, change in electrical resistance of the SMA wires, during actuation, has been explored to be used as a measure of the response of the system being actuated. Note, that the electrical resistance of SMA wire varies due to change in electrical resistivity of the material as well as due to the geometric changes of the wire. In this way, the SMA wire can be used as a sensor in addition to being an actuator. This is what is called as 'self-sensing actuator'. This is really effective, particularly in small scale applications, e.g., MEMS, where fine SMA wires can be used as actuator as well as a sensor. In this thesis, efforts are being made to use SMA wires as self-sensing actuators following Kalman filters.

Shape Memory Wire Actuator :

In the last few decades, SMA wires are becoming a lucrative choice as actuators and the

TH-1636_10610313

reasons are,

(i) **Large force and displacement :** The SMA wire actuators offer large displacement and force. The maximum displacement is 3 - 4% of the length of the SMA wire and it can generate a force equivalent to 300 - 400 MPa.

(ii) **High Power to weight ratio :** Compared to any conventional actuator, SMA wire actuator possesses high power to weight ratio. This implies that for a given volume, SMA wire can offer more work output than any other conventional actuator. This offers tremendous potential of the SMA wires in miniature applications.

(iii) **Clean and Silent Operation :** Unlike, other conventional actuators, SMA actuators does not involve moving parts. Consequently, it offers noiseless and clean operation. Moreover, it does not require any maintenance. These features are mostly suitable for robotic and biomedical applications.

(iv) **Simple and Compact :** The SMA wires can be activated by resistive heating, i.e., using Joule effect. Very low driving voltage is required to control these actuators. Thus actuation is very simple and cost-effective.

(v) **Self-sensing capabilities :** The SMA can be used as actuator as well as a sensor. This will eliminate the need of additional feedback sensor, required for controlling the SMA actuator and makes the SMA based system simple and economical.

Besides, it also offers following challenges,

(i) **Actuation Frequency :** Even under forced convection, the SMA wire actuators can operate at a frequency of 10 Hz. Under natural cooling it can operate at 1Hz frequency. This limits the applications of SMA.

TH-1636_10610313

(ii) **Nonlinear and hysteretic behavior :** The response of a SMA wire actuator is nonlinear and exhibits hysteresis between heating and cooling path. This makes control more challenging.

(iii) **Uncertain behavior :** An unstabilized SMA wire exhibits uncertain behavior in first few actuation cycles, even under identical loading conditions.

(iv) **Fatigue Life :** The fatigue life of a SMA wire actuator becomes limited provided very large strain and stress are exploited. It has been reported, that if the maximum strain is kept below 3% and maximum stress harnessed is less than 400 MPa, then these actuators can last for millions of cycles.

1.2 Literature Review

The Shape Memory Alloys have been in the lime light of research for the last few decades. Thus several hundred research papers are available related to the material synthesis, characterization, modeling and applications of Shape Memory Alloys. Here, only the research papers related to modeling and applications of shape memory alloys are presented. However, the author agrees that the collection is not exhaustive.

1.2.1 History and Application of SMA

In the year 1932, Arne Olander [4], a Swedish physicist, first reported to observe an interesting behavior while working with gold cadmium (Au-Cd) alloy. He noticed that the behavior of this alloy is very similar to rubber, i.e., this alloy can easily be deformed to a large extent upon loading and recover the same when heated. In 1938, Greninger & Mooradian [5] also

TH-1636_10610313

observed similar behavior in Cu-Zn alloy. Around 1950, the shape recovery capability were observed in other alloys like in Ni-Ti, and Cu-Al-Ni. In 1951, Chang and Read [6] clearly illustrated the rubber effects and the associated phase transformation between martensite and austenite phases and vice versa. However, due to high cost and complexity involved in developing these alloys, practical applications of these alloys were not pursued.

In 1961, Buhler [7] and his co-workers at the U.S. Naval Ordnance Laboratory discovered the shape memory effect in nickel and titanium (Ni-Ti) alloy, which is considered as a big breakthrough in the field of shape memory alloy. This Ni-Ti alloy is popular as NITINOL (Nickel-Titanium Naval Ordnance Laboratory). This newly discovered alloy is reported to be having better electrical, mechanical properties and is also bio-compatible. Because of the shape memory and super-elastic capabilities, the Ni-Ti alloy become widely used in mechanical, aerospace, civil, robotics and bio-medical applications.

Applications of SMA in robotics, as actuators, began in the late 1980's and 1990's. It started gaining commercial interest. The shape memory alloys were found to be used as connecting elements, actuators, and in variety of electronic, mechanical, hydraulic and thermal applications [8].

SMAs are being proposed in fire safety system, where heat assisted recovery of the material is exploited to make a indication of the ensuing danger in the system. These are useful in petrochemical, pharmaceutical, large oil and gas reservoirs etc. These are also used as circuit breakers, for avoiding damage of sensitive instruments [9]. SMA based valves are also very popular, to control flow of a fluid or proper mixing of two fluids having different temperatures. SMAs were also used in defense industry as electrical connectors and fasteners such as rivets, clamps and seals, etc. SMAs are also used in pipe coupling, as super-elastic materials for eyeglass frames and antennas for portable cellular telephones [10]. The appli-

TH-1636_10610313

cations of SMA actuators also include, controlling the door of a self-cleaning oven. It is also used in the domestic safety devices for preventing the flow of excessively hot water in sink, tub, and shower, using the anti-scald valve [11]. Various SMA based thermal actuators are also used in electric appliances and automobile engineering in adjusting the oil level in the gearbox [12].

In biomedical applications, the use of SMA is indispensable. SMA based stents are basically tubular structure placed inside arteries to maintain vessel patency [13]. The SMA based stents are superior over the normal stainless steel stents, in the sense that, the former one can undergo large deformation with a marginal increment in resistance, and can subsequently recover the shape once the load is removed. Here, super-elasticity of SMA is used. Moreover, the wires used in orthodontic applications [14], offer constant pressure on the required portion of the gum to ensure proper shape. Other SMA based surgical instruments, retractable spatula, hinge-less instruments are also being developed and used [15]. These are also used in micro-endoscopes which are used in mini-invasive surgery [16, 17], as catheters, in laparoscopic applications [18].

SMA has also been used to develop robotic grippers [19]. SMA based grippers with multiple degree-of-freedom can be used as artificial hand for grasping and picking the objects, [20]. Researchers have explored the use of SMA for moving the flaps of airplane. Two SMA wires are being used, one helps the flap to move up and other wire brings it down [21]. SMA actuators are used in MEMs devices [22], to hold lens [23], to move certain parts by certain amount in a required direction [24]. In civil and aerospace applications, SMA elements are employed to suppress vibration by harnessing the inherent energy dissipating capability of SMA [25]. Song *et al* [26] further demonstrated the use of SMA in detecting the crack in civil structures and reducing the extent of damage due to environmental impacts, e.g., earthquake.

TH-1636_10610313

1.2.2 Modeling of SMA Behavior

In the late 80s and 90s, numerous models have been proposed and developed to capture or explain the characteristics of SMAs. Most of the models are developed in terms of their hysteretic thermo-mechanical relations, in order to simulate the behavior of SMAs. There are two common approaches for modeling the behavior of SMA - (a) Phenomenological model and (b) Thermodynamic model. The phenomenological models consist of constitutive law, that gives the relationship between stress, strain, and temperature; and are related using the martensite volume fraction. The martensite volume fraction is determined through the experimentally developed kinetic law which determines the extent of transformation. Phenomenological models are comparatively simple and include less number of parameters, and thus are widely used for engineering and control applications. The material parameters involved in this approach can easily be obtained following a series of tensile test experiment.

Tanaka [27] first proposed the phenomenological model for SMA, assuming material parameters such as elastic modulus, coefficient of thermal expansion and transformation tensor, to be constant and taking martensite volume fraction (ξ) as an internal variable. Here, ξ, varies with temperature and stress. In this model, exponential rule is proposed, to relate the martensite volume fraction with stress and temperature. Liang and Rogers [28] adopted the same constitutive law, as that of Tanaka's Model. However, the phase kinetics are expressed in terms of cosine functions instead of exponential function to avoid numerical complexity.

In both the above-defined model martensite volume fraction (ξ) varies from '1', complete martensite to '0' complete austenite phase and vice versa. One of the most important limitation of these two models is that, they are capable of explaining only the pseudoelasticity effect, but not the shape memory effect. To overcome this, Brinson [29] proposed a modified model. In the Brinson's model, the constitutive relation and the martensite volume fractions

TH-1636_10610313

are redefined using a new internal state variable. The martensite phase is divided into two components, as temperature induced or twinned martensite (ξ_T), and stress induced or detwinned martensite (ξ_S). Thus, the total martensite fraction ξ can be given as $\xi = \xi_S + \xi_T$. Khandelwal and Buravalla [30] modifies the phase kinetics, so as to overcome the problem of Brinsons model. In that model under certain conditions i.e. in the dual transformation zone where the austenite phase is transformed to both temperature and stress-induced martensite, the martensite volume fraction exceeds 1; which is not possible, as 'ξ' can vary only from (1 to 0) for complete reverse transformation and (0 to 1) for forward transformation. This happens because of the independent kinetics of twinned and detwinned martensite as proposed by Brinson [29]. The two main assumptions of the model are

- There should be a coupling between the evolution of twinned and detwinned fractions.
- The twinned martensite fraction can in turn convert into the detwinned fraction due to loading, whereas the detwinned fraction cannot convert to twinned fraction through a decrease in temperature (irreversibility of detwinning transformation).

Buravalla and Khandelwal [31] further modified the Brinson model [29] to address the discrepancy between the differential and integrated form of the constitutive equation of SMA. In this model, the transformation tensor (Ω) has been modified as,

$$\Omega(\xi, \varepsilon) = -\epsilon_l D(\xi) + (\epsilon - \epsilon_l \xi_S)(D_M - D_A). \tag{1.1}$$

Accordingly, the differential form of the constitutive equation has been modified and following which the original integrated form can be derived. The above defined models are applicable for complete transformation, where the load are either monotonically increases or decreases, so as to complete the transformation. But there are cases where, within the transformation zone the phase transformation may not be continuous during thermo-mechanical

TH-1636_10610313

(stress and temperature vary simultaneously) loading. In the case of partial transformation, where the load may vary arbitrarily, different models are proposed, to capture the SMA behavior during arbitrarily loading and unloading.

It has been noted that the martensite volume fraction (ξ) does not depend only on the current stress and temperature, but it also depends on the loading history. To simulate this Bekker and Brinson [32] propose a mathematical model for any thermo-mechanical loading. According to this the phase transformation at a point of loading path occurs only if the direction of loading path has a component in the direction of transformation. It has been proposed that the amount of phase transformation is proportional to the distance traveled along the loading direction. A switching point has been introduced, distinguishing the portion of the path, where the transformation is active, from the rest of the loading path where transformation is inactive. Buravalla and Khandelwal [33] also proposed a path dependency (memory) approach for modeling the behavior of SMA during arbitrarily thermo mechanical loading. According to this the memory within the transformation zone, is defined as the minimum distance on the loading path from the finish transformation boundary of all the points previously traversed. Moreover, within the transformation zone, the transformation will occur only if the distance between the point of interest and the finish boundary is less than the memory parameter, otherwise the transformation will not happen.

Banerjee *et al* [3], proposes a algorithm for updating the above defined memory parameter, when dealing with time varying voltage. According to the above discussed model [32], the transformation in a particular zone is active only if the loading path has a component in the direction of transformation. Hence for this case, the priori knowledge of the loading path is important. But for the cases, where the loading path is not known beforehand, e.g., in a SMA actuated beam or spring biased system. Here, a time varying voltage is applied across the SMA wire to deform and undeform the beam or spring. It has been shown that in these

TH-1636_10610313

cases the state of transformation depends on the rate of the temperature in a given transformation zone. The authors also discusses the algorithm to determine the transformation zone as well as to update the memory parameters. These are very useful so as to implement the Bekker and Brinson [32] model.

All the above defined constitutive equation was derived from the principles of thermodynamics taking martensite fraction as an internal variable. Whereas, Li. *et al* [34] proposed a constitutive model in strain form during both temperature and stress loading process as

$$\begin{aligned} \varepsilon &= \varepsilon^R + \varepsilon^E + \varepsilon^T + \varepsilon^P \\ &= \varepsilon_{res}\xi_{SM} + \frac{\sigma}{\left(\xi_{SM}E_{SM}+\xi_{TM}E_{TM}+\xi_A E_A\right)} \\ &+ \left(\xi_{SM}\eta_{SM} + \xi_{TM}\eta_{TM} + \xi_A\eta_A\right)(T - T_0) + \varepsilon^P \end{aligned} \tag{1.2}$$

Here, the first term in the RHS is the recoverable strain, the second term denotes elastic strain and third and fourth term represents the thermal expansion and plastic strain respectively. E_{SM}, E_{TM} and E_A denote the elastic moduli of detwinned martensite, twinned martensite and austenite, respectively. η_{SM}, η_{TM} and η_A represents the coefficients of thermal expansion in the respective phase. Here the martensite volume fraction of twinned martensite (ξ_{TM}), detwinned martensite (ξ_{SM}) and austenite (ξ_A) phase is determined experimentally using DSC and uniaxial tension test. For this three crystal structures, six different phase transformation processes are proposed.

Researchers have also modified the above mentioned models so as to avoid the discrepancies or complexities depending on the applications [35, 36]. Mathematical model of shape memory alloy that can take care of the hysteretic behavior of SMA is developed in [37]. The thermodynamic model based on free energy and dissipation potential is presented in [38]. The main shortcoming of this model is that it requires a large number of material parameters, which in turn increases the computational time and hence, restricting the model

TH-1636_10610313

for real time applications.

1.2.3 Feedback Control

In the last few decades, Shape Memory Alloy has drawn significant attention as an actuator because of its large strain recovering capability under non-trivial loading condition. These properties emerge because of stress and temperature dependent reversible phase transformation, resulting in drastic change in mechanical, thermal and electrical properties. Consequently, these changes offer non-linear and hysteretic stress-strain response, causing major set-back in using SMA in open loop. To obviate this difficulty, various feedback control strategies are proposed in the literature, necessitating one or more feedback sensor/s to measure the actual response of SMA actuated system in terms of displacement or other kind of motion [39, 40]. These controllers encompass nonlinear and very advanced ones, as presented in [41], where based on variable structure control a nonlinear robust control algorithm is proposed for controlling SMA actuated manipulator. The similar control scheme was implemented by Grant and Hayward [42] for controlling multiple SMA wires placed in antagonistic position. In order to control the SMA actuator, frequency response analysis is carried out by Teh and Featherstone [43], determining the transfer function between input power and output force based on which feedback controller is designed. Few more researchers have developed robust nonlinear feedback controller for precisely controlling the SMA actuator.

Song *et al* [44] presents a new control approach which includes feedforward control action (supplying a current to the actuator to compensate the environmental heat loss), a PD controller, and a robust compensator (increasing the accuracy and stability by compensating the nonlinearities associated with the actuator) for controlling the position of an SMA

TH-1636_10610313

wires embedded composite beam having honeycomb structure. The algorithm is proposed for vibration reduction in rotor-craft blade. Lee and Lee [45] developed a time delay controller (TDC) for controlling the position of spring biased SMA actuator. The dynamics of the actuator is followed based on the Liang's model [28]. The comparison of TDC with another controller, demonstrates that the high gain tuned TDC is more robust than the low gain tuned PID controller in terms of settling time, narrow range of error and overshoot. Teh and Featherstone [46] present a control strategy for fast and accurate control of SMA actuator connected antagonistically. Three control elements namely, anti-slack, rapid-heating and anti-overload mechanisms along with a PID controller are used. These three elements are implemented in the inner loop and in the outer position loop a PID controller is used. Russel and Goret [47] describes a mobile heat sink mechanism for a rotary SMA actuator, so as to increase the operating frequency of the SMA actuator. Position control of the actuator with mobile heat sink yields faster response in comparison to without heat sink. As the tracking control of the SMA actuator is difficult, due to highly nonlinear dynamic behavior of SMAs, hence, in order to achieve a precise tracking control Tai and Ahn [48] propose an adaptive sliding mode control with a PID controller (PIDSMC). In this work, a sliding mode controller is used in addition with PID controller, so as to compensate the hysteresis effect and to perform position tracking more accurately. A gain scheduled controller is designed by Jayender *et al* [49], so as to determine the strain of SMA wire actuator. Based on the difference between the calculated and reference strain, PI controller is developed for controlling the SMA actuator. The results illustrate that the response of the controller is satisfactory for frequencies lower than 0.1Hz. However, if the reference input varies rapidly, then the response of the controller deteriorates.

A novel methodology for tuning the gain of PID controller using fuzzy logic has been presented in [50, 51]. Fuzzy based self tunning PID controller has also been proposed by

TH-1636_10610313

Khodayari *et al* [52] for controlling the SMA actuated artificial finger having 3 degrees of freedom (DOF). The self-tuning fuzzy PID controller has been also adopted for controlling the gripping force in three finger gripper, actuated by SMA wire [53]. For controlling antagonistically connected SMA wire actuator, useful for robotic application, a self-tuning fuzzy PID controller [54] is implemented, using strain as a feedback signal.

1.2.4 SMA as Self-sensing Actuator

It is evident from the above section, that to obviate the nonlinear and hysteretic behavior of SMA wire actuators, various advanced feedback controllers are employed. A feedback controller does need one or more feedback sensors to measure the system responses. This makes the system bulky and costly. To get rid of the requirement of a sensor, researchers explored the change in electrical resistance of SMA during phase transformation as a measure of the system output. In short, this gives rise to the use of SMA wires as a self-sensing actuator.

IKuta *et al* [55] first reported to explore the change in electrical resistance of a SMA wire actuator to control the position of the tip of an endoscope. It has been reported that the electrical resistance of SMA in cold state (martensite phase) is higher than the same at high temperature (austenite phase). He *et al* [56] investigated the effects of R-phase in the electrical resistance of SMA and also discussed the use of electrical resistance of SMA to identify critical transformation temperatures. Using this information the stress-temperature phase diagram of SMA is constructed. Novak *et al* [57] investigated the variation of electrical resistivity of SMA in presence of R-phase. The electrical resistivity of SMA at different phases are proposed to be dependent on stress and temperature and a model has been proposed to determine the electrical resistance of SMA in presence of R-phase. It has been reported that the resistivity in R-phase is higher than the same at austenite and martensite

TH-1636_10610313

phases, individually. Brammajyosula *et al* [58] proposed a model to represent the electrical resistance variation of SMA during phase transformation. In this model the presence of intermediate R-phase is considered.

Several other researchers have explored the use of electrical resistance variation in SMA to control the system response. Ma *et al* [59] developed a multi-layered neural network model to harness the self-sensing capability of SMA actuator. Based on the displacement estimated from electrical resistance, a proportional derivative (PD) controller is used to control the position of the spring biased SMA actuator. Lan and Fan [60] explored the self-sensing technique for controlling the SMA based flexure. First, repeated experiments are carried out to accumulate the data representing strain-electrical resistance relationship of the SMA wire actuator. Sufficient pretension is employed to get rid of hysteresis gap. Then strain-resistance relationships are derived from curving fitting of the experimental data. These fitted polynomials are then used to control the flexure. Lan and Fan [61] investigated the effect of pretension force on the hysteresis gap of strain-resistance and force-resistance relation. As the pretension force increases the hysteresis gap reduces, for a large pretension force the hysteresis gap of strain-resistance curve is almost zero becomes negligible; however it persists in force-resistance behavior. Using these relations the deflection of a flexure finger is controlled.

Lan *et al* [62] also explored the self-sensing capability of SMA for compliant two fingered micro-gripper; mimicking the actuation of a human finger. The polynomial model with force-resistance relation is found to be convenient in comparison to strain- resistance relation; as the bending angle of the finger can directly be obtained from the measure electrical resistance. The Pulse Width Modulation (PWM) based self-sensing feedback controller with inverse hysteresis compensation is used for accurately controlling the SMA actuator [63]. Using the experimental data of voltage and displacement, the mathematical relation between

TH-1636_10610313

the same is obtained following curve fitting. For compensating the major and minor hysteresis loops, inverse hysteresis compensator is used, which is also used to estimate the duty cycle of the PWM signal.

Frust *et al* [64] proposed the use of the self-sensing capability of SMA in controlling the flexible nozzle of a smart inhaler system. The displacement-resistance relation is used as a feedback for the proportional integral controller for controlling the position of the nozzle. Zhang and Yin [65] exploited the self-sensing capability for controlling a SMA actuated robotic ankle. The experimentally derived strain-resistance relation is used as a feedback. A fuzzy tuned PID controller is implemented to control the robotic foot. Liu *et al* [66] studied the self-sensing property of both Ni-Ti and Ni-Ti-Cu and shows that the resistance of Ni-Ti or Ni-Ti-Cu are very sensitive to strain variation and are thus potential candidates for civil structures, e.g., buildings, bridges, dams etc. It has been shown that Ni-Ti-Cu is a better candidate as sensor because of the absence of R-phase; in presence of which the model becomes complicated. Kratz *et al* [67] designed and implemented an SMA wire bundle actuator being used in a bipedal walking robot. A phenomenological model has been derived, that describes the relation between contraction (c) and electrical resistance of SMA (r) as $c = -0.15r + 9.1$. Based on this model a control approach has been established, where resistance can be used as a linear position encoder; thus eliminates the need for external sensors. Tung *et al* [68] developed an active catheter making use of the self-sensing property of NITINOL. The proposed model has been analyzed using finite element method. It has been fabricated in a rapid prototyping machine, followed by laser machining and electro-polishing.

Dunlop and Garcia [69] presented a binary actuated Stewart platform, using NITINOL wire actuators; which are switched on and off to control the position of the platform. The platform links were replaced by bow-like components with SMA wires as the bowstring. The

TH-1636_10610313

electrical resistance of SMA actuator is used to determine the actuator length and is used in a feedback controller for controlling the position of the platform. Li *et al* [70] developed a damper, exploiting the hysteresis involved in the SMA wire behavior. The SMA wires are used as displacement transducers, because of their inherent capability to reveal strain from the electrical resistance behavior. The self-sensing property of SMA has been investigated under different loading frequencies. It has been shown that the effect of loading frequency on strain sensitivity coefficient, i.e., the ratio of the change in electrical resistance and strain, is negligible. However, the effect of loading frequency of the stress-strain response is significant.

Cui *et al* [71] proposed a mathematical model to obtain a relation between the ratio of change in electrical resistance upon initial resistance ($\frac{\Delta R}{R}$) and strain (ϵ) of the SMA. In this model, the electrical resistivity of SMA in individual phase is taken as the linear function of temperature and the total resistivity is assumed to be a linear combination of resistivity of individual phases. It has been shown that in martensite phase, the variation of $\Delta R/R$ with strain is linear and remains unaltered with temperature change. However, in presence of partial or complete austenite, it changes with temperature. Malukhin and Ehmann [72] also explored the self-sensing capability of SMA wire actuator. It has been shown that in case of high temperature and low prestrain, the relation between displacement and the electrical resistance of SMA is linear. To determine the feasibility of self-sensing concept, the sensitivity and the resolution of the method are obtained experimentally. It has been reported that; using self-sensing, the resolution is less than 2 μm and sensitivity is less than 1 μm/mv. The response of an insulated SMA wire has also been compared with that of a SMA wire without insulation. It is observed that the time constant of the insulated wire is three times higher than the non-insulted wire; however, there are less fluctuations in case of the insulated one.

TH-1636_10610313

All the above defined applications of the self-sensing technique are based on the experimentally obtained empirical relation between the resistance variation of SMA actuator with system output; restricting it to a particular system, undergoing a particular thermo-mechanical load for which the empirical relations are derived. Because, with different system parameters and/or with different extent of transformation in SMA, the corresponding resistance and system output relationship changes. In case of neural network one has to repeat a series of experiments for any change in any of the system parameters.

Since the self-sensing approach is a sensor-less control of SMA actuator, hence, instead of using empirical relation, researches have developed mathematical models to estimate the strain from the electrical resistance of SMA [73]. Obviously, the model has to be accurate enough to replace the experimental data. However, this may not be a very practical solution, as various assumptions are involved in a given model. To obviate these difficulties, in this work, a novel approach based on Kalman Filter has been proposed and implemented to explore the self-sensing capability of SMA wire actuators.

1.2.5 Kalman Filter (KF)

Kalman Filter (KF) is a mathematical tool that provides a recursive mean for optimal state estimation of a linear system. KF is used for estimating the state of the system, which is defined by linear stochastic difference equations. In case of systems governed by non-linear equations, the Kalman filters can be used by linearizing the equations about the current operating point. This modified approach is known as Extended Kalman Filter. EKF has been used in various applications for estimating the state of a dynamic system in presence of some or all of the measured noisy state. KF has been proposed in the tracking of flights using radar, condition health monitoring of turbofan engine following parameter estimation technique,

TH-1636_10610313

etc. [74, 75]. Though there are numerous literature available related to the development of Kalman filter and its applications, the one that are related to the state estimation of SMA wire actuated systems, are only presented.

Elahinia *et al* [76] developed an EKF model for estimating the state variables of SMA wire actuated single DOF manipulator. This is done to avoid measuring the state variables in case of very thin SMA wire actuators. The applied voltage is taken as input to the system model and the angular position of the arm of the manipulator is measured to correct the estimated state. The estimation is reported to very sensitive to the sampling time, process and measurement noise. Elahinia *et al* [77] coupled inverse dynamics of the system with variable structure control algorithm to control the position of a single degree of freedom rotary manipulator. The desired stress is calculated using the model based sliding mode control algorithm and the angular position of the arm. The error between the desired stress and the actual stress is fed to the PID controller to decide the control voltage. Here the actual stress is taken to be the estimated stress obtained from the EKF model of the system. The applied voltage and the angular position are the inputs to the EKF model. This nontrivial control strategy reported to yield better results compared to the earlier approaches. Elahinia and Ahmadian [78] employed two nonlinear control algorithms using EKF and variable structure control. The variable structure control is based on a combination of errors in angular position and velocity of a single DOF rotary manipulator. The stress, temperature of the SMA wire and angular velocity of the arm are not measured; rather estimated using an EKF model of the system. The EKF model intakes the applied voltage and the measured angular position of the manipulator to estimate the temperature, stress, and angular velocity. In one of the controllers, the input voltage is so chosen that the temperature of the SMA remains in the active zone. Similar concept but using stress is implemented in another controller. The superior performance of these two controllers are reported. Hassanzadeh *et al* [79] developed

TH-1636_10610313

and implemented an Extended Kalman Filter to estimate the state variables of SMA wire actuated single DOF rotary system. In addition to the state variables, some of the system parameters, namely, the stiffness and damping constant, are also estimated by augmenting the state vector. The estimation is reported to be very close to the model outputs.

To the best of author's knowledge, the Kalman Filter has not been reported to be used for harnessing the self-sensing capability of the SMA wire actuators.

1.3 Motivation and Objective

Due to the large force and displacement that the Shape Memory Alloy wires offer, these have become one of the potential candidates as actuators for low frequency operating conditions. The nonlinear and hysteresis behavior of the SMA actuators can be tamed using sophisticated feedback controllers, which requires feedback sensors. This can be avoided provided the SMA wire itself can be used to feedback the information of the extent of transformation in SMA or the output response of the system being actuated. This has been implemented by correlating the change in electrical resistance of SMA wire with the system output. This is how the SMA wire can be used as a self-sensing actuator. In this direction, researchers have performed experiments on the system of interest under different loading conditions and collected data to correlate electrical resistance and system outputs, e.g., displacement or strain or force etc. Using these data, empirical relations are derived, mostly following curve fitting. These relations are then used to obtain the system output information from the change in electrical resistance information of the SMA wire during actuation and thus allowing SMA wire to be used as a self-sensing actuator. This strategy offers significant accuracy. However, these approach is system specific; this implies that for each system the experiments are to be repeated and the relations are to be derived. If any of the system parameters are changed

TH-1636_10610313

the relations are to be recalculated following a number of experiments. Furthermore, it is to be noted that, the state to electrical resistance is a many to one function and therefore, its inverse may lead to non-unique solution. Hence one needs to be cautious in choosing the inversion method.

Moreover, in most of the systems taken in the literature, either the pretension in the SMA wires are maintained or the system stiffness has been so chosen, that the hysteresis gap becomes insignificant. In case if the hysteresis is significant, then it becomes impossible to derive a unique relation between the resistance of the wire and the system output; as there are infinite possible minor loops. Thus for the soft system, where hysteresis gap is significant, this approach does not provide a practical solution. Furthermore, the electrical resistance of SMA wires measured using voltage divider circuit is found to be very noisy, particularly at low voltage. Thus in presence of noisy data, unique resistance-system output relation cannot be obtained without use of a proper filter. This aspect has not been discussed in the literature.

In another approach, a mathematical model of the system has been developed so as to provide the system response from the resistance variation of the SMA wire. In that case, the model has to be accurate enough to substitute the role of a feedback sensor. In presence of assumptions behind the governing equations, approximations in the system parameters, and external disturbances, the latter approach is not practical. To address these issues a novel approach has been proposed and implemented in this work. The objectives are as follows,

(i) Developing Kalman Filter based model for the SMA wire actuated system, to estimate the system response from the electrical resistance variation of the SMA wire actuator. In this way, the model will take care of the noisy measured resistance of the wire as well as the uncertainties associated with the model. The model has to be developed in such a way, that a time-varying input voltage signals can be used.

TH-1636_10610313

(ii) The developed algorithm has to be implemented in real-time hardware; so that the system response can be estimated online from the measured electrical resistance of the wire. In this direction, an experimental set-up is to be developed, where the SMA wire will be activated through resistive heating for the desired voltage signal and the corresponding variation in electrical resistance of the SMA wire can be measured. In addition, the system response has also to be measured to evaluate the performance of the developed estimator.

(iii) The noise statistics are to be properly decided so as to obtain improved accuracy.

(iv) The effect of the unknown system parameters should also be taken into account.

(v) Finally, the developed algorithm needs to be implemented in low-end hardware so as to facilitate the use of such algorithm in field applications.

1.3.1 Organization of the Present Work

- **chapter 2 :** The complete description of the Shape Memory Alloy (SMA) is presented in this chapter. Two interesting phenomena namely, Shape memory effect and Pseudo-elasticity or Super-elasticity, with the underlying mechanism are discussed. The stress and temperature dependent phase transformation, dictating the extraordinary behavior of SMA are discussed. In this context, the phase diagram is also introduced. The phenomenological constitutive relation and the associated phase kinetics, that are used in this work, are described. The algorithms required for selection of transformation domain as well for updating the memory parameters, that are adopted in this work are also presented. Finally, determination of the temperature of the SMA wire, subjected to resistive heating and convective cooling, following a heat balance equation is also discussed.

TH-1636_10610313

- **chapter 3 :** The development of the Extended Kalman Filter for exploring the self-sensing capability of the SMA wire actuator is presented in this chapter. Two systems, having linear and nonlinear stiffnesses, respectively, are considered to be actuated by the SMA wire actuator. The mathematical models of these two systems, as required for the Kalman filter, are presented. The model comprises of heat balance equation and the constitutive relation of the SMA wire coupled with the stiffness of the system. Next, the implementation of the Kalman filter using two numerical schemes, namely implicit and explicit methods, are discussed. Then the computational advantage of the using implicit scheme over the explicit one is illustrated. Finally, the EKF estimated response of the systems is compared with the response obtained from the model, to validate the potential of the developed EKF model.

- **chapter 4 :** The experimental set-up developed to test the performance of the EKF model is presented. The set-up comprises of an SMA actuated system, a data acquisition system, voltage divider circuit, and a displacement sensor. The voltage divider circuit is designed and developed to measure the electrical resistance of the SMA wire online. The displacement sensor measures the response of the system being actuated by the SMA wire. Two systems are considered. The first one is a linear spring being stretched by the SMA wire actuator, and the second one comprises of a flexible beam being bent by an SMA wire place above the surface of the beam. In the latter case, the force-displacement relation as offered to the SMA wire actuator is non-linear; as the beam is designed to undergo large deformation. For different voltage signals applied across the SMA wire, the system response as estimated by the EKF, using the experimentally measured resistance of the SMA wire, and are compared with the measured response of the systems.

- **chapter 5 :** In this chapter, the development and implementation of an Unscented

TH-1636_10610313

Kalman filter model for a linear spring biased SMA wire actuator are discussed. It starts with the mathematical details involved in an UKF, followed by the detailed steps required to implement the same for self-sensing application of the SMA wire actuators. The UKF estimated system response are compared with that of the same obtained using EKF. Though it offers the same level of accuracy as in case of EKF, however, it is found to be computationally less rigorous as compared to the EKF.

- **chapter 6 :** In this chapter, couple of steps are reported to improve the accuracy of the estimation. Firstly, the transformation temperatures of the SMA wire is obtained following a DSC test. Next, an artificial neural network has been developed based on the EKF estimation and is found to perform better in comparison to another artificial neural network trained only based on experimental data. Then an attempt has been made to take care of the various uncertainties in the model as well as the parameters using variable process noise covariance. However, this approach failed to improve the estimation accuracy. Finally, two uncertain parameters are augmented with EKF model so as to estimate the same along with the state variables. In this approach, a drastic improvement in the estimation accuracy is observed.

- **chapter 7 :** In this chapter, the implementation details of the developed EKF model in a low end hardware, namely, Arduino Uno, is presented. The details of the set-up are discussed followed by a couple of responses that has been obtained using the Arduino board.

- **chapter 8:** In this chapter the research contribution of the work has been summarized and the possible extensions of the current work are presented.

TH-1636_10610313

Chapter 2

Modelling of Shape Memory Alloy (SMA) Wire Behavior

2.1 Introduction

Shape Memory Alloys (SMAs) are basically metallic alloys, undergo large deformation under external load at low temperature and can recover the same upon heating above certain temperature. This capability of remembering its initial undeformed shape, renders these group of metallic alloys the name Shape Memory Alloy. This particular phenomenon is known as Shape Memory Effect. In general, this is widely used in actuator applications, pipe couplings, valves, circuit breakers etc. Another interesting behavior, these group of alloys offer, is referred as Pseudo-Elasticity or Super-Elasticity. Above a certain temperature, the material exhibits large deformation with external load and successively recovers the same upon unloading. It is used in biomedical applications, where a member can undergo large strain without an effective change in stiffness and can recover completely once

TH-1636_10610313

the external load is withdrawn. The Shape Memory Effect (SME) and Pseudo-Elasticity (PE) or Super-Elasticity (SE) emerge because of the reversible solid-solid phase transformation among various variants of Martensite [**M**], and Austenite [**A**]. In this chapter, a brief overview of these phenomena and the underlying mechanics are presented. Then the available phenomenological model to simulate these phenomena are discussed.

2.2 Constituent phases in SMA materials

In general, two different phases are reported to be available in shape memory alloy group. The low temperature phase is called Martensite [**M**] and the one, stable at high temperature, is referred as Austenite [**A**]. In what follows, the basic details of these two phases are illustrated.

2.2.1 Martensite Phase

Martensite [**M**] is stable at low temperature and possess monoclinic or rhombic crystal lattice. In this phase, SMA is having low elastic modulus and thus can easily be deformed. If the SMA is cooled from high temperature below martensite start temperature (M_s) in absence of stress, monoclinic lattice starts forming (refer Fig. 2.1a). This transformation continues till martensite finish temperature (M_f). In literature, twenty four variants of such lattices are reported. However, in absence stress, these lattices accommodate themselves in the twin form as shown in Fig. 2.1a. As a result, insignificant macroscopic change is observed due to this transformation. The resulting phase is referred as twinned martensite (TM). Due to the application of external load, as the stress increases above a certain value, σ_s^{cr}, the stress preferred variants grow, resulting in rhombic structure, referred as detwinned

TH-1636_10610313

martensite (DTM) or stress induced martensite; shown in Fig. 2.1b. This process is called detwinning and it continues till the exhaustion of TM. The stress values at which this stress induced transformation stops is denoted as σ_f^{cr}.

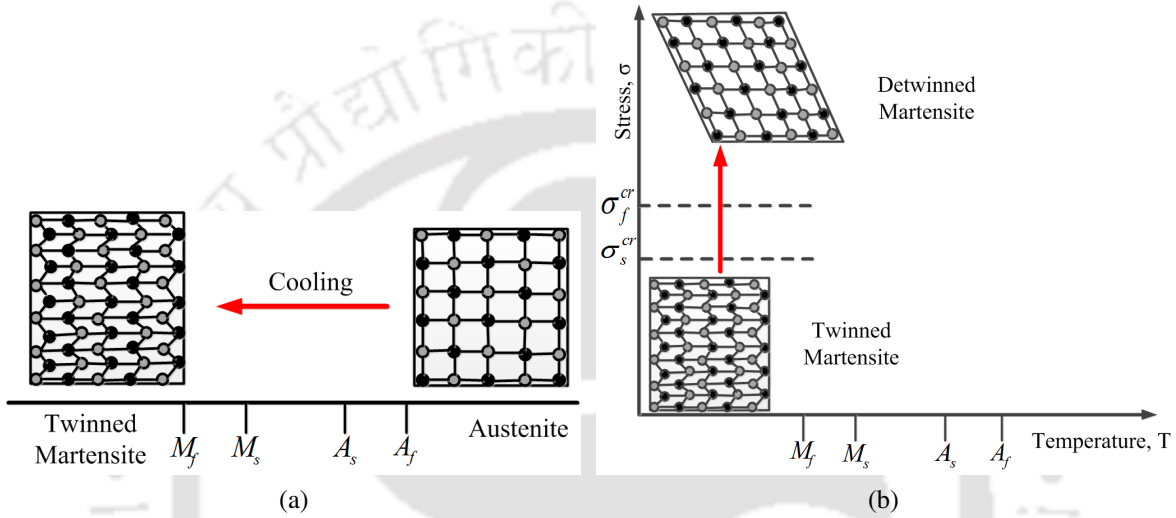

Figure 2.1: (a) Twinned martensite and (b) Detwinned martensite [1].

2.2.2 Austenite Phase

As the low temperature martensite phase is heated above a particular temperature, austenite phase [**A**] starts forming. This temperature is marked as austenite start temperature (A_s) and this transformation continues till austenite finish temperature (A_f). It comprises of body-centered-cubic lattice (BCC) and is very stable at high temperature. This phase is also referred as parent phase and the temperature induced transformation is known as reverse transformation, (see Fig. 2.2). In this phase, the material possesses higher modulus of elasticity compared to the martensite phase.

TH-1636_10610313

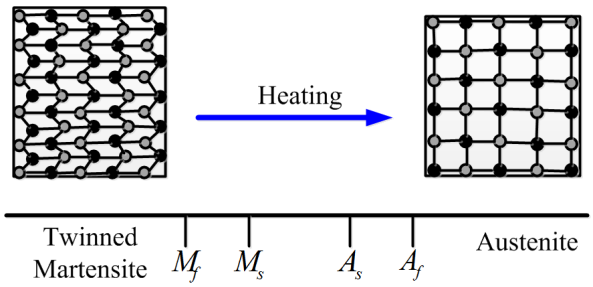

Figure 2.2: Reverse phase transformation in SMA [1].

2.3 SMA Wire Behavior

The stress and temperature induced transformations offers two interesting phenomena namely, (a) Shape Memory Effect (SME) and (b) Super-Elasticity (SE) or Pseudo-Elasticity (PE). Each of these are described briefly in the following section.

2.3.1 Shape Memory Effect (SME)

Figure 2.3a illustrates the formation of twinned martensite (TM), as the material is cooled from high temperature phase austenite, in absence of any external load. This process is referred as forward transformation. Because of the formation of self-accommodating monoclinic lattice, no macroscopic change is observed. Due to the application of external load, initially the material behaves elastically and once the stress exceeds a critical value, referred as σ_s^{cr} in Fig. 2.3a, large strain sets in with a very small change in stress. This happens because of the formation of stress preferred martensite, called as detwinned martensite or stress induced martensite (DTM). This process continues till the point where almost no twinned martensite left. The corresponding stress value is marked as σ_f^{cr}. The process of formation of DTM from TM is called as detwinning transformation. The stress-strain behavior during detwinning is illustrated in Fig. 2.3b. Upon loading above σ_f^{cr}, the material again behaves

TH-1636_10610313

elastically. After unloading, large residual strain, typically 4 - 6%, can be observed following a small elastic strain recovery, as depicted in Fig. 2.3b. At this point, the SMA comprises of only detwinned martensite (refer Fig. 2.3b). This strain starts diminishing, when the material is heated above austenite start temperature (A_s). This happens due to the formation of austenite from detwinned martensite. This temperature induced transformation, often termed as reverse transformation, continues till all the martensite get transformed to austenite at a temperature above austenite finish temperature (A_f). This strain recovery is illustrated in the strain-temperature plane in Fig. 2.3b. This unique capability of SMA to undergo large deformation under external load and subsequently recovering the same upon heating above certain temperature is termed as Shape Memory Effect. The complete cycle of SME is illustrated in Fig. 2.3b.

In practice, the shape recovery of a pre-deformed SMA is exploited in actuator applications. One needs to cool the SMA from above austenite finish temperature to below martensite finish temperature and then deform it by applying an external load to impart a residual strain in it. The recovery of which offers the actuation. Hence, at the end of every actuation, there has to be a mechanism to bring the SMA back to the deformed state, so as to harness actuation in the successive cycles. This behavior is referred as One-Way shape memory effect. However, it is possible to train the material in such a way, that detwinned martensite will automatically form, during cooling, directly from austenite, even in absence of significant stress. This is known as Two-Way shape memory effect. The training often leads to uncertain behavior and reduction in transformation strain.

2.3.2 Pseudo-elasticity

During loading above austenite finish temperature, the material behaves elastically till

TH-1636_10610313

a certain value of stress, denoted as σ_s^M, above which detwinned martensite starts forming directly from austenite. This accompanies a large change in strain with the small change in stress. It continues till the stress value reaches σ_f^M, where austenite get completely converted to detwinned martensite. Beyond σ_f^M, the material again behaves elastically, exhibiting a lesser modulus of elasticity. The stress strain behavior is presented in Fig. 2.4. At the end of loading, large strain ($\sim$6%) can be observed. As the load is removed, the material behaves elastically till the stress decreases to σ_s^A; after which the reverse transformation starts and SMA starts to recover the strain at a larger rate. When the stress value goes below σ_f^A, reverse transformation completes; following which material will again behave elastically for the rest of the unloading path. At the end of unloading, the SMA will recover its initial undeformed shape. The loading and unloading path are different exhibiting large hysteresis, as shown in Fig. 2.4. The capability to undergo large deformation due to loading and subsequently recovering the same upon unloading is referred as Pseudo-Elasticity or Super-Elasticity.

2.4 Phase Diagram

The existence of different constituent phases can be illustrated in a stress-temperature plane, referred as phase diagram. Figure 2.5 depicts a typical phase diagram and its associated parameters. The transformation temperature in absence of any stress are austenite start (A_s), austenite finish (A_f), martensite start (M_s), and martensite finish (M_f) temperatures. These transformation temperatures increase with stress and are described by the inclined straight lines starting through the corresponding temperatures at zeros stress values. For example, the straight line starting from A_s refers to variation of austenite start temperature with stress and similarly, the straight line passing through the A_f denotes increment in austenite finish temperature with stress. Thus the domain marked by the pair of straight lines passing

TH-1636_10610313

through A_s and A_f, respectively, denote the reverse transformation zone, where martensite to austenite transformation takes place. These two straight lines are assumed to be parallel for simplicity in modeling and slope is denoted as C_A. Similarly, the forward transformation zone is denoted by a pair of parallel straight lines, slopes of which is presented by C_M. The two horizontal straight lines represent the stress induced transformation zone, where detwinning transformation starts and finishes at σ_s^{cr} and σ_f^{cr}, respectively. These parameters can easily be determined from Differential Scanning Calorimetry (DSC), followed by a series of isothermal loading-unloading experiment of a SMA sample [80].

TH-1636_10610313

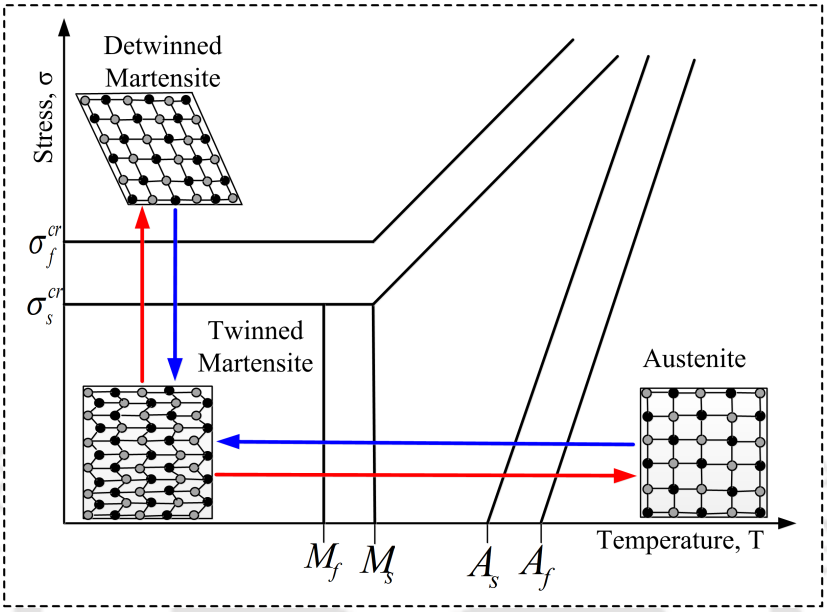

(a)

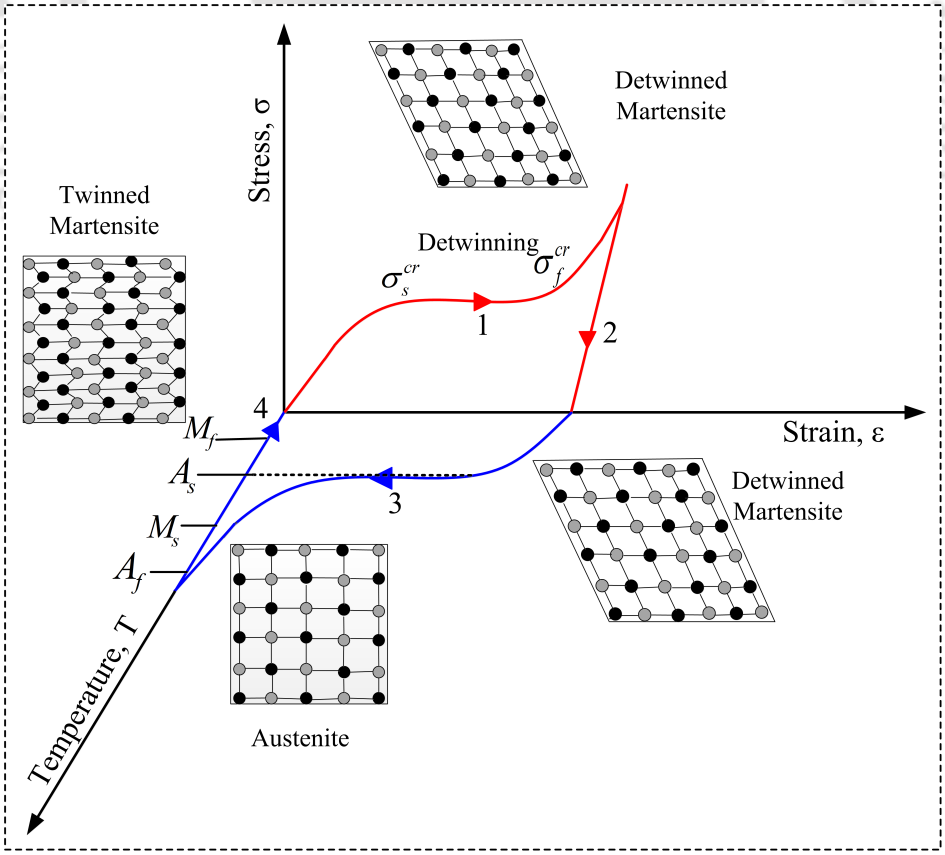

(b)

Figure 2.3: (a) Typical phase diagram of SMA, and (b) Stress-Strain response in SMA during Shape Memory Effect.

TH-1636_10610313

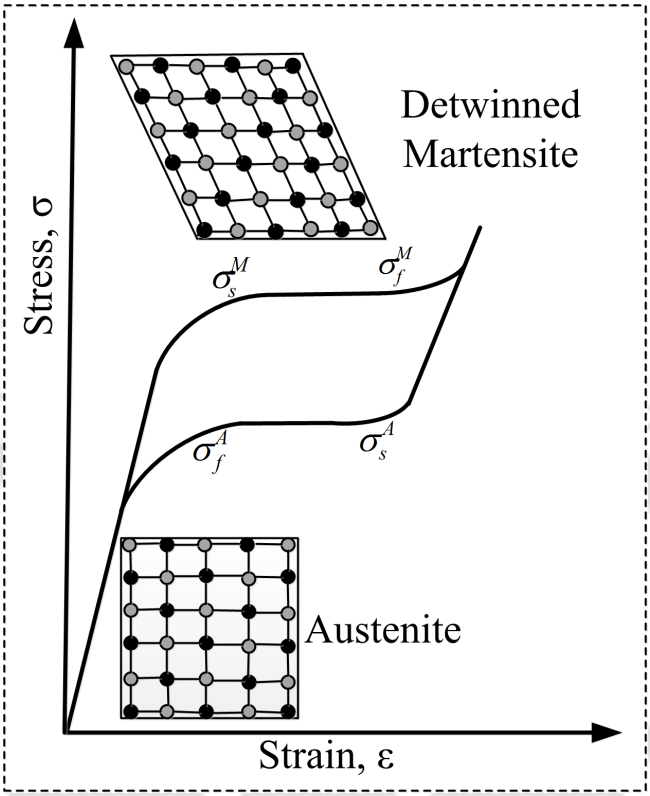

Figure 2.4: Stress-Strain response in SMA during Pseudo-elasticity.

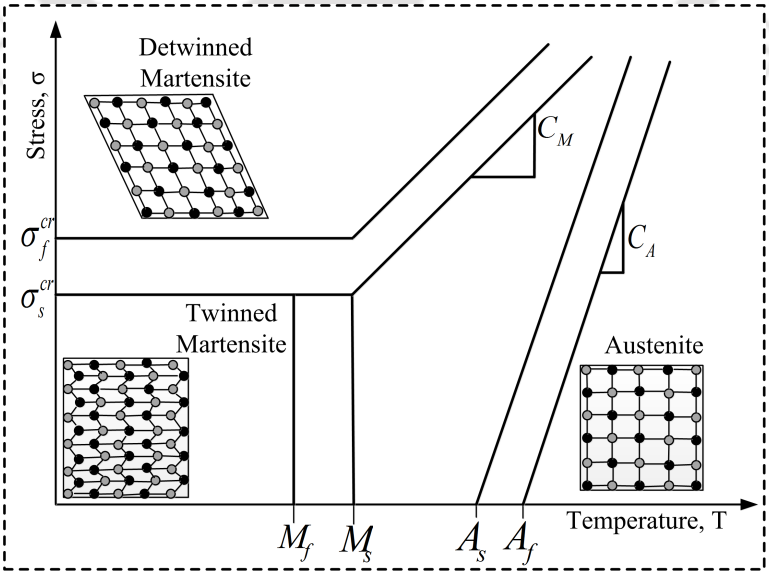

Figure 2.5: Phase diagram of SMA.

TH-1636_10610313

2.5 SMA Actuators

An actuator is a device that can convert electrical energy into mechanical energy. Among all smart materials, SMA based actuators possess high energy density and offers noise-less operation. These are capable of providing large displacement, typically 3 - 4% of its length, and can generate high recovery stress, in the range of 300 - 400 MPa. Of late, SMAs are available in different forms, e.g., wires, helical springs, thin strips, plates, torsion tubes etc. [81]. Out of the different forms available, the SMA wires are mostly used as actuators, as these can easily be heated using Joule effect. Particularly for miniature applications, the fine SMA wires are the potential candidate as actuators, since only few hundred mA current is required for activating the SMA wires.

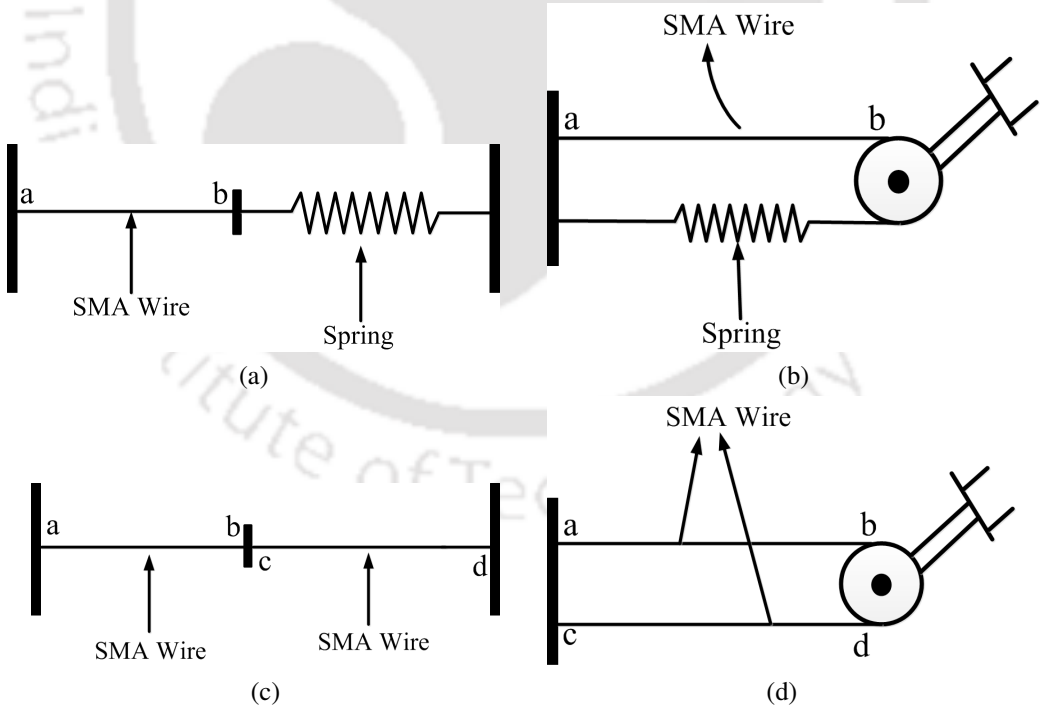

Figure 2.6: (a) Spring biased SMA actuator for linear motion, (b) spring biased SMA actuator for rotational motion, (c) antagonistically placed SMA actuators for linear motion, and (d) antagonistically placed SMA actuators for rotational motion.

TH-1636_10610313

The SMA wire actuators can be used to produce linear as well as rotational motion. Figure 2.6 illustrates different possible configurations in using SMA wire actuators. In Fig. 2.6a, the SMA wire is used against a linear spring, and the application is often referred as spring biased SMA wire actuator. First, a pre-strained SMA wire actuator is fixed with the linear spring or a physical system having stiffness same as that of the spring. As the SMA contracts during heating, the spring resists, resulting in the development of recovery stress in the SMA wire; which in turn deforms the spring or displaces the system. During cooling the austenite phase becomes unstable and in presence of stress or force offered by the deformed spring, the SMA wire extends back to its initial deformed length and is ready for the next actuation cycle. The presence of bias spring is extremely necessary for the SMA wire actuator to work in the next cycle. Based on the similar principle, rotary motion can be generated using a configuration shown in Fig. 2.6b. Figure 2.6c depicts the use of two SMA wires working antagonistically to produce linear motion. This configuration renders higher actuation frequency as the time taken by a SMA wire to extend back to its deformed length solely due to cooling can be shortened by the active extension of the antagonistically placed SMA wire. Based on the similar principle, a rotary joint application can also be conceived as illustrated in Fig. 2.6d. In the present work, linear spring biased SMA wire actuator is considered for simplicity.

2.6 Modeling of SMA

In past few decades, an increasing interest in SMA modeling is observed. This is mainly because of the increasing SMA applications in various fields of engineering and biomedicine. In literature, broadly two approaches are available, namely, (a) Phenomenological model and (b) Thermodynamic model. The phenomenological model comprises of constitutive re-

TH-1636_10610313

lation derived using thermo-mechanics and experimentally obtained phase kinetics. In the constitutive relation, the stress, strain and temperature are related using martensite volume fractions as internal variable. Whereas, the variation of martensite volume fractions with stress and temperature are expressed through phase kinetics. Tanaka [27] first proposed the constitutive model following the basic laws of thermodynamics and derived the phase kinetics from the available experimental data. Brinson [29] modified the constitutive relation by considering non-constant material parameters and two variants of martensite, namely, temperature (TM) and stress induced (DTM) martensite. For SMA wire application, the model proposed by Brinson [29] is mostly referred because of its simplicity in implementation and the ease in determination of the material parameters from simple tensile test experiments. Later on, Buravalla and Khandelwal [31] modified the former approach to remove some of its inconsistencies. A brief description of the 1-D phenomenological model, as proposed by Brinson and later on modified by Buravalla and Khandelwal, are presented in the following subsections.

2.6.1 One-Dimensional Constitutive Behavior of SMA

Following the approach proposed by Liang and Rogers [82] and Brinson [29], the 1-D constitutive model of SMA can be derived from,

$$\sigma = \sigma\left(\epsilon,\ \xi_S,\ \xi_T,\ T\right). \tag{2.1}$$

Here, ϵ refers to the total strain, ξ_S and ξ_T represents the stress and temperature induced martensite volume fraction respectively, and T is the temperature of the wire. The differential

TH-1636_10610313

form of the constitutive relation can be obtained from Eqn. (2.1) as,

$$d\sigma = D\left(\xi\right) d\epsilon + \Omega_S\left(\xi\right) d\xi_S + \Omega_T\left(\xi\right) d\xi_T + \Theta\left(\xi\right) dT. \tag{2.2}$$

Here, Θ denotes the coefficient of thermal expansion and D is the elastic modulus and is determined using rule of mixture as,

$$D(\xi) = D_M \xi + (1-\xi) D_A. \tag{2.3}$$

Here D_A and D_M represents the modulus of elasticity of [**A**] and [**M**] phases, respectively. Similarly, the transformation tensor (Ω) can be defined as,

$$\Omega(\xi) = -\epsilon_l D(\xi). \tag{2.4}$$

Where, ϵ_l represents the maximum residual strain. Following Buravalla and Khandelwal [31] and Brinson [29] the modified form of the transformation tensor appears to be,

$$\begin{aligned} \Omega_S &= -\epsilon_l D(\xi) + \left(\epsilon - \epsilon_l \xi_S\right)\left(D_M - D_A\right), \\ \Omega_T &= \left(\epsilon - \epsilon_l \xi_S\right)\left(D_M - D_A\right). \end{aligned} \tag{2.5}$$

Thus the constitutive relation, as shown in Eqn. (2.2) takes the final form as,

$$\frac{d\sigma}{dt} = D(\xi)\frac{d\epsilon}{dt} - \epsilon_l D(\xi)\frac{d\xi_S}{dt} + (\epsilon - \epsilon_l \xi_S)(D_M - D_A)\frac{d\xi}{dt} + \Theta\frac{dT}{dt}. \tag{2.6}$$

The integrated form however remains the same and can be expressed as,

$$\sigma - \sigma_0 = D\left(\xi\right)\left(\epsilon - \epsilon_0\right) - \epsilon_l D\left(\xi\right)\left(\xi_S - \xi_{S_0}\right) + \left(\epsilon - \epsilon_l \xi_S\right)\left(D_M - D_A\right)\left(\xi - \xi_0\right) + \Theta\left(T - T_0\right). \tag{2.7}$$

TH-1636_10610313

Here, $(.)_0$ represents the initial condition of the parameter within the parenthesis, and ξ is the total martensite volume fraction.

2.6.2 Phase Kinetics

The martensite volume fraction, used to express the extent of any phases present, varies with stress and temperature. The rules, expressing the variations of these phase fractions with stress and temperature are referred as phase kinetics. In phenomenological approach, the phase kinetics are derived first by Tanaka [27], from experimental data following curve fitting. An exponential rule was proposed. Liang and Rogers [82], suggested a cosine rule for computational convenience. In these two approaches, only the total martensite volume fraction was used. Brinson [29] first distinguished the temperature and stress induced martensite and proposed the rules accordingly. The total martensite volume fraction comprises of the temperature and stress induced martensite. However, these rules do not take care of the partial transformation cases. Later, Bekker and Brinson [32] proposed a phase diagram based rule for arbitrary loading cases. Both the models will be discussed briefly in the following subsections.

2.6.2.1 Simple Loading

As discussed earlier, the total martensite volume fraction consists of the volume fractions of temperature and stress induced martensite. In reverse transformation, martensite volume fraction reduces from a non-zero value to zero, as both forms of martensite get transformed to austenite. On the other hand, the martensite volume fraction increases from zero value to one at the end of the forward transformation. In what follows, the transformation rules are discussed zone-wise.

TH-1636_10610313

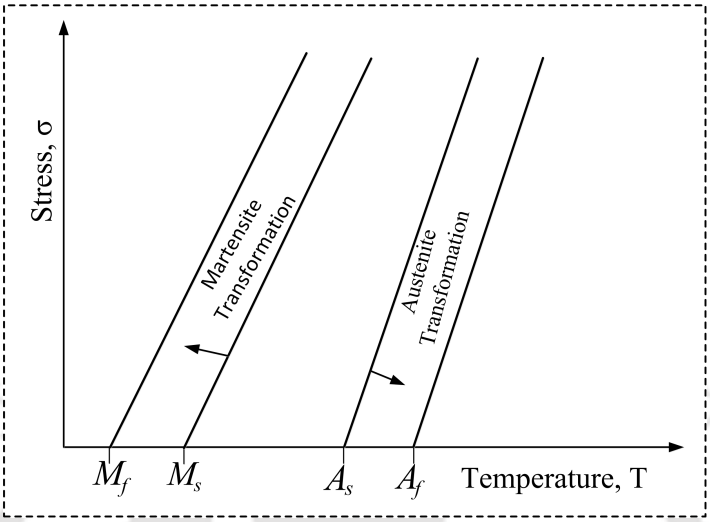

Figure 2.7: Simplified phase diagram of SMA.

2.6.2.1.1 Forward Transformation : According to the Brinson [29], during forward transformation, depending on temperature and stress, the transformation is divided into three cases (refer Fig. 2.5). The variation of ξ_S and ξ_T for all these three cases is presented below.

- For, $T \geq M_s$ and $\sigma_s^{cr} + C_M(T - M_s) < \sigma < \sigma_f^{cr} + C_M(T - M_s)$

$$\xi_S = \frac{1-\xi_{S_0}}{2}\left\{\cos\left[\frac{\pi}{\left(\sigma_f^{cr}-\sigma_s^{cr}\right)}\left\{\sigma-\sigma_f^{cr}-C_M\left(T-M_s\right)\right\}\right]\right\}+\frac{1+\xi_{S_0}}{2}, \quad (2.8)$$

and,

$$\xi_T = \xi_{T_0} - \frac{\xi_{T_0}}{1-\xi_{S_0}}\left(\xi_S - \xi_{S_0}\right). \quad (2.9)$$

Here, M_s and M_f represent the martensite start and finish transformation temperatures respectively, and C_M is the slope of the forward transformation. σ_s^{cr} and σ_f^{cr} are the critical stresses at which stress induced transformation starts and stops and ξ_{T_0} is the initial value of the temperature induced martensite.

TH-1636_10610313

- For, $T < M_s$ and $\sigma_s^{cr} < \sigma < \sigma_f^{cr}$

$$\xi_S = \frac{1-\xi_{S_0}}{2}\cos\left[\frac{\pi}{\left(\sigma_f^{cr}-\sigma_s^{cr}\right)}\left(\sigma-\sigma_f^{cr}\right)\right]+\frac{1+\xi_{S_0}}{2}, \tag{2.10}$$

and,

$$\xi_T = \frac{1-\xi_S}{1-\xi_{S_0}}\Delta_{t\xi}. \tag{2.11}$$

where, if $T > M_f$

$$\Delta_{t\xi} = \frac{1-\xi_{S_0}-\xi_{T_0}}{2}\left\{\cos\left[\frac{\pi}{\left(\sigma_f^{cr}-\sigma_s^{cr}\right)}\left(T-M_f\right)\right]\right\}+\frac{1-\xi_{S_0}+\xi_{T_0}}{2}. \tag{2.12}$$

else

$$\Delta_{t\xi} = 1-\xi_{S_0}. \tag{2.13}$$

- For, $T \geq M_f$ and $T \leq M_s$ and $\sigma \geq \sigma_s^{cr}$ and $\sigma \leq \sigma_f^{cr}$

$$\xi_S = \xi_{S_0}, \tag{2.14}$$

and,

$$\xi_T = \frac{\xi_{T_0}\left(1-\xi_S\right)}{1-\xi_{S_0}}+\frac{1-\xi_{T_0}}{2}\left[\cos\left\{\frac{\pi}{\left(\sigma_f^{cr}-\sigma_s^{cr}\right)}\left(T-M_f\right)\right\}+1\right]. \tag{2.15}$$

For all the above defined cases, the total martensite volume fraction ξ can be calculated as,

$$\xi = \xi_S + \xi_T. \tag{2.16}$$

TH-1636_10610313

2.6.2.1.2 Reverse Transformation : The variation of stress and temperature induced martensite volume fractions over the reverse transformation zone, as shown in Fig. 2.7, are presented for the range, $T > A_s$ and $C_A\left(T - A_f\right) < \sigma < C_A\left(T - A_s\right)$ as,

$$\xi_{M\to A} = \frac{\xi_0}{2}\left\{\cos\left[\frac{\pi}{(A_f - A_s)}\left(T - A_s - \frac{\sigma}{C_A}\right)\right] + 1\right\}, \tag{2.17}$$

and

$$\xi_S = \xi_{S_0} - \frac{\xi_{S_0}}{\xi_0}\left(\xi_0 - \xi\right), \tag{2.18}$$

where

$$\xi_T = \xi - \xi_S. \tag{2.19}$$

The total martensite volume fraction at any instant can be obtained as the sum of the individual ones. Where, A_s and A_f refers to the austenite start and finish temperature, respectively and C_A is the slope of the reverse transformation zone. Here, ξ_0 and ξ_{S_0} represent the initial value of total and stress induced martensite volume fractions.

The above defined model are applicable for complete transformation, where the load either monotonically increases or decreases, so as to complete the transformation. But there are cases, where, within the transformation zone the phase transformation may not be continuous during thermo-mechanical (stress and temperature vary simultaneously) loading. In these type for partial transformation cases, transformation even within a transformation zone may stop and resume depending upon loading conditions. For these type of loading cases, Bekker and Brinson [32] proposed a phase diagram based approach; which has been followed in this work and is discussed briefly in the next section.

TH-1636_10610313

2.6.2.2 Arbitrary Thermo-mechanical Loading

The extent of phase transformation in SMA does not depend only on the present stress and temperature, but also on the loading history. A typical arbitrary loading path in the forward and reverse transformation zones of a phase diagram are depicted in Fig. 2.8a and 2.8b, respectively. The variation of martensite volume fractions along the arbitrary thermo-mechanical loading path can be obtained from the phase kinetics rule proposed by Bekker and Brinson [32]. This model suggests that phase transformation occurs only when the tangent $(\bar{\tau})$ of loading path at the point of interest, has a component in the direction of transformation $(\bar{n}^M)$ in case of forward transformation (refer Fig. 2.8a) and $(\bar{n}^A)$ for reverse transformation (see Fig. 2.8b) [32]. It implies, say, in Fig. 2.8a, the transformation is active if at any point on the loading path $\bar{\tau} \cdot \bar{n}^M$ is positive; otherwise transformation is passive. It has been proposed, that the extent of transformation is proportional to the distance traveled along the same direction. S_j, as shown in Figs. 2.8 are termed as switching points, at which, the status of the transformation changes from active to passive or vice-versa. Thus each segment contains only two switching points (start and stop of transformation) at the boundary. The points at which loading starts within the transformation path is called base point and the variable at this point is called memory parameters, which are referred as σ_j, T_j, ξ_j and ξ_{s_j}. The normalized form of the distance traveled between S_j and S_{j+1} within the loading path can be expressed as,

$$Z^i(\sigma, T; \sigma_j, T_j) = \frac{\left(P^i(\sigma, T) - P^i_j\right)}{\left(P^i_0 - P^i_j\right)}. \tag{2.20}$$

Here, $P^i_j = P^i(\sigma_j, T_j) = \bar{r}^i_j \cdot \bar{n}^i$, $P^i_0 = P^i(\sigma_0, T_0) =$ width of the strip along $\bar{n}^i$ and $P^i(\sigma, T) = \bar{r}^i \cdot \bar{n}^i$, and i takes $[M]$ or $[A]$ for martensite or austenite zone, respectively. Here, $\bar{r}^i_j$ and $\bar{r}^i$ are the position vectors as shown in Figs. 2.8. In what follows, the phase kinetics in each of the transformation zones are defined in detail.

TH-1636_10610313

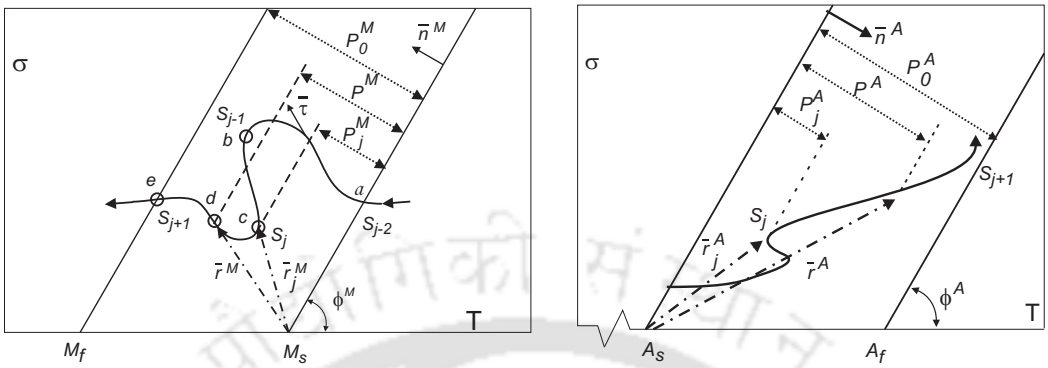

Figure 2.8: Arbitrary thermo-mechanical loading path in (a) forward transformation zone, and (b) reverse transformation zone of phase diagram.

2.6.2.2.1 Forward Transformation : As the temperature reaches the M_s, the austenite phase starts transforming to martensite phase. Thus ξ increases from initial value ξ_0 to 1, in case of complete transformation. For arbitrarily loading, ξ can be determined following the rule proposed by Bekker and Brinson [32]. The normalized distance in the j^{th} segment, i.e., between S_j to S_{j+1} (refer Fig. 2.8a), can be derived from Eqn. (2.20), as

$$Z^M(\sigma, T; \sigma_j, T_j) = \frac{\left(P^M(\sigma, T) - P_j^M\right)}{\left(P_0^M - P_j^M\right)}. \tag{2.21}$$

Here, $P_j^M = \sigma_j \cos\phi^M + (M_s - M_f)\sin\phi^M$, $P^M = \sigma\cos\phi^M + (M_s - T)\cos\phi^M$ and $P_0^M = (M_s - M_f)\cos\phi^M$. Using the cosine rule proposed by Brinson [29], the phase kinetics in $[M]$ phase can be expressed as,

$$\xi = \xi_j + 0.5(1 - \xi_j)(1 - \cos(\pi Z^M)), \tag{2.22}$$

and,

$$\xi_s = \xi_{s_j} + 0.5(\xi' - \xi_{s_j})(1 - \cos(\pi Z^M)). \tag{2.23}$$

TH-1636_10610313

Here, $Z^M = \left\{ \frac{(\sigma \cos\phi^M + (M_s - T)\cos\phi^M) - (\sigma_j \cos\phi^M + (M_s - M_f)\sin\phi^M)}{(M_s - M_f)\cos\phi^M - (\sigma_j \cos\phi^M + (M_s - M_f)\sin\phi^M)} \right\}$,

$\xi' = 0.5(1 + \tanh(\pi Z^\sigma))$, and $Z^\sigma = \frac{\sigma - \sigma_s^{cr}}{\sigma_f^{cr} - \sigma_s^{cr}}$. σ_s^{cr} and σ_f^{cr} are stresses required for initiation and completion of stress induced transformation, respectively.

The rate form of the phase kinetics, can be derived from Eqns. (2.22) and (2.23) as,

$$\frac{d\xi}{dt} = 0.5\pi(1 - \xi_j)\sin(\pi Z^M)\frac{dZ^M}{dt}, \tag{2.24}$$

and,

$$\frac{d\xi_S}{dt} = 0.5\frac{d\xi'}{dt}(1 - \cos(\pi Z^M)) + 0.5\pi(\xi' - \xi_{S_j})\sin(\pi Z^M)\frac{dZ^M}{dt}. \tag{2.25}$$

Here, $\frac{d\xi'}{dt} = \frac{\pi}{(\cosh(\pi Z^\sigma))^2}\frac{dZ^\sigma}{dt}$, $\frac{dZ^\sigma}{dt} = \frac{1}{\sigma_f^{cr} - \sigma_s^{cr}}\frac{d\sigma}{dt}$, and

$\frac{dZ^M}{dt} = \frac{\cos\phi^M \frac{d\sigma}{dt} + \sin\phi^M \frac{dT}{dt}}{(T_j - M_f)\sin\phi^M - \sigma_j \cos\phi^M}$.

2.6.2.2.2 Reverse Transformation : Similarly, in reverse transformation, above A_s, the martensite phase gets converted to austenite phase. During this transformation, 'ξ' varies from initial non-zero value, ξ_0, to 0, in case of complete reverse transformation. For partial transformation, the variation in 'ξ' can be determined following the rule proposed by Bekker and Brinson [32]. Referring Fig. 2.8b, the normalized distance travelled in the j^{th} segment is obtained as,

$$Z^A(\sigma, T; \sigma_j, T_j) = \frac{\left(P^A(\sigma, T) - P_j^A\right)}{\left(P_0^A - P_j^A\right)}. \tag{2.26}$$

Here, $P_j^A = -\sigma_j \cos\phi^A + (T_j - A_s)\sin\phi^A$, $P^A = -\sigma\cos\phi^A + (T - A_s)\sin\phi^A$ and $P_0^A = (A_f - A_s)\sin\phi^A$. Following Brinson [29], the phase kinetics for reverse transformation zone are expressed as,

$$\xi = 0.5\xi_j(1 + \cos(\pi Z^A)), \tag{2.27}$$

TH-1636_10610313

and,

$$\xi_S = 0.5\xi_{S_j}(1 + \cos(\pi Z^A)). \tag{2.28}$$

Here, $Z^A = \left\{ \frac{(-\sigma \cos\phi^A + (T - A_s)\sin\phi^A) - (-\sigma_j \cos\phi^A + (T_j - A_s)\sin\phi^A)}{(A_f - A_s)\sin\phi^A - (-\sigma_j \cos\phi^A + (T_j - A_s)\sin\phi^A)} \right\}$. The rate form of the phase kinetics can be derived from Eqns. (2.27) and (2.28) as,

$$\frac{d\xi}{dt} = -0.5\pi\xi_j \sin(\pi Z^A)\frac{dZ^A}{dt}, \tag{2.29}$$

and,

$$\frac{d\xi_S}{dt} = -0.5\pi\xi_{S_j} \sin(\pi Z^A)\frac{dZ^A}{dt}. \tag{2.30}$$

Here, $\frac{dZ^A}{dt} = \frac{-\cos\phi^A \frac{d\sigma}{dt} + \sin\phi^A \frac{dT}{dt}}{(A_f - T_j)\sin(\phi^A) + \sigma_j \cos(\phi^A)}$.

2.6.2.2.3 Passive Transformation : Other than the two above mentioned zone, any other portion of the phase diagram is referred as dead zone of passive zone; as no phase transformation takes place in these portions of the phase diagram. Here, 'ξ' and 'ξ_S' remain constant; same as the final value of the martensite volume fractions when the transformation stopped. Therefore, 'ξ' and 'ξ_S' can be obtained as,

$$\xi = \xi_j, \tag{2.31}$$

and,

$$\xi_S = \xi_{S_j}. \tag{2.32}$$

and the rate form of phase kinetics becomes,

$$\frac{d\xi}{dt} = 0, \tag{2.33}$$

TH-1636_10610313

and,

$$\frac{d\xi_S}{dt} = 0. \tag{2.34}$$

The phase kinetics for all the above discussed zones can be simply represented as

$$\frac{d\xi}{dt} = \psi_1(\sigma, T; \sigma_j, T_j, \xi_j)\frac{d\sigma}{dt} + \psi_2(\sigma, T; \sigma_j, T_j, \xi_j)\frac{dT}{dt}, \tag{2.35}$$

$$\frac{d\xi_S}{dt} = \psi_3(\sigma, T; \sigma_j, T_j, \xi_j)\frac{d\sigma}{dt} + \psi_4(\sigma, T; \sigma_j, T_j, \xi_j)\frac{dT}{dt}. \tag{2.36}$$

The functions ψ_1, ψ_2, ψ_3 and ψ_4 for each of the transformation zones, can be obtained as the coefficients of $\frac{d\sigma}{dt}$ and $\frac{dT}{dt}$ from Eqns. (2.22) to (2.36). Here, σ_j, T_j, ξ_j and ξ_{s_j} refer to the memory parameters for the current active segment. The memory parameters are basically the values of stress, temperature and martensite volume fractions, at the instant when the transformation stops (referred by 'b' in Fig. 2.8a) and are updated at each time step till the transformation resumes (denoted as 'c' in the same figure). Once the transformation resumes these parameters remains constant for that active segment of the loading path. The algorithm followed to determine the transformation zone and updating the memory parameters, are described in details in the next section.

2.7 Implementation of Phase Kinetics

The phase kinetics proposed by Bekker and Brinson [32] requires some special consideration. Since the loading path is not known in advance, then how can someone determine the component of the loading direction in the transformation direction. For the loading cases considered in the present work, it can easily be conceived, that the increase in temperature will always lead to stress increment in the reverse transformation zone. Similarly, stress

TH-1636_10610313

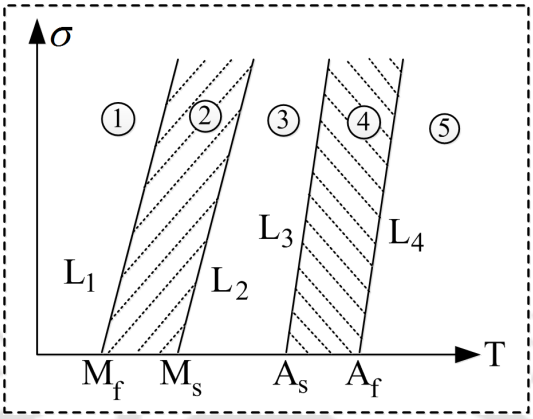

Figure 2.9: Phase transformation zone of SMA.

will decrease while the temperature decreases in the forward transformation zone. Thus the problem lies in the determination of current transformation zone and then apply the phase kinetics appropriately. In this case, the algorithm proposed by Banerjee *et al* [3] is followed for determination of the zone and updating the memory parameters.

2.7.1 Algorithm for Zone Selection

Figure 2.9 presents a phase diagram of SMA, showing forward, reverse and passive transformation zones. The forward transformation zone of SMA is represented by '2', and the reverse transformation zone is presented by '4', while the '1', '3' and '5' refer the passive transformation zones. The algorithm is all about determining which side a point lies with respect to a given straight line. It is discussed zone wise as follows.

- **Forward Transformation Zone :** The equation of the two straight lines defining the forward transformation zone can derived as,

$$\begin{aligned} f_{L_1}(T,\sigma) &\Rightarrow \sigma - (T - M_f)\tan\phi^M = 0, \\ f_{L_2}(T,\sigma) &\Rightarrow \sigma - (T - M_s)\tan\phi^M = 0. \end{aligned} \tag{2.37}$$

TH-1636_10610313

Thus for a given point in the phase diagram, defined as (T, σ), if $f_{L_1} \leq 0$ and $f_{L_2} \geq 0$, then the point lies in the forward transformation zone and the equations defined in section 2.6.2.2.1 are to be used to model the phase kinetics.

- **Reverse Transformation Zone :** Similarly, the equation of the two straight lines describing the reverse transformation zone can be obtained as,

$$\begin{aligned} f_{L_3}(T, \sigma) &\Rightarrow \sigma - (T - A_s) \tan \phi^A = 0, \\ f_{L_4}(T, \sigma) &\Rightarrow \sigma - (T - A_f) \tan \phi^A = 0. \end{aligned} \tag{2.38}$$

  Therefore, for a given (T, σ) in the phase diagram, if $f_{L_3} \leq 0$ and $f_{L_4} \geq 0$, then the point is currently in the reverse transformation zone and the phase kinetics defined in section 2.6.2.2.2 are used.

- **Passive Transformation Zone :** If the above defined two conditions are not satisfied then the point lies in, i.e., either in zone '1', '3' and '5'. In that case, the phase kinetics as discussed in section 2.6.2.2.3 need to be used.

Following this above mentioned algorithm, the zone where the current point's lies are determined. Now, in an active segment, one needs to know the memory parameters, and hence those are to be updated as soon as there is any change in the status of transformation. The following section discusses the same.

2.7.2 Algorithm for Updating the Memory Parameters

In this section, the algorithm proposed by Banerjee *et al* [3] for updating the memory parameters are discussed. According to this algorithm, once the domain in which the SMA is currently in, is identified, then the memory parameters are updated according to the following

TH-1636_10610313

steps,

(a) If the current point (T, σ) is in reverse transformation zone and the rate of change of temperature ($\frac{dT}{dt}$) > 0, then reverse transformation is active and the ψ_1, ψ_2, ψ_3 and ψ_4 are determined from Eqns. (2.29) - (2.30).

(b) Similarly, if the current point (T, σ) is in forward transformation zone, and $\frac{dT}{dt} < 0$, then forward transformation is active and ψ_1, ψ_2, ψ_3 and ψ_4 are computed using Eqns. (2.24) - (2.25).

(c) Else SMA belongs to passive zone and ψ_1, ψ_2, ψ_3 and ψ_4 are equal to zero. Then memory parameters are updated.

2.8 Heat Balance Equation

In practice, the temperature of the SMA wire is raised through Joule heating. As the electrical resistivity of Ni-Ti alloy wire is high, it can easily be heated using few hundred mA electric current. To obtain the temperature of the SMA wire, a heat balance equation is derived considering the wire as a thin cylinder, having heat source, heat loss terms due to convection and latent heat during transformation. Since in the present study a voltage source has been used, the heat input is written in terms of the time varying voltage $V(t)$. The differential form of the heat balance equation appears to be as,

$$C_v \frac{dT}{dt} = \frac{1}{V_m}\left(\frac{V(t)^2}{R} - hA_{surf}(T - T_0)\right) + \lambda\frac{d\xi}{dt}. \tag{2.39}$$

The term in the Left-Hand-Side (LHS) represents the heat required per unit volume to raise the temperature of SMA wire, where V_m is the total volume of the wire. C_v represents the

TH-1636_10610313

and specific heat capacity of the SMA wire and is obtained using the rule of mixture as,

$$C_v = C_{vM}\xi + (1-\xi)C_{vA}. \tag{2.40}$$

Here, C_{vM} and C_{vA} denote the specific heat of SMA material when it is completely in martensite and austenite phases, respectively. The first term in the Right-Hand-Side (RHS) of Eqn. (2.39), refers to the rate of heat generation due to application of the time dependent voltage, $V(t)$, and R is the total electrical resistance of the SMA wire. The second term in the RHS depicts the convective heat loss, where A_{surf} is the total surface area of the wire and h represents the coefficient of convective heat transfer between the SMA wire and the environment. To make it more realistic, h is approximated, following Elahinia and Ahmadian [41], as second order polynomial of temperature (T) as,

$$h = h_0 + h_1 T^2. \tag{2.41}$$

Here, h_0 and h_1 are constants. The third term in the RHS of Eqn. (2.39) is used to take care the latent heat of absorption and emission per unit volume of the wire during reverse and forward transformations, respectively. Here λ denotes the latent heat of transformation per unit volume.

TH-1636_10610313

2.9 Summary

This chapter presents a brief description of SMA behavior. Two interesting phenomena namely, Shape Memory Effect and Pseudo-Elasticity or Super-Elasticity exhibited by shape memory alloy are described. The underlying micro-structural changes are also illustrated. The details of phase transformation depending on stress and temperature of SMA are also discussed. A typical phase diagram of SMA is also presented. The various forms of commercially available SMA and different types of SMA wire based actuators are also discussed. The mostly referred phenomenological model for modeling the behavior of 1-D SMA element is presented. The modifications in the constitutive and phase kinetics of SMA, for arbitrary thermo-mechanical loading are also discussed. Two important algorithms required for the determination of the transformation domain and updating the memory parameters are also presented. The heat balance equation which has been used in the present work to determine the temperature of SMA, is also discussed.

TH-1636_10610313

Chapter 3

Development of Extended Kalman Filter for Self-sensing Application of Shape Memory Wire Actuator

3.1 Introduction

This chapter presents the development of an Extended Kalman Filter (EKF) to harness the self-sensing capability of Shape Memory Alloy (SMA) wire actuator. The self-sensing property of SMA has been explored for both SMA actuated linear and nonlinear systems. As discussed in the earlier chapter, the recovery stress developed during reverse transformation is being used to harness the SMA wires, as actuators. During phase transformation the modulus of elasticity, thermal conductivity, specific heat as well as electrical resistivity of SMA varies. Due to change in electrical resistivity and geometry, the electrical resistance of SMA wire changes significantly. This information can be used as a measure of the output of the

TH-1636_10610313

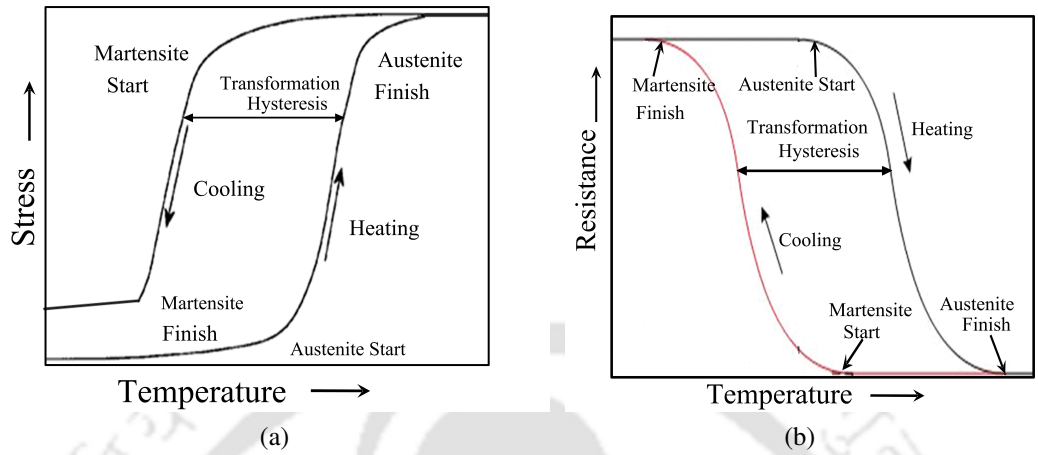

Figure 3.1: (a) Variation of stress with temperature in SMA wire, and (b) corresponding change in electrical resistance of SMA with temperature.

system being actuated. This is referred as a self-sensing actuator. In this chapter, an Extended Kalman Filter models of two SMA wire actuated systems are developed to estimate the stress and temperature of the wire from the measured electrical resistance of the same. First, the system dynamics are being presented, as are required for developing the Kalman Filter. Then some of the implementation issues are discussed followed by the simulation results, validating the developed models.

3.2 Self-sensing SMA Wire Actuator

A pre-deformed SMA wire during heating, start contracting above austenite start temperature. If this free contraction is prevented, recovery stress develops to move the system, that is preventing it from recovery. This recovery stress is exploited in actuator applications of SMA wires, e.g., in pulling a load against gravity, working against a linear or torsional spring etc. The variation of stress with temperature in a typical case of constrained recovery is depicted in Fig. 3.1a. The nonlinear and hysteresis behavior can be observed. Thus to control the system output, one needs to resort to a sophisticated control system, where a feedback sensor is

TH-1636_10610313

inevitable. This yields the whole system bulky and makes SMA wire a less preferable choice as actuator, particularly, for small scale applications. To obviate this, the electrical resistance variation in SMA wires during phase transformation, has been harnessed as a measure of the output of the system. The typical electrical resistance variation during constrained recovery (Fig. 3.1a) is shown in Fig. 3.1b. It decreases during reverse phase transformation, as the electrical resistivity of SMA in complete austenite phase is significantly less (18%) than that of the same in complete martensite phase. Moreover, the change in geometry also plays a role in the variation of electrical resistance of SMA. If the change in electrical resistance information is harnessed, to measure the recovery stress or the output of the system being actuated, then one can get rid of the feedback sensors; making SMA wire a potential candidate as actuators for micro-scale applications. In other words, SMA wire can be harnessed as self-sensing actuators. In this work, Kalman Filters are explored to develop self-sensing application of SMA wire actuators. In this approach, starting from a known state of SMA, at each time step the state is calculated from the system dynamics and are updated following the measurement; and hence are expected to obviate the concern of non-unique estimate.

3.3 SMA Wire Actuated Systems

In the present study, SMA wire actuated (a) linear and (b) nonlinear systems are considered. A brief description of both the systems are presented below.

(a) Linear system

A linear spring biased SMA wire actuator is shown in Fig. 3.2. The linear spring represents a physical system offering a resistance force proportional to the displacement. An undeformed SMA wire is stretched beyond the stress, σ_s^{cr} and unloaded, producing a desired

TH-1636_10610313

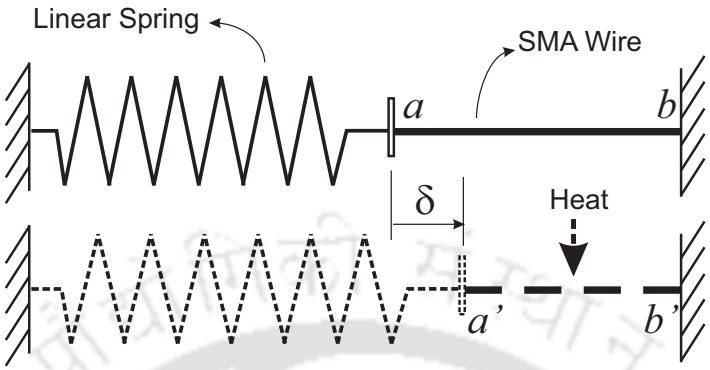

Figure 3.2: Schematic of a linear spring biased SMA wire actuator.

pre-strain in the wire. Then the pre-deformed SMA wire is connected to the linear spring with an acrylic block in between at 'a', as shown in Fig. 3.2. The other ends of the SMA wire and the spring are fixed to two rigid walls. As the SMA wire is heated using Joule's effect, by applying voltage across the SMA wire, austenite phase starts forming above austenite start temperature. Consequently, the SMA wire tries to contract, which is resisted by the spring force. Hence a recovery stress develops in the wire which in turn deforms the spring. The recovered SMA wire is presented by $a'b'$ and the displacement of the acrylic block or the stretch in the spring is depicted as δ in Fig. 3.2. Note that during this process the electrical resistance of the SMA wire drops, due to the formation of austenite and change in geometry of the wire.

Once the voltage applied is reduced or cut-off, the temperature of the SMA wire reduces, mainly due to the convective or natural cooling. Below martensite start temperature, twinned martensite forms, which in the presence of the restoring force of the spring gets converted to detwinned martensite, stretching the SMA wire back to its initial deformed length. This enables the SMA wire to actuate in the next cycle. During cooling the electrical resistance the SMA wire again increases back to its initial value. The main objective of this work is to determine the change in the length of the spring (δ), without using any displacement or force sensor; rather from the change in electrical resistance of the SMA wire during phase

TH-1636_10610313

transformation. This will allow one to exploit the self-sensing property of SMA and use SMA wire as a sensor as well as an actuator. In what follows, the development of an Extended Kalman Filter (EKF) is presented to estimate the change in length of SMA actuated spring from the noisy electrical resistance signal of the SMA.

(b) Nonlinear System

The nonlinear system as depicted in Fig. 3.3, consists of a SMA wire actuated cantilever

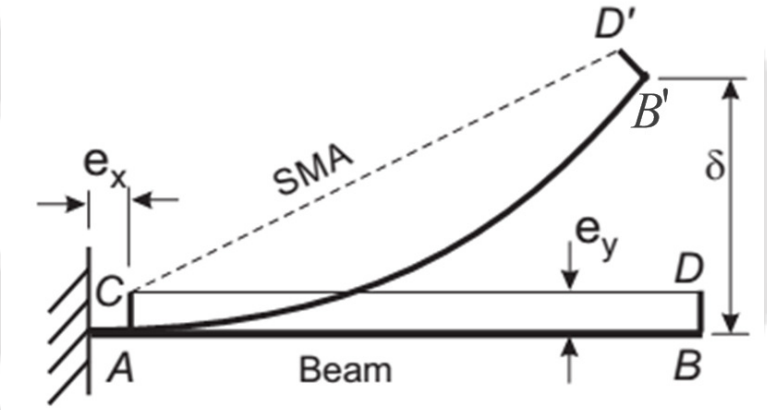

Figure 3.3: Schematic of a SMA wire actuated cantilever beam.

beam. Here *AB* is the undeformed beam and SMA wire *CD* attached to it with an offset e_y. The purpose of keeping the offset is to enhance the moment applied by the SMA wire to produce larger displacement. Determination of the optimum offset value, rendering maximum end displacement of the beam, is discussed in Banerjee *et al* [83]. As the temperature of the SMA wire actuator is increased through resistive heating (Joule's effect), the SMA undergoes constrained recovery as discussed above; resulting in the deformation of the beam to a new configuration *AB*′. During this process, the offsets AC and BD are assumed to be perfectly rigid, undergoing only rigid body motion. Here, the objective is to determine the end displacement of the beam without using any external sensor. Rather, the change in

TH-1636_10610313

electrical resistance of the SMA wire during phase transformation has to be used to estimate the deformation of the beam. Following a similar approach, as in case of the linear system mentioned above, an EKF based tool has been developed for this purpose.

3.4 Extended Kalman Filter (EKF)

Kalman filter is a recursive linear estimator. An estimator refers to a tool, capable of estimating the future behavior of a system from the available information up to the current instant. Various different filters are developed in literature, applicable for different purposes. Among which the Kalman filter is reported to be the simplest and optimal for linear system. Since the dynamics of the SMA wire actuator involves non-linearity, a modified version of the Kalman filter, known as Extended Kalman Filter is adopted for the present case. Extended Kalman filter is basically a Kalman filter applied over the linearized version of a nonlinear dynamic system.

Application of EKF :

EKF are commonly used in those application, where measuring the variable of interest is difficult and the use of the sensor makes the system bulky and expensive. Some of the applications of EKF are presented below :

1. EKF is use to estimate the positions and velocities of a tactile ballistic missile [84].
2. To estimate the position and velocity of a free falling body towards earth [85].
3. To estimate the concentrations of different constituents and their growth rate in a chemical process [86].
4. In addition to state estimation, EKF can also be used to estimate the parameters of a

TH-1636_10610313

given system. It has been used to estimate the electrical resistance and inductance of the induction motor [87], condition health monitoring of turbofan engine [75], etc.

The basic steps of Extended Kalman Fitler are discussed in the following section. Briefly, the EKF is a nonlinear state estimator, that provides the recursive means to estimate the state of a discrete time controlled system [88]. An EKF model estimates the current state of the system using

- The nonlinear system dynamics,
- The statistical information of the process and measurement noise,
- Information of the state variables at previous instant,
- Available measurement at the current instant.

In view of describing the basic steps of EKF, a discrete nonlinear system model and observation or output model are presented below.

(a) **Discrete time nonlinear system model**

At any time instant t_k, the non-linear dynamic system comprises of,

- **Process model** : It describes how the state propagates in time based on the external influences, such as input and noise.

$$\mathbf{X}_{t_k} = \boldsymbol{\eta}(\mathbf{X}_{t_{k-1}}, \mathbf{u}_{t_k}) + \mathbf{w}_{t_{k-1}}. \tag{3.1}$$

Here, $\{\mathbf{w}\}$ represents the process noise vector, which is used to take care of the following errors :

  - Modelling uncertainties.

TH-1636_10610313

- Parametric uncertainty - Uncertain variation in parameters associated with the model.
- Discretization error - As the higher order terms are neglected while linearizing the nonlinear terms.

- **Measurement model** : It represents the outputs or observations ($\mathbf{Y}$) in terms of state of the dynamic system and measurement noise as

$$\mathbf{Y}_{t_k} = \mathbf{\Gamma}(\mathbf{X}_{t_k}) + \mathbf{v}_{t_k}. \tag{3.2}$$

Similarly, $\{\mathbf{v}\}$ denotes the measurement noise vector, representing uncertainty in the measurement.

(b) **Assumptions**

The basic assumptions are as follows:

(i) **White Gaussian Noise**

In Kalman filter, the process and measurement noises are assumed to be white Gaussian. Gaussian noise refers to a random signal, which can be uniquely characterized only by mean and variance. Here, white refers to equal power distribution over all frequencies. It implies,

$$\begin{aligned} p(\mathbf{w}) &\sim N\left(0,\ \mathbf{Q}\right), \\ p(\mathbf{v}) &\sim N\left(0,\ \mathbf{M}_n\right). \end{aligned} \tag{3.3}$$

where,

$$\begin{aligned} \mathbf{Q} &= E\left[\mathbf{w}\mathbf{w}^{\intercal}\right], \\ \mathbf{M}_n &= E\left[\mathbf{v}\mathbf{v}^{\intercal}\right]. \end{aligned} \tag{3.4}$$

Here, $\mathbf{Q}$ represents the process noise covariance matrix and $\mathbf{M}_n$ is the measurement noise covariance.

TH-1636_10610313

(ii) **Independent Process and Measurement Noise.**

- Both noises are independent and uncorrelated to each other i.e. variation in one doesn't affects the other.

$$E\left[\mathbf{w}\mathbf{v}^{\intercal}\right] = 0. \tag{3.5}$$

(c) **Algorithm**

In each time step, EKF consists of two steps, namely, **"Time Update"** and **"Measurement Update"**. These are discussed below.

(i) **Time update :**

In this step, EKF at current instant estimate the state variables of the system from the same correponding to the previous instant, using process nonlinear vector function $\{\boldsymbol{\eta}\}$. This can be expressed as,

$$\hat{\mathbf{X}}_{t_k}^{-} = \boldsymbol{\eta}(\hat{\mathbf{X}}_{t_{k-1}}^{+}, \mathbf{u}_{t_k}). \tag{3.6}$$

The obtained state ($\hat{\mathbf{X}}_{t_k}^{-}$) is called a-priori state estimate and is computed using the process model. The state error covariance matrix ($\mathbf{P}$), defined as $\mathbf{P} = E\left[(\mathbf{X} - \hat{\mathbf{X}})(\mathbf{X} - \hat{\mathbf{X}})^{\intercal}\right]$, is calculated following

$$\mathbf{P}_{t_k}^{-} = \mathbf{J}_{t_{k-1}} \mathbf{P}_{t_{k-1}}^{+} \mathbf{J}_{t_{k-1}}^{T} + \mathbf{Q}_{t_{k-1}}. \tag{3.7}$$

(ii) **Measurement Update :**

In this step, the a-priori state, obtained using Eqn. (3.6), and the state error covariance, determined from Eqn. (3.7), are updated using measurement data available at

TH-1636_10610313

current instant. The a-priori state is updated following,

$$\hat{\mathbf{X}}_{t_k}^{+} = \hat{\mathbf{X}}_{t_k}^{-} + \mathbf{G}_{t_k}[\mathbf{Y}_{t_k} - \mathbf{\Gamma}(\hat{\mathbf{X}}_{t_k}^{-})]. \tag{3.8}$$

Here, the posteriori state ($\hat{\mathbf{X}}_{t_k}^{+}$) can be viewed as a weighted average of the a-priori state and the measurement residual ($\mathbf{Y}_{t_k} - \mathbf{\Gamma}(\hat{\mathbf{X}}_{t_k}^{-})$), which, represents the discrepancy between the actual measurement and the estimated output. This is also referred as innovation. If the estimated output is very close to the actual measurement, then the state estimation can be assumed to be accurate. On the other hand, if the difference between the measured and the estimated output is large, then the estimated state is inaccurate. Here comes the role of Kalman gain, which decides the influence of the a-priori estimation and experimental data. The Kalman gain is determined based on the covariance of process and measurement noises. If the measurement is very noisy, manifested by large $\mathbf{M}_n$, the Kalman gain becomes small; giving more credit to the a-priori state and vice-versa. Similarly, Kalman gain will be large, for high process noise covariance; implying high weightage to the measurement. The Kalman gain is obtained using,

$$\mathbf{G}_{t_k} = \mathbf{P}_{t_k}^{-}\mathbf{H}_{t_k}^{T}(\mathbf{H}_{t_k}\mathbf{P}_{t_k}^{-}\mathbf{H}_{t_k}^{T} + \mathbf{M}_{n,\,t_k})^{-1}. \tag{3.9}$$

The inverse term in the RHS of Eqn. (3.9) is called residual covariance, representing the uncertainty in the estimated output of the system. Finally, the a-priori state error covariance matrix is updated following,

$$\mathbf{P}_{t_k}^{+} = (\mathbf{I} - \mathbf{G}_{t_k}\mathbf{H}_{t_k})\mathbf{P}_{t_k}^{-}. \tag{3.10}$$

TH-1636_10610313

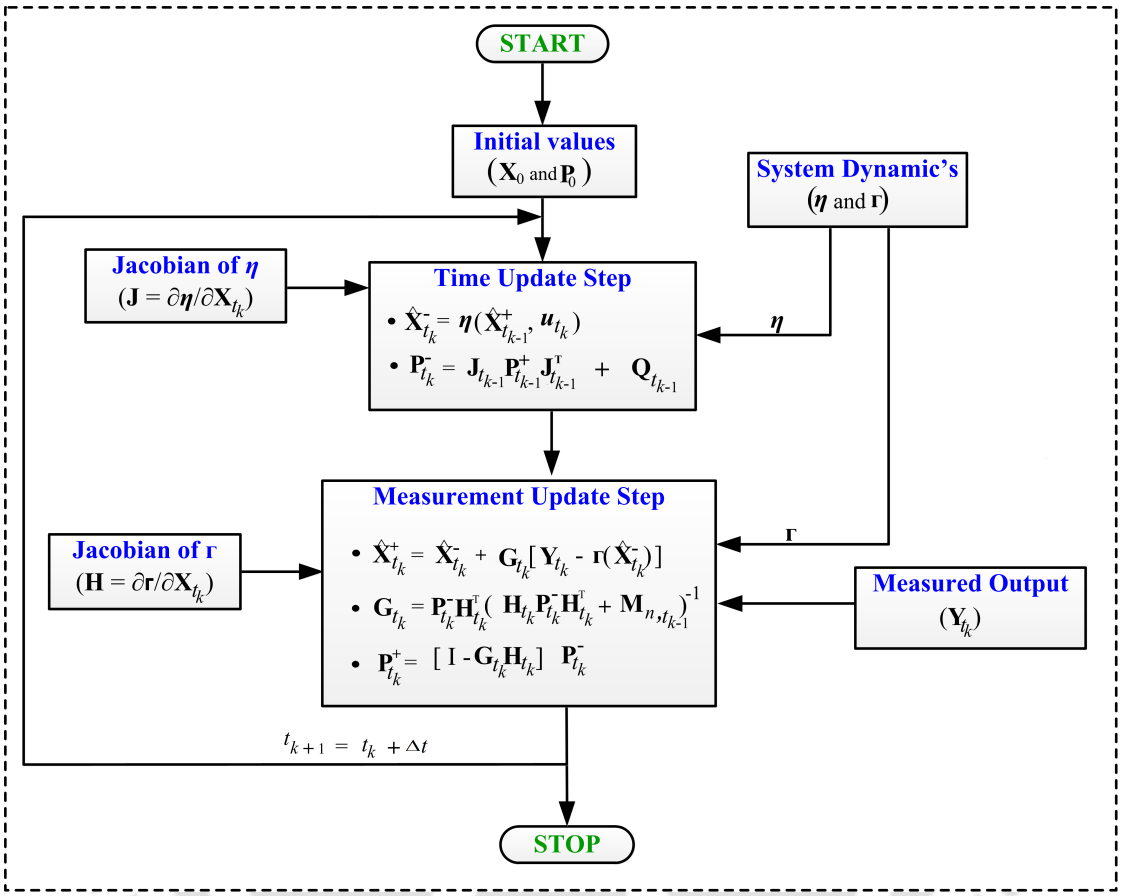

Figure 3.4: Flow diagram of the EKF model.

The above stated algorithm is shown schematically in Fig. 3.4. To make use of this estimator for the present case, i.e., estimating the output of the SMA actuated system from the electrical resistance variation of the wire, one needs to derive the dynamics of the system, determine the noise statistics and to establish an experimental setup for measuring electrical resistance of the SMA wire during actuation. The first two are discussed in the following sections.

TH-1636_10610313

3.5 Modeling

In the present study, the input to the system is applied voltage, ($V(t)$), and the output or observation is the electrical resistance of SMA wire actuator. Physically, the applied voltage controls the temperature of the SMA wire, which in turn activates phase transformation; resulting in the development of recovery stress in the wire due to the constraint posed on it. Thus one needs the heat balance equation to obtain temperature variation in the wire over time and the constitutive relation of the SMA wire, helps in determining the stress in the wire for the temperature change. In addition, the martensite volume fractions should vary following the phase kinetics. Note, that the force-displacement relation of the system should also be taken into account. Moreover, the electrical resistance needs to be expressed in terms of the state variables, in order to facilitate the computation of the innovation term. These basic equations for each of the systems, described in section 3.3, are discussed below.

Following Eqn. (2.6), the difference form of the constitutive equation can be written as,

$$\Delta\sigma = D(\xi)\Delta\epsilon - \epsilon_l D(\xi)\Delta\xi_s + (\epsilon - \epsilon_l\xi_s)\Delta D_\epsilon \Delta\xi. \tag{3.11}$$

Here, $\Delta D_\epsilon = (\epsilon - \epsilon_l\xi_s)\,(D_M - D_A)$, D is the modulus of elasticity, ϵ and ϵ_l represent the current and residual strain, respecively. ξ and ξ_s are the total and stress induced martensite volume fractions, respectively.

Similarly, the difference form of the phase kinection as defined in section 2.6.2.2 can be expressed as

$$\Delta\xi = \psi_1\Delta\sigma + \psi_2\Delta T, \tag{3.12}$$

$$\Delta\xi_s = \psi_3\Delta\sigma + \psi_4\Delta T. \tag{3.13}$$

TH-1636_10610313

Substituting, $\Delta\xi$ and $\Delta\xi_s$ from Eqns. (3.12) and (3.13) into Eqn. (3.11), renders

$$X_a\Delta\sigma = D\Delta\epsilon + Y_a\Delta T. \tag{3.14}$$

Here, $X_a = [1 - \{\Delta D_\epsilon \psi_1 - \epsilon_l D\psi_3\}]$ and $Y_a = [\Delta D_\epsilon \psi_2 - \epsilon_l D\psi_4 + \Theta]$.

Similarly, following Eqn. (2.39) the difference form of the heat balance equation, can be expressed as,

$$C_v\Delta T = \frac{1}{V_m}\left(\frac{V(t)^2}{R} - hA_{surf}(T - T_0)\right)\Delta t + \lambda\Delta\xi. \tag{3.15}$$

Replacing Eqn. (3.12) into Eqn. (3.15), gives

$$\Delta T = X_b\Delta t + Y_b\Delta\sigma, \tag{3.16}$$

where, $X_b = \frac{\frac{1}{V_m}\left(\frac{V(t)^2}{R} - hA_{surf}(T-T_0)\right)}{(C_v - \lambda\psi_2)}$, and $Y_b = \frac{\lambda\psi_1}{(C_v - \lambda\psi_2)}$.

From Eqns. (3.14) and (3.16), $\Delta\sigma$ and ΔT can be explicitly obtained as

$$\Delta\sigma = \left(\frac{D\Delta\epsilon + Y_a X_b \Delta t}{X_a - Y_a Y_b}\right), \tag{3.17}$$

and

$$\Delta T = \left(\frac{DY_b\Delta\epsilon + X_a X_b \Delta t}{X_a - Y_a Y_b}\right). \tag{3.18}$$

3.5.1 Force Equilibrium and Kinematic Constraint

The force displacement relations for the linear and non-linear systems are different and are derived below.

TH-1636_10610313

3.5.1.1 Linear system

As the voltage applied across the SMA wire increases, the temperature raises and its starts contracting above austenite start temperature. Due to stiffness of the spring, the wire cannot contract freely, as a result, recover stress gets developed, which in turn stretches the spring. The elongation in the spring, depicted by δ in Fig. 3.2, is manifested by the displacement of the block in between the SMA wire and the spring. If the recovery stress is 'σ' and the corresponding displacement is 'δ', then using force equilibrium one can write,

$$\delta = \frac{\sigma A}{K_s}. \tag{3.19}$$

Here, K_s represents the spring stiffness and A is the cross-sectional area of the SMA wire. Again, since the total length of the SMA wire and the spring is constant, from the kinematic point of view, the stretch in the spring is related to the change in strain of the SMA wire following,

$$\delta = L_0(1 + \epsilon_0) - L_0(1 + \epsilon). \tag{3.20}$$

Replacing the expression of 'δ' from Eqn. (3.19) in Eqn. (3.20), the final form of the stress-strain relation can be obtained as,

$$\epsilon = \epsilon_0 - \frac{\sigma A}{K_s L_0}. \tag{3.21}$$

From Eqn. (3.21), the rate form of the strain can be written as,

$$\frac{d\epsilon}{dt} = -\frac{A}{K_s L_0}\frac{d\sigma}{dt}. \tag{3.22}$$

TH-1636_10610313

The difference form of the above equation can be given as

$$\Delta\epsilon = -\frac{A}{K_s L_0}\Delta\sigma. \tag{3.23}$$

By substituting $\Delta\epsilon$ in Eqn. (3.17) from Eqn. (3.23), one gets

$$\Delta\sigma = \frac{Y_a X_b}{X_a + \frac{DA}{K_s L_0} - Y_a Y_b}\Delta t. \tag{3.24}$$

In discrete form, Eqn. (3.24) can be written as

$$\sigma_{t_k} = \sigma_{t_{k-1}} + \frac{Y_a X_b}{X_a + \frac{DA}{K_s L_0} - Y_a Y_b}\Delta t. \tag{3.25}$$

Similarly, from Eqn. (3.18) and Eqn. (3.23), the difference form of the temperature equation is obtained as

$$\Delta T = \frac{X_b\left(X_a + \frac{DA}{K_s L_0}\right)}{X_a + \frac{DA}{K_s L_0} - Y_a Y_b}\Delta t. \tag{3.26}$$

The discrete form of Eqn. (3.26) can be derived as

$$T_{t_k} = T_{t_{k-1}} + \frac{X_b\left(X_a + \frac{DA}{K_s L_0}\right)}{X_a + \frac{DA}{K_s L_0} - Y_a Y_b}\Delta t. \tag{3.27}$$

3.5.1.2 Nonlinear system

Following the approach proposed by Banerjee *et al* [83], the deflection of a discretely attached cantilever beam due to the follower force applied by SMA wire, has been modeled. Figure 3.5a represents the undeformed beam (AB) attached with the SMA wire (CD) at an offset e_y. Depending on the temperature, the SMA wire contracts (CD′) and causes the beam to deflect to the new configuration (AB′). Figure 3.5b illustrates the deflection of the

TH-1636_10610313

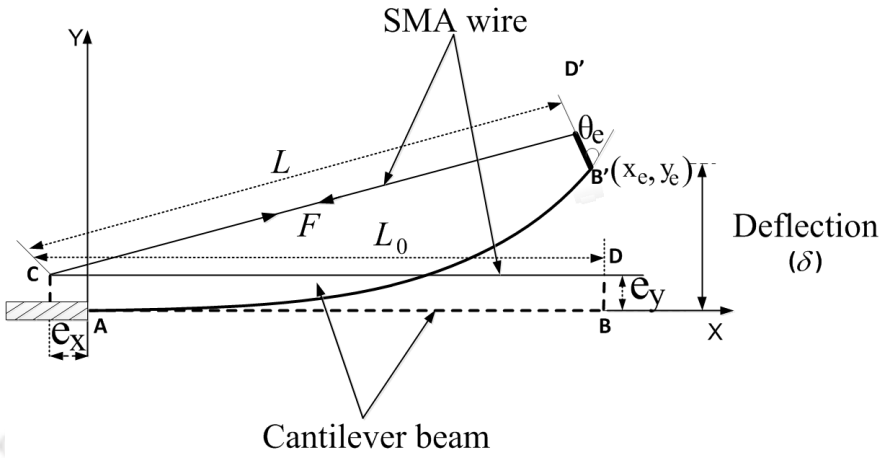

(a)

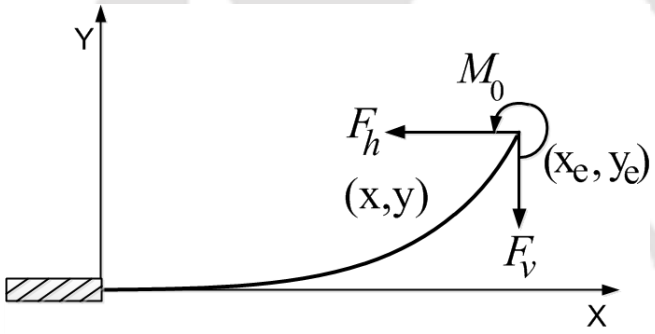

(b)

Figure 3.5: (a) A cantilever beam actuated by a discretely placed SMA wire actuator, and (b) forces and moment applied by the SMA wire on the free end of the beam.

beam due to the moment and force acting on it. Following Euler-Bernoulli beam theory, the moment-curvature relation becomes,

$$\frac{d\theta}{ds} = \frac{M_0}{EI}. \tag{3.28}$$

Here, M_0 is the end moment, EI represents the flexural rigidity of the beam and $\frac{d\theta}{ds}$ is the curvature at the point of interest, where θ denotes the slope of the beam at a distance 's' along the length of beam from the fixed end. Considering the effect of the end forces, as

TH-1636_10610313

depicted in Fig. 3.5b, the bending moment at any point (x,y) of the beam can be obtained as

$$M\left(x(s), y(s)\right) = M_0 + F_h\left(y_e - y(s)\right) - F_v\left(x_e - x(s)\right). \tag{3.29}$$

Here, $M_0 = Fe_y\cos\left(\theta_0 - \alpha\right)$, $F_h = F\cos\alpha$ and $F_v = F\sin\alpha$. F represents the force applied by the SMA wire on the beam and can be written in terms of the recovery stress as $F = \sigma A$; where 'A' denotes the cross-sectional area of the SMA wire. F_h and F_v represent the horizontal and vertical forces applied by the SMA wire at the end of the beam. Following Eqns. (3.28) and (3.29), the end delection of the beam has to be obtained by solving the following set of coupled nonlinear ordinary differential equations (ODEs),

$$\begin{aligned}
&\tfrac{d\theta}{ds} = \tfrac{F}{EI}\left\{e_y\cos\left(\theta_0 - \alpha\right) + \left(y_e - y(s)\right)\cos\alpha - \left(x_e - x(s)\right)\sin\alpha\right\},\\
&\tfrac{dx}{ds} = \cos\theta(s),\\
&\tfrac{dy}{ds} = \sin\theta(s).
\end{aligned} \tag{3.30}$$

The initial conditions are,

$$\begin{cases}
\theta\,|_{s=0} &= 0,\\
x\,|_{s=0} &= 0,\\
y\,|_{s=0} &= 0.
\end{cases} \tag{3.31}$$

The set of above defined ODEs are numerically integrated using the initial condition mentioned in Eqn. (3.31), to obtain the final length of SMA wire after contraction as,

$$L = \left\{\left(y_2 - y_1 - e_y(\cos\theta_1 - \cos\theta_2)\right)^2 + \left(x_2 - x_1 - e_y(\sin\theta_1 - \sin\theta_2)\right)^2\right\}^{1/2}. \tag{3.32}$$

Then, the strain in the SMA wire is calculated as,

$$\epsilon = \left\{\frac{L(1+\epsilon_0)}{L_0} - 1\right\}. \tag{3.33}$$

TH-1636_10610313

Here, ϵ_0 and L_0 represent the amount of prestrain and the length of the SMA wire corresponding to the undeformed state of the beam. From the above analysis, the strain, ϵ, in the SMA wire is derived as a function of the recovery stress, σ, which can be expressed as,

$$\epsilon = \Psi(\sigma). \tag{3.34}$$

The rate of strain from Eqn. (3.34) can be obtainted as

$$\begin{aligned} \frac{d\epsilon}{dt} &= \frac{d\Psi}{d\sigma}\frac{d\sigma}{dt}, \\ &= A_1(\sigma)\frac{d\sigma}{dt}. \end{aligned} \tag{3.35}$$

Here, $A_1 = \frac{d\Psi}{d\sigma}$. The difference form of Eqn. (3.35) can be written as,

$$\Delta\epsilon = A_1\Delta\sigma. \tag{3.36}$$

From the same analysis one can also derive a relationship between the end deflection of the beam, δ, and the stress, σ, in the SMA wire as,

$$\delta = \Upsilon(\sigma). \tag{3.37}$$

Therefore, combining Eqns. (3.17) and (3.36), the final form of $\Delta\sigma$ can be written as,

$$\Delta\sigma = \frac{Y_a X_b}{X_a + DA_1 - Y_a Y_b}\Delta t. \tag{3.38}$$

The discrete form of Eqn. (3.38) appears to be,

$$\sigma_{t_{k+1}} = \sigma_{t_k} + \frac{Y_a X_b}{X_a + DA_1 - Y_a Y_b}\Delta t. \tag{3.39}$$

TH-1636_10610313

Similarly, using Eqns. (3.18) and (3.36) the difference form of the temperature equation is found to be

$$\Delta T = \frac{X_b \left(X_a - DA_1 \right)}{X_a + DA_1 - Y_a Y_b} \Delta t. \tag{3.40}$$

The discrete form of Eqn. (3.40) is obtained as,

$$T_{t_k} = T_{t_{k-1}} + \frac{X_b \left(X_a - DA_1 \right)}{X_a + DA_1 - Y_a Y_b} \Delta t. \tag{3.41}$$

3.5.2 Relation between Electrical Resistance and Strain

Similar to any other conductor, the electrical resistance of the SMA wire depends on the electrical resistivity and the geometry. The electrical resistance of the SMA wire of length (L) and cross-section (A) can be written as,

$$R = \frac{\rho L}{A}, \tag{3.42}$$

where, ρ is the electrical resistivity of the SMA; which has to be determined from the electrical resistivity of the individual phases, using the rule of mixture as,

$$\rho = \rho_{_M} \xi + (1 - \xi) \rho_{_A}. \tag{3.43}$$

Here, $\rho_{_M}$ and $\rho_{_A}$ represents the resistivity of the martensite and austenite phases, respectively. Note that the martensite volume fraction is a dimensionless quantity and is a function of stress and temperature of SMA, referring section 2.6.2.2. This implies that the electrical resistivity (ρ) is also a function of stress (σ) and temperature (T) of the SMA. According to Eqn. (3.42), the electrical resistance of SMA also changes due to the change in the length of the SMA and the cross-sectional area of SMA during actuation. The present length of the

TH-1636_10610313

SMA wire involves the current strain, which in turn depends on the current stress. Thus one can write,

$$L = L_0(1 + \epsilon(\sigma)). \tag{3.44}$$

Here, $\epsilon(\sigma)$ represents the strain of the SMA wire as a function of stress, which are presented as Eqn. (3.21) for linear system and Eqn. (3.34) for nonlinear system. The change in cross-sectional area of the SMA wire has been neglected in the analysis. This change in the strain and the difference in electrical resistivity of SMA between the austenite and martensite phases, give rise to a significant variation in the electrical resistance of SMA wire during thermo-mechanical loading. Thus the expression for electrical resistance, following Eqn. (3.42), can be rewritten as,

$$R = \frac{(\rho_M \xi(T,\sigma) + \rho_A (1 - \xi(T,\sigma))) L_0 (1 + (\epsilon_0 - \frac{\sigma A}{K_s L_0}))}{A}. \tag{3.45}$$

3.6 EKF for SMA Actuated System

Here, the Extended Kalman filter model for the SMA actuated systems, following the dynamics discussed in the previous section, are presented. The state of the SMA wire actuator at a given instant can be completely defined by the stress, temperature, and martensite volume fractions. However, as the martensite volume fractions are completely known at the previous instant (from the posteriori estimate) and for sufficiently small time step, only stress and temperature of SMA are assumed to form the state vector. This helps in reducing the size of the system from 4 to 2, taking care of the loading history and reducing the computational burden. However, at each time step, as soon as the stress and temperature of SMA is updated, the martensite volume fractions are also updated. This helps in reducing the error, if

TH-1636_10610313

any, because of the assumption. Thus, the state vector is represented as,

$$\mathbf{X} = \lfloor T \quad \sigma \rfloor^{\intercal}. \tag{3.46}$$

According to Eqn. (3.6), one requires a process nonlinear vector function, to compute the current state vector ($\mathbf{X}_{t_k}$) of the system from the previous state vector ($\mathbf{X}_{t_{k-1}}$) and current input ($\mathbf{u}_{t_k}$). For the present system, this step has been implemented either using *Implicit method* or *Multiple Step Explicit method*. Here, both the methods are explored and discussed, for SMA actuated linear system. The nonlinear process and observation required for state estimation of both linear and nonlinear system are derived and discussed below.

3.6.1 Linear System

For the SMA actuated linear system, shown in Fig. 3.2, both the implicit and explicit schemes are adopted and each of the these approaches are discussed in the following sections.

3.6.1.1 Implicit Method

For this approach, both the heat balance and constitutive equations are written in difference form, where the unknowns, i.e., the states of the system at the current instant appear on both the sides of the non-linear equations. Therefore, at each time step, one needs to solve for the stress and temperature of SMA using advanced iterative technique. Following Eqn. (3.27) and Eqn. (3.25) the discrete form of the heat balance and constitutive equation for the SMA wire actuated linear system are found to be,

$$T_{t_k} = T_{t_{k-1}} + \frac{X_b \left(X_a + \frac{DA}{K_s L_0} \right)}{X_a + \frac{DA}{K_s L_0} - Y_a Y_b} \Delta t, \tag{3.47}$$

TH-1636_10610313

and

$$\sigma_{t_k} = \sigma_{t_{k-1}} + \frac{Y_a X_b}{X_a + \frac{DA}{K_s L_0} - Y_a Y_b}\Delta t. \tag{3.48}$$

Here, $X_a = \{1 - (\epsilon(\sigma) - \epsilon_l \xi_S)(D_M - D_A)\psi_1(T_{t_k}, \sigma_{t_k}) + \epsilon_l D(\xi)\psi_3(T_{t_k}, \sigma_{t_k})\}$,
$Y_a = \{(\epsilon(\sigma) - \epsilon_l \xi_S)(D_M - D_A)\psi_2(T_{t_k}, \sigma_{t_k}) - \epsilon_l D\psi_4(T_{t_k}, \sigma_{t_k}) + \Theta\}$,
$X_b = \frac{1}{V_m(C_v - \lambda\psi_2)}\left(\frac{V^2}{R} - hA_{surf}(T - T_0)\right)$ and $Y_b = \frac{\lambda\psi_1(T_{t_k}, \sigma_{t_k})}{\left(C_v - \lambda\psi_2(T_{t_k}, \sigma_{t_k})\right)}$.
Thus, the η_1 and η_2 can be obtained as

$$\begin{aligned} T_{t_k} &= \eta_1, \\ \sigma_{t_k} &= \eta_2. \end{aligned} \tag{3.49}$$

Here, η_1 and η_2 represent the element of the nonlinear process vector function ($\boldsymbol{\eta}$). For the self-sensing application, the output of the system has to be estimated from the electrical resistance variation of the SMA wire. Thus, the electrical resistance of the SMA wire has been taken as the observation or measurement. As discussed in section 3.5.2, the electrical resistance of the SMA wire can finally be determined in terms of stress and temperature of the wire. Referring Eqns. (3.2) and (3.45), the nonlinear observation function for the problem in hand is defined as

$$\begin{aligned} &\mathbf{Y}_{t_k} = R_{t_k}, \\ \text{i.e.,} \quad &\Gamma_1(\mathrm{T}_{t_k}, \sigma_{t_k}) = \left\{ \frac{(\rho_M \xi(T_{t_k}, \sigma_{t_k}) + \rho_A(1 - \xi(T_{t_k}, \sigma_{t_k})))L_0(1 + (\epsilon_0 - \frac{\sigma A}{K_s L_0}))}{A} \right\}. \end{aligned} \tag{3.50}$$

Here, Γ_1 is the element of $\{\mathbf{\Gamma}\}$ and $\xi(T, \sigma)$ represents the dependence of martensite volume fraction on stress and temperature of the SMA wire. The martensite volume fraction is determined from the a-priori estimate of stress and temperature, using the phase kinetics described by Eqns. (2.35) and (2.36). The coupled non-linear equations Eqns. (3.47) and (3.48) are solved using the trust-region dogleg method [89] to obtain (T_k) and (σ_k) from

TH-1636_10610313

known (T_{k-1}, σ_{k-1}, ξ_k, ξ_{s_k}) and applied voltage (V_k).

The Jacobian ($\mathbf{J}$) of the nonlinear process vector function ($\boldsymbol{\eta}$) are determined by differentiating each element of $\{\boldsymbol{\eta}\}$ with respect to state vector (σ and T), and can be expressed as

$$\mathbf{J}_{t_{k-1}} = \left[\begin{array}{cc} \frac{d\eta_1}{dT} & \frac{d\eta_1}{d\sigma} \\ \frac{d\eta_2}{dT} & \frac{d\eta_2}{d\sigma} \end{array} \right]_{(T_{t_{k-1}},\, \sigma_{t_{k-1}},\, \xi_{t_{k-1}},\, \xi_{S_{t_{k-1}}})} . \tag{3.51}$$

The Jacobian $\mathbf{J}$ at t_{k-1} is calculated numerically, following,

$$\mathbf{J}_{t_{k-1}} = \left[\begin{array}{cc} \frac{\eta_1'(T_{t_{k-1}}+\Delta T, \sigma_{t_{k-1}}) - \eta_1(T_{t_{k-1}}, \sigma_{t_{k-1}})}{\Delta T} & \frac{\eta_1''(T_{t_{k-1}}, \sigma_{t_{k-1}}+\Delta\sigma) - \eta_1(T_{t_{k-1}}, \sigma_{t_{k-1}})}{\Delta\sigma} \\ \frac{\eta_2'(T_{t_{k-1}}+\Delta T, \sigma_{t_{k-1}}) - \eta_2(T_{t_{k-1}}, \sigma_{t_{k-1}})}{\Delta T} & \frac{\eta_2''(T_{t_{k-1}}, \sigma_{t_{k-1}}+\Delta\sigma) - \eta_2(T_{t_{k-1}}, \sigma_{t_{k-1}})}{\Delta\sigma} \end{array} \right]. \tag{3.52}$$

Here, η_1 and η_2 represent the numerical solution of the Eqns. (3.47) and (3.48) with initial guess as the posteriori estimate of temperature and stress at previous instant, i.e., $(T_{t_{k-1}}, \sigma_{t_{k-1}})$ and with the input at the current instant $V(t_k)$. η_1' and η_2' denote the solution of the same two equations with the initial guess as $\{(T_{t_{k-1}} + \Delta T), \sigma_{t_{k-1}}\}$ and for the same input. Similarly, with initial guess as $\{T_{t_{k-1}}, (\sigma_{t_{k-1}} + \Delta\sigma)\}$, the solution of the Eqns. (3.47) and (3.48) are represented as η_1'' and η_2''. Here, ΔT and $\Delta\sigma$ are very small changes in σ_{t_k} and T_{t_k}, respectively.

Also, the Jacobian ($\mathbf{H}$) of the observation vector function ($\boldsymbol{\Gamma}$) with respect to the state, are

$$\mathbf{H}_{t_k} = \left[\begin{array}{cc} \frac{d\Gamma_1}{dT} & \frac{d\Gamma_1}{d\sigma} \end{array} \right]_{(T_{t_k}, \sigma_{t_k}, \xi_{t_k}, \xi_{S_{t_k}})}. \tag{3.53}$$

This is calculated numerically as,

$$\mathbf{H}_{t_k} = \left[\begin{array}{cc} \frac{\Gamma_1(T_{t_k}+\Delta T, \sigma_{t_k}) - \Gamma_1(T_{t_k}, \sigma_{t_k})}{\Delta T} & \frac{\Gamma_1(T_{t_k}, \sigma_{t_k}+\Delta\sigma) - \Gamma_1(T_{t_k}, \sigma_{t_k})}{\Delta\sigma} \end{array} \right]. \tag{3.54}$$

TH-1636_10610313

For the present case Γ_1 is the electrical resistance of SMA, expressed by Eqn. (3.45), discussed in section 3.5.2.

3.6.1.2 Explicit Method

In this approach, the state of the system at any given instant is obtained following explicit numerical integration. For this purpose, the rate form derived in Eqns. (3.24) and (3.26) are rewritten as,

$$\frac{d\sigma}{dt} = \frac{Y_a X_b}{X_a + \frac{DA}{K_s L_0} - Y_a Y_b}, \tag{3.55}$$

and,

$$\frac{dT}{dt} = \frac{X_b \left(X_a + \frac{DA}{K_s L_0} \right)}{X_a + \frac{DA}{K_s L_0} - Y_a Y_b} \Delta t. \tag{3.56}$$

Substituting X_a, X_b, Y_a and Y_b in the Eqns. (3.55) and. (3.56), the final rate form becomes,

$$\frac{dT}{dt} = \frac{\frac{V^2}{R} - hA_{surf}(T_{t_{k-1}} - T_0)}{c_v V_m + \lambda\psi_2 + \lambda\psi_1 F_5(\sigma, T)}, \tag{3.57}$$

and,

$$\frac{d\sigma}{dt} = \frac{F_5(\sigma, T)(\frac{V^2}{R} - hA_{surf}(T - T_0))}{C_v V_m + \lambda\psi_2 + \lambda\psi_1 F_5}. \tag{3.58}$$

Here, $F_5(\sigma, T) = \frac{(\epsilon - \epsilon_l \xi_s)(D_M - D_A)\psi_2 - \epsilon_l D\psi_4 + \Theta}{1 - \{(\epsilon - \epsilon_l \xi_s)(D_M - D_A)\psi_1 - \epsilon_l D\psi_3\} + \frac{A}{K_s L_0}}$, and the functions ψ_1, ψ_2, ψ_3 and ψ_4 are the coefficients of $\frac{d\sigma}{dt}$ and $\frac{dT}{dt}$, in the phase kinetics, defined by Eqns. (2.35) and (2.36). In this work, the Runge-Kutta (RKDP) method has been followed to compute the present state ($\mathbf{X}_{t_k}$) of the system by evaluating the RHS of Eqns. (3.57) and (3.58) at six intermediate points between t_{k-1} and t_k as proposed by Dormand and Prince [90]. Once the present state, $\mathbf{X}_{t_k}$, is obtained, the output ($\mathbf{\Gamma}_{t_k}$), and Jacobians $\mathbf{J}_{t_{k-1}}$ and $\mathbf{H}_{t_k}$ are cal-

TH-1636_10610313

culated using Eqns. (3.50), (3.51) and (3.53), respectively. Following the discussion in section 2.6.2.2, ψ_1, ψ_2, ψ_3 and ψ_4 are different for different transformation zones.

- **Forward Transformation :**

  Following Eqn. (2.24), rate form of the phase kinetics, can be obtained as,

$$\frac{d\xi}{dt} = \left(\frac{\pi(1-\xi_j)\sin(\pi Z^M)}{(T_j - M_f)\sin\phi^M - \sigma_j\cos\phi^M}\right)\left(\cos\phi^M\frac{d\sigma}{dt} + \sin\phi^M\frac{dT}{dt}\right). \tag{3.59}$$

  Here, $Z^M = \frac{\sigma\cos\phi^M + (M_s - T)\cos\phi^M - \sigma_j\cos\phi^M + (M_s - M_f)\sin\phi^M}{(M_s - M_f)\cos\phi^M - \sigma_j\cos\phi^M + (M_s - M_f)\sin\phi^M}$.

  Comparing Eqn. (3.59) with Eqn. (2.35) one gets,

$$\begin{aligned}\psi_1 &= \frac{0.5\pi(1-\xi_j)\sin(\pi Z^M)\cos\phi^M}{(T_j - M_f)\sin\phi^M - \sigma_j\cos\phi^M},\\ \psi_2 &= \frac{-0.5\pi(1-\xi_j)\sin(\pi Z^M)\sin\phi^M}{(T_j - M_f)\sin\phi^M - \sigma_j\cos\phi^M}.\end{aligned} \tag{3.60}$$

  Similarly, following Eqn. (2.25) the stress induced martenite volume fraction varies, as,

$$\begin{aligned}\frac{d\xi_S}{dt} = &\left(\frac{0.5\pi\left(1-\cos\left(\pi Z^M\right)\right)\left(\sec h(\pi(2Z^\sigma - 1))\right)^2}{(\sigma_f - \sigma_s)}\right) + \\ &\left(\frac{0.5\pi(\xi' - \xi_{sj})\sin\left(\pi Z^M\right)}{(T_j - M_f)\sin\phi^M - \sigma_j\cos\phi^M}\right)\left(\cos\phi^M\dot{\sigma} + \sin\phi^M\dot{T}\right)\end{aligned}. \tag{3.61}$$

  Here, $\xi' = 0.5(1 + \tanh(\pi Z^\sigma))$ and $Z^\sigma = \frac{\sigma - \sigma_s}{\sigma_f - \sigma_s}$. Comparing Eqn. (3.61) with Eqn. (2.36) one obtains,

$$\begin{aligned}\psi_3 &= \frac{0.5\pi(1-\cos(\pi Z^M))(\mathrm{sech}(\pi(2Z^\sigma - 1)))^2}{(\sigma_f^{cr} - \sigma_s^{cr})} + \frac{0.5\pi(\xi' - \xi_{sj})\sin(\pi Z^M)\cos\phi^M}{(T_j - M_f)\sin\phi^M - \sigma_j\cos\phi^M},\\ \psi_4 &= \frac{-0.5\pi(\xi' - \xi_{sj})\sin(\pi Z^M)\sin\phi^M}{(T_j - M_f)\sin\phi^M - \sigma_j\cos\phi^M}.\end{aligned} \tag{3.62}$$

TH-1636_10610313

- **Reverse Transformation :**

  Using Eqn. (2.29), the rate form of phase kinetics is written as,

$$\frac{d\xi}{dt} = \left(\frac{-0.5\pi\xi_j \sin(\pi Z^A)}{(A_f - T_j)\sin\phi^A + \sigma_j \cos\phi^A}\right)\left(-\cos\phi^A \frac{d\sigma}{dt} + \sin\phi^A \frac{dT}{dt}\right). \tag{3.63}$$

  Here, $Z^A = \frac{-\sigma\cos\phi^A + (T - A_s)\sin\phi^A + \sigma_j \cos\phi^A - (T_j - A_s)\sin\phi^A}{(A_f - A_s)\sin\phi^A - -\sigma_j\cos\phi^A + (T_j - A_s)\sin\phi^A}$. Comparing Eqns. (2.35) and (3.63) one can write,

$$\begin{aligned} \psi_1 &= \frac{0.5\xi_j\pi\sin(\pi Z^A)\cos\phi^A}{(A_f - T_j)\sin(\phi^A) + \sigma_j\cos(\phi^A)}, \\ \psi_2 &= \frac{-0.5\xi_j\pi\sin(\pi Z^A)\sin\phi^A}{(A_f - T_j)\sin(\phi^A) + \sigma_j\cos(\phi^A)}. \end{aligned} \tag{3.64}$$

  Similarly, following Eqn. (2.30), $\frac{d\xi_s}{dt}$ is found to be,

$$\frac{d\xi_s}{dt} = \left(\frac{-0.5\pi\xi_{sj} \sin(\pi Z^A)}{(A_f - T_j)\sin\phi^A + \sigma_j \cos\phi^A}\right)\left(-\cos\phi^A \frac{d\sigma}{dt} + \sin\phi^A \frac{dT}{dt}\right). \tag{3.65}$$

  From Eqns. (2.36) and (3.65), one can obtain,

$$\begin{aligned} \psi_3 &= \frac{0.5\xi_{sj}\pi\sin(\pi Z^A)\cos\phi^A}{(A_f - T_j)\sin(\phi^A) + \sigma_j\cos(\phi^A)}, \\ \psi_4 &= \frac{-0.5\xi_{sj}\pi\sin(\pi Z^A)\cos\phi^A}{(A_f - T_j)\sin(\phi^A) + \sigma_j\cos(\phi^A)}. \end{aligned} \tag{3.66}$$

- **Passive Transformation :**

  In this zones no phase transformation occur; which keeps ξ and ξ_s constant. This

TH-1636_10610313

Table 3.1: Properties assumed for the linear spring biased SMA wire actuated system [3].

Symbol	Value	Symbol	Value
C_{va}	5.92x10^{-3}J/K-mm^3	C_{vm}	4.506x10^{-3} J/K-mm^3
ρ_a	8.37x$10^{-4}\Omega$mm	ρ_m	9.603x$10^{-4}\Omega$mm
D_a	75 GPa	D_m	28 GPa
C_m	10 MPa/^{o}C	C_a	12 MPa/^{o}C
A_s	60 ^{o}C	A_f	75 ^{o}C
M_s	58 ^{o}C	M_f	45 ^{o} C
σ_s	70 MPa	σ_f	100 MPa
ϵ_0	0.033	K_s	0.24 N/mm

implies,

$$\begin{aligned} \psi_1 &= 0, \\ \psi_2 &= 0, \\ \psi_3 &= 0, \\ \psi_4 &= 0. \end{aligned} \tag{3.67}$$

Following, both the schemes discussed in this section, the EKF model is implemented in MATLAB©MathWorks.

3.6.1.3 Comparison between the EKF Models

To compare the performance of the implicit and explicit methods based EKF models, simulations are carried out with different time steps (Δt) and fixed input. The developed EKF based on these two methods, are implemented in MATLAB©MathWorks Inc. installed in a desktop PC having i5-processor (2.6 GHz) and 8 GB RAM. Firstly, the stress and temperature variations of the SMA wire actuator under constrained recovery, are computed following the algorithm presented by Banerjee *et al* [3], for a given input voltage. Corresponding change in electrical resistance of SMA, is also determined from the simulated data and using Eqn. (3.45). The assumed SMA wire properties and the spring stiffness are listed in Ta-

TH-1636_10610313

ble 3.1. The initial conditions are taken as $\sigma_0 = 80$ MPa, $T_0 = 26$ °C, $\xi_0 = 1$, and $\xi_{S_0} = 0.71$. The assumed voltage signal and the corresponding change in electrical resistance, as computed using the model [3], are shown in Figs. 3.6a and 3.6b, respectively.

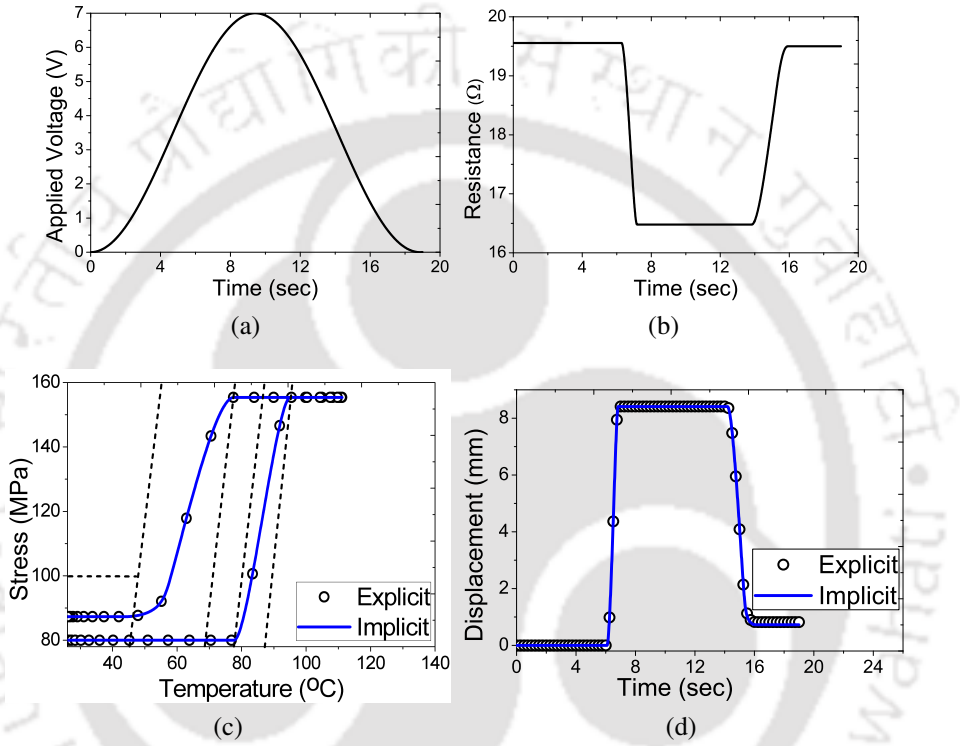

Figure 3.6: (a) Voltage applied across the SMA wire, (b) variation of electrical resistance of SMA as obtained from the model, (c) estimated stress with that of temperature of SMA, and (d) estimated displacement of the SMA actuated system.

From the results, it can be noted that as the voltage increases initially, the resistance of SMA remains constant, which indicates that the temperature is below the transformation temperature. When the voltage is further increased, after 6 sec, the SMA enters into the austenite transformation zone and the resistance of SMA starts to decrease and continue up to austenite finish temperature. Once the temperature reaches the A_f, further increase in the voltage doesn't cause any change in the resistance of SMA. Similarly, during cooling it can be seen from the resistance and voltage plot, as in Fig. 3.6b, that though the voltage

TH-1636_10610313

starts decreasing after 11 sec, but the resistance of SMA remains constant. This is because, the temperature of SMA remains above martensite start temperature. Further decrease in the voltage, causes austenite to convert into martensite and hence, results in the increase of SMA resistance.

Now using the same voltage signal as input and the calculated electrical resistance of the SMA wire as observation, the developed EKF models are simulated to estimate the stress and temperature of the SMA for different time steps. Figure 3.6c depicts, the variation in temperature and stress of SMA, corresponding to the applied voltage and the resistance of SMA. Result illustrates that with the increase of temperature, initially the stress of SMA increases very slowly. Once, the temperature reaches the transformation temperature, due to constrained recovery the large stress is generated within the wire. As it can be seen from the results, that the stress changes sharply from 80 MPa to 155 MPa upto A_f, after that stress remains constant. Whereas, during cooling above M_s, there is no change in the stress, but below M_s stress decreases sharply and continue up to M_f. The dashed lines in the same figure indicate the transformation zones. From the estimated stress, the change in the length of the spring is estimated and are depicted in Fig. 3.6d. The results reveal that both methods yield results with same accuracy. A comparison has been made between two methods in

Table 3.2: Computational time of the explicit and implicit methods based EKF models.

	Explicit method			Implicit method		
Δt	σ_{max}(MPa)	T_{max}(°C)	t_c(sec)	σ_{max}(MPa)	T_{max}(°C)	t_c(sec)
0.5	—	—	—	155.9912	109.105	0.075295
0.1	155.2546	111.6253	0.114282	155.9362	111.1967	0.100435
0.05	155.3564	111.8213	0.222480	155.2899	111.4963	0.185306
0.02	155.3640	111.8030	0.524520	155.4119	111.6881	0.435270
0.01	155.3959	111.8131	1.076631	155.3981	111.7486	0.717825
0.005	155.3966	111.8124	2.104103	155.4078	111.7815	1.362285

TH-1636_10610313

terms of computational time. For this, the maximum value of stress (σ_{max}) and temperature (T_{max}) of the SMA wire and the computational time (t_c) estimated by the implicit and explicit methods for each time steps are tabulated in Table 3.2. It can be observed that the simulation using explicit method takes larger computational time for time steps, $\Delta t < 0.05$ sec, compared to that of the implicit method. This might be because in explicit method at every iteration, state equations are evaluated at six intermediate time steps. Whereas, in implicit method (Trust region Dogleg method), lesser function evaluations are involved at each iteration. Thus, it can be concluded that the implicit method produces same accuracy as that of the explicit method, but with less computational time. It implies, that the implicit method based EKF is more effective so far the real time implementation is concerned. Thus, in the rest of the work implicit method based EKF, with a time step of 0.01 sec has been used to estimate the state of the system.

3.6.1.4 Validation of EKF Model

(a) **SMA Wire Actuated Linear System :**

To validate the developed EKF, the estimated results are compared with that of the model and shown in Fig. 3.7 for full transformation and Fig. 3.8 for partial transformation, respectively. The equations representing the dynamics of the SMA actuated system, given by Eqn. (3.49), are numerically integrated for a given input voltage (refer Figs. 3.7a and 3.8a) following Bekker and Brinson [32] and Banerjee *et al* [3]. This yields the variations of stress, temperature and martensite volume fractions with time, from which the electrical resistance of SMA is calculated using Eqn. (3.45). An artificial Gaussian noise is added to the electrical resistance data as depicted in Fig. 3.7b and 3.8b, and is used in the developed EKF model to estimate the output of the system, i.e., the displacement of the block (δ), for the same input voltage. The estimated stress, temperature and system

TH-1636_10610313

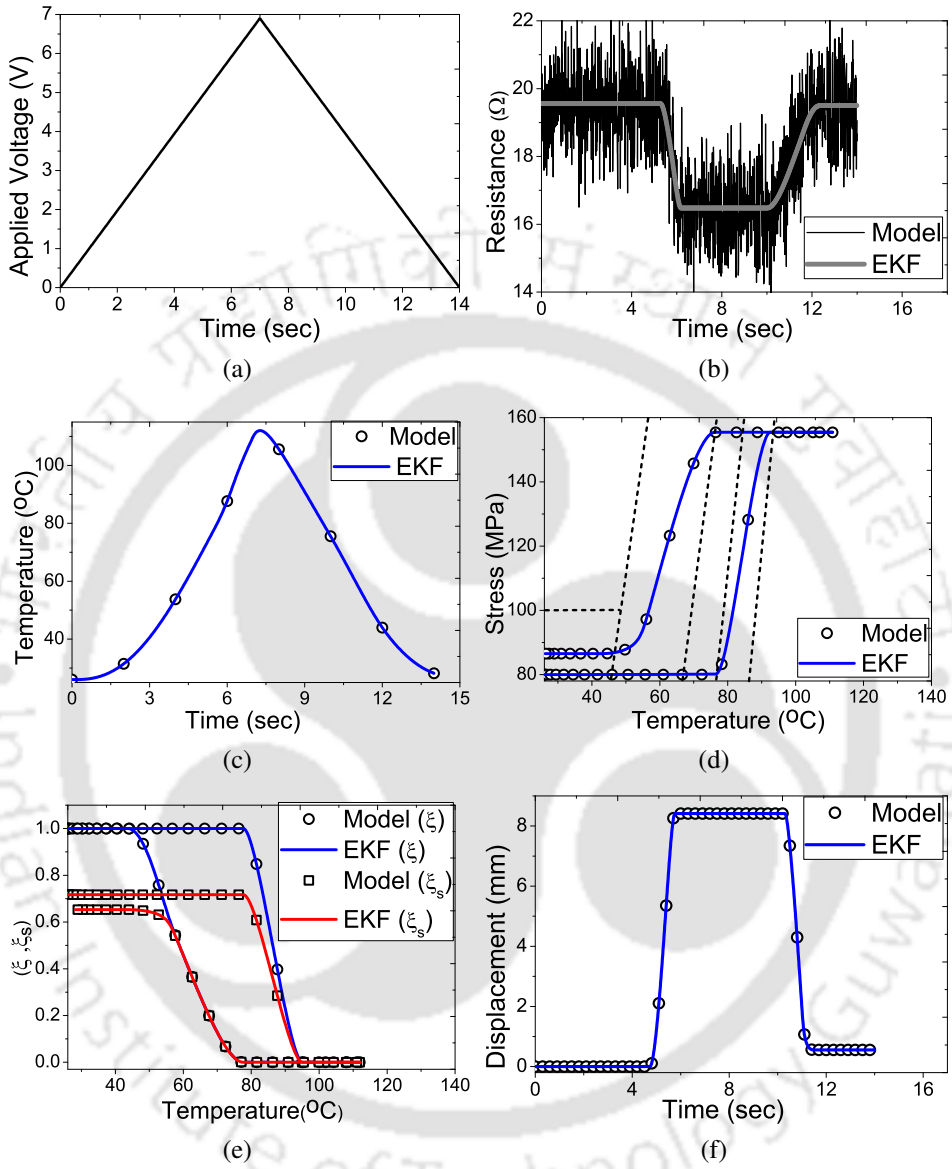

Figure 3.7: Comparison of system responses obtained using SMA model [2] and EKF for the (a) input voltage, (b) electrical resistance variation in SMA, (c) temperature of the SMA wire, (d) stress variation with temperature, (e) martensite volume fractions with temperature, and (f) spring displacement.

output are compared for different inputs.

Figures 3.7c and 3.8c present the temperature of the SMA wire corresponding to the applied voltages depicted in Fig. 3.7a and 3.8a, respectively. Figure 3.7c illustrates a full

TH-1636_10610313

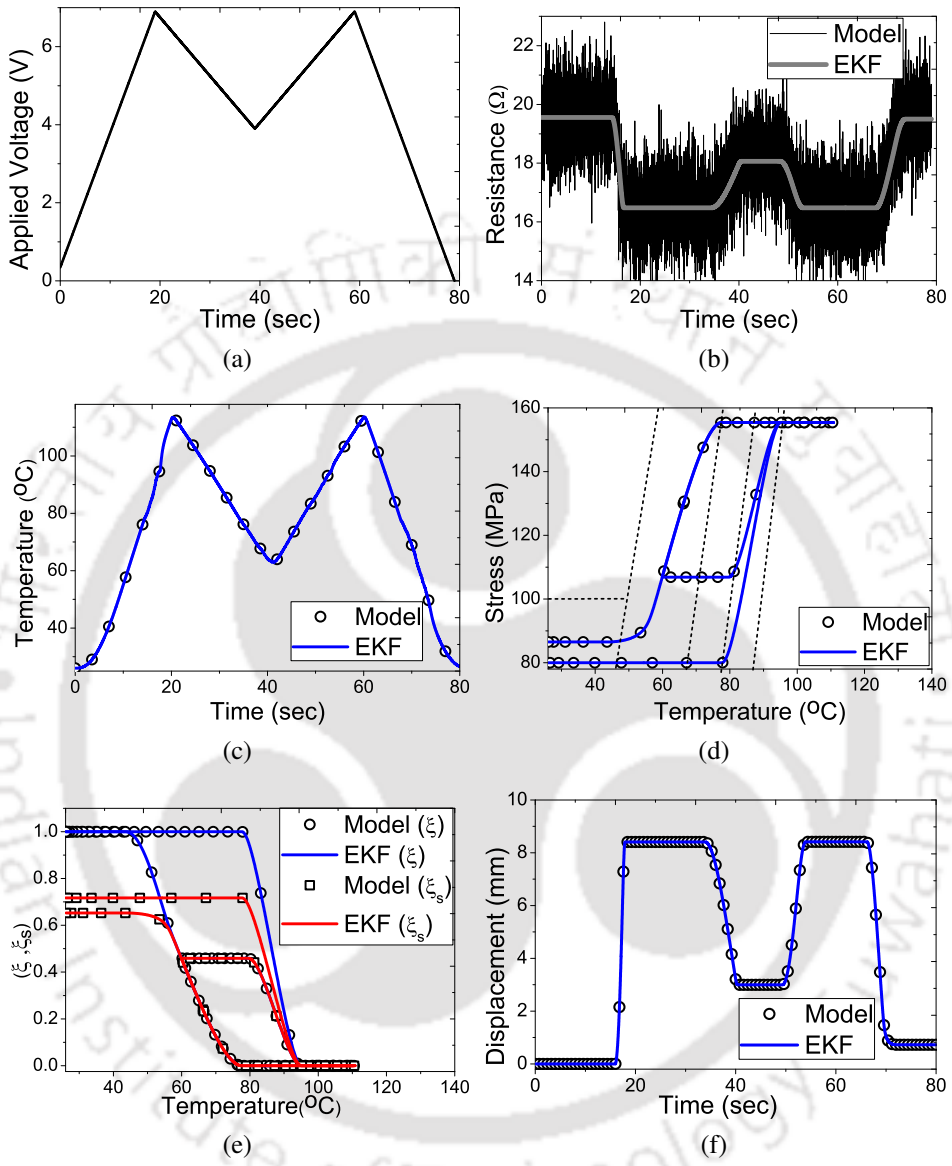

Figure 3.8: Comparison of system responses obtained using SMA model [2] and EKF during partial transformation for (a) input voltage across SMA, (b) electrical resistance variation in SMA (c) temperature of the SMA wire, (d) stress with temperature, (e) martensite volume fractions with temperature, and (f) spring displacement

transformation case, where the temperature of the SMA wire monotonically increases with applied voltage from 26 °C to 111.15 °C, and then decreases to 26 °C, as the voltage decerases. Whereas during partial transformation, initially both voltage and temperature

TH-1636_10610313

increases till 20 sec. After that voltage is decreased form 7 V to 3.9 V and consequently, the temperature of the wire decreases from 111.15 °C to 56 °C. After 40 sec, the voltage is again increased from 3.9 V to 7V for next 20 sec and the temperature of the wire again increases to 111.15 °C. Finally, the voltage decreased to 0 V and temperature of the wire decreases from 111.15 °C to 26 °C.

Figure 3.7d and 3.8d demonstrate the variations in stress in the SMA wire as the temperature changes, presented in Fig. 3.7c and 3.8c, respectively. A complete transformation case is illustrated in Fig. 3.7d, where stress increases monotonically with temperature in the reverse transformation zone, decreases monotonically with temperature in the forward transformation zone, and remains constant in any other conditions. A partial transformation case has been depicted in Fig. 3.8d, capturing a minor loop during forward transformation. In both the cases, the final stress in the SMA is found to be non-zero (89 MPa), as the stress is sufficient to induce detwinned martensite, stretching the SMA further.

This can be visualized in Fig. 3.7e and 3.8e, illustrating the corresponding variations in martensite volume fractions with temperature. In case of full transformation, total martensite volume fraction ξ decreased from ξ_0 =1 to 0 in reverse transformation and increases from 0 to 1 in forward transformation. However, the detwinned martensite volume fraction ξ_S doesnot return back to the initial value of 0.71 at the end of forward transformation. Similar, response is found in case of partial transformation (refer Fig. 3.8e) as well. Finally, the estimated displacements for the applied voltages shown in Fig. 3.7a and 3.8a are presented in Fig. 3.7f and 3.8f, respectively.

It is to be noted that the stress, temperature, martensite volume fractions and the displacement are estimated using developed EKF model for the applied voltages shown in Fig. 3.7a and 3.8a and using the corresponding noisy electrical resistance variation of

TH-1636_10610313

the SMA wire depicted in Fig. 3.7b and 3.8b. These estimated variables are compared with the same obtained from simulating a model presented by Banerjee *et al* [3]. It can be seen in Figs. (3.7c-3.7f) and (3.8c-3.8f) that in spite of the added noise in the electrical resistance data, EKF model has been able to estimate the state as well as the output displacement pretty accurately. Moreover, it is also able to represent the minor loops, revealing the correct implementation of the algorithm taking care of the parameters.

(b) **SMA Wire Actuated Non-Linear System :**

For the nonlinear system depicted in Fig. 3.3, the state vector comprises of stress (σ) and temperature (T) of the SMA wire; as represented by Eqn. (3.46). Following the findings discussed in section 3.6.1.3, the implicit scheme based EKF has been adopted in this case. The only difference between this case and the earlier one is the stress-strain relation, given by Eqn. (3.34), obtained from the analysis of the flexible beam (refer section 3.5.1.2). Thus the discrete form of the heat balance and constitutive equations are obtained as,

$$T_{t_k} = T_{t_{k-1}} + \frac{X_b\left(X_a - DA_1\right)}{X_a - DA_1 - Y_a Y_b}\Delta t, \tag{3.68}$$

$$\sigma_{t_k} = \sigma_{t_{k-1}} + \frac{Y_a X_b}{X_a - DA_1 - Y_a Y_b}\Delta t. \tag{3.69}$$

Here, ϵ_{t_k} can be expressed in terms of the present stress σ_{t_k} using Eqn. (3.34). Following the implicit method based EKF discussed in section 3.6.1.1, and using the SMA wire and the host beam properties mentioned in Table 3.1 and Table 3.3, respectively, the state of the system as well as the end displacement of the beam are estimated for a given applied voltage across the SMA wire. To verify the EKF model, the estimated state and the output displacement of the system are compared with that of the SMA model [3] and is presented in the next section.

TH-1636_10610313

Table 3.3: Properties of the cantilever beam.

Beam(Acrylic material); Elastic modulus = 1.209 GPa.		
Thickness (mm)	Width (mm)	Flexural rigidity (N mm^2)
1.4	10	2764.58

3.6.1.5 Comparison between EKF Estimation and SMA Model for SMA Actuated Cantilever Beam

The EKF relies on the system model to estimate the state of the system at each time instant. The modeling of SMA behavior under varying temperature and stress requires meticulous implementation of the algorithm in updating the memory parameters. To evaluate the correctness of the implemented code of EKF, the estimated state of the system is compared with the response from a well-established model [3]. Firstly, the system response is obtained following the algorithm suggested by Banerjee *et al* [3], for the assumed voltage shown in Fig. 3.9a. The properties of SMA wire are enlisted in Table 3.1. Using the system response the change in electrical resistance is also computed using Eqn. (3.45) and is presented in Fig. 3.9b. Now, the same voltage and the computed electrical resistance variation in SMA is used in the developed EKF, to estimate the state of the system. The same are then compared with that the state obtained from the model. The stress, temperature, volume fractions of martensite and the end-displacement as obtained from the model and the EKF are compared in Figs. 3.9c - 3.9f, respectively. This reveals the correctness of the implementation of EKF, particularly, at the transition of transformations.

TH-1636_10610313

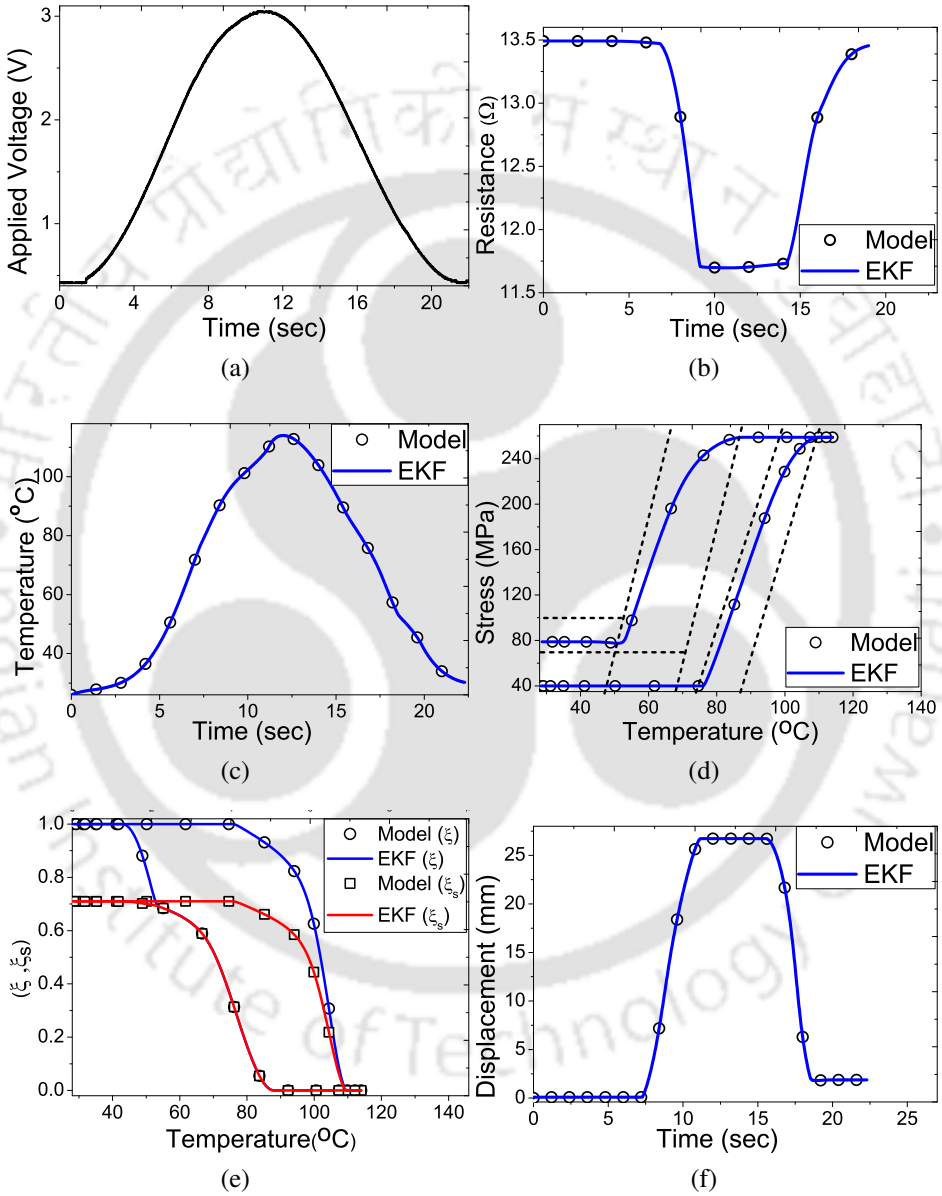

Figure 3.9: (a) Voltage applied across SMA, (b) electrical resistance of SMA, (c) temperature of the SMA, (d) stress variation with temperature, (e) martensite volume fractions, and (f) end-displacement of the link, as obtained from the SMA model [2] and EKF model.

TH-1636_10610313

3.7 Summary

An EKF model has been developed for estimating the response of SMA wire actuated systems from the electrical resistance variation of the wire. Two numerical schemes, namely, implicit and explicit integration techniques, are explored for the EKF model. It has been found that for the same time step, implicit scheme based EKF is computationally more effective compared to the explicit method based EKF. Thus for real-time implementation of the EKF model, implicit method based EKF is more suitable. The EKF model has been verified by comparing the estimated state as well as the system's responses with the same obtained from one of the well established models for different voltage inputs and artificially simulated noisy electrical resistance of SMA wire. The results reveal the true potential of the developed EKF model in harnessing the self-sensing ability of the SMA wire actuator.

TH-1636_10610313

Chapter 4

Experimental Validation of EKF Model for Self-sensing Application of SMA Wire Actuator

4.1 Introduction

In the previous chapter, an Extended Kalman Filter model has been developed to estimate the output of the SMA actuated system from the variation in electrical resistance of the SMA wire. Both explicit and implicit schemes are adopted to obtain the a-priori estimate of the stress and temperature of SMA wire and are found to yield results with same accuracy. Moreover, for the same time step, implicit scheme is found to be computationally less expensive compared to the explicit scheme. In these cases, change in electrical resistance of SMA during actuation is artificially simulated following the same model used in the EKF. A known random noise was added to the data of electrical resistance to make it realistic. In this chap-

TH-1636_10610313

ter, a set-up is developed for measuring the change in electrical resistance of the SMA wire for a desired voltage applied across it. Both the linear and nonlinear systems, described in the previous chapter, are fabricated and are being actuated using SMA wire; output of which are estimated using the developed EKF in real-time. In this chapter, the experimental set-up is discussed at the beginning, followed by the experimental observations.

4.2 Experimental Set-up and Procedure

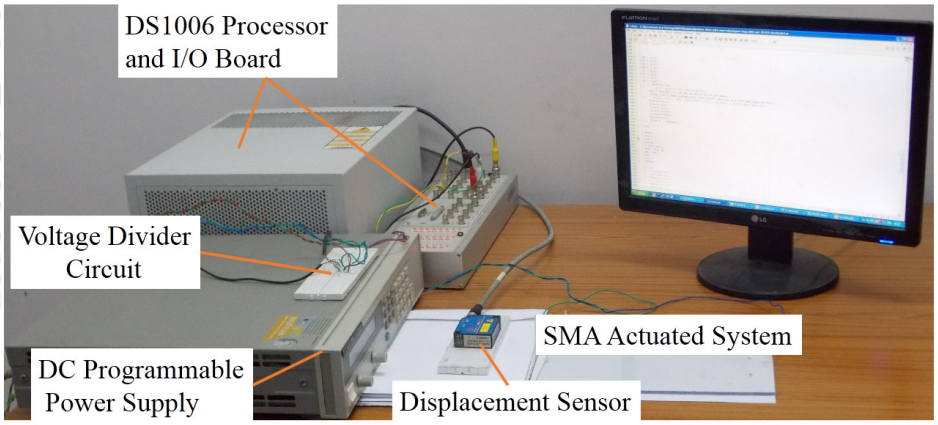

Figure 4.1: Experimental set-up.

An experimental set-up has been developed for measuring the electrical resistance of the SMA and the displacement of the SMA actuated systems. For linear and non-linear systems, same experimental set-up has been used. The experimental set-up, as shown in Fig. 4.1, comprises of a data acquisition system (DAQ)-DS1006©dSPACE, a DC programmable power supply (6642A from Agilent), a laser displacement sensor (opto NCDT-1402-100 from Micro-Epsilon), a voltage divider circuit and a PC having SIMULINK©MathWorks installed. Detailed description of each of these equipments are provided below.

TH-1636_10610313

(a) **dSPACE DS1006:** dSPACE (DS1006), shown in Fig. 4.2a, is a real time controller, having an extension box, referred as DS1006 controller board. The dSPACE hardware may be connected to the desktop-PC through bus interface or via Ethernet. The I/O board of DS1006 contains 20 analog input ports (the yellow box shown in Fig. 4.2a), out of which three ports have been used in the experiment to acquire the analog voltage signals from different sensors. Among these ports, one is occupied by the displacement sensor and the rest are connected to the voltage divider circuit, discussed later. Out of the 8 analog output ports (the blue box shown in Fig. 4.2a) on the controller board, one is used to send the voltage signal to be applied across the SMA wire. The complete working principle of dSPACE is presented in Fig. 4.2b. To make use of the dSPACE, a Simulink model has to be developed, which is connected to the dSPACE hardware through I/O interfaces, provided by dSPACE's RTI (Real-Time Interface). The Real-Time Workshop, generates the C code automatically from the model. The cross compiler compiles the C code and links the object files and libraries into an executable application for real-time processor. The generated real-time application is downloaded to the dPSACE hardware using Control Desk. The processed signals are acquired accordingly using the I/O board for real time application.

(b) **Programmable Power Amplifier:** The programmable power supply (PPS), 6642A from Agilent, shown in Fig. 4.3a, is used to amplify the analog output signal from DS1006, before it is applied across the SMA. It is called PPS because, in this power supply, the output voltage and current can be adjusted by the user, by using the knobs or buttons, provided at the front panel of the power supply. Depending on the application and system requirements, voltage and current can be set to any values in between the minimum and maximum rated value. The PPS can be used in two different modes namely, voltage control mode and current control mode.

TH-1636_10610313

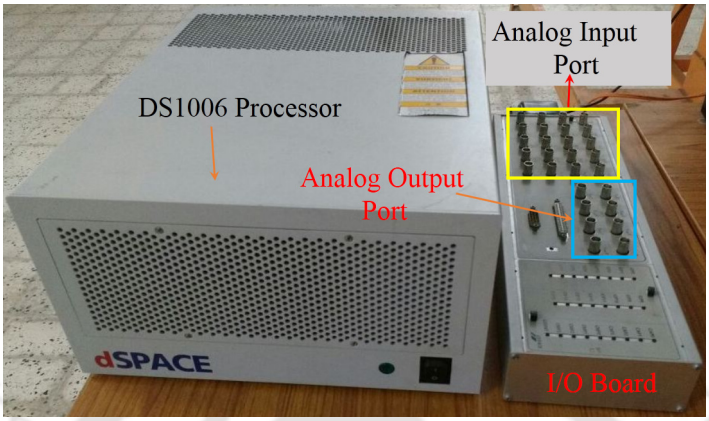

(a)

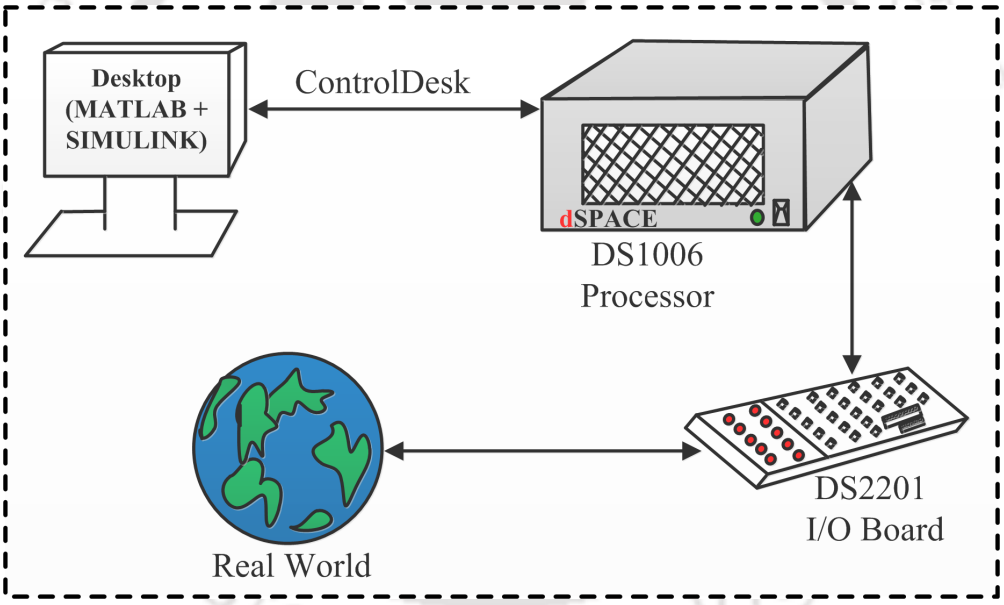

(b)

Figure 4.2: (a) dSPACE with DS1006 processor and I/O board and (b) schematic of the working principle of dSPACE.

- **Voltage Control Mode :** In the voltage control mode, the power supply maintains a constant output voltage as current can vary from 0 to maximum rated current (10 A). In this mode, the power supply provides an output voltage proportional to input voltage.

TH-1636_10610313

- **Current Control Mode :** The working principle of the current control mode is opposite in comparison to that of the voltage control mode. In this mode, the power supply delivers an output current, which is proportional to an input voltage.

In this work, the voltage control mode has been used for all the experiments. The power supply has an input voltage range of 0 to -5 V and output range of 0 to 20 V or 0 to 10 A, respectively; offering a gain of '4' during voltage control mode and '2' for current control mode. The analog signal coming from the I/O board of dSPACE (DS1006) is applied to the input port of power amplifier, as shown by the green box in Fig. 4.3b . The power amplifier amplifies the signal 4 times and is sent through the output port, presented in the same figure, by the yellow box. The amplified voltage signal from the output port is applied across the SMA, so as to induce resistive heating of the wire and raise the temperature of the same.

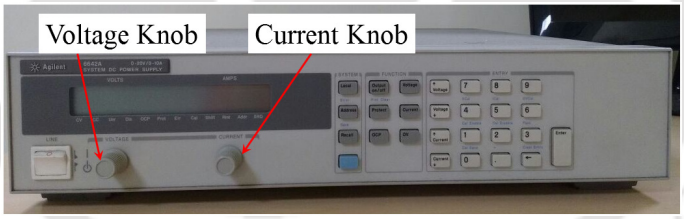

(a)

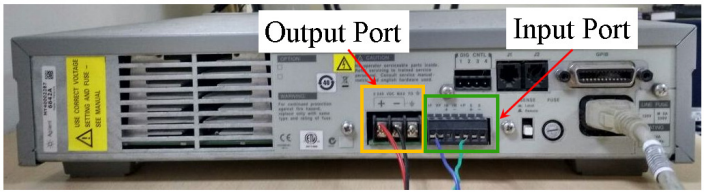

(b)

Figure 4.3: (a) Front and (b) back panel of the DC programmable power supply.

(c) **Laser Displacement Sensor:** A laser displacement sensor, opto NCDT-1402 - 100, Micro-Epsilon, Germany, as depicted in Fig. 4.4, is used to measure the displacement

TH-1636_10610313

of the SMA actuated system. The sensor has a measuring range of 0 to 100 mm, with a resolution of 10 μm and provides an analog output voltage of 1 to 5 V. The analog output voltage (V_{out}) of the displacement sensor is acquired using one of the analog input ports of DS1006. From the output voltage, the displacement of the system is calculated as,

$$\delta_m = 25(V_{out} - V_0) \ \text{mm} \tag{4.1}$$

Here, V_0 is the analog voltage signal obtained from the displacement sensor corresponding to its initial position with respect to the object.

Figure 4.4: Laser displacement sensor (opto NCDT-1402-100).

(d) **Voltage Divider Circuit:** To measure the electrical resistance of the SMA wire during phase transformation, a simple voltage divider circuit is designed and fabricated. The schematic of the circuit is shown in Fig. 4.5. Here the SMA wire, whose electrical resistance has to be measured, is serially connected with a known resistance (R_0). In this work, R_0 = 5 Ω is taken. The total voltage drop (V_T) across the SMA wire and the known resistance R_0, and the voltage drop (V_{SMA}) only across the SMA (R_{SMA}), are acquired using two analog input ports of DS1006. From these two voltages, the

TH-1636_10610313

electrical resistance of the SMA wire (R_{SMA}) is calculated following,

$$R_{SMA} = \left(\frac{V_{SMA}}{V_T - V_{SMA}} \right) R_0. \tag{4.2}$$

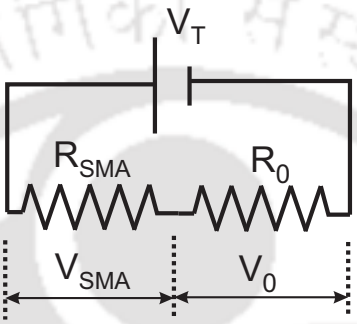

Figure 4.5: Schematic of the voltage divider circuit.

At each time step, the measured electrical resistance is used in the developed EKF model to have the posteriori estimate of the stress and temperature of SMA wire.

4.2.1 Experimental Procedure

The schematic of the complete experimental procedure is depicted in Fig. 4.6. Here, SMA actuated linear spring is considered, for explaining the experimental procedure. The voltage profile required for SMA actuation is implemented in the Simulink. This voltage signal is then converted to analog form using dSPACE - DS1006 and is sent through the analog output port of the I/O board of DS1006. The output signal from dSPACE is applied to the input port of the PPS (shown by black wire (1)), amplifying the signal 4 times. The amplified voltage signal (V_T) is acquired through the output pin of the PPS (green and red wire) and is applied across both the SMA wire and resistance, (R_0). The electrical resistance of SMA is measured using the voltage divider circuit following Eqn. (4.2), where the required voltages i.e. V_T and

TH-1636_10610313

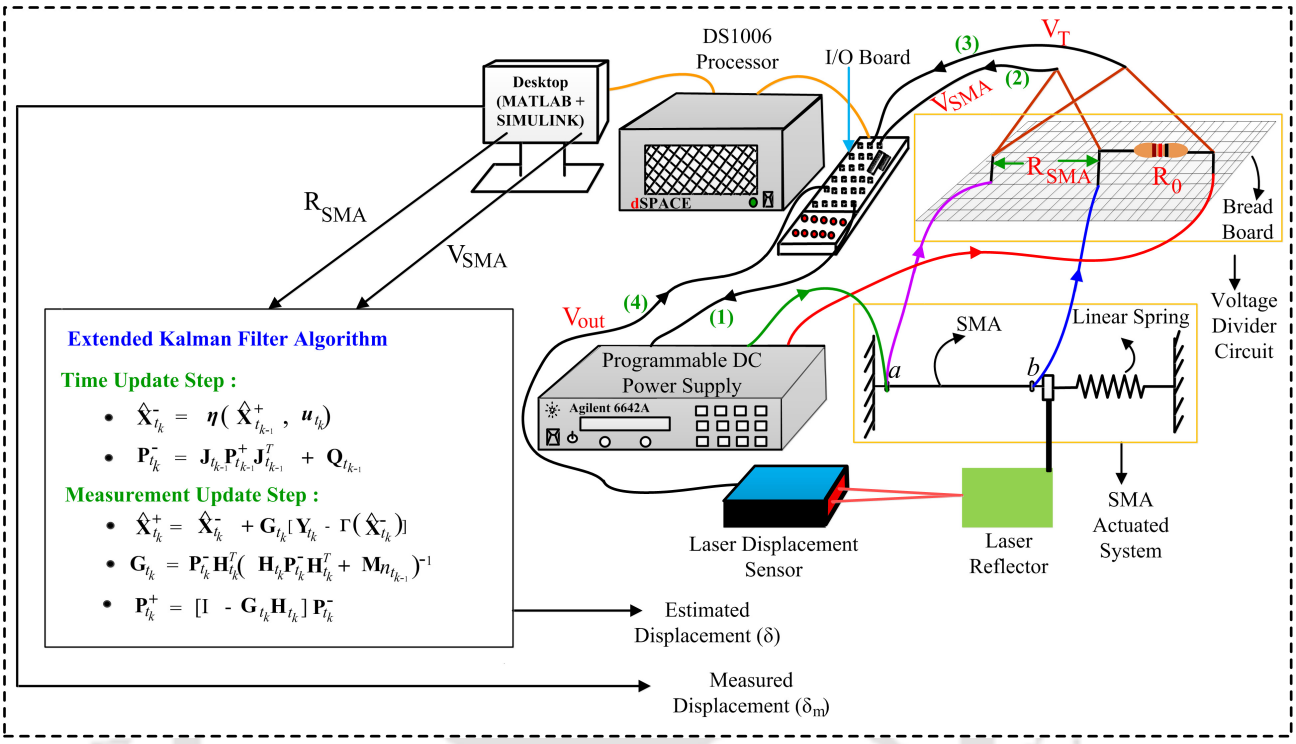

Figure 4.6: (a) Schematic of experimental set-up.

V_{SMA} are acquired through two analog input ports of the I/O board of DS 1006. The output of the displacement sensor V_{out} is acquired through the I/O board, from which the displacement is calculated following Eqn. (4.1). The voltage applied across the SMA wire (V_{SMA}) and the measured electrical resistance of SMA (R_{SMA}) are used in the estimator for estimating the stress and temperature of the SMA wire. From the estimated stress, displacement of the system is calculated and is compared with the experimental response; so as to verify the accuracy of the EKF estimation.

TH-1636_10610313

4.3 EKF Model for Linear Spring Biased Wire Actuator

Here, the implementation details of the EKF model for the linear spring biased SMA wire actuator are presented.

4.3.1 Linear Spring biased SMA Wire Actuator

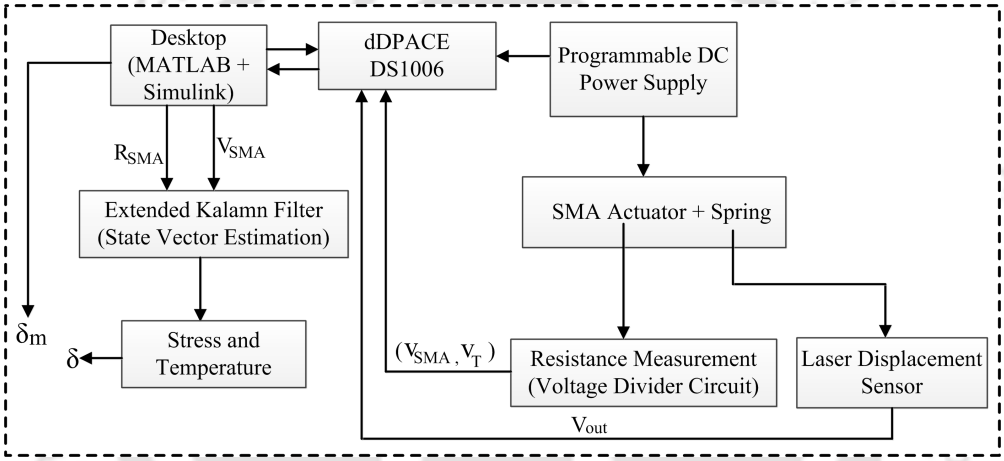

Figure 4.7: Flow diagram of the experiment.

Following the schematic of a linear spring biased SMA wire actuator shown in Fig. 3.2, SMA wire actuated linear system is fabricated and shown in Fig. 4.8. It consists of a SMA wire of length 250 mm and diameter of 125 μm. The wire is procured from memry corporation, Germany. As can be seen in the figure, the SMA and the springs are connected through a block of acrylic. The other ends of the SMA wire and the springs are fixed to rigid walls. In this case, two springs are used so as to ensure that at the end of cooling of the SMA wire, the springs are stiff enough to bring the SMA back to its initial deformed length. As the SMA wire contracts due to Joule heating, the spring stretches and the displacement of the block is measured using the displacement sensor. The change in resistance of the SMA wire

TH-1636_10610313

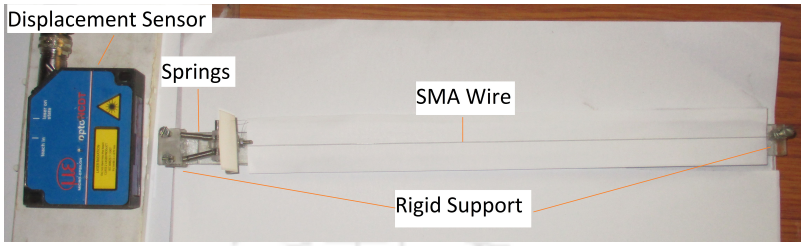

(a)

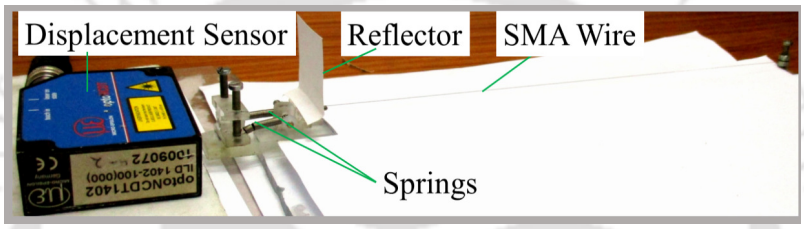

(b)

Figure 4.8: (a) Top and (b) isometric view of linear spring biased SMA wire actuator.

is obtained using the voltage divider circuit mentioned above. The voltage signals required for the displacement and resistance measurement are acquired in the Simulink environment through dSPACE (PC ← dSPACE).

4.3.2 Determination of Spring Stiffness

A small set-up is developed to determine the spring stiffness, as the springs are too soft for the load cells available in the existing UTM. It comprises of a force sensor, Gamma-9105, Schunk and the laser displacement sensor described above. Gamma-9105, is basically a six-axis force sensor, capable of measuring three force components along three orthogonal directions and three moment components about three orthogonal directions. It can measure up to 65 N in X and Y direction, with a resolution of 0.0125 N and 200 N in the Z direction having resolution 0.025 N. It contains six analog outputs, each in the range of 1 to 5 V. The

TH-1636_10610313

six analog signals need to be acquired simultaneously and once multiplied by the calibration matrix yields force and moment data. In this case, the linear spring is placed along the X-axis of the sensor, and thus only the force along X-axis is of interest. The pair of springs are fixed to two acrylic blocks at its end, as shown in the schematic of the experimental set-up in Fig. 4.9a. One block is fixed to the force sensor (along X direction) and at the other end, a load holder is attached. The extension of the spring is measured using the same displacement sensor. The obtained force-displacement data are plotted in Fig. 4.9b. Following a linear fit, the stiffness is found to be 0.24 N/mm.

4.3.3 Determination of Process and Measurement Noise Covariance

The process and measurement noises play an important role in EKF estimation. Here, the measurement noise covariance has been determined experimentally and the process noise covariance is obtained heuristically.

(a) **Measurement Noise Covariance :**

In the voltage divider circuit illustrated in Fig. 4.5, the SMA wire is replaced by a known resistance $R_1 = 20\ \Omega$. The other resistance in the voltage divided circuit is kept same, i.e., 5 Ω. A constant voltage of 0.1 V is applied across the R_1, as well as, R_0. The electrical resistance of R_1 is calculated from the voltage drops measured across R_1 and both R_1 and R_0, following Eqn. (4.2). The resistance calculated from the voltage drops is shown in Fig. 4.10, from which the measurement noise covariance is calculated. In this case, M_n is found to be 8, and is used in the rest of the work.

(b) **Process Noise Covariance :**

Process noise covariance is determined following a heuristic approach. Firstly, a periodic continuous voltage signal, having frequency 0.1 Hz, amplitude 2.7 V and offset 3.8

TH-1636_10610313

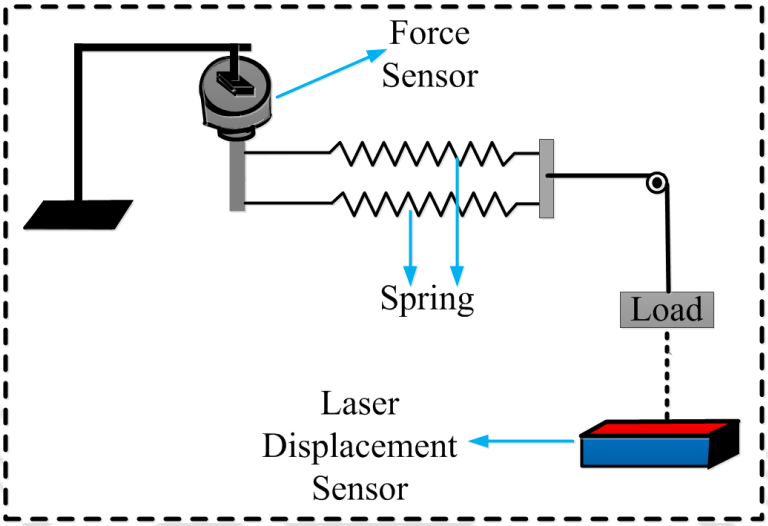

(a)

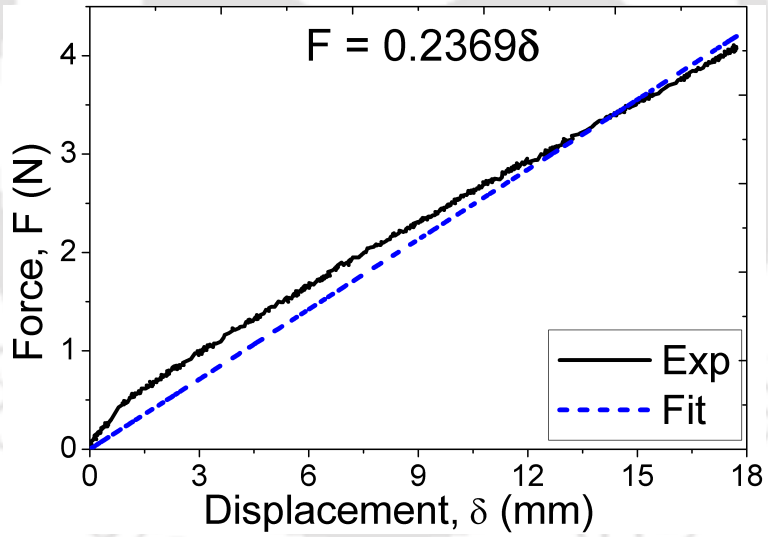

(b)

Figure 4.9: (a) Set-up for spring stiffness measurement and (b) force-displacement response of the spring.

V, is applied across the SMA wire. Following the procedure described in section 4.2.1, the variation in electrical resistance of the SMA wire and the displacement of the block between the spring and the SMA are measured. The applied voltage and the measured displacement are presented in Figs. 4.11a and 4.11b, respectively. Using the developed

TH-1636_10610313

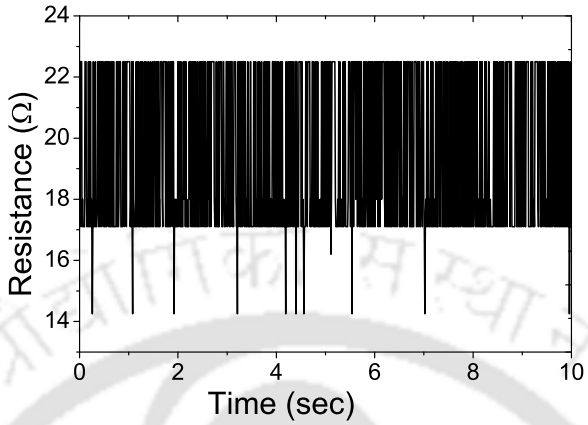

Figure 4.10: Experimentally determined electrical resistance of R_1 for $V_T = 0.1$ V.

EKF model, the displacement of the block is also estimated from the measured resistance and the applied voltage. Then the difference between the measured and estimated displacement is calculated at each time instant of the whole time span. This difference is termed as estimation error (e_δ). The value of the estimation error for different values of process noise covariance, ranging from 10^{-6} to 1, are calculated and shown in Fig. 4.11c. To get a conclusion, a cumulative error is defined as, RMSE = $\sqrt{\frac{\sum_{i=1}^{ndp} e_{\delta,i}^2}{\sum_{i=1}^{ndp} i}}$, where $e_{\delta,i}$ is the difference between EKF estimated spring displacement (δ) and the same obtained experimentally at the i^{th} instant and ndp is the total number of data points. The corresponding cumulative error, i.e., RMSE, for different $\mathbf{Q}$ are calculated and presented in Fig. 4.11d. It is evident that when the process noise covariance ($\mathbf{Q}$) is small, filter relies more on the prediction data, leading to small estimation error. Based on this result, the process noise covariance $\mathbf{Q} = 10^{-6}$ is used for EKF estimation.

TH-1636_10610313

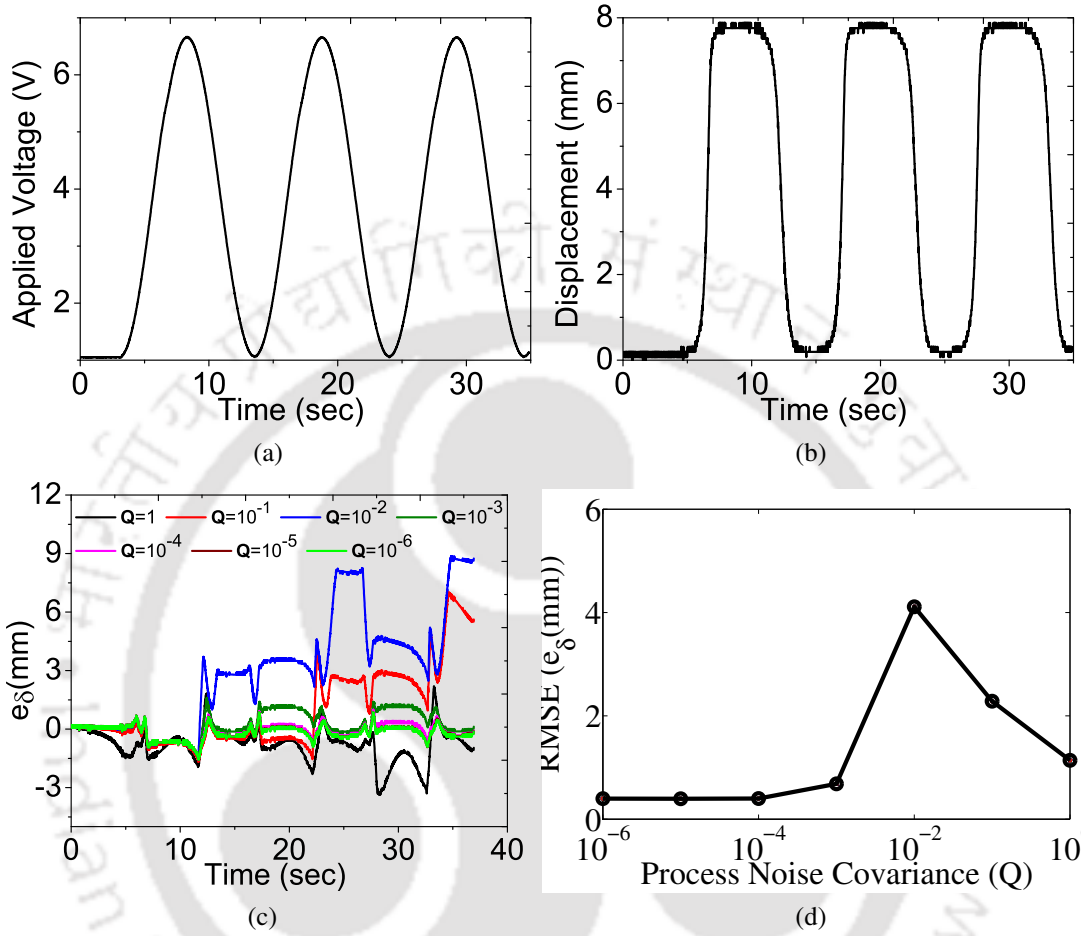

Figure 4.11: (a) Applied voltage across the SMA wire, (b) estimated and measured displacement of the system, (c) estimation error with time for different process noise covariance (**Q**), and (d) RMSE for different (**Q**).

4.3.4 Results and Discussion

A periodic voltage with decreasing amplitude, presented in Fig. 4.12a, is applied to the SMA wire actuator through Simulink → DS1006 → PPS. The change in electrical resistance of the SMA wire is measured using the voltage divider circuit. The measured electrical resistance of the SMA wire is shown in Fig. 4.12b. One can note the noise associated with resistance information measured using the voltage divider circuit. Following the developed

TH-1636_10610313

EKF model, the state of the SMA, i.e., the stress and temperature are estimated. From the estimated stress, the displacement of the block has been calculated using Eqn. (3.19). The estimated displacement with applied voltage is shown in Fig. 4.12c. The hysteresis in the SMA behavior can be observed in this figure. The voltage signal has been chosen so as to reveal the minor loops in addition to the major loops. The estimated displacement over the measured resistance is depicted in Fig. 4.12d. This shows all the minor loops distinctly, revealing the self-sensing capability of the SMA wire actuator at all possible input voltage.

Finally, the estimated and measured displacements are compared in Fig. 4.12e. The performance of the developed EKF is also evaluated for different input voltages and are presented in Figs. 4.13 and 4.14. The displacement of the spring estimated using EKF, for two continuous periodic input voltages, having time periods 10 sec and 5 sec, are compared with that of the experimentally measured displacements and are presented in Figs. 4.13a and 4.13b, respectively. Similarly, for two different step inputs, having time period 10 sec and 5 sec, the estimated and experimentally observed spring displacements are shown in Figs. 4.14a and 4.14b, respectively. These results reveal the potential of the developed EKF for self-sensing application of SMA. The quantitative discrepancy can be attributed to the modeling inaccuracies, unknown material properties of the SMA wire and the physical parameters, e.g., convective heat transfer coefficient.

4.4 EKF for SMA Actuated Cantilever Beam

The complete description of the SMA actuated nonlinear system is presented in this section. The determination of elastic modulus of beam material and the noise statistics, required for EKF estimation, are discussed below.

TH-1636_10610313

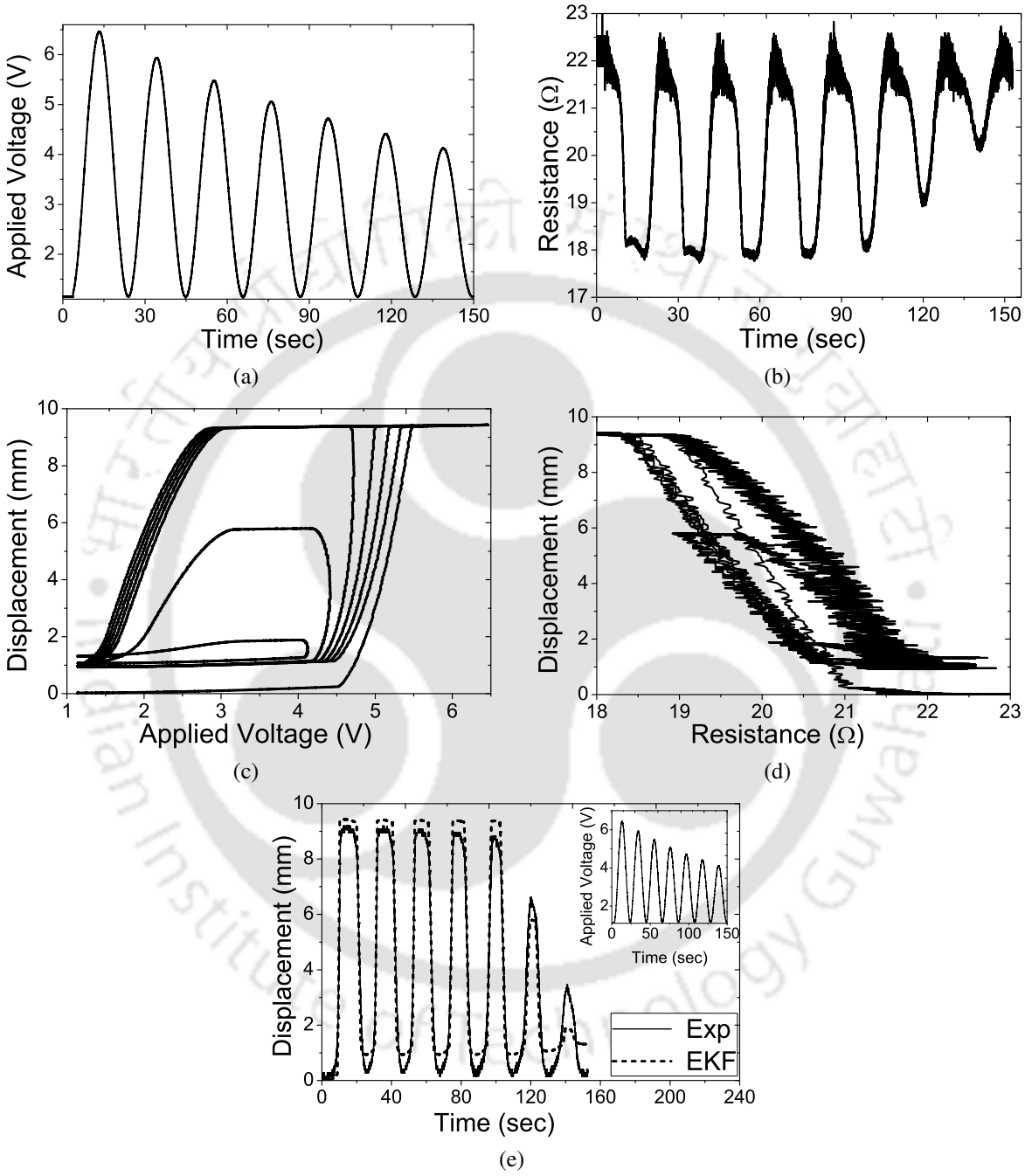

Figure 4.12: (a) Applied voltage across SMA wire, (b) measured electrical resistance of SMA, (c) variation of measured displacement with applied voltage, (d) change in measured displacement with electrical resistance of SMA, and (e) comparison between measured and estimated displacement of the system.

TH-1636_10610313

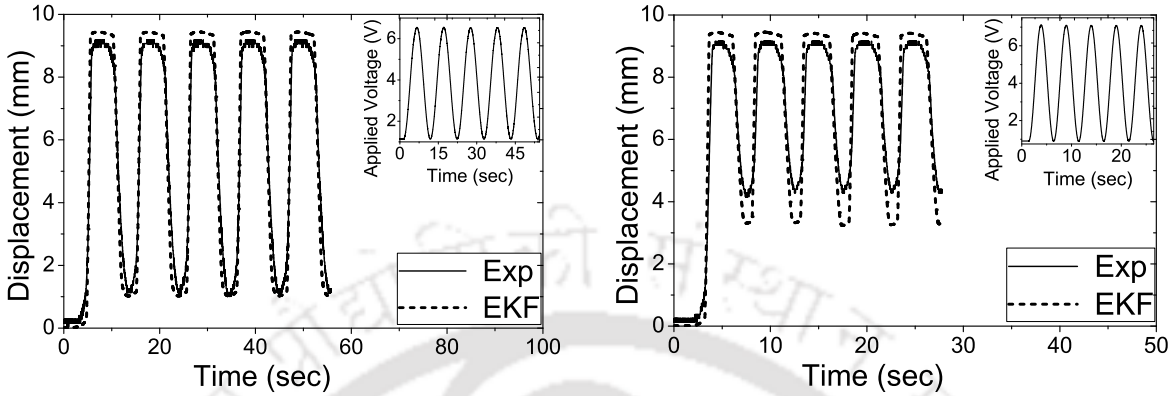

Figure 4.13: Comparison between EKF estimated and experimental responses for continuous periodic input voltage having time period of (a) 10 sec and (b) 5 sec.

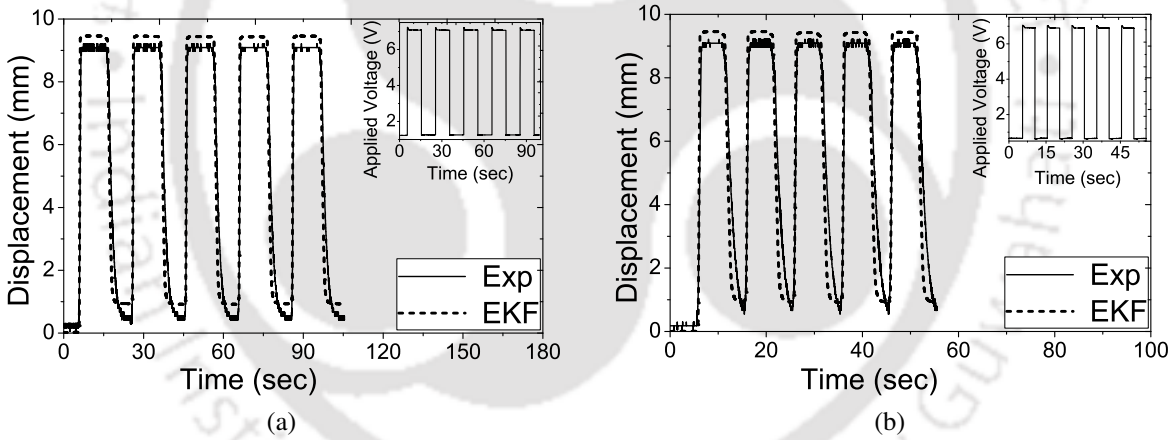

Figure 4.14: Comparison between EKF estimated and experimental responses for step input voltage for time period of (a) 10 sec and (b) 5 sec.

4.4.1 SMA Actuated Nonlinear System

For this case, the experimental set-up discussed in section 4.2 has been used to apply a desired voltage to the SMA wire actuator and measure the corresponding change in electrical resistance as well as the output displacement. In the present case, the system comprises of a cantilever beam actuated by a discretely placed SMA wire actuator, as illustrated in

TH-1636_10610313

Fig. 4.15a. As the beam undergoes large deformation, it offers a nonlinear stiffness to the wire actuator. The beam is made out of a acrylic sheet, having length, width, and thickness as 100 mm, 10 mm and 1.4 mm, respectively. The effective length of the SMA wire is 90 mm, having diameter 125 μm. It is from the same manufacturer as the one used for the linear system. The wire is attached to the beam using two screws keeping an offset of 2 mm from the neutral axis of the beam. As the wire is heated using resistive heating, it tries to contract and effectively producing a bending moment on the beam at its two ends; resulting in the bending of the beam as shown in Fig. 4.15b. In this case, the end displacement of the beam is measured by the displacement sensor and is also being estimated using EKF. Here, the offset is kept so as to produce large end displacement of the beam. Similar to the case of linear system, the resistance is obtained using the voltage divider circuit.

To make use of the developed EKF model, the system parameters like modulus of elasticity of the host beam, and the noise statistics are required. In what follows, determination of the same are discussed.

4.4.2 Modulus of Elasticity

Following ASTM standard, six samples are prepared out of the acrylic sheet material, from which the beam is made. The samples are shown in Fig. 4.16a. The samples are tested in UTM, INSTRON 8801. One of the stress - strain response is presented in Fig. 4.16b. The average slope of the initial part of the stress-strain response, is found to be 1.2 $\times 10^3$ N/mm^2.

TH-1636_10610313

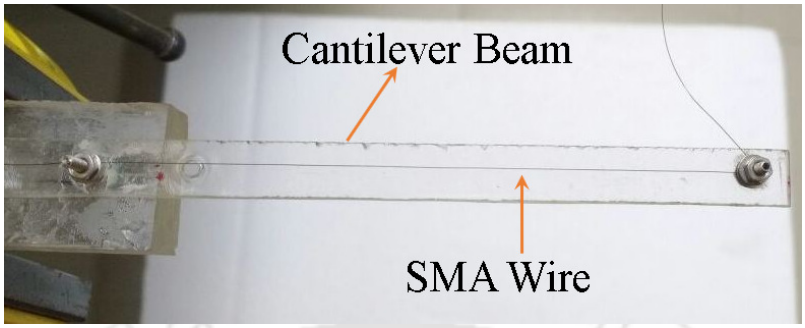

(a)

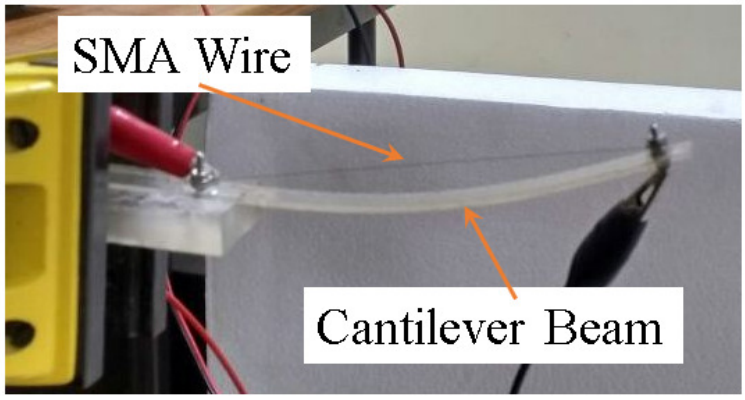

(b)

Figure 4.15: (a) Undeformed and (b) deformed shape of the SMA wire actuated cantilever beam.

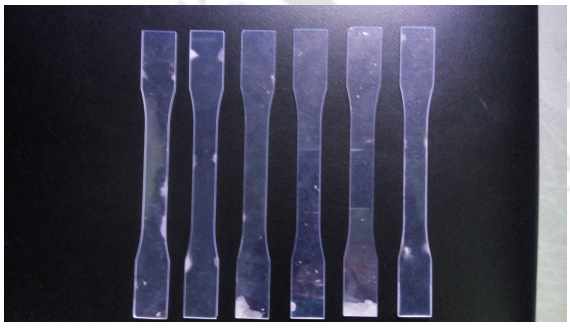

(a)

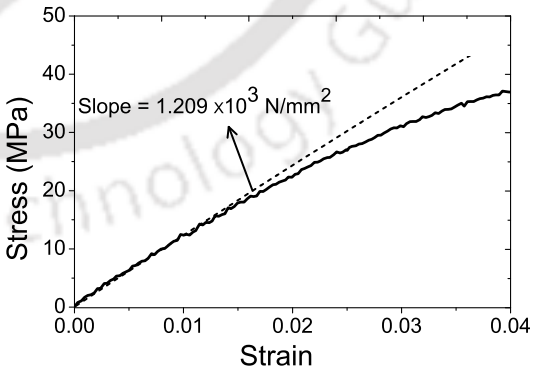

(b)

Figure 4.16: (a) Specimens of the tensile test and (b) experimental stress-strain curve of the beam material.

TH-1636_10610313

4.4.3 Determination of Process and Measurement Noise Covariance

The accuracy of EKF estimation depends heavily on the measurement and process noise statistics. These are obtained following the strategy discussed in case of linear system, section 4.3.3

(a) **Measurement Noise Covariance :** The measurement noise covariance for the present system is taken to same as in case of the linear system. Referring section 4.3.3, $\mathbf{M}_n$ = 8 is assumed.

(b) **Process noise covariance :** Following the heuristic approach discussed in section 4.3.3, the process noise covariance is determined for the present nonlinear system from the cumulative estimation error. First a periodic voltage signal is applied across the SMA wire and the corresponding change in electrical resistance of the SMA and the end-displacement of the beam are measured. These are shown in Figs. 4.17a and 4.17b. Using the developed EKF, the stress and temperature variation of the SMA are estimated, from which the end-displacement of the beam is determined. The estimation error is calculated as the difference between the measured and estimated end-displacement of the beam at a given instant. Figure 4.17c presents the estimation error for different values of $\mathbf{Q}$ for the whole time span of actuation. From this the cumulative error is calculated as RMSE = $\sqrt{\frac{\sum_{i=1}^{ndp} e_{\delta,i}^2}{\sum_{i=1}^{ndp} i}}$. The cumulative error is shown in Fig. 4.17d for different values of $\mathbf{Q}$. Thus $\mathbf{Q}$ = 10e^{-6} is used for the nonlinear system. It can be observed that the values of $\mathbf{Q}$ is same for both linear and nonlinear system. This may be because the system models for linear and nonlinear systems, are almost same expect the system's stiffness.

Finally, with these values of $\mathbf{Q}$ and $\mathbf{M}_n$, for a continuous periodic voltage with decreasing amplitude, the estimated end-displacement of the beam is compare with the

TH-1636_10610313

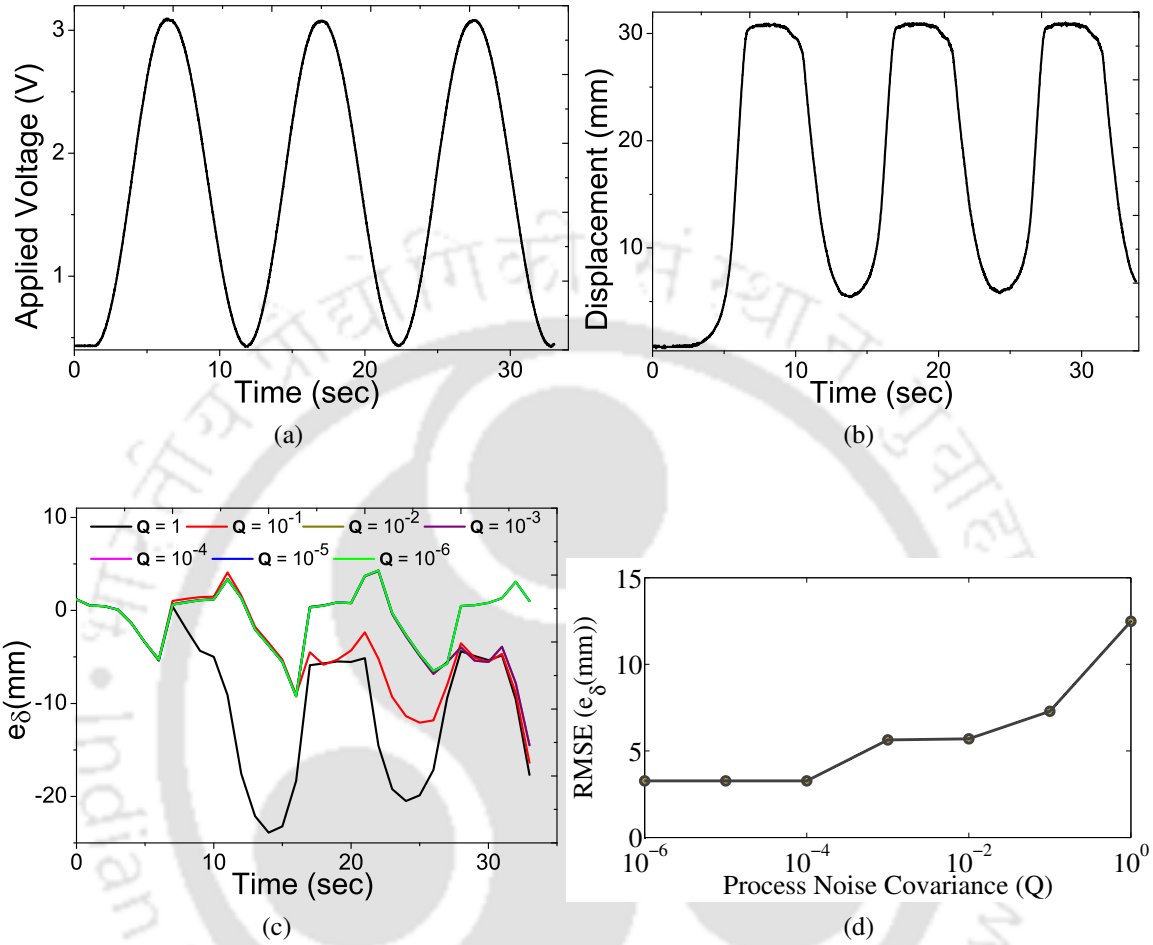

Figure 4.17: (a) Voltage applied across the SMA wire, (b) estimated and measured displacement of the system, (c) effect of process noise covariance (Q) on estimation error, and (d) effect of Q on RMSE.

measured one, and presented in Fig. 4.18. The applied voltage is shown at the inset of the same figure. The SMA wire properties and other system parameters, used in the EKF, are presented in Tables 3.1 and 3.3, respectively. The result reveals, that the EKF model can estimate the system response only qualitatively. It is needless to say that better estimation accuracy has to be achieved in order to make use of the developed EKF for harnessing the self-sensing capability of SMA wire actuator.

This quantitative discrepancy may be due to parametric and modeling inaccuracies. It

TH-1636_10610313

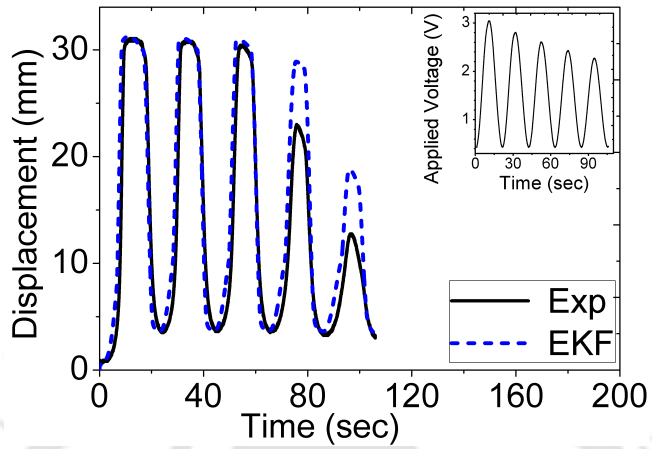

Figure 4.18: Comparison between EKF estimated and experimental responses before optimization.

has been observed that among the various parameters, the effect of the magnitude of convective heat transfer coefficient (h), on the EKF estimation is the most significant. A very small change in the value of 'h', say in the order of 1e^{-6}, hugely alters the estimated displacement. Moreover, in literature, a large range of values of 'h', from 1.552×10^{-6} [49] to 1.4×10^{-4} Jmm^{-2}s^{-1}K^{-1} [91], are used. Thus, an optimization problem is formulated to calculated a suitable 'h', which provides least difference between the estimated and experimental displacement for a particular input voltage. This procedure has been discussed in the following section.

4.4.4 Determination of Convective Heat Transfer Coefficient

Observing the different empirical relations between the convective heat transfer coefficient and temperature, as available in the literature [63, 73, 78], a relation of the following form is taken in the present work.

$$h = a_0 + b_0(T - T_0) + b_0(T - T_0)^2. \tag{4.3}$$

TH-1636_10610313

Table 4.1: Initial and final values of the co-efficient of convective heat transfer.

	Initial		Optimum	
	Heating	Cooling	Heating	Cooling
a_0	1.8×10^{-4}	2×10^{-4}	2.716×10^{-4}	2.15×10^{-4}
b_0	1×10^{-6}	1×10^{-6}	9.407×10^{-7}	1.215×10^{-6}
c_0	1×10^{-8}	1×10^{-8}	6.9841×10^{-9}	6.62×10^{-9}

Here, a_0 , b_0 and c_0 are constants to be decided and T and T_0 are the temperature of the SMA wire and of ambient, respectively. Moreover, the coefficients are assumed to be different during heating and cooling of the SMA wire [92]. It implies that there are six design variables, i.e., a pair of values of each of the coefficients a_0, b_0 and c_0. The objective is to minimize the difference between the estimated and the measured displacement of the beam for a given input voltage. Thus the objective function is defined as

$$f_{obj} = \sqrt{\sum_{i=0}^{n} (\delta_i^{es} - \delta_i^{ex})^2}. \tag{4.4}$$

Here, $\delta_i^{es}$and δ_i^{ex} are the estimated and experimentally obtained displacements, respectively, at the i^{th} data point. n represents the total data points in the whole time span. For this minimization problem, the simplex search algorithm is used [93]. For this purpose the experimental data corresponding to the one in Fig. 4.18 is used. The initial and final values of the co-efficients (a_0, b_0, c_0) are enlisted in Table 4.1 and corresponding change in objective function with number of iterations is shown Fig. 4.19a. The estimated displacement, obtained using the final optimized values of the constants listed in Table 4.1, is presented in Fig. 4.19b. Compared to the experimental displacement shown in Fig. 4.19b, a significant improvement in the estimation can be observed.

TH-1636_10610313

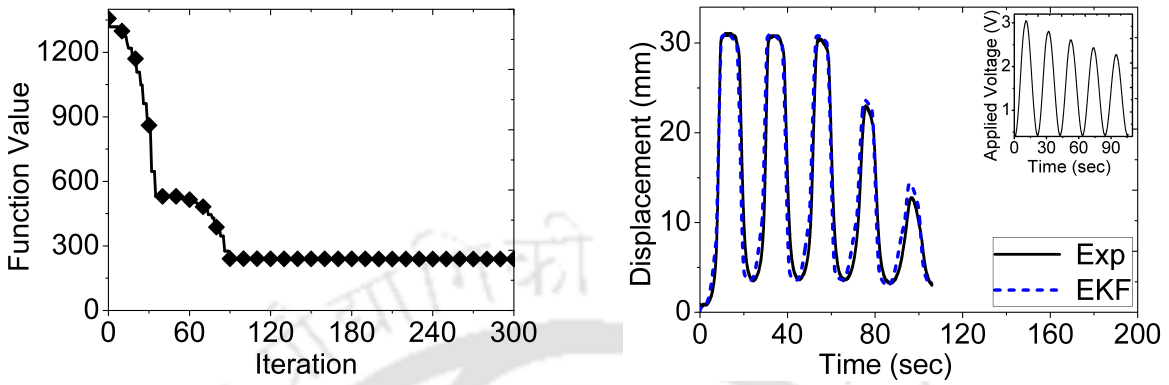

Figure 4.19: a) Change in objective function with number of iteration, (b) comparison between the EKF estimated and experimentally measured displacement with optimized h.

4.4.5 Results and Discussion

With the newly derived expression for convective heat transfer coefficient, the performance of the developed EKF is evaluated for different set of input voltage signals. Firstly, three continuous periodic voltage signals are considered; having frequencies 0.1 Hz, 0.2 Hz, and 0.5 Hz. The corresponding estimated and measured displacements are compared in Fig. 4.20. The voltage signal having frequency 0.1 Hz, induces complete forward and reverse phase transformation and the corresponding estimation accuracy is appreciable. However, for the rest of the inputs, the forward transformation is incomplete, i.e., the frequency of actuation is high enough not allowing the SMA to cool down below M_f temperature. In these two cases the estimation is inaccurate, mostly at the cooling side of a given cycle. The estimated displacement against that of the measured one for three different step inputs are presented in Fig. 4.21. These three step inputs are having step size of 10 sec, 5 sec and 2 sec with a maximum voltage as 3 V. In first two cases, i.e., for step size 10 sec and 5 sec, the SMA wire gets enough time to undergo complete phase transformation during both heating and cooling and hence accuracy of estimation is appreciable. However, for the final step input, as per the

TH-1636_10610313

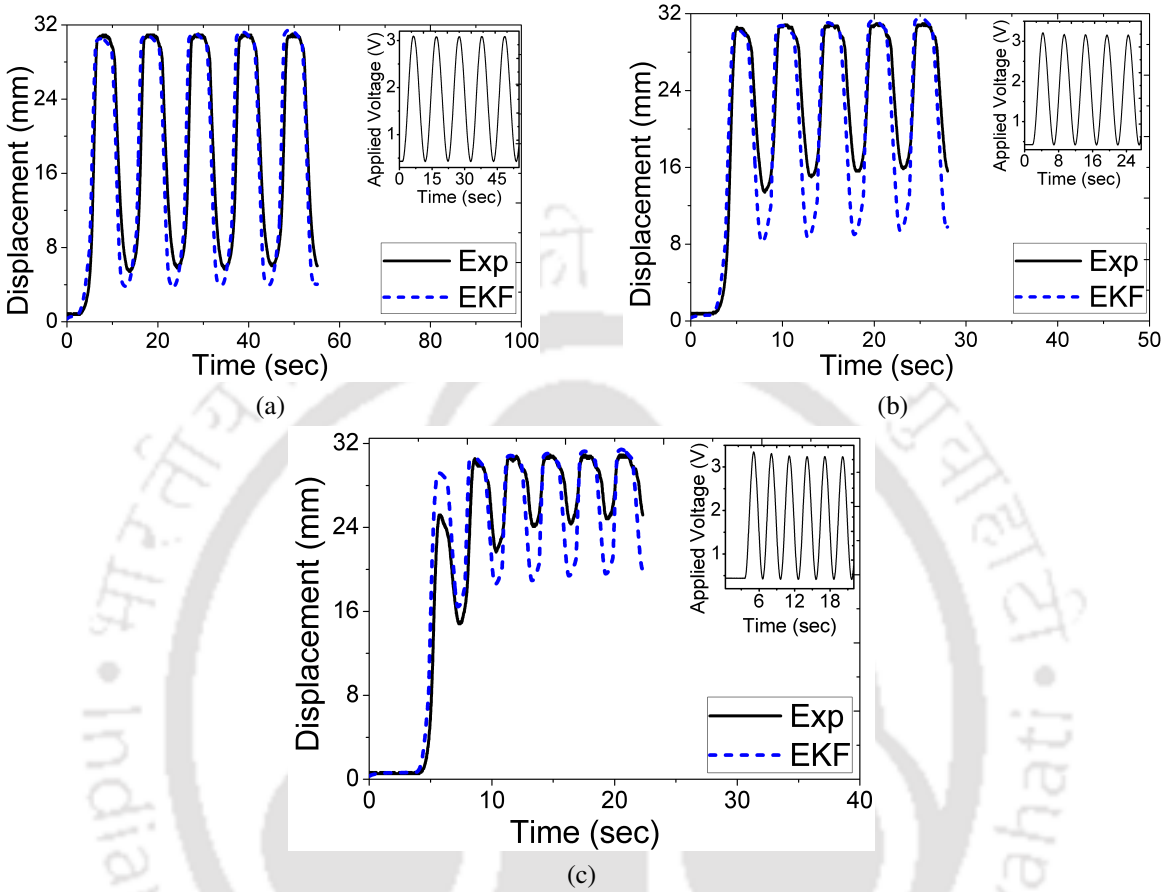

Figure 4.20: Comparison between EKF estimated and experimental responses for continuous periodic voltage having frequency, (a) 0.1 Hz, (b) 0.2 Hz, and (c) 0.5 Hz.

model, the SMA is not getting enough time to undergo forward transformation. All these results imply, that the convective heat transfer coefficient must depend on the frequency of actuation. Physically, it is meaningful, as the SMA wire is moving through the ambient with higher velocity for high actuation frequency, resulting in forced convective cooling of the wire. This feature is absent in the model, and may be contributing to the inaccuracy for higher actuation frequency.

TH-1636_10610313

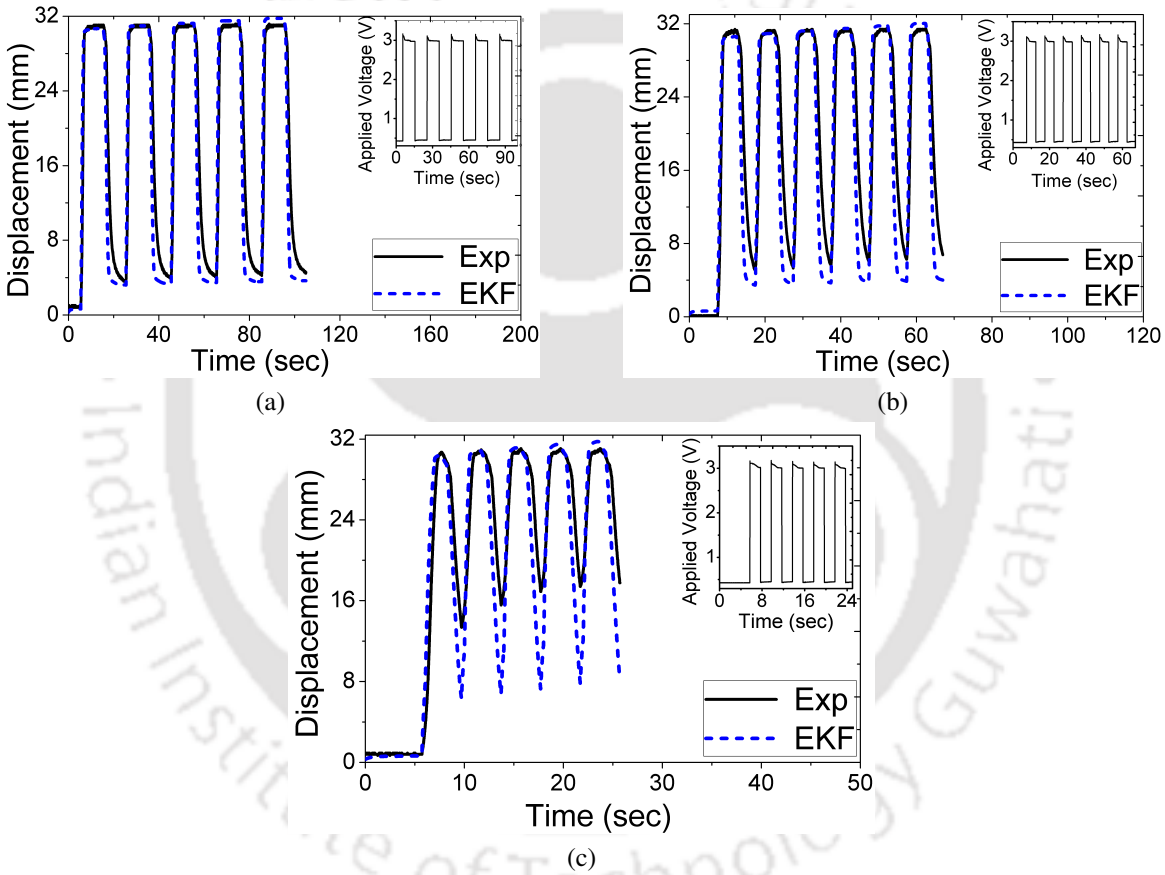

Figure 4.21: Comparison between EKF estimated and experimental responses for step voltage having time period, (a) 10 sec, (b) 5 sec, and (c) 2 sec.

TH-1636_10610313

4.5 Summary

An experimental set-up is developed to implement the EKF model for harnessing the self-sensing ability of an SMA wire actuator for both linear and nonlinear system. A desired voltage signal is applied across the SMA wire actuator and the corresponding change in electrical resistance of the same wire is measured. Alongside, the system response is also measured which is used to evaluate the performance of the developed EKF algorithm.

Some of the system parameters and noise statistics, as required for the EKF model are determined. For different input voltages, the estimated response are found to qualitatively agree with the measured response. This reveals the potential of the developed EKF model. The quantitative discrepancy may be attributed to the unknown properties of the SMA wire used, as well as, the unknown nature of some of the physical parameters e.g., convective heat transfer coefficient 'h'. An attempt has been made to determine the convective heat transfer coefficient, which minimizes the quantitative discrepancy between the estimated and the experimentally measured responses. This approach is found to render a significant improvement in the estimation accuracy.

TH-1636_10610313

Chapter 5

Unscented Kalman Filter for Self-sensing SMA Wire Actuator

5.1 Introduction

In the earlier chapter, self-sensing capability of SMA wire actuator has been explored based on an Extended Kalman Filter model. From the change in electrical resistance behavior of SMA and the state equations, the state and response of the system are estimated and compared with the measured responses. It has been observed, that the estimated response is only qualitatively accurate. In order to substitute the external sensor completely, one needs to improve the estimation quantitatively. Particularly, for partial transformation and fast actuation, large estimation error is observed. The difference can be attributed to the modeling accuracy, parametric uncertainty and the error induced in the EKF model due to the linearization of the state equations. To obviate the need of linearization, Unscented Kalman Filter has been explored in this chapter for the same applications. In Unscented Kalman

TH-1636_10610313

Filter, one need not take the linearized system model, rather it works with the nonlinear model as it is. In this chapter, the self-sensing capability of SMA wire actuator has been explored with the help of Unscented Kalman Filter. In what follows, the detailed steps of the UKF and the development of the same for SMA wire actuator are discussed, followed by the experimental verification of the developed model.

5.2 Unscented Kalman Filter (UKF)

Unscented Kalman Filter (UKF) is a mathematical tool that provides a recursive mean for state estimation of any dynamic system, from some of the measured state or functions of the state, called outputs [88, 94]. Unlike, EKF, which relies on linearization to propagate the mean and covariance of the state, the UKF uses unscented transformation. Unscented transformation is way to calculate the mean ($\hat{\mathbf{X}}$) and covariance ($\mathbf{P}$) of a random variable $\mathbf{X}$ undergoing a nonlinear transformation ($\boldsymbol{\eta}$). The main idea behind the UT, is to approximate the probability distribution of a random variable undergoing nonlinear transformation based on a set of weighted samples, which are called sigma points ($\boldsymbol{\chi}$). In other words, the sigma points and the corresponding weights basically represent the statistical characteristics of the output transformed variable. It has been shown that the mean and covariance obtained by this method are accurate up to second order for any nonlinearity [95]. In what follows, the basics steps of UKF are described briefly. In discrete form, the system dynamics are presented below as,

State Equation :

$$\mathbf{X}_{t_k} = \boldsymbol{\eta}(\mathbf{X}_{t_{k-1}}, \mathbf{u}_{t_k}) + \mathbf{w}_{t_{k-1}}. \tag{5.1}$$

Output Equation :

$$\mathbf{Y}_{t_k} = \boldsymbol{\Gamma}(\mathbf{X}_{t_k}) + \mathbf{v}_{t_k}. \tag{5.2}$$

TH-1636_10610313

Here, $\mathbf{X}$ represents state vector of the system and $\boldsymbol{\eta}$ is a vector of the nonlinear process functions, to be evaluated from the state at previous instant (t_{k-1}) and the input vector denoted by $\mathbf{u}_{t_k}$. The vector $\mathbf{w}_{t_{k-1}}$ implies the process noise; used to take care of the modeling inaccuracy and parametric uncertainty. In Eqn. (5.2), $\mathbf{Y}_{t_k}$ refers to the observation vector and $\boldsymbol{\Gamma}$ is a vector of nonlinear observation functions, and is a function of state $[\mathbf{X}_{t_k}]$. The uncertainty in the sensor reading is presented by a vector of random variable $\mathbf{v}_{t_k}$. Here, the noises are assumed to be white Gaussian, and are uncorrelated. This implies,

$$\begin{aligned} & w_k \sim (0, Q_k)\,, \\ & v_k \sim \left(0, M_{n,k}\right), \\ & E\left[w_k {w_j}^T\right] = Q_k \delta_{k-j}, \\ & E\left[v_k {v_j}^T\right] = M_{n,k} \delta_{k-j}, \\ & E\left[v_k {w_j}^T\right] = 0. \end{aligned} \tag{5.3}$$

5.2.1 The Unscented Kalman Filter

As in case of EKF, the UKF comprises of two steps, namely, "**Time update**" and "**Measurement update**". Each of the steps are discussed in details below.

1. **Time update :**

   (i) At current instant (t_k), $(2n+1)$ the sigma points $\hat{\mathbf{X}}_{t_k}$ are generated from the updated state at the previous instant ($\hat{\mathbf{X}}^+_{t_{k-1}}$) and the covariance ($\mathbf{P}^+_{t_{k-1}}$), following,

$$\begin{aligned} \hat{\mathbf{X}}^{(0)}_{t_{k-1}} &= \hat{\mathbf{X}}^+_{t_{k-1}}, \\ \hat{\mathbf{X}}^{(i)}_{t_{k-1}} &= \hat{\mathbf{X}}^+_{t_{k-1}} + \bar{\mathbf{X}}^{(i)}, \qquad \text{where} \quad i = 1, \cdots, 2n. \\ \text{Here,} \quad \bar{\mathbf{X}}^{(i)} &= \left(\sqrt{(n+\kappa)\mathbf{P}^+_{t_{k-1}}}\right)^T. \qquad \text{where} i = 1, \cdots, n. \end{aligned}$$

TH-1636_10610313

$$\text{and,} \quad \bar{\mathbf{X}}^{(n+i)} = -\left(\sqrt{(n+\kappa)\mathbf{P}^{+}_{t_{k-1}}}\right)^{T}. \qquad \text{where} \quad i = 1, \cdots, n \tag{5.4}$$

Here, $\left(\sqrt{(n+\kappa)\mathbf{P}^{-}_{t_{k-1}}}\right)$ represents the i^{th} row of the matrix $\sqrt{(n+\kappa)\mathbf{P}_{t_{k-1}}}$, κ is a constant used to reduce the higher order errors and n represents the number of state to be estimated. The weight coefficients ($W^{(i)}$) corresponding to each sigma points are as follows.

$$\begin{aligned} W^{(0)} &= \tfrac{\kappa}{n+\kappa}, \\ W^{(i)} &= \tfrac{1}{n+\kappa}. \quad \text{where} \quad i = 1, \cdots, 2n. \end{aligned} \tag{5.5}$$

(ii) Using the nonlinear process function ($\boldsymbol{\eta}$) given in Eqn. (5.1), the sigma points are transformed as,

$$\hat{\mathbf{X}}^{(i)}_{t_k} = \boldsymbol{\eta}(\hat{\mathbf{X}}^{(i)}_{t_{k-1}}, \mathbf{u}_{t_k}, t_k). \tag{5.6}$$

(iii) The a-priori state estimate at time t_k is obtained from $\hat{\mathbf{X}}^{(i)}_{t_k}$ following,

$$\hat{\mathbf{X}}^{-}_{t_k} = \sum_{i=0}^{2n} W^{(i)} \hat{\mathbf{X}}^{(i)}_{t_k}. \tag{5.7}$$

(iv) The estimate of the a-priori state error covariance ($\mathbf{P}^{-}_{t_k}$) is obtained as,

$$\mathbf{P}^{-}_{t_k} = \sum_{i=0}^{2n} W^{(i)} (\hat{\mathbf{X}}^{(i)}_{t_k} - \hat{\mathbf{X}}^{-}_{t_k})(\hat{\mathbf{X}}^{(i)}_{t_k} - \hat{\mathbf{X}}^{-}_{t_k})^{T} + \mathbf{Q}_{t_{k-1}}. \tag{5.8}$$

Here, $\hat{\mathbf{X}}^{(i)}_{t_k}$ represent the transformed sigma points, calculated using Eqn. (5.6) at current instant t_k, and $W^{(i)}$ are the corresponding weights, defined in Eqn. (5.5). $\hat{\mathbf{X}}^{-}_{t_k}$ denotes the a-priori estimate of the state of system of order $\{n \times 1\}$ and $\mathbf{Q}$ is the process noise covariance matrix of order $\{n \times n\}$.

TH-1636_10610313

2. **Measurement update** :

(i) Here the sigma points are obtained based on the a-priori mean $(\hat{\mathbf{X}}_{t_k}^{-})$ and covariance $(\mathbf{P}_{t_k}^{-})$ as,

$$\begin{aligned}
\hat{\mathbf{X}}_{t_{k-1}}^{(0)} &= \hat{\mathbf{X}}_{t_{k-1}}^{+}, \\
\hat{\mathbf{X}}_{t_{k-1}}^{(i)} &= \hat{\mathbf{X}}_{t_{k-1}}^{+} + \bar{\mathbf{X}}^{(i)}, \qquad \text{where} \quad i = 1, \cdots, 2n. \\
\text{Here,} \quad \bar{\mathbf{X}}^{(i)} &= \left(\sqrt{(n+\kappa)\mathbf{P}_{t_{k-1}}^{+}}\right)^{T}. \qquad \text{where} i = 1, \cdots, n. \\
\text{and,} \quad \bar{\mathbf{X}}^{(n+i)} &= -\left(\sqrt{(n+\kappa)\mathbf{P}_{t_{k-1}}^{+}}\right)^{T}. \qquad \text{where} \quad i = 1, \cdots, n.
\end{aligned} \tag{5.9}$$

(ii) Now the sigma points are transformed using observation function ($\mathbf{\Gamma}$) presented in Eqn. (5.2) to obtain the estimated measurement as,

$$\hat{\mathbf{Y}}_{t_k}^{(i)} = \mathbf{\Gamma}(\hat{\mathbf{X}}_{t_k}^{(i)}, t_k). \tag{5.10}$$

(iii) The estimated measurement is obtained from $\hat{\mathbf{Y}}_{k}^{(i)}$ following,

$$\hat{\mathbf{Y}}_{t_k} = \sum_{i=0}^{2n} W^{(i)} \hat{\mathbf{Y}}_{t_k}^{(i)}. \tag{5.11}$$

(iv) Similarly, the covariance of the estimated measurement is obtained using,

$$\mathbf{P}_Y = \sum_{i=0}^{2n} W^{(i)} (\hat{\mathbf{Y}}_{t_k}^{(i)} - \hat{\mathbf{Y}}_{t_k})(\hat{\mathbf{Y}}_{t_k}^{(i)} - \hat{\mathbf{Y}}_{k})^{T} + \mathbf{M}_{n,t_k}\,. \tag{5.12}$$

Here, $\mathbf{P}_Y$ denotes the measurement error covariance of order $\{p \times 1\}$, $\hat{\mathbf{Y}}_{t_k}^{(i)}$ represents the transformed sigma point, calculated using Eqn. (5.10), and $\hat{\mathbf{Y}}_{t_k}^{-}$ is the estimated observation at time t_k, having order $\{p \times 1\}$. $\mathbf{M}_n$ denotes the measurement noise covariance matrix of order $\{p \times p\}$. Here, p represents the number of

TH-1636_10610313

output or observation.

(v) Cross covariance between the $\hat{\mathbf{X}}_{t_k}^{-}$ and $\hat{\mathbf{Y}}_{t_k}$, which is of order $\{n \times p\}$, is obtained following,

$$\mathbf{P}_{XY} = \sum_{i=0}^{2n} W^{(i)} (\hat{\mathbf{X}}_{t_k}^{(i)} - \hat{\mathbf{X}}_{t_k}^{-})(\hat{\mathbf{Y}}_{t_k}^{(i)} - \hat{\mathbf{Y}}_{t_k})^T. \tag{5.13}$$

(vi) The state estimation of the system are updated using the measured data ($\mathbf{Y}_{t_k}$) and Kalman gain ($\mathbf{G}_{t_k}$), following,

$$\hat{\mathbf{X}}_{t_k}^{+} = \hat{\mathbf{X}}_{t_k}^{-} + \mathbf{G}_{t_k}(\mathbf{Y}_{t_k} - \hat{\mathbf{Y}}_{t_k}). \tag{5.14}$$

Here, the first term $\{\hat{\mathbf{X}}_{t_k}^{-}\}$ represents the a-priori estimated state of the system, computed using Eqn. (5.7) and the second term denotes the product of Kalman gain ($\mathbf{G}_{t_k}$) and innovation ($\mathbf{Y}_{t_k} - \hat{\mathbf{Y}}_{t_k}$). The innovation is also called measurement residual, as it represents the difference between measured and estimated output. The smaller the innovation is, the better is the estimation. The role of Kalman gain (refer Eqn. (5.14)) in UKF estimation is same as that of the EKF. It is the Kalman gain, which decides the weight on the a-priori estimation and measurement data, following which a-priori estimation is updated. The Kalman gain is computed, depending on the covariance of the estimated measurement ($\mathbf{P}_Y$) and the cross covariance ($\mathbf{P}_{XY}$); between the estimated state and measurement and can be expressed as,

$$\mathbf{G}_{t_k} = \mathbf{P}_{XY}\mathbf{P}_Y^{-1}. \tag{5.15}$$

Next, the posteriori estimation of the state error covariance matrix is calculated following,

$$\mathbf{P}_{t_k}^{+} = \mathbf{P}_{t_k}^{-} - \mathbf{G}_{t_k}\mathbf{P}_Y\mathbf{G}_{t_k}^T. \tag{5.16}$$

TH-1636_10610313

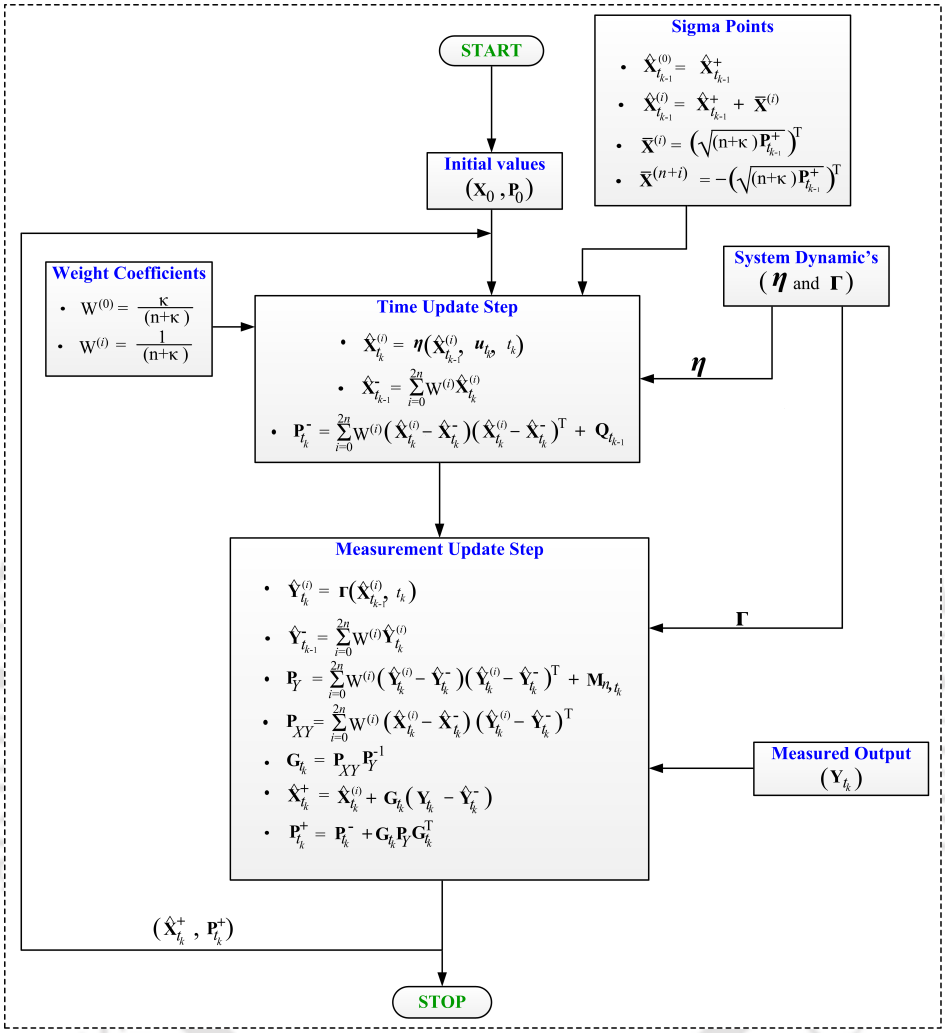

Figure 5.1: Steps in Unscented Kalman Filter.

The sequence of evaluations in an UKF model is illustrated in Fig. 5.1. In order to make use of this algorithm, one requires the system dynamics in the form of Eqns. (5.1) and (5.2). For the SMA actuated system, the system dynamics comprises of one-dimensional constitutive behavior of the SMA wire, heat (energy) balance equation, phase kinetics of the SMA, force-deformation relation of the system being actuated and the electrical resistance-strain relationship of the SMA. The details of all these equations are presented in sections 2.6 and 3.5.

TH-1636_10610313

5.3 System Description

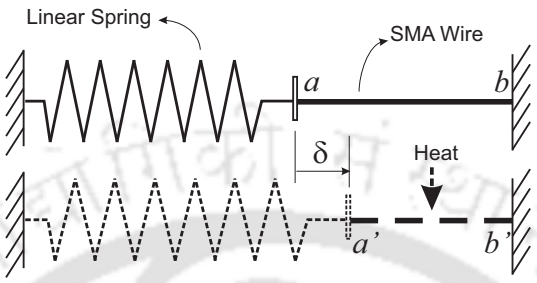

Figure 5.2: Schematic of the SMA actuated system.

The SMA actuated linear system used in case of EKF model, is presented in Fig. 5.2. The pre-strained (due to the application of load above σ_s^{cr}) SMA actuator (a - b) is serially connected with the linear spring through a small block of acrylic sheet, which is movable. The other end of both SMA wire and spring is kept fixed. As the voltage is applied across the pre-strained SMA wire (a - b), the temperature of the SMA wire starts increasing. As the temperature reaches the austenite start temperature (A_s), the detwinned martensite starts converting to austenite phase and SMA starts contracting. As the spring prevents the SMA from contracting, large recovery stress is generated within the wire and consequently stretched the spring by an amount (δ). The contracted length of the SMA wire is presented by (a'- b'). Similarly, during cooling, as the voltage is reduced, the restoring force of the spring stretches the SMA wire to its initial deformed length. Thus the SMA wire becomes ready for the next actuation. Here, the main objective is to estimate the displacement (δ) of the system from the measured electrical resistance of the SMA using UKF.

TH-1636_10610313

5.4 UKF for SMA Actuated System

The motivation of the present section is to derive the process and observation vector functions for the SMA actuated linear system (refer Fig. 5.2), so as to develop its UKF model. As in the case of EKF, the state of the SMA wire at any instant comprises of stress (σ), and temperature (T); which is written as,

$$\mathbf{X} = \begin{bmatrix} T & \sigma \end{bmatrix}^{\intercal}. \tag{5.17}$$

- **Nonlinear Process Vector Function (η) :**

  The dynamics of the defined system, in the forms given by Eqns. (5.1) and (5.2), are derived from the coupled thermo-mechanical model of the SMA wire and the behavior of the linear spring. The rate form of the stress and temperature, following Eqns. (3.57) and (3.58), as discussed in section 3.6.1.2, are rewritten as,

$$\frac{dT}{dt} = \frac{\frac{V(t)^2}{R} - hA_{surf}(T - T_0)}{V_m C_v - \lambda\left(\psi_2 + \psi_1\psi_5\right)} \Rightarrow \phi_1. \tag{5.18}$$

$$\frac{d\sigma}{dt} = \frac{F_5\left(\frac{V(t)^2}{R} - hA_{surf}(T - T_0)\right)}{V_m C_v - \lambda\left(\psi_2 + \psi_1 F_5\right)} \Rightarrow \phi_2. \tag{5.19}$$

  Here, $F_5 = \left(\frac{-\epsilon_l D\psi_4 + (\epsilon - \epsilon_l\xi_s)(D_m - D_a)\psi_2 + \Theta}{1 - D\frac{\partial\epsilon}{\partial\sigma} + \epsilon_l D\psi_3 - (\epsilon - \epsilon_l\xi_s)(D_m - D_a)\psi_1}\right)$, $\psi_1 = \frac{d\xi}{d\sigma}$, $\psi_2 = \frac{d\xi}{dT}$, $\psi_3 = \frac{d\xi_s}{d\sigma}$ and $\psi_4 = \frac{d\xi_s}{dT}$. Here, for each transformation zone, the four functions $\psi_1, \psi_2, \psi_3, \psi_4$, are determined by collecting the coefficients of $\dot{\sigma}$ and $\dot{T}$, from the rate form of the phase kinetics given by Eqns. (2.35) and (2.36). These equations can be rewritten as,

$$\frac{d\xi}{dt} = \psi_1(\sigma, T; \sigma_j, T_j, \xi_j)\frac{d\sigma}{dt} + \psi_2(\sigma, T; \sigma_j, T_j, \xi_j)\frac{dT}{dt}. \tag{5.20}$$

$$\frac{d\xi_s}{dt} = \psi_3(\sigma, T; \sigma_j, T_j, \xi_j)\frac{d\sigma}{dt} + \psi_4(\sigma, T; \sigma_j, T_j, \xi_j)\frac{dT}{dt}. \tag{5.21}$$

TH-1636_10610313

The detailed derivations of ψ_1, ψ_2, ψ_3 and ψ_4, for each transformation zones are presented in section 3.6.1.2. These expressions are listed as,

– **Forward Transformation :**

$$\begin{aligned}
\psi_1 &= \frac{0.5\pi(1-\xi_j)\sin(\pi Z^M)\cos\phi^M}{(T_j-M_f)\sin\phi^M-\sigma_j\cos\phi^M}.\\
\psi_2 &= \frac{-0.5\pi(1-\xi_j)\sin(\pi Z^M)\sin\phi^M}{(T_j-M_f)\sin\phi^M-\sigma_j\cos\phi^M}.\\
\psi_3 &= \frac{0.5\pi(1-\cos(\pi Z^M))(\text{sech}(\pi(2Z^\sigma-1)))^2}{(\sigma_f^{cr}-\sigma_s^{cr})} + \frac{0.5\pi(\xi'-\xi_{sj})\sin(\pi Z^M)\cos\phi^M}{(T_j-M_f)\sin\phi^M-\sigma_j\cos\phi^M}.\\
\psi_4 &= \frac{-0.5\pi(\xi'-\xi_{sj})\sin(\pi Z^M)\sin\phi^M}{(T_j-M_f)\sin\phi^M-\sigma_j\cos\phi^M}.
\end{aligned} \tag{5.22}$$

– **Reverse Transformation :**

$$\begin{aligned}
\psi_1 &= \frac{0.5\xi_j\pi\sin(\pi Z^A)\cos\phi^A}{(A_f-T_j)\sin(\phi^A)+\sigma_j\cos(\phi^A)}.\\
\psi_2 &= \frac{-0.5\xi_j\pi\sin(\pi Z^A)\sin\phi^A}{(A_f-T_j)\sin(\phi^A)+\sigma_j\cos(\phi^A)}.\\
\psi_3 &= \frac{0.5\xi_{sj}\pi\sin(\pi Z^A)\cos\phi^A}{(A_f-T_j)\sin(\phi^A)+\sigma_j\cos(\phi^A)}.\\
\psi_4 &= \frac{-0.5\xi_{sj}\pi\sin(\pi Z^A)\cos\phi^A}{(A_f-T_j)\sin(\phi^A)+\sigma_j\cos(\phi^A)}.
\end{aligned} \tag{5.23}$$

– **Passive Transformation :**

$$\begin{aligned}
\psi_1 &= 0.\\
\psi_2 &= 0.\\
\psi_3 &= 0.\\
\psi_4 &= 0.
\end{aligned} \tag{5.24}$$

TH-1636_10610313

If the right hand side of Eqns. (5.18) and (5.19) are denoted as ϕ_1 and ϕ_2, respectively, then the state equation can be obtained as,

$$\begin{bmatrix} T_{t_k} \\ \sigma_{t_k} \end{bmatrix} = \begin{bmatrix} T_{t_{k-1}} + \phi_1(T,\sigma)\Delta t \\ \sigma_{t_{k-1}} + \phi_2(T,\sigma)\Delta t \end{bmatrix} + \mathbf{w}_{t_{k-1}}. \tag{5.25}$$

Here, Δt represents the time step, and is defined as $\Delta t = t_k - t_{k-1}$. Recalling Eqn. (5.25), the process nonlinear vector function ($\boldsymbol{\eta}$) appears to be,

$$\boldsymbol{\eta}(\mathbf{X}_{t_k}) = \begin{bmatrix} T_{t_k} + \phi_1(T_{t_{k-1}}, \sigma_{t_{k-1}})\Delta t \\ \sigma_{t_k} + \phi_2(T_{t_{k-1}}, \sigma_{t_{k-1}})\Delta t \end{bmatrix}. \tag{5.26}$$

- **Nonlinear Observation Functions ($\boldsymbol{\Gamma}$) :**

  As the goal is to make use of the measured electrical resistance of the SMA wire to estimate the state, the electrical resistance (R_{SMA}) of the SMA wire is taken as the only observation. Following the discussion in section 3.5.2, the electrical resistance of the SMA wire is expressed in terms of stress and temperature as,

$$\mathbf{Y_{t_k}} = R_{t_k},$$

This implies, (5.27)

$$\boldsymbol{\Gamma}(\mathbf{X}_{t_k}) = \frac{(\rho_M \xi(T,\sigma) + \rho_A(1-\xi(T,\sigma)))L_0(1+(\epsilon_0 - \frac{\sigma A}{K_s L_0}))}{A}. \tag{5.28}$$

Here, $\xi(T,\sigma)$ represents the variation of martensite volume fraction with stress and temperature of the SMA wire. It is determined from the a-priori estimate of stress and temperature obtained at the previous instant, using the phase kinetics described in section 2.6.2.2.

TH-1636_10610313

5.4.1 Validation of the UKF Model

UKF is implemented for the SMA wire actuated system following the steps mentioned below.

- At any time step t_k, first the sigma points ($\hat{\mathbf{X}}^{(i)}_{t_{k-1}}$) and the weights ($W^i$) corresponding to each sigma points, are computed using the covariance ($\mathbf{P}^{+}_{t_{k-1}}$) obtained at the previous time step, following the Eqns. (5.4) and (5.5), respectively. For the SMA actuated system, n = 2, as two state variables (T and σ) are estimated using UKF. Here, κ is assumed to be 1 and Δt is taken as 0.01 sec.

- Next, the calculated sigma points are now transformed using the process vector functions ($\boldsymbol{\eta}$) given by Eqn. (5.26); from which the a-priori mean ($\hat{\mathbf{X}}^{-}_{t_k}$) and covariance ($\mathbf{P}^{-}_{t_k}$) are determined following Eqns. (5.7) and (5.8), respectively. In the present case, the size of the $\mathbf{P}$ matrix is $\{2 \times 2\}$.

- Then from the a-priori estimate of stress and temperature, the martensite volume fractions(ξ, ξ_s) are calculated using Eqn. (2.35) and (2.36). Next, instead of determining the new sigma points from the a-priori estimate of the covariance (as in Eqn. (5.9)), the sigma points, determined in the '**Time update**' past of the same time step, are used in the '**measurement update**' step. This is done to reduce the computational effort.

- Next the sigma points are transformed using the observation vector function ($\boldsymbol{\Gamma}$), given by Eqn. (5.28). From the transformed sigma points the output ($\hat{\mathbf{Y}}_{t_k}$) of the system is estimated following Eqn. (5.11). For the present system, the electrical resistance of SMA is the only observation, thus, p = 1. From the same sigma points and $\hat{\mathbf{Y}}_{t_k}$, the required covariance matrices $\mathbf{P}_{Y_{t_k}}$ and $\mathbf{P}_{XY_{t_k}}$, are determined following Eqns. (5.12) and (5.13), respectively. For the given system the size of $\mathbf{P}_Y$ is $\{1 \times 1\}$ and that of $\mathbf{P}_{XY}$ is $\{2 \times 1\}$.

TH-1636_10610313

- Then the state and covariance are updated following Eqns. (5.14) and (5.16), respectively. With the updated values of stress and temperature, the martensite volume fractions are updated following Eqns. (2.35) and (2.36).

- At this stage, the current value of stress, temperature and martensite volume fractions are assigned to the memory parameters, only if the transformation is passive. The active or passive state of the transformation is determined using the algorithm discussed in section 2.7.1. Finally, the displacement of the spring is estimated by inserting the updated value of stress in Eqn. (3.19).

5.5 Results and Discussion

Following the same experimental set-up, presented in Fig. 4.1, the variation of the electrical resistance of the SMA wire and the corresponding change in length of the spring are measured for a given time varying voltage applied across the SMA wire actuator depicted in Fig. 4.12a. The UKF model stated in section 5.4 is implemented in MATLAB, to estimate the stress and temperature of the SMA wire for the same voltage and the corresponding experimentally measured electrical resistance of the SMA wire. Finally, the change in length of the spring is estimated from the estimated stress of the SMA wire actuator following Eqn. (3.19). The properties of the SMA wire, used in the UKF model, are enlisted in Table 3.1. In this model, the initial conditions are assumed as σ_0 = 80 MPa, T_0 = 26 °C, ξ_0 = 1 and ξ_{S_0} = 0.71. Following section 4.3.3 , the process and measurement noise covariance are assumed as $\mathbf{Q} = 10e^{-6}\mathbf{I}$ and $\mathbf{M}_n$ = 8, respectively. Here, $\mathbf{I}$ stands for an identity matrix of order 2×2.

For two different time varying voltage signals, the estimated displacement of the linear

TH-1636_10610313

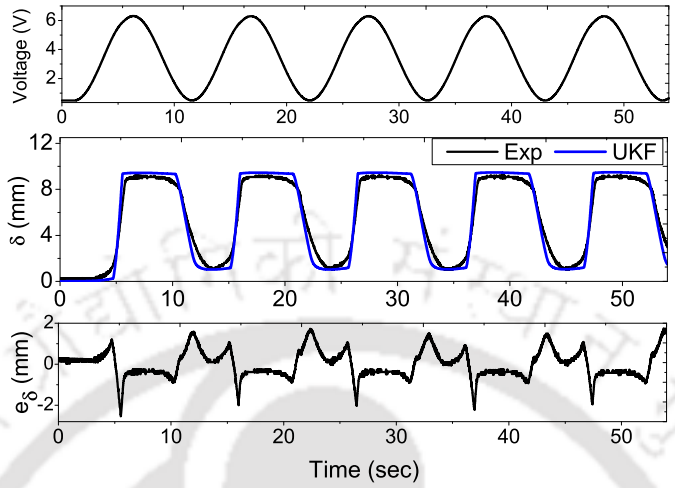

(a)

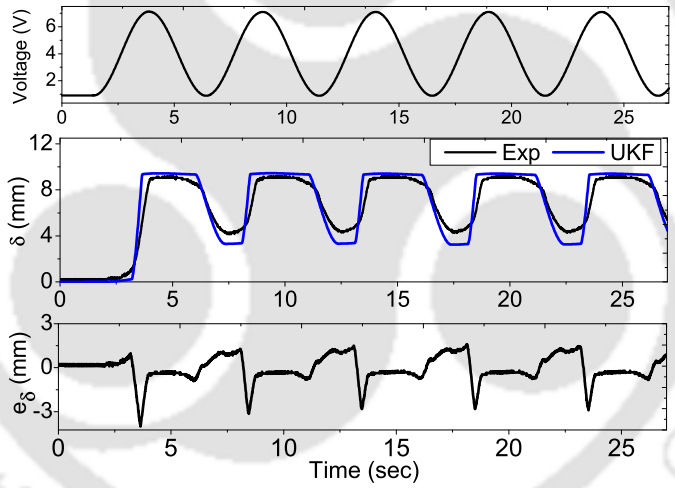

(b)

Figure 5.3: Comparison between experimental response and UKF estimation for continuous periodic signal of time period, (a) 10 sec, and (b) 5sec.

system (δ), obtained using the developed UKF are compared with that of the same, measured experimentally (δ_m) and presented in Fig. 5.3. The voltage signals being applied across the SMA wire are continuous and periodic and are depicted in the top most plot of each of these figures. The time periods of the voltage signals presented in Fig. 5.3a and 5.3b are 10 sec and 5 sec, respectively. The corresponding estimation error (e_δ), calculated as e_δ =

TH-1636_10610313

δ_m - δ, are shown in the bottom most plot of each of the figures. Though the estimated and measured displacements agree qualitatively, the quantitative discrepancy between the two are significantly large; particularly during the transient part of the response.

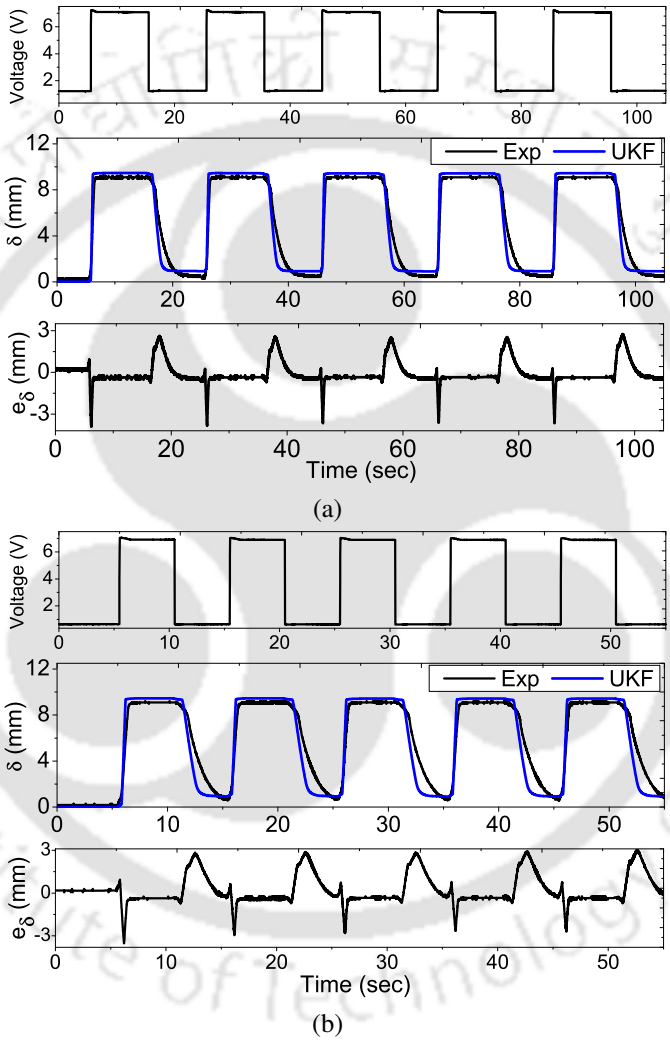

Figure 5.4: Comparison between experimental response and UKF estimation for step input of time period, (a) 10 sec, and (b) 5sec.

Similar responses are observed for two different square wave signals, having time periods 10 sec and 5 sec, and are presented in Fig. 5.4a and 5.4b, respectively. In each of the figures, the first subplot shows the voltage signal applied across the SMA wire, the corre-

TH-1636_10610313

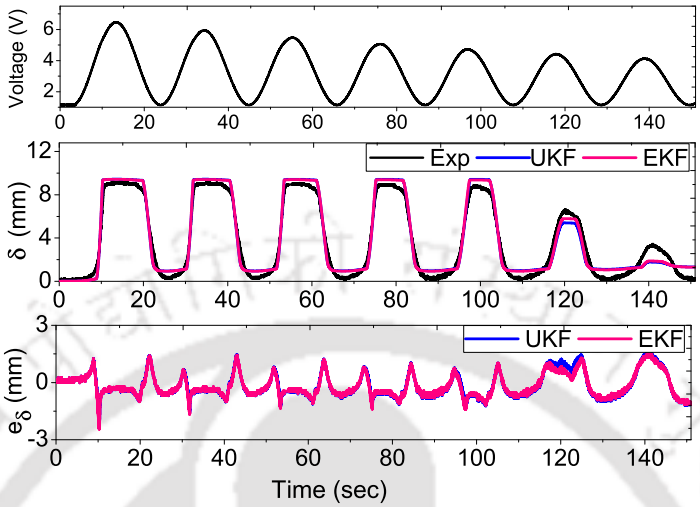

Figure 5.5: Comparison between Experimental Response, EKF and UKF estimation for a continuous decreasing periodic signal of time period 10 sec.

sponding estimated and measured displacements are compared in the second subplot. The last subplot depicts the calculated error in estimation. The maximum error is found to occur during the heating and cooling part of the responses. In all the above cases, the amplitude of the voltage signal is chosen so as to ensure the complete phase transformation in SMA wire actuator. To understand the accuracy of the developed UKF model, in case of partial phase transformation in SMA wire, a continuous periodic voltage signal with decreasing amplitude is applied across the SMA wire, as shown in the first subplot of Fig. 5.5. The corresponding estimated displacements obtained using both, EKF and UKF models, are presented in the second subplot of Fig. 5.5. The measured displacement is also shown in the same figure. The estimation errors, i.e., the difference between the measured and estimated displacements obtained from both the models are plotted in the last subplot of Fig. 5.5. This shows that the accuracy of the developed UKF model is almost same as that of the EKF model. However, it has been observed that the computational time for UKF model is much less compared to the computational time for EKF model. To illustrate this, the computational time taken by the developed EKF model, denoted as $(\mathbf{T_{EKF}})$, and the same consumed by the UKF model

TH-1636_10610313

Table 5.1: Computational time of the EKF and UKF models.

Signal	Time Period (sec)	$T_{UKF}(sec)$	$T_{EKF}(sec)$
Continuous Input (Fig. 5.3a)	10	1.26799	2.438
Continuous Input (Fig. 5.3b)	5	0.66748	1.2115
Step Input (Fig. 5.4a)	10	2.48178	4.950198
Step Input (Fig. 5.4b)	5	1.28178	2.50198
Decreasing Input (Fig. 5.5)	30	1.34698	2.6528

($\mathbf{T_{UKF}}$) are compared in Table 5.1. Both the models are simulated in the same desktop PC and using version of MATLAB. It can be observed that the computational time for the UKF model is much less compared to that of the EKF model. Since the accuracy level of both the models are same, it can be concluded that the developed UKF model is computationally cheaper compared to the EKF model.

TH-1636_10610313

5.6 Summary

In this chapter, the development and implementation of an Unscented Kalman Filter model for the self-sensing application of Shape Memory alloy wire actuator have been presented. The dynamics of the system, comprising of a heat balance equation, one-dimensional constitutive behavior, phase kinetics, strain-electrical resistance relationship of a SMA wire and force equilibrium equation, are used in an UKF to estimate the displacement of linear system from the voltage input to the system as well the the measured electrical resistance of the SMA wire. The estimated system responses are compared with their measured counterparts, qualitatively validating the developed model. The performance of the UKF model is also compared with that of the EKF model, developed in the earlier chapter. It has been found that both the models yield the same level of accuracy. However, the simulation time for the UKF model is found to be almost 50% as that of the EKF model. This renders the developed UKF model as a preferable choice over the EKF model, particularly for real-time applications.

TH-1636_10610313

Chapter 6

Modified Kalman Filters

6.1 Introduction

In the earlier chapters, Extended and Unscented Kalman filters are explored in relation to the self-sensing applications of Shape Memory Alloy wire actuator. The purpose of these explorations is to have an estimate of the system responses actuated by the SMA wire actuators, from the variation of electrical resistance of the wire, while undergoing resistive heating. For different input voltage signals, the estimated responses are compared with the same obtained experimentally. With both EKF and UKF, only qualitative agreement between the estimated and experimentally measured system responses, is observed. Large quantitative difference is found for partial loading cases, as well as, in case of faster actuation. These are may be due to the modeling inaccuracy and parametric uncertainties. It has to be noted, that there has been a number of assumptions incorporated, to simplify the model. Firstly, a lumped parameter model is used assuming uniform temperature and stress all through out the wire. This may not be valid, as the SMA wire is wound around the metallic screws at the ends.

TH-1636_10610313

Sufficient heat loss might be there due to conduction. Besides, the phase kinetics followed in the model may not be adequately accurate, particularly, in case of partial transformation cases.

Moreover, the transformation zones are reported to have nonlinear boundaries in practice, whereas, in the model the boundaries are assumed to be linear and parallel for a given transformation zone. Besides, the material properties of the SMA wire are taken from the literature and not necessarily be the same as that of the wire being used in the experiments. Finally, the convective heat transfer coefficient (h) is found to have a very large impact on the system response. However, a large range of values of 'h' has been reported in the literature. In this chapter, to improve the accuracy of the estimation, different approaches are undertaken, modifying the developed EKF model.

6.2 Differential Scanning Calorimetry (DSC)

To determine the transformation temperature of the SMA wire, used in the experiments, DSC has been conducted. DSC is a thermal analysis technique, providing the phase transformation temperature of the sample. In this experiment, the rate of change of temperature of the sample, as well as the reference, are kept same. However, during phase transformation, sample either absorbs (in case of endothermic) or emits (for exothermic case) extra amount of heat with respect to the reference, which is being measured so as to identify the phase transformation temperature. The wire has been cut into small pieces, and a sample of 10 mg is used. The experiment has been conducted in SAIF, IISC Bangalore. Both, heating and cooling rate are kept 5 °C per minute and is repeated two times, as shown in Fig. 6.1. The transformation temperatures are noted as, $A_s = 46.75$ °C, $A_f = 61.75$ °C, $M_s = 57.58$ °C, and $M_f = 47.24$ °C.

TH-1636_10610313

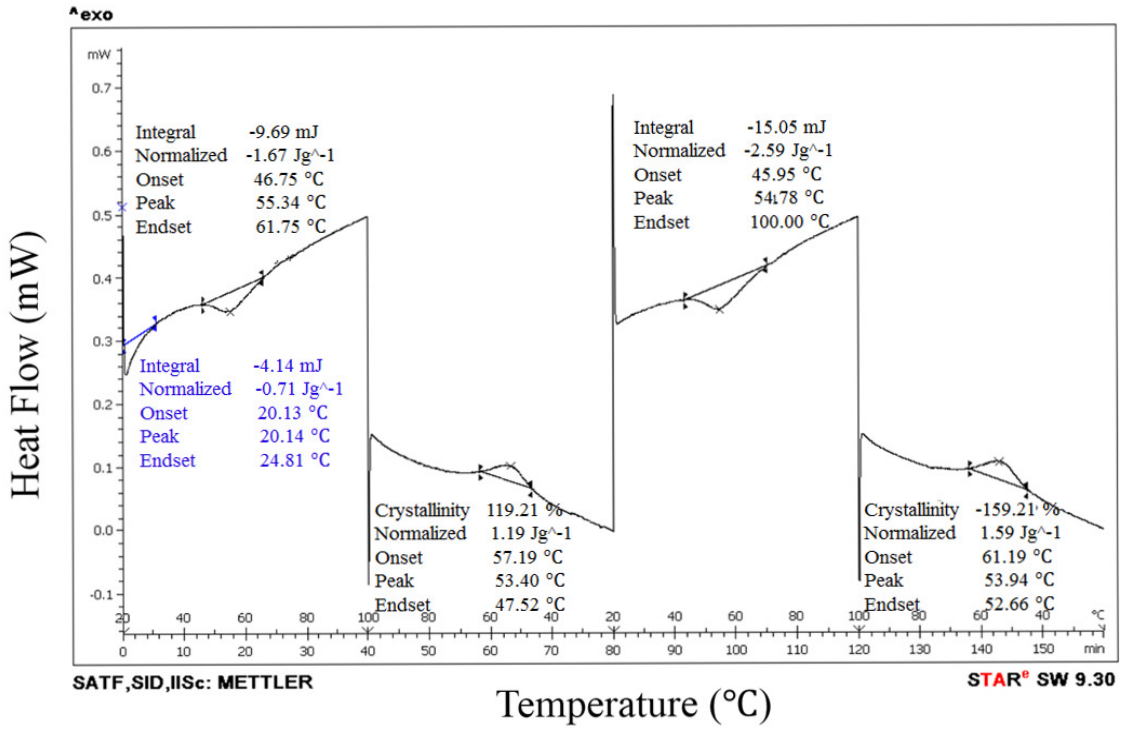

Figure 6.1: Results obtained from the DSC test conducted for two cycles at a rate of 5 °C.

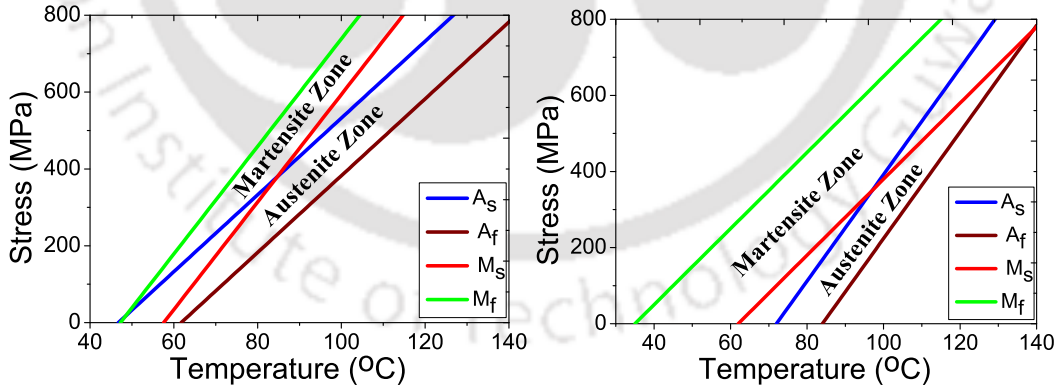

Figure 6.2: Phase diagram of the SMA wire with transformation temperatures, (a) obtained from DSC test, and (b) obtained from literature [2].

Figure 6.2a depicts the phase diagram drawn using the transformation temperature obtained from DSC experiment, for C_A = 15 MPa/°C and C_M = 10 MPa/°C. The phase diagram based on the transformation temperature, reported in the literature, and is used in

TH-1636_10610313

the previous chapters, is shown in Fig. 6.2b. In the present case, a clear overlap between the forward and reverse transformation zones can be observed, which is not the case considered till now. Moreover, this type of phase diagrams are not very common in the literature as well. As there is an overlap between the two transformation zones, the algorithm, discussed in section 2.7.1, used to identify the transformation zone is no more applicable. The modified algorithm is discussed in the next section.

6.2.1 Determination of Transformation Current Zone

Unlike the phase diagram used in the earlier chapters, as presented in Fig. 2.9, in the present case, there is a overlap between the transformation zones illustrated in Fig. 6.2a. In the earlier case, to identify the transformation status at the current point (T, σ), the relative location of the point with respect to the start and finish boundary of a given transformation zone has been used. This method does not apply in this case, as there is a common area between both, forward and reverse transformation zones. Following Eqns. (2.37) and (2.38), the equation of the straight lines, marking the boundaries of the phase transformation zones are rewritten as,

$$\begin{aligned} f_{L_1}(T,\sigma) &\Rightarrow \sigma - (T - M_f)\tan\phi^M = 0, \\ f_{L_2}(T,\sigma) &\Rightarrow \sigma - (T - M_s)\tan\phi^M = 0, \\ f_{L_3}(T,\sigma) &\Rightarrow \sigma - (T - A_s)\tan\phi^A = 0, \\ f_{L_4}(T,\sigma) &\Rightarrow \sigma - (T - A_f)\tan\phi^A = 0. \end{aligned} \tag{6.1}$$

The modified algorithm is as follows. Firstly, the reverse transformation zone is denoted as '1', forward transformation is marked as '2' and all other zones are presented by '3'. A new variable 'P_{status}' is introduced which basically assumes the value '1',' 2' or '3', depending on the current transformation status. At the beginning, P_{status} is assigned as 1.

TH-1636_10610313

Case 1 : For a given value of (T, σ), if $f_{L_1} \leq 0$ and $f_{L_2} \geq 0$ and $\frac{dT}{dt} > 0$, then the current point is in the reverse transformation zone. Now in case of posteriori estimate, if $P_{status} \sim =$ 1, then first update the memory parameters and assign P_{status} = 1. Then following the phase kinetics given by Eqns. (3.64) and (3.66), ψ_1 ψ_2, ψ_3, and ψ_4, are determined.

Case 2 : For a given value of (T, σ), if $f_{L_3} \leq 0$ and $f_{L_4} \geq 0$ and $\frac{dT}{dt} < 0$, then the current point is in the forward transformation zone. Now, in case of posteriori estimate, if $P_{status} \sim$ = 2, then first update the memory parameters and assign P_{status} = 2. Then following the phase kinetics given by Eqns. (3.60) and (3.62), ψ_1 ψ_2, ψ_3, and ψ_4,are calculated.

Case 3 : In all the other cases, transformation is inactive. However, in the posteriori step, if $P_{status} \sim$ = 3, then update the memory parameters as the final value of stress, temperature and martensite volume fractions obtained in the last time step. Then assign P_{status} = 3. Else, the martensite volume fractions are same as their corresponding values in memory parameters. Finally, the functions, ψ_1 ψ_2, ψ_3, and ψ_4, are assigned as zero.

6.3 Artificial Neural Network (ANN)

In this approach, the self-sensing capability of SMA wire actuator has been explored using Extended Kalman Filter assisted Artificial Neural Network. The change in length of a linear spring, actuated using a Shape Memory Alloy wire is first estimated from the variation of its electrical resistance using Extended Kalman Filter model; discussed in section 3.6. Though the estimation is qualitatively in agreement with the experiment, the quantitative mismatch makes it difficult to control the stretch of the spring solely based on the Extended Kalman Filter estimation. Hence, an Artificial Neural Network has been used to bridge the gap

TH-1636_10610313

between the Extended Kalman Filter estimation and the actual stretch of the spring. To evaluate the effectiveness of the Extended Kalman Filter based Artificial Neural Network model, the responses of the same are compared with that of another Artificial Neural Network model, trained only using the experimental data. It has been observed that for the same number of neurons and same training data, Extended Kalman Filter based Artificial Neural Network model yields better results, even at higher frequencies.

6.3.1 Description of the System

The system as described in section 5.3 is used to explore the self-sensing capability of SMA using EKF and ANN. In what follows, the details of the ANN models are discussed.

6.3.2 EKF based Artificial Neural Network (ANN)

For the system of interest, an EKF has already been developed to estimate the change in length of the spring from the measured electrical resistance (ER) variation of the SMA wire. For a given applied voltage, and the corresponding change in electrical resistance, as measured using the set-up discussed in section 4.2, the estimated displacement of the spring and the same measured experimentally are compared, and is again presented in Fig. 6.3a. One can note the quantitative discrepancy between the two. To reduce the gap, two ANN models are explored. Each ANN model consists of one hidden layer having ten neurons, three inputs, and one output. The models differ from the perspective of inputs only. The first model, referred as ANN-I, intakes the temperature of the SMA as estimated by EKF (T_{EKF}), its rate of change ($\dot{T}_{EKF}$) and change in length of the spring estimated by the EKF (δ_{EKF}). On the other hand, ANN-II model concedes the applied voltage across SMA (V), its rate of change ($\frac{dV}{dt}$) and the change in electrical resistance of SMA as obtained from the experiment. In

TH-1636_10610313

both the models, the output is the displacement of the spring. The whole process is explained using a flow diagram as shown in Fig. 6.3b. Thus the main difference between the two models is that, ANN-I intakes the output of the estimation of the EKF; whereas ANN-II accepts the measured voltages and resistance. The ANN models are depicted in Figs. 6.3c and 6.3d, respectively. The rate of temperature and voltage are included as inputs to distinguish the heating and cooling part of the actuation cycles, taking care of hysteresis in SMA behavior. Both ANN-I and ANN-II are trained using the data corresponding to the response shown in Fig. 6.3a. The neural network toolbox of MATLAB©MathWorks is used in this study.

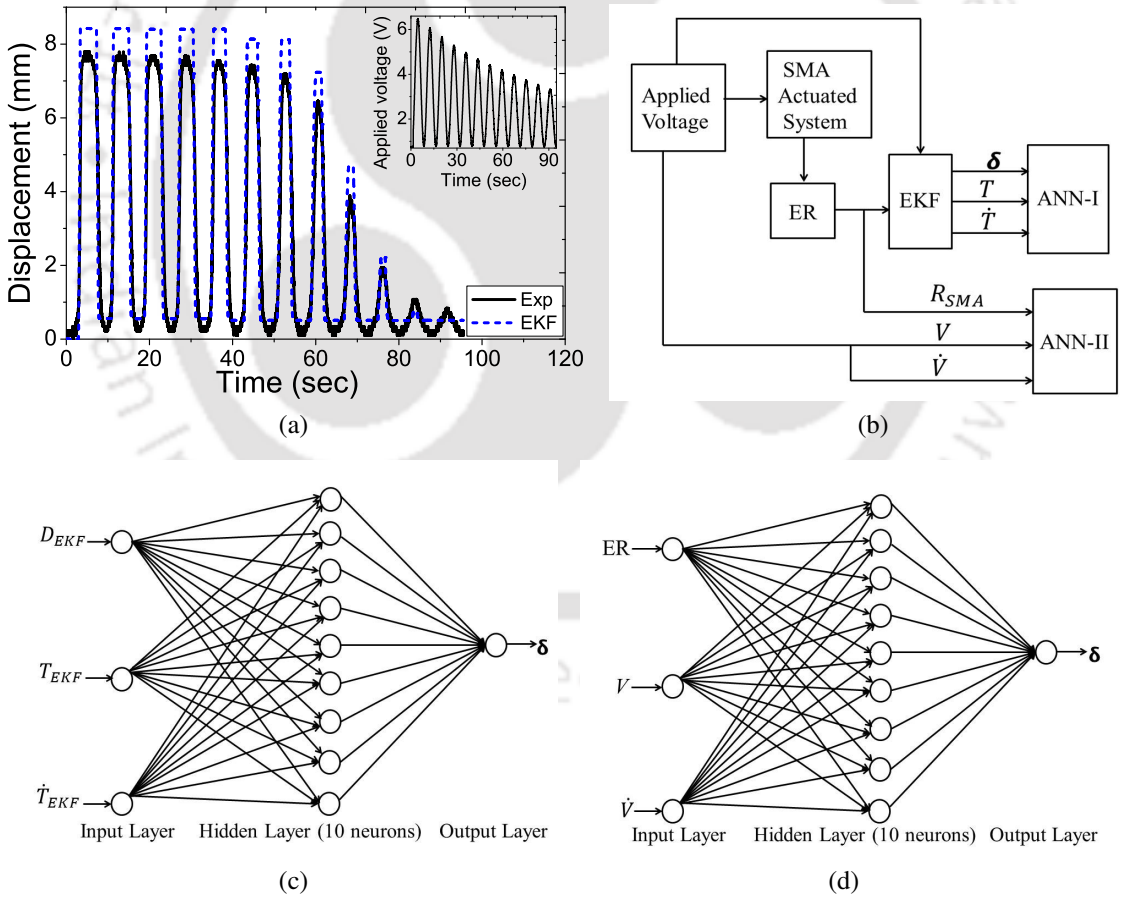

Figure 6.3: (a) Comparison between EKF estimated and experimental response, (b) schematic of the ANN models, (c) details of ANN-I and (d) details of ANN-II.

TH-1636_10610313

6.3.3 Experimental Details

For measuring the electrical resistance of SMA and the actual displacement of the SMA actuated system, the experimental set-up presented in section 4.2 is used.

6.3.4 Results and Discussion

First, few continuous voltage signals, having different frequency and amplitude are applied across the SMA wire, and the corresponding change in electrical resistance of the SMA wire and the corresponding spring displacement are measured experimentally. Then EKF is used to estimate the temperature of the SMA wire (T_{EKF}) and spring displacement (δ_{EKF}) from the experimentally measured electrical resistance of the SMA wire. All these are then used in ANN-I, which has been trained using the estimated data obtained for the input is shown in Fig. 6.3a, so as to obtain the actual displacement δ_1. Besides, ANN-II directly uses the experimental data and yields actual displacement δ_2. These are then compared and shown in Figs. 6.4 and 6.5. The responses, shown in Fig. 6.4a correspond to continuous periodic voltage signals having, frequency 0.1 Hz and amplitude 6.4 V. It can be observed that both the ANN models predict the displacement of the spring with reasonable accuracy. The outputs of the ANN models, for a similar voltage signal of frequency 0.2 Hz rad/sec, are presented in Fig. 6.4b. It can be observed that the output of ANN-II model is slightly erroneous, particularly in the last part of cooling. This may be because ANN-II has been trained for different input frequency as shown in Fig. 6.3a. Though the ANN-I model has also been trained for the same input as that of ANN-II, however, the governing equations, representing SMA behavior, inculcated in the EKF helps ANN-I model in avoiding the discrepancy. The responses for similar inputs with amplitude 4.5 V and frequency 0.1 Hz are presented in Fig. 6.4a. In this case, the SMA wire undergoes partial transformation and both models have

TH-1636_10610313

accurately captured the same.

However, with inputs having slightly higher frequency (0.2 Hz), the responses from these models are depicted in Fig. 6.4b. This result clearly reveals the limitation of ANN-II over ANN-I. It might be possible to improve the performance of ANN-II model by increasing more hidden layers and training data; however, that requires more computational resource and training time.

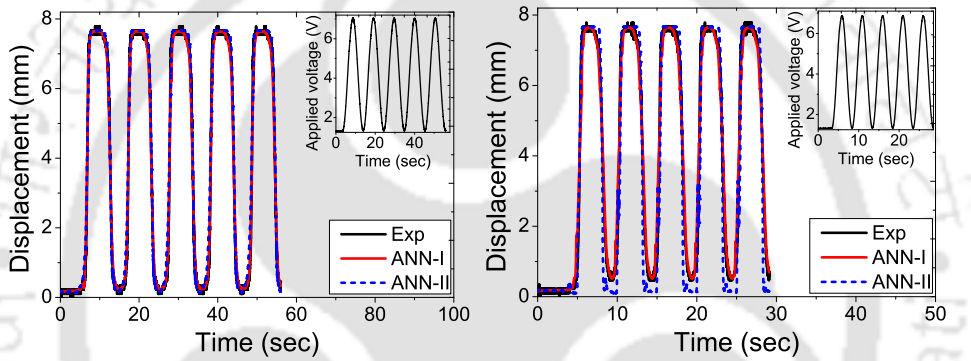

Figure 6.4: Comparison between EKF estimated and experimental responses for continuous periodic input voltage signal of (a) amplitude = 6.4 V and frequency = 0.1 Hz, and (b) amplitude = 6.4 V and frequency = 0.2 Hz.

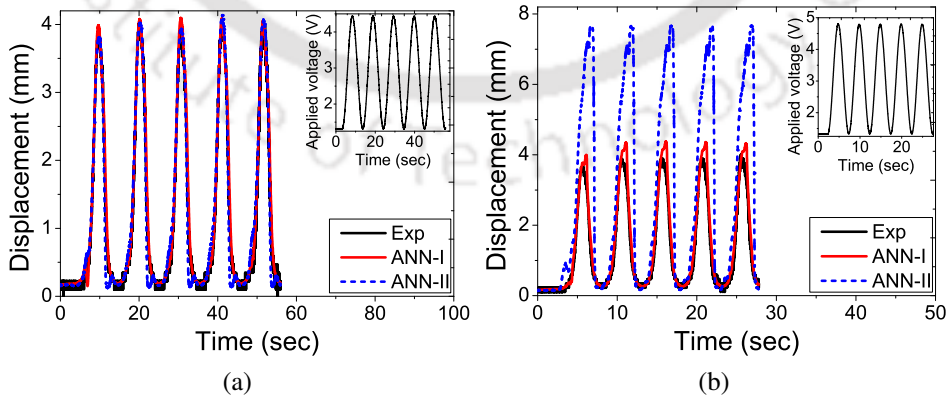

Figure 6.5: Comparison between EKF estimated and experimental responses for continuous periodic input voltage signal of (a) amplitude = 4.5 V and frequency = 0.1 Hz, and (b) amplitude = 4.5 V and frequency = 0.2 Hz.

TH-1636_10610313

Thus with the EKF based ANN, one can estimate the response of an SMA actuated system, for both partial and complete transformation cases, with significant accuracy. Moreover, it requires lesser training data and relatively small number of neuron and hidden layers.

6.4 EKF model with Varying Process Noise

In this approach, the parametric and structural uncertainties of the model, expected to be contributing to the quantitative discrepancies between the EKF estimated system response and the measured one, are taken into account through a varying process noise covariance. The uncertainties may be listed as follows:

1. The behavior of a SMA actuator heavily depends on the loading history. Thus the exact knowledge of the initial condition is essential. However, it is very difficult to accurately estimate the initial condition.

2. A lumped parameter model is assumed, expecting uniform temperature through out the wire length. This is not very practical, as the wire is fixed with metallic screws at its ends.

3. For partial loading cases, the phase kinetics are derived based on the phase diagram. There is no experimental proof of the proposed method. Thus the extent of transformation, depending on the stress and temperature, as estimated by the phase kinetics may not be adequately accurate.

4. The convective heat transfer coefficient, particularly for this type of thin wire, depends on several factors. The magnitude of 'h' is found to affect the simulated response significantly.

TH-1636_10610313

5. The properties of the SMA wire, say, modulus of elasticity, specific heat, electrical resistivity, are not constant during phase transformation. The use of linear mixture rule may not be appropriate to model the true variation of these properties.

6. In absence of the required experimental facility, some of the properties of the SMA wire, i.e., C_A, C_M, D_A, D_M, ϵ_l, σ_s^{cr} and σ_f^{cr} are adopted from the literature. This may also affect the estimation significantly.

Thus in presence of all these uncertainties, assumption of a constant process noise covariance may not be a good choice. Motivated by this logic, the EKF model has been modified following the approach of Valappil and Georgakis [96], yielding a time varying process noise covariance matrix. The details of this method is discussed in the following section.

6.4.1 Modified Extended Kalman Filter (EKF)

As discussed in section 3.4, the Extended Kalman filter (EKF) is a nonlinear estimator, that provides a recursive means for optimal state estimation of the system. In the presence of parametric uncertainties, the dynamics of the nonlinear system can be expressed as,

$$\dot{\mathbf{X}}(t) = \boldsymbol{\eta}[\mathbf{X}(t),\ \mathbf{u}(t),\ t,\ \mathbf{p}(t)] + \mathbf{w}(t). \tag{6.2}$$

$$\mathbf{Y}(t) = \boldsymbol{\Gamma}[\mathbf{X}(t),\ \mathbf{u}(t), t] + \mathbf{v}(t). \tag{6.3}$$

Here, $\mathbf{p}$ refers to the vector containing all the parameters contributing to the uncertainty in the model. As usual, the process and measurement noises are presented using $\mathbf{w}$ and $\mathbf{v}$, respectively.

As discussed earlier, the EKF comprises of "**Time update**" and "**Measurement update**". In a given time step, first the a-priori state is estimated from the posteriori state of the previous

TH-1636_10610313

instant, using system dynamics. Next, the a-priori state is updated using the measurement available. These steps are discussed in detail in section 3.4. There is a small change that has been introduced in the present case and is discussed below.

Following numerical integration, the time update is implemented as,

$$\hat{\mathbf{X}}_{t_k} = \mathbf{X}_{t_{k-1}} + \int_{k-1}^{k} \boldsymbol{\eta}(\mathbf{X}_{t_{k-1}},\ \mathbf{u}_{t_k},\ t)dt. \tag{6.4}$$

The a-priori state error covariance matrix is estimated as,

$$\hat{\mathbf{P}}_{t_k} = \mathbf{J}_{t_{k-1}} \mathbf{P}_{t_{k-1}} \mathbf{J}_{t_{k-1}}^{T} + \mathbf{Q}_{t_{k-1}}. \tag{6.5}$$

Here, $\mathbf{J}_{t_{k-1}}$ represents the Jacobian of the process vector function ($\boldsymbol{\eta}$) evaluated at t_{k-1}, and is calculated using the state transition matrix ($\mathbf{A}$) following,

$$\mathbf{J}_{t_{k-1}} = e^{\mathbf{A(t)}\Delta t}. \tag{6.6}$$

Here, Δt refers to the time step and is assumed to be small enough to ignore the higher order terms. The state transition matrix can be determined by differentiating the process vector with respect to the state as,

$$\mathbf{A}(t) = \left.\frac{\partial \boldsymbol{\eta}}{\partial \mathbf{X}}\right|_{(\hat{\mathbf{X}}^{+}_{t_{k-1}},\ \mathbf{u}_{t_k},\ \mathbf{p}_{nom})}. \tag{6.7}$$

Here, $\mathbf{p}_{nom}$ refers to the nominal values of the parameters. In this case, the exact expression of the state transition matrix ($\mathbf{A}$) is derived for the spring biased SMA wire actuated system, instead of calculating the same numerically as in section 3.6.1.2. In the following discussion the derivation of the time varying process noise covariance $\mathbf{Q}$ is presented.

TH-1636_10610313

6.4.2 Varying Process Noise Covariance

The effect of parametric uncertainties can be taken care, by modifying the process noise covariance matrix, following the approach of Valappil and Georgakis [96]. In this direction, the nonlinear process function can be expressed as,

$$\begin{aligned}\boldsymbol{\eta}[\mathbf{X}_{t_k}, \mathbf{u}_{t_k}, \mathbf{p}] = \boldsymbol{\eta}[\hat{\mathbf{X}}^+_{t_{k-1}}, \mathbf{u}_{t_k}, \mathbf{p}_{nom}] + \left(\frac{\partial \boldsymbol{\eta}}{\partial \mathbf{X}}\right)_{(\hat{\mathbf{X}}^+_{t_{k-1}}, \mathbf{u}_{t_k}, \mathbf{p}_{nom})} \left(\mathbf{X}_{t_k} - \hat{\mathbf{X}}^+_{t_{k-1}}\right) \\ \left(\frac{\partial \boldsymbol{\eta}}{\partial \mathbf{p}}\right)_{(\hat{\mathbf{X}}^+_{t_{k-1}}, \mathbf{u}_{t_k}, \mathbf{p}_{nom})} (\mathbf{p} - \mathbf{p}_{nom}) + \text{Higher order terms.}\end{aligned} \tag{6.8}$$

Here, the process noise $\mathbf{w}_{t_k}$ can be written as,

$$\mathbf{w}_{t_k} = \boldsymbol{\eta}[\mathbf{X}_{t_k},\ \mathbf{u}_{t_k},\ \mathbf{p}] - \boldsymbol{\eta}[\hat{\mathbf{X}}^+_{t_{k-1}},\ \mathbf{u}_{t_k},\ \mathbf{p}_{nom}]. \tag{6.9}$$

Equations (6.8) and (6.9) imply,

$$\begin{aligned}\mathbf{w}_{t_k} &= \left(\frac{\partial \boldsymbol{\eta}}{\partial \mathbf{X}}\right)_{(\hat{\mathbf{X}}^+_{t_{k-1}},\ \mathbf{u}_{t_k},\ \mathbf{p}_{nom})} \left(\mathbf{X}_{t_k} - \hat{\mathbf{X}}^+_{t_{k-1}}\right) + \left(\frac{\partial \boldsymbol{\eta}}{\partial \mathbf{p}}\right)_{(\hat{\mathbf{X}}^+_{t_{k-1}},\ \mathbf{u}_{t_k},\ \mathbf{p}_{nom})} (\mathbf{p} - \mathbf{p}_{nom}) \\ &= \mathbf{J}|_{\hat{\mathbf{X}}^+_{t_{k-1}}} \left(\mathbf{X}_{t_k} - \hat{\mathbf{X}}^+_{t_{k-1}}\right) + \mathbf{J}_{\mathbf{p}}|_{\mathbf{p}_{nom}} (\mathbf{p} - \mathbf{p}_{nom}).\end{aligned} \tag{6.10}$$

Here, the higher order terms are neglected for the small values of time step. Now one can obtain the expected value of the process noise as,

$$E[\mathbf{w}_{t_k}] = 0. \tag{6.11}$$

This is because $E[\mathbf{X}_{t_k} - \hat{\mathbf{X}}^+_{t_{k-1}}] = 0$ and $E[\mathbf{p} - \mathbf{p}_{nom}] = 0$. This implies that the mean of the noise $\mathbf{w}_{t_k}$ is zero. From Eqn. (6.10), the process noise covariance $\mathbf{Q}$ can determined as,

$$\mathbf{Q}_{t_k} = \mathbf{J}_{\mathbf{p}} \mathbf{C}_p \mathbf{J}_{\mathbf{p}}^{\intercal}. \tag{6.12}$$

TH-1636_10610313

Here $\mathbf{C}_p$, the parameter covariance matrix, is defined as,

$$\mathbf{C}_p = E[(\mathbf{p} - \mathbf{p}_{nom})(\mathbf{p} - \mathbf{p}_{nom})^\intercal]. \tag{6.13}$$

In this work $\mathbf{C}_p$ has been calculated according to the method proposed by Salau *et al* [97] as,

$$\mathbf{C}_p = s^2(\mathbf{S}^\intercal\mathbf{S})^{-1}. \tag{6.14}$$

Here, s refers to be a constant, usually determined from SELEST algorithm [98]. The sensitivity matrix has been numerically calculated at every instant following,

$$\begin{aligned} \dot{\mathbf{S}} &= \left(\tfrac{\partial \boldsymbol{\eta}}{\partial \mathbf{X}}\right)\mathbf{S} + \left(\tfrac{\partial \boldsymbol{\eta}}{\partial \mathbf{p}}\right), \\ &= \mathbf{JS} + \mathbf{J_p}. \end{aligned} \tag{6.15}$$

6.4.3 Determination of Process Noise Covariance Q

In this section, the detailed derivation of the process noise covariance is presented. Five parameters, namely, convective heat transfer coefficient (h), the starting temperatures of forward and reverse transformation (M_s and A_s), the width of the forward and reverse transformation zones, denoted as W_M and W_A, respectively, are considered to be constituting the vector $\mathbf{p}$. Thus,

$$\mathbf{p} = \begin{bmatrix} h & M_s & A_s & W_A & W_M \end{bmatrix}^\intercal. \tag{6.16}$$

Similarly, the two elements (η_1 and η_1), of the process nonlinear vector function ($\boldsymbol{\eta}$), required for a-priori state estimation (refer Eqn. (6.4)) can be expressed as,

$$\begin{aligned} \frac{dT}{dt} &= \eta_1, \\ \frac{d\sigma}{dt} &= \eta_2. \end{aligned} \tag{6.17}$$

TH-1636_10610313

Following Eqn. (3.57) and (3.58), the $\frac{dT}{dt}$ and $\frac{d\sigma}{dt}$ can be expressed as,

$$\frac{dT}{dt} = \frac{\frac{V^2}{R} - hA_{surf}(T_{t_{k-1}} - T_0)}{c_v V_m + \lambda\psi_2 + \lambda\psi_1 F_5(\sigma, T)}. \tag{6.18}$$

$$\frac{d\sigma}{dt} = F_5(\sigma, T)\frac{\frac{V^2}{R} - hA_{surf}(T_{t_{k-1}} - T_0)}{c_v V_m + \lambda\psi_2 + \lambda\psi_1 F_5(\sigma, T)}. \tag{6.19}$$

Here,

$$F_5(\sigma, T) = \frac{(\epsilon - \epsilon_l\xi_s)(D_M - D_A)\psi_2 - \epsilon_l D\psi_4 + \Theta}{1 - \{(\epsilon - \epsilon_l\xi_s)(D_M - D_A)\psi_1 - \epsilon_l D\psi_3\} + \frac{A}{K_s L_0}}. \tag{6.20}$$

Similarly, the state transition matrix ($\mathbf{A}$) required for the calculation of the Jacobian, $\mathbf{J}$ (refer Eqn. (6.6)), be obtained following Eqn. (6.7) as,

$$\mathbf{A} = \begin{bmatrix} \frac{d\eta_1}{dT} & \frac{d\eta_1}{d\sigma} \\ \frac{d\eta_2}{dT} & \frac{d\eta_2}{d\sigma} \end{bmatrix}. \tag{6.21}$$

Further, the Jacobian of the process function with respect to the parameter ($\mathbf{p}$), can be expressed as,

$$\mathbf{J_p} = \begin{bmatrix} \frac{d\eta_1}{dh} & \frac{d\eta_1}{dM_s} & \frac{d\eta_1}{dA_s} & \frac{d\eta_1}{dW_A} & \frac{d\eta_1}{dW_M} \\ \frac{d\eta_2}{dh} & \frac{d\eta_2}{dM_s} & \frac{d\eta_2}{dA_s} & \frac{d\eta_2}{dW_A} & \frac{d\eta_2}{dW_M} \end{bmatrix}_{(\hat{\mathbf{X}}^+_{t_{k-1}}, \mathbf{u}_{t_k}, \mathbf{p}_{nom})}. \tag{6.22}$$

Further the parameter covariance matrix ($\mathbf{C}_p$) required in Eqn. (6.12), can be calculated according to Eqn. (6.14). Here, the sensitivity matrix is obtained numerically from Eqn. (6.15),

TH-1636_10610313

which can be written as,

$$\underbrace{\begin{bmatrix} \frac{\partial \dot{T}}{\partial M_s} & \frac{\partial \dot{T}}{\partial A_s} & \frac{\partial \dot{T}}{\partial h} & \frac{\partial \dot{T}}{\partial W_A} & \frac{\partial \dot{T}}{\partial W_M} \\ \frac{\partial \dot{\sigma}}{\partial M_s} & \frac{\partial \dot{\sigma}}{\partial A_s} & \frac{\partial \dot{\sigma}}{\partial h} & \frac{\partial \dot{\sigma}}{\partial W_A} & \frac{\partial \dot{\sigma}}{\partial W_M} \end{bmatrix}}_{\dot{\mathbf{S}}} = \underbrace{\begin{bmatrix} \frac{\partial \eta_1}{\partial T} & \frac{\partial \eta_1}{\partial \sigma} \\ \frac{\partial \eta_2}{\partial T} & \frac{\partial \eta_2}{\partial \sigma} \end{bmatrix}}_{\mathbf{J}} \underbrace{\begin{bmatrix} \frac{\partial T}{\partial M_s} & \frac{\partial T}{\partial A_s} & \frac{\partial T}{\partial h} & \frac{\partial T}{\partial W_A} & \frac{\partial T}{\partial W_M} \\ \frac{\partial \sigma}{\partial M_s} & \frac{\partial \sigma}{\partial A_s} & \frac{\partial \sigma}{\partial h} & \frac{\partial \sigma}{\partial W_A} & \frac{\partial \sigma}{\partial W_M} \end{bmatrix}}_{\mathbf{S}} + \underbrace{\begin{bmatrix} \frac{\partial \eta_1}{\partial M_s} & \frac{\partial \eta_1}{\partial A_s} & \frac{\partial \eta_1}{\partial h} & \frac{\partial \eta_1}{\partial W_A} & \frac{\partial \eta_1}{\partial W_M} \\ \frac{\partial \eta_2}{\partial M_s} & \frac{\partial \eta_2}{\partial A_s} & \frac{\partial \eta_2}{\partial h} & \frac{\partial \eta_2}{\partial W_A} & \frac{\partial \eta_2}{\partial W_M} \end{bmatrix}}_{\mathbf{J_P}}. \tag{6.23}$$

The set of ODE's as obtained from Eqn. (6.23) are explicitly written as,

$$\begin{aligned}
\frac{\partial}{\partial t}\left(\frac{\partial T}{\partial M_s}\right) &= \frac{\partial \eta_1}{\partial T}\frac{\partial T}{\partial M_s} + \frac{\partial \eta_1}{\partial \sigma}\frac{\partial \sigma}{\partial M_s} + \frac{\partial \eta_1}{\partial M_s}, \\
\frac{\partial}{\partial t}\left(\frac{\partial T}{\partial A_s}\right) &= \frac{\partial \eta_1}{\partial T}\frac{\partial T}{\partial A_s} + \frac{\partial \eta_1}{\partial \sigma}\frac{\partial \sigma}{\partial A_s} + \frac{\partial \eta_1}{\partial A_s}, \\
\frac{\partial}{\partial t}\left(\frac{\partial T}{\partial h}\right) &= \frac{\partial \eta_1}{\partial T}\frac{\partial T}{\partial h} + \frac{\partial \eta_1}{\partial \sigma}\frac{\partial \sigma}{\partial h} + \frac{\partial \eta_1}{\partial h}, \\
\frac{\partial}{\partial t}\left(\frac{\partial T}{\partial W_A}\right) &= \frac{\partial \eta_1}{\partial T}\frac{\partial T}{\partial W_A} + \frac{\partial \eta_1}{\partial \sigma}\frac{\partial \sigma}{\partial W_A} + \frac{\partial \eta_1}{\partial W_A}, \\
\frac{\partial}{\partial t}\left(\frac{\partial T}{\partial W_M}\right) &= \frac{\partial \eta_1}{\partial T}\frac{\partial T}{\partial W_M} + \frac{\partial \eta_1}{\partial \sigma}\frac{\partial \sigma}{\partial W_M} + \frac{\partial \eta_1}{\partial W_M}.
\end{aligned} \tag{6.24}$$

$$\begin{aligned}
\frac{\partial}{\partial t}\left(\frac{\partial \sigma}{\partial M_s}\right) &= \frac{\partial \eta_2}{\partial \sigma}\frac{\partial T}{\partial M_s} + \frac{\partial \eta_2}{\partial \sigma}\frac{\partial \sigma}{\partial M_s} + \frac{\partial \eta_2}{\partial M_s}, \\
\frac{\partial}{\partial t}\left(\frac{\partial \sigma}{\partial A_s}\right) &= \frac{\partial \eta_2}{\partial T}\frac{\partial T}{\partial A_s} + \frac{\partial \eta_2}{\partial \sigma}\frac{\partial \sigma}{\partial A_s} + \frac{\partial \eta_2}{\partial A_s}, \\
\frac{\partial}{\partial t}\left(\frac{\partial \sigma}{\partial h}\right) &= \frac{\partial \eta_2}{\partial T}\frac{\partial T}{\partial h} + \frac{\partial \eta_2}{\partial \sigma}\frac{\partial \sigma}{\partial h} + \frac{\partial \eta_2}{\partial h}, \\
\frac{\partial}{\partial t}\left(\frac{\partial \sigma}{\partial W_A}\right) &= \frac{\partial \eta_2}{\partial T}\frac{\partial T}{\partial W_A} + \frac{\partial \eta_2}{\partial \sigma}\frac{\partial \sigma}{\partial W_A} + \frac{\partial \eta_2}{\partial W_A}, \\
\frac{\partial}{\partial t}\left(\frac{\partial \sigma}{\partial W_M}\right) &= \frac{\partial \eta_2}{\partial T}\frac{\partial T}{\partial W_M} + \frac{\partial \eta_2}{\partial \sigma}\frac{\partial \sigma}{\partial W_M} + \frac{\partial \eta_2}{\partial W_M}.
\end{aligned} \tag{6.25}$$

The set of equations presented in Eqn. (6.24) and (6.25) are numerically integrated to calculate the elements of $\mathbf{S}$ at every time instant.

TH-1636_10610313

Table 6.1: Properties assumed for the linear spring biased SMA wire actuated system [3].

Symbol	Value	Symbol	Value
C_{va}	5.92x10^{-3}J/K-mm^3	C_{vm}	4.506x10^{-3} J/K-mm^3
ρ_a	8.37x$10^{-4}\Omega$mm	ρ_m	9.603x$10^{-4}\Omega$mm
D_a	75 GPa	D_m	28 GPa
C_m	10 MPa/^{o}C	C_a	12 MPa/^{o}C
A_s	46.75 ^{o}C	A_f	61.75 ^{o}C
M_s	57.58 ^{o}C	M_f	47.24 ^{o} C
σ_s	70 MPa	σ_f	100 MPa
ϵ_0	0.033	K_s	0.24 N/mm

Further, in the present application, the observation comprises of the electrical resistance of the SMA wire. Following section 3.5.2, the observation function is rewritten as,

$$\Gamma_1(\mathbf{X}_{t_k}) = \frac{(\rho_M \xi(T,\sigma) + \rho_A(1-\xi(T,\sigma)))L_0(1+(\epsilon_0 - \frac{\sigma A}{K_s L_0}))}{A}. \tag{6.26}$$

Thus, the Jacobian of the observation function $\mathbf{H}$, required in the "**Measurement update** " step, can be calculated following Eqn. (6.26), as,

$$\mathbf{H} = \begin{bmatrix} \frac{d\Gamma_1}{dT} & \frac{d\Gamma_1}{d\sigma} \end{bmatrix}. \tag{6.27}$$

6.4.4 Results and Discussion

The modified EKF model, with varying $\mathbf{Q}$, is implemented in MATLAB, and is used to estimate the displacement of the linear spring for the continuous periodic voltage with decreasing amplitude, presented in Fig. 4.12a. The corresponding measured electrical resistance of the SMA wire is taken as the observation. The properties of the SMA wire and the spring, used in the model, are shown in Table 6.1. Figure 6.6 shows the comparison between the estimated displacements of the linear spring obtained using the earlier EKF model, having

TH-1636_10610313

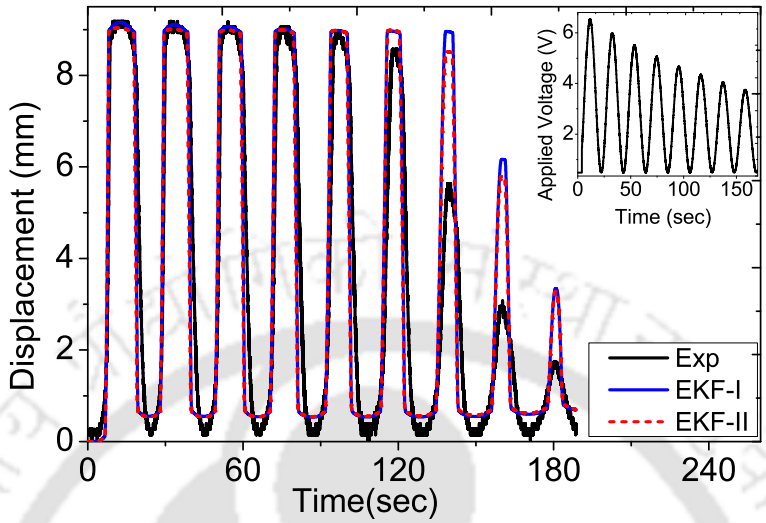

Figure 6.6: Comparison between EKF estimation and experimental response for different process noise covariance (**Q**).

constant **Q** as discussed in Chapter 4, and the modified EKF model with varying **Q**, presented in the above section. Here, EKF-I and EKF-II, refer to the EKF models using constant and varying **Q**, respectively. The corresponding experimentally measured response is also presented in the same figure. It can be seen that, only in case of partial phase transformation, there is a slight difference in the estimation. As a whole, in this approach, the improvement is insignificant.

6.5 Parameter Estimation

In literature, Kalman Filter has also been used to estimate parameters of dynamic systems in addition to the state. For example, EKF has been proposed in estimating the health of turbofan blades [75]. Following this approach, in this study, some of the parameters of model, which are affecting the system behavior to a great extent, are estimated in addition to the state of the system.

TH-1636_10610313

The expression for convective heat transfer coefficient (h) and specific heat of SMA (C_v), are modified, introducing two new unknowns, which are being estimated along with the state of the system. Additionally, the relation between the electrical resistivity and martensite volume fraction has also been modified to reduce the qualitative discrepancy between the theoretical and measured electrical resistance of the SMA. These modifications are introduced in the EKF model and implemented.

With the modified EKF model, the displacement of the spring-biased SMA wire actuated system is estimated from the measured electrical resistance of SMA subjected to different applied voltages. The results reveal the potential of the developed EKF model, harnessing the self-sensing capability of SMA wire actuators.

6.5.1 Modified Extended Kalman Filter

Considering the process functions as a function of process noise, the modified state equations are written as,

$$\dot{\mathbf{X}} = \boldsymbol{\eta}\left(\mathbf{X}, \mathbf{u}, \mathbf{w}\right). \tag{6.28}$$

Here, the state is assumed to be nonlinear function of the noise as well. However, in case of the output equation, noise is considered as simply of additive type. This necessitates the following change in the equation estimating, the a-priori state error covariance matrix. The modified form of Eqn. (3.7) appears as,

$$\mathbf{P}^{-}_{t_k} = \mathbf{J}_{t_{k-1}} \mathbf{P}^{+}_{t_{k-1}} \mathbf{J}^{T}_{t_{k-1}} + \mathbf{J}_{w,\, t_{k-1}} \mathbf{Q}_{t_{k-1}} \mathbf{J}^{T}_{w,\, t_{k-1}}. \tag{6.29}$$

TH-1636_10610313

Here, $\mathbf{J}$ is the Jacobian of the process function with respect to the state, obtained using,

$$\begin{aligned}\mathbf{J} &= e^{\mathbf{A(t)}\Delta t}. \\ &= \left[\mathbf{I}_{4\times 4} + \mathbf{A}\Delta t + \frac{(\mathbf{A}\Delta t)^2}{2}\right].\end{aligned} \tag{6.30}$$

$\mathbf{A}$, represents the state transition matrix. Here, $\mathbf{J}_w$ is another Jacobian, defined as Jacobian of the uncertainty. This has been calculated following,

$$\mathbf{J}_w = \mathbf{\Lambda}\Delta t. \tag{6.31}$$

Here, $\mathbf{\Lambda}$ is calculated as,

$$\mathbf{\Lambda} = \frac{\partial \boldsymbol{\eta}}{\partial \mathbf{w}}. \tag{6.32}$$

Rest of the steps remain same as is discussed in section 3.4.

6.5.1.1 Modified System Model

In the present work, following modifications are introduced in the model.

1. **Convective heat transfer coefficient :** The variation of heat transfer coefficient with temperature of SMA wire is taken as,

$$h = h_0\left(1 + \alpha_1(T - T_0) + w_T\right). \tag{6.33}$$

Here, h_0 is a constant, representing the value of heat transfer coefficient at $T = T_0$. α_1 is a constant, which is introduced in the model to take care of the effect of temperature variation on the magnitude of 'h'. This has been assumed to be an unknown and is being estimated using EKF. w_T is the uncertainty associated with this model and is an

TH-1636_10610313

element of process noise vector $\mathbf{w}$.

2. **Specific heat capacity of SMA :** Similarly, specific heat C_v, is expressed as,

$$C_v = C_{v_0}\left(1 + \alpha_2 + w_T\right). \tag{6.34}$$

Here, C_{v_0} is determined from the rule of mixture as, $C_{v_0} = C_{vM}\xi + (1-\xi)C_{vA}$. The unknown constant, α_2, is basically a multiplier and has been estimated following EKF.

3. **Electrical resistivity model of SMA :** Figure 6.7a shows the electrical resistance variation of the SMA wire as estimated from the EKF model, discussed in chapter 4, and the corresponding measured resistance for a voltage signal shown in Fig. 4.12b. This sudden increase in resistance may be due to the formation of R-phase at the begin-

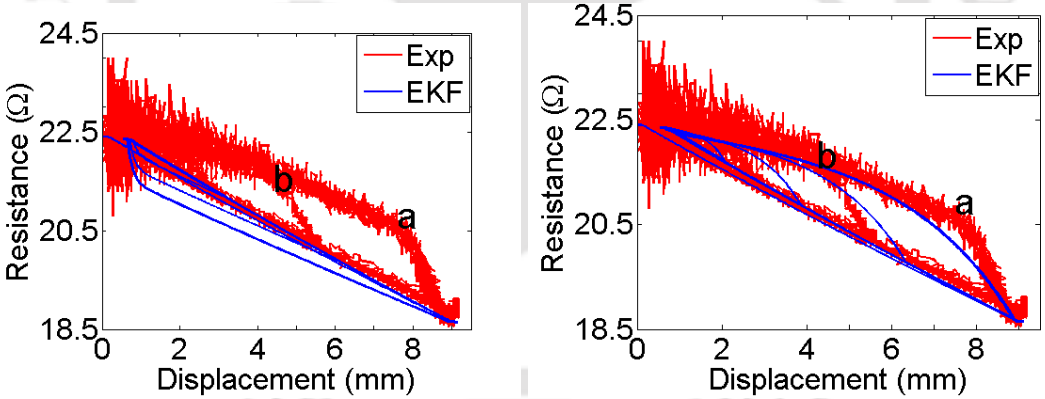

Figure 6.7: (a) Comparison between estimated and measured electrical resistance of SMA wire (b) before and (c) after modification.

ning of forward transformation. However, the DSC result does not reveal the presence of any R-phase. Furthermore, the present model fails to capture such sharp change in resistance at the beginning of forward transformation. During cooling the resistivity model is expressed using exponential function relating resistivity to the martensite

TH-1636_10610313

volume fraction. Therefore, during cooling the resistivity is modeled as,

$$\rho = \rho_M - (\rho_M - \rho_A)\, e^{\left(\frac{-4(\xi-\xi_0)}{(1-\xi_0)}\right)}. \tag{6.35}$$

Here, ξ_0 represents the initial value of the martensite volume fraction (ξ). Whereas, during reverse transformation the electrical resistance of SMA decreases linearly and hence, the electrical resistivity of SMA is determined following,

$$\rho = \rho_M \xi + (1-\xi)\rho_A. \tag{6.36}$$

Using the modified model, as mentioned by Eqns. (6.35) and (6.36), the electrical resistance of SMA is calculated for the same input voltage stated in Fig. 4.12a and is compared with the measured one, in Fig. 6.7b. The result illustrates that the modified approach is able to represent the electrical resistance behavior of the SMA wire satisfactorily.

6.5.2 Modified EKF model for linear spring biased SMA wire

As two new unknowns, α_1 and α_2 are to be estimated in addition to the stress and temperature of the SMA wire, the appended state vector appears as,

$$\mathbf{X} = \begin{bmatrix} T & \sigma & \alpha_1 & \alpha_2 \end{bmatrix}^T. \tag{6.37}$$

Thus the additional process functions are,

$$\frac{d\alpha_1}{dt} \Rightarrow \eta_3 = 0, \tag{6.38}$$

TH-1636_10610313

and,

$$\frac{d\alpha_2}{dt} \Rightarrow \eta_4 = 0. \tag{6.39}$$

Note that the other two process functions remain same as described by Eqns. (6.18) and (6.19). Thus, the process nonlinear vector becomes $\{4 \times 1\}$, and can be presented as,

$$\begin{aligned} \frac{dT}{dt} &= \eta_1, \\ \frac{d\sigma}{dt} &= \eta_2, \\ \frac{d\alpha_1}{dt} &= \eta_3, \\ \frac{d\alpha_2}{dt} &= \eta_4. \end{aligned} \tag{6.40}$$

For the present case, the state transition matrix becomes 4×4, and can be obtained following Eqn. (6.7) as,

$$\mathbf{A} = \begin{bmatrix} \frac{d\eta_1}{dT} & \frac{d\eta_1}{d\sigma} & \frac{d\eta_1}{d\alpha_1} & \frac{d\eta_1}{d\alpha_2} \\ \frac{d\eta_2}{dT} & \frac{d\eta_2}{d\sigma} & \frac{d\eta_2}{d\alpha_1} & \frac{d\eta_2}{d\alpha_2} \\ \frac{d\eta_3}{dT} & \frac{d\eta_3}{d\sigma} & \frac{d\eta_3}{d\alpha_1} & \frac{d\eta_3}{d\alpha_2} \\ \frac{d\eta_4}{dT} & \frac{d\eta_4}{d\sigma} & \frac{d\eta_4}{d\alpha_1} & \frac{d\eta_4}{d\alpha_2} \end{bmatrix}. \tag{6.41}$$

From the $\mathbf{A}$ matrix, the Jacobian $\mathbf{J}$ required in Eqn. (6.29) can be calculated using Eqns. (6.30) and (6.41). Further, the other Jacobian $\mathbf{J}_w$, used in state error covariance matrix '$\mathbf{P}$' (refer Eqn. (6.29)) is calculated following Eqn. (6.31). Here, the required $\mathbf{\Lambda}$ matrix are determined following Eqn. (6.32) as,

$$\mathbf{\Lambda} = \begin{bmatrix} \frac{d\eta_1}{dW_T} & 0 & 0 & 0 \\ \frac{d\eta_2}{dW_T} & 1 & 0 & 0 \\ 0 & 0 & 1 & 0 \\ 0 & 0 & 0 & 1 \end{bmatrix}. \tag{6.42}$$

TH-1636_10610313

The rest of the steps remain the same as in the case of the EKF discussed in section 3.6.1.2. Since, in this case, the size of the state error covariance ($\mathbf{P}$) and process noise covariance ($\mathbf{Q}$) has increased, simultaneously, the computation effort also has increased.

6.5.3 Results and Discussion

Here, the state of the SMA actuated linear system has been estimated using two different EKF models. The system response estimated using the earlier EKF model, discussed in section 3.4, is denoted as EKF-I. The estimated displacement as obtained using the modified approach, discussed in this section, is referred as EKF-III.

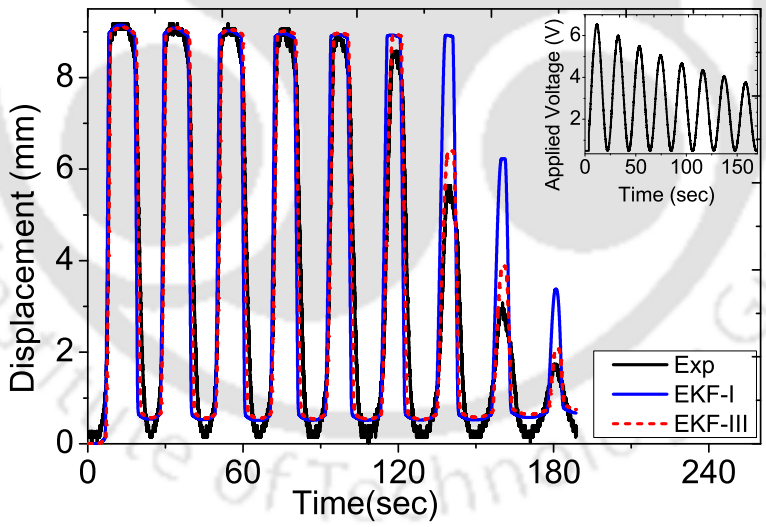

Figure 6.8: Comparison between EKF-I, EKF-III and experimental response for continuous decreasing periodic input voltage of amplitude = 6.2 V and time period = 25 sec.

For the same periodic voltage signal with decreasing amplitude , shown in Fig. 6.8, the estimated spring displacement obtained using EKF-I and EKF-III, are compared with the experimental response and is presented in Fig. 6.8. The applied voltage signal has been shown in the inset of the same figure. The result shows that the EKF-III model has been

TH-1636_10610313

able to estimate the response quite satisfactorily. The maximum discrepancy between the estimation of the EKF-III model and the measured one is less than 1 mm. The improvement in the estimation accuracy may be due to the modified resistivity model, and the ability of the present EKF model to incorporate the variation of the heat transfer coefficient with temperature.

For different continuous voltage signals, the estimated displacements obtained using EKF-

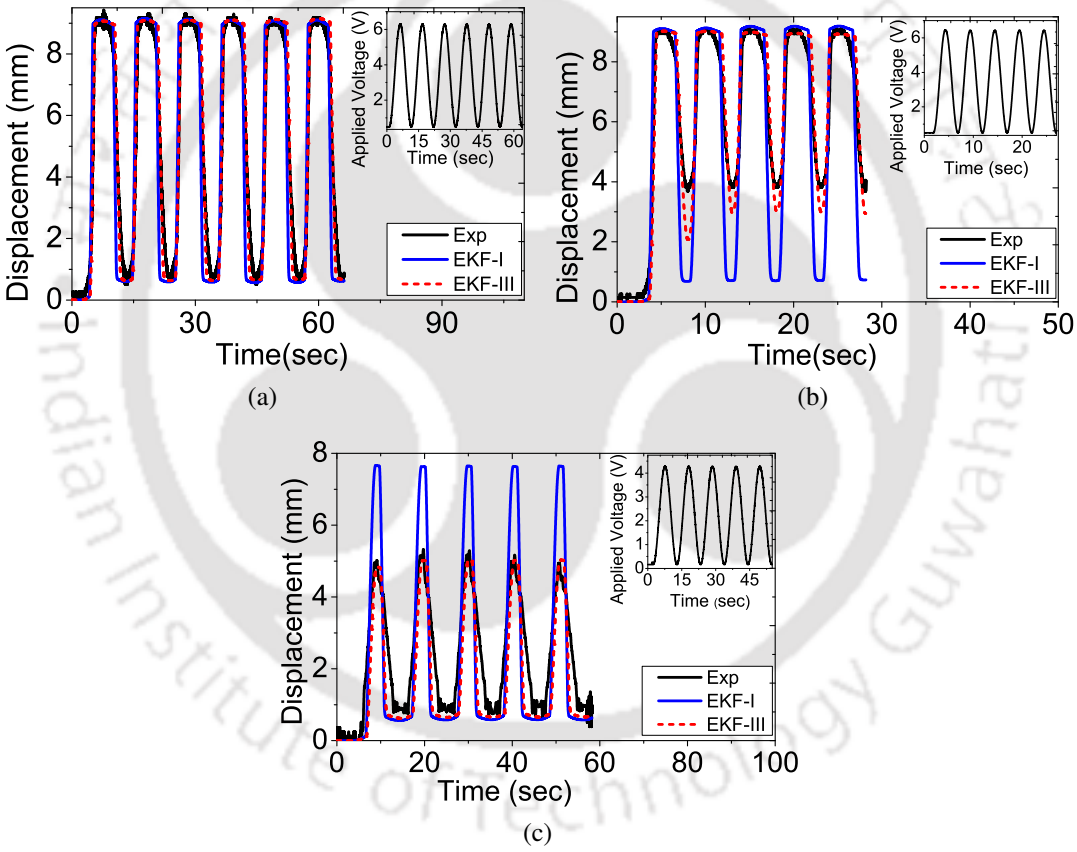

Figure 6.9: Comparison between EKF-I, EKF-III and experimental response for continuous input voltage (a) amplitude = 6.2 V and time period =10 sec (b) amplitude = 6.2 V, time period = 5 sec and (c) amplitude = 4 V, time period = 10 sec.

I and EKF-III, are compared with the measured responses and are shown in Fig. 6.9. In Fig. 6.9a, the complete transformation in SMA has taken place for a continuous periodic voltage of amplitude 6.5 V and time period 10 sec, and the estimation of both the EKF models

TH-1636_10610313

are accurate. In Fig. 6.9b, a continuous voltage of same amplitude but of time period 5 sec is used, so as to ensure partial transformation in SMA. Significant improvement in estimation is observed while using EKF-III instead of EKF-I. A similar response is observed, in Fig. 6.9c, as the partial transformation is achieved for the continuous input voltage of amplitude 4 V and time period 10 sec.

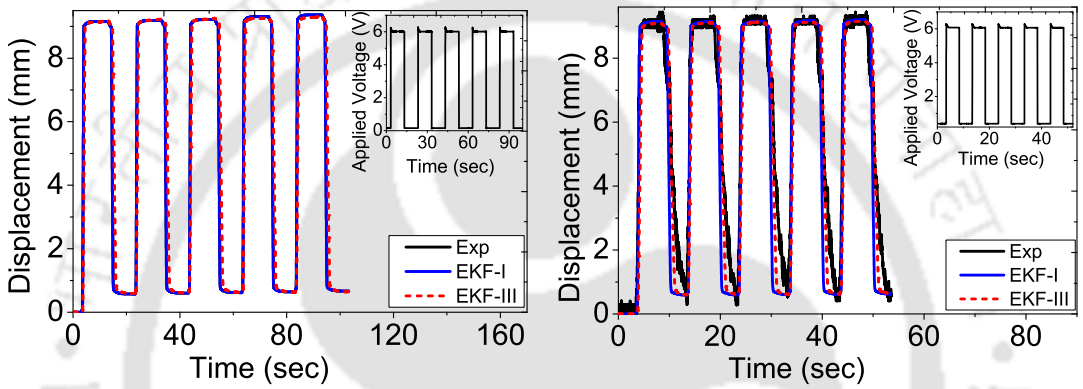

Figure 6.10: Comparison between EKF-I, EKF-III and experimental response for step input voltage (a) amplitude = 6.2 V, time period = 10 sec and (b) amplitude = 6.2 V, time period = 5 sec.

The performance of the EKF models are also evaluated for different step inputs and are shown in Fig. 6.10. It has been observed that, in these cases also the EKF-III model performs equally well.

TH-1636_10610313

6.6 Summary

The phase transformation temperatures of the SMA wire, being used in the experiment, are determined following DSC. The transformation status are found to have a overlap. Accordingly, the algorithm for identification of the transformation zone has been modified.

To reduce the quantitative discrepancies between the estimated and experimental responses, an ANN model based on EKF estimated state is developed. Results illustrate that for the same number of neurons and for the same training data, EKF based ANN model yields satisfactory performance in comparison to the ANN model, solely based on the experimental data; even in at higher frequencies.

To bridge the gap between estimation and experimental response, a modified EKF model with varying process noise covariance is developed and implemented. The process noise covariance matrix ($\mathbf{Q}$), is determined numerically from an additional set of equations involving sensitivity matrix. However, in the present study, no significant improvement is observed.

In another approach, modifications are incorporated in the electrical resistivity model of SMA, and in the expressions of heat transfer coefficient, and specific heat. Two unknown constants are introduced in the expressions of convective heat transfer coefficient and specific heat of the SMA. These are estimated following EKF model along with the state of the system. This approach yield very accurate estimation of the system response for different range of input signals.

TH-1636_10610313

Chapter 7

EKF Implementation using Microcontroller

In the earlier chapters, various Kalman filters are used to explore the self-sensing capability of Shape Memory Alloy wire actuators. Both Extended and Unscented Kalman filters are explored in this perspective. The temperature and stress of the SMA wire actuator during its constrained recovery is estimated from its electrical resistance variation. The response of the system, being actuated by the SMA wire actuator, is estimated from the estimated stress of the actuator. A couple of modifications are proposed to improve the accuracy of the EKF based estimation. These algorithms are implemented in a real-time hardware, DS1006 from dSPACE. This is a resourceful and expensive hardware. Being bulky and costly, this hardware may not be a good choice for field applications. Therefore, an effort has been made to implement the developed EKF based tool in less expensive, low end hardware, e.g., Arduino boards. In this chapter, the implementation of the developed EKF in Arduino Uno Atmega328 is discussed.

TH-1636_10610313

7.1 Arduino UN0 328

The Arduino UNO board, as shown in Fig. 7.1, is basically a microcontroller development board, which comprises of ATmega328P microcontroller [99]. It is developed mainly so as to easily access the application of the object and environment. The Arduino Uno has clock frequency of 16 MHz. It has 32 KB flash memory of which 0.5 KB is used by the boot loader. It has 6 analog input pin and 16 digital input/output pin. Out of these 16 digital pins, 6 pins, i.e., pin number 3, 5, 6, 9, 10 and 11 are used for PWM output. The operating voltage of the board is 5V. This board includes everything needed for a microcontroller to work. The user simply has to connect the USB cable and AC-DC adapter to power the board. The complete specification of the board is listed in Table 7.1.

Programming : The Arduino's open source software IDE (Integrated Development

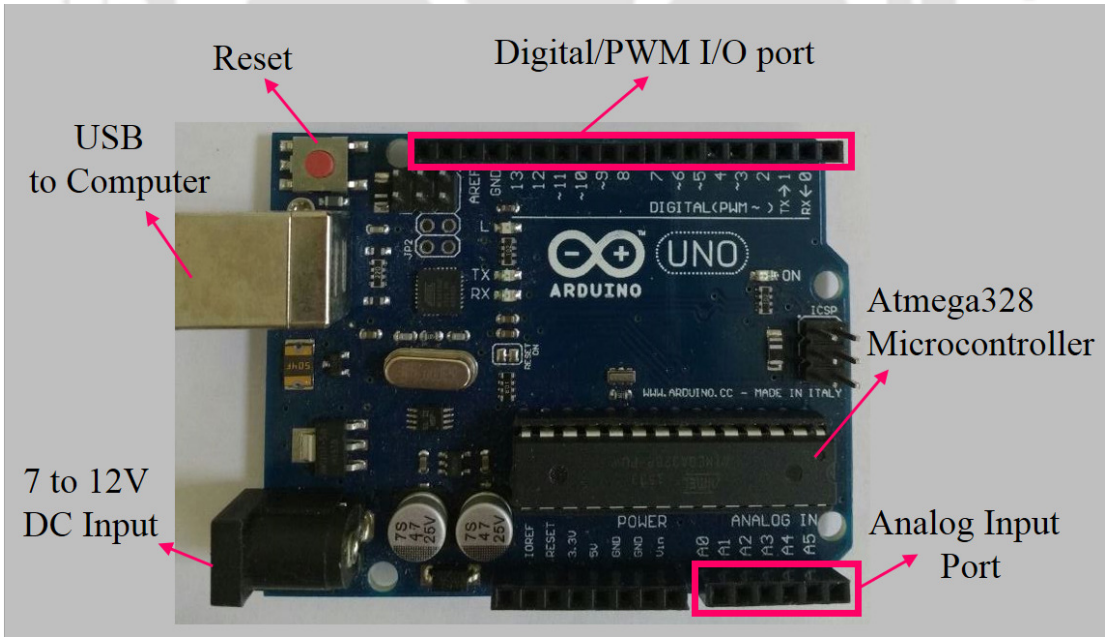

Figure 7.1: Arduino UNO development board.

Environment) [100] can be downloaded for Windows, Mac OS X, and Linux. IDE contains a

TH-1636_10610313

text editor for writing the code/program in C language, which is called sketches and the program is to be saved with an extension filename.ino. There are different options on the main window, which allows the verification of the code and download the same on the Arduino board.

Table 7.1: Arduino UNO development board technical specifications.

Symbol	Value	Symbol	Value
Microcontroller	ATmega328	Operating Voltage	5V
Input Voltage (recommended)	7-12V	Input Voltage (limits)	6-20V
Digital I/O Pins	14(of which 6 provide PWM output)	DC Current per I/O Pin	40 mA
DC Current for 3.3V Pin	50 mA	Flash Memory	32 KB
SRAM	2 KB	EEPROM	1 KB
Clock Spped	16 MHz		

7.2 Experimental Set-up

An experimental set-up is developed using the Arduino board and the linear spring biased SMA wire actuator, as described in section 4.2. The experimental procedure is shown schematically in Fig. 7.2a. The complete set-up is presented in Fig. 7.2b. First, the desired voltage signal, programmed in Arduino IDE is sent through one of the PWM pin of Arduino UNO. The PWM signal is converted to continuous form using the RC low pass filter. Then the voltage signal is inverted using an OPAMP and is fed to the power amplifier, Agilent 6642A. The output of the amplifier is applied to the SMA wire actuator. The voltage

TH-1636_10610313

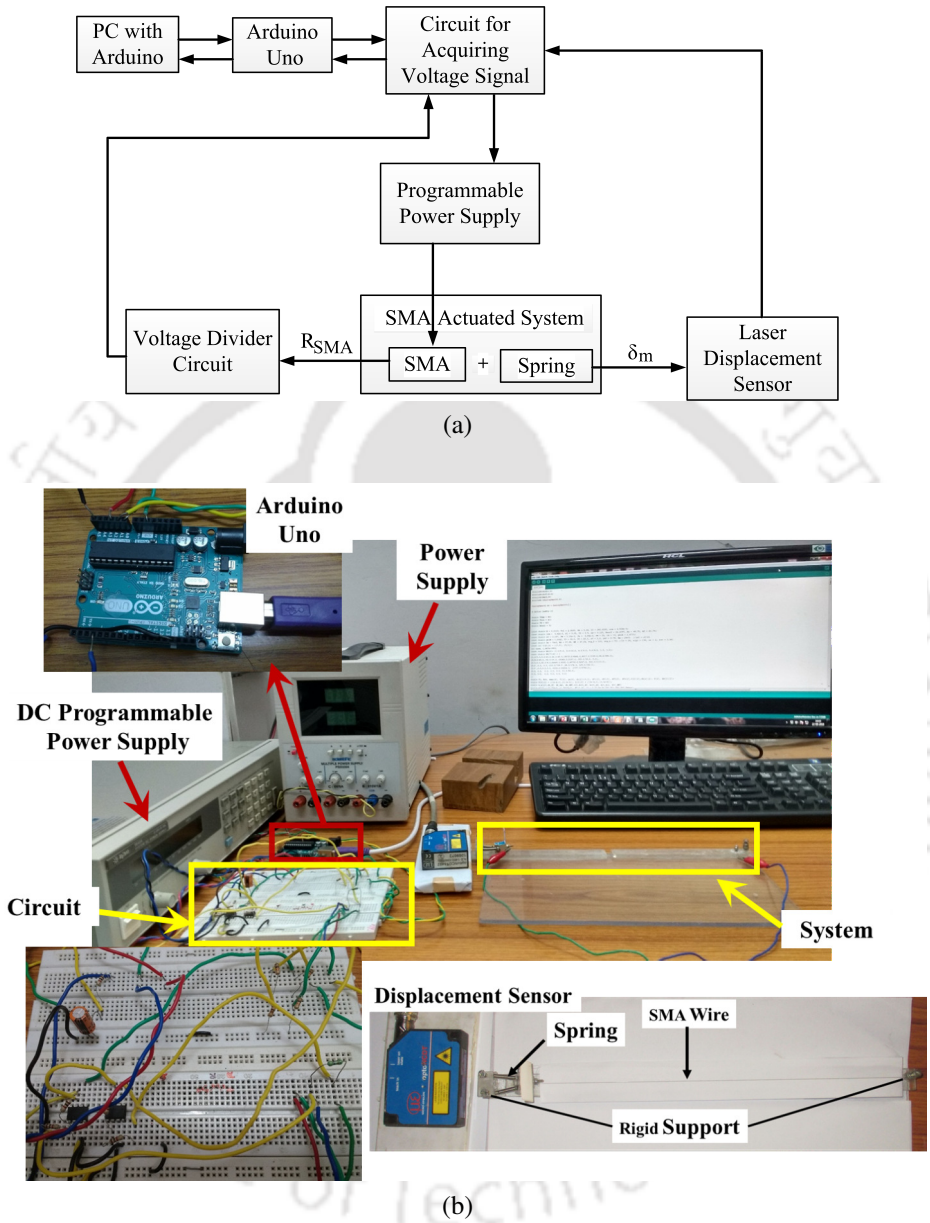

Figure 7.2: (a) Flow diagram of the experimental set-up and (b) actual experimental set-up.

drops across the SMA wire and the total circuit are measured via a voltage divider circuit and the analog input pins of the Arduino board. These voltage signals are used to calculate the electrical resistance of the SMA wire actuator, which will be used in the EKF model to estimate the displacement of the spring. It is to be noted that, the EKF model discussed in

TH-1636_10610313

section 3.6.1.2, with temperature and stress of SMA constituting the state vector, has been implemented in the Arduino. The modified EKF model, discussed in section 6.5.2, comprising of four state variables, requiring more computational effort, could not be implemented in real-time using this Arduino board. In what follows, the details of the low pass filter, inverting amplifier and voltage divider circuits are discussed.

(a) Firstly, EKF algorithm, developed using explicit numerical integration scheme as discussed in section 3.6.1.2, is implemented in C language. This is essential to implement the model in Arduino boards. The compiler converts this code to assembly language and then to machine language, that the processor can understand. This is done by the software Arduino 1.6.7 ©Arduino.

(b) The voltage signal required to be applied across the SMA, to ensure resistive heating of the SMA wire actuator, is developed in one of the subroutine of the C-code. This voltage signal is then passed through the PWM pin of the Arduino board. The PWM signal is then converted to analog signal using RC low pass filter (LPF), presented in Fig. 7.3a. The schematic of the process is shown in Fig. 7.3b. This voltage signal is then sent to the power amplifier, to amplify this analog signal.

(c) Since, the existing power amplifier (Agilent 6642A) takes input from 0 to -5 V, and the microcontroller's working range is from 0 to 5 V. Hence, to invert the voltage signal, the output of the low pass filter is passed through an op-amp (UA-741), working as unity gain amplifier. Figure 7.4a represents the pin configuration of the 741 op-amp. Pin 1 and Pin 5 of the opamp is used to making the offset voltage zero. Pin 2 and pin 3 are the inverting and non-inverting inputs terminal, respectively. Pin 4 and 7 is used for the supply voltage.

Inverting Amplifier : This means that if the positive input voltage is applied to

TH-1636_10610313

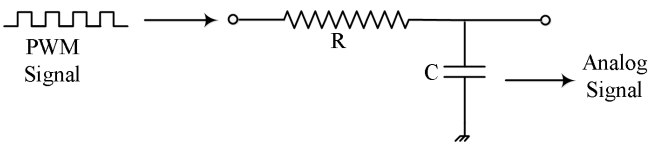

(a)

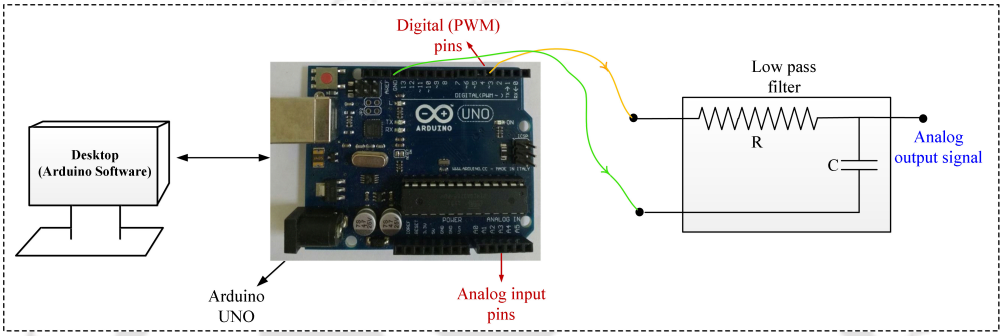

(b)

Figure 7.3: Schematic of (a) low pass filter, and (b) connection between Arduino and low pass filter.

the 741 op-amp, it is converted to a negative voltage signal. It implies, that the output signal has reverse polarity than that of the input signal. Here, the gain is decided by the two resistors (R_1 and R_2), connected with the 741 chip, as shown in Fig. 7.4b. If R_1 = R_2, then the amplifier is called unity gain amplifier, offering a gain of 1. In unity gain amplifier, the polarity of the output signal is opposite to that of an input signal, but the magnitude of the both signal remains same. The output and input signals are related as,

$$V_{out} = -\frac{R_2}{R_1} V_{in}. \tag{7.1}$$

Here, V_{in} is the positive input voltage, R_1 and R_2 are taken as, 100 Ω and V_{out} represents the negative output voltage, which is being applied to the input pin of the power amplifier. This process is schematically shown in Fig. 7.4c. It illustrates that, PWM signal obtained from the board is converted in analog form using the low pass filter and is then inverted

TH-1636_10610313

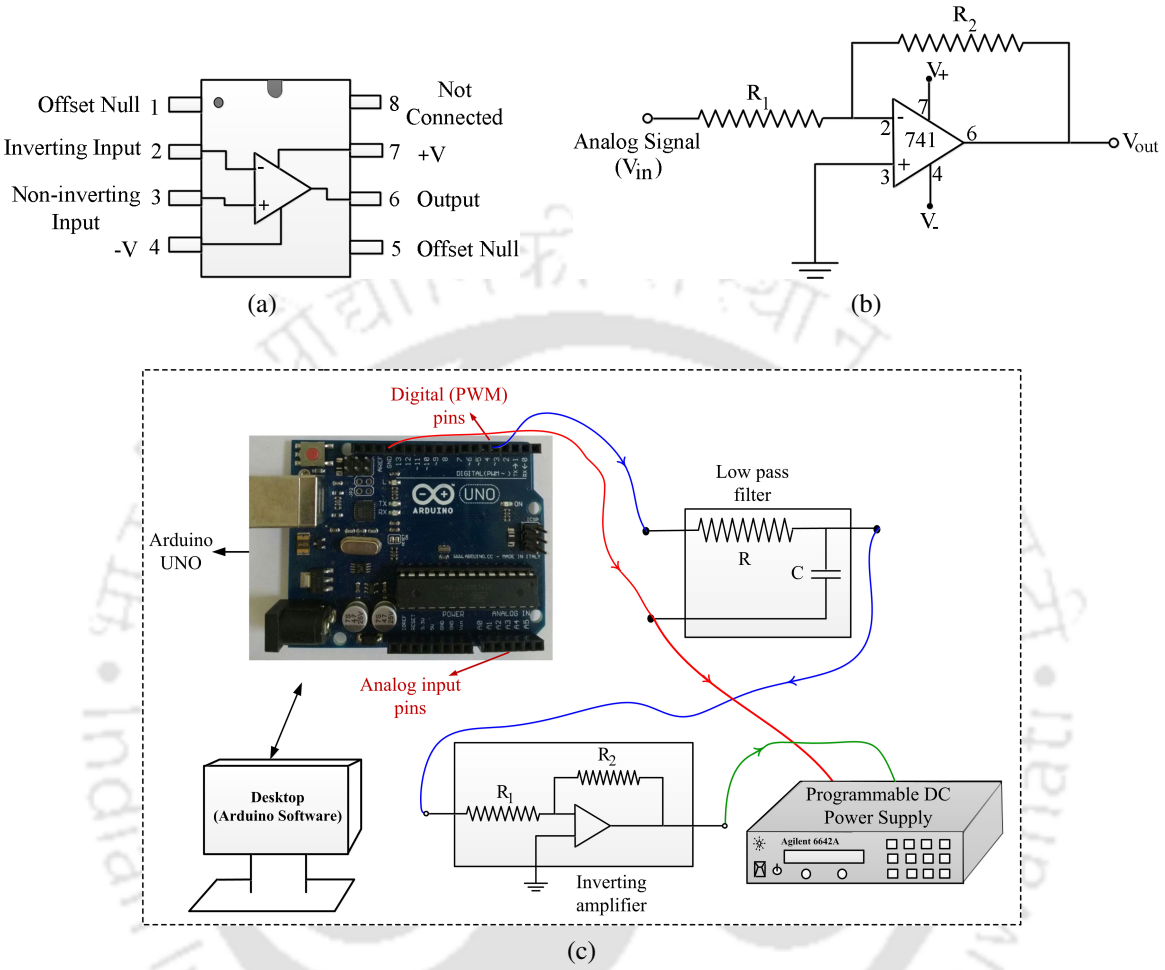

Figure 7.4: (a) Pin configuration of 741 op-amp, (b) inverting amplifier of unity gain, and (c) signal flow diagram using inverting amplifier.

using unity gain amplifier; and finally fed to the existing power amplifier.

(d) The power amplifier amplifies the voltage signal by a gain of 4. The amplified voltage signal is then applied across the SMA wire, as shown in Fig. 7.5. Then depending on the applied voltage, SMA wire gets heated or cooled, resulting in change in length of the spring.

(e) This displacement of the SMA actuated linear spring is measured by the laser displacement sensor, discussed in section 4.2. The analog output voltage (V_{out}) of the sensor

TH-1636_10610313

which is proportional to the displacement of the system, is acquired using one of the analog input pins of the board as depicted in Fig. 7.5. Using this measured output voltage of the sensor, the displacement of the SMA actuated system has been calculated using Eqn. (4.1) as

$$\delta = 25(V_{out} - V_0) \ \text{mm} \tag{7.2}$$

(f) Similarly, for measuring the electrical resistance of the SMA wire, the required voltage signals across the SMA and the total circuit, are acquired using two other analog pins of the Arduino UNO, shown in Fig. 7.5. Following Eqn. (4.2), the electrical resistance of SMA is calculated as

$$R_{SMA} = \left(\frac{V_{SMA}}{V_T - V_{SMA}}\right) R_0. \tag{7.3}$$

(g) To ensure complete transformation in the SMA wire of length 250 mm, the amplitude of voltage signal needs to be 7 V. However, the analog input pins of the Arduino board has a measuring range of 0 - 5 V. To obviate this problem, another voltage divider circuit, shown in Fig. 7.6a, is designed and used.

TH-1636_10610313

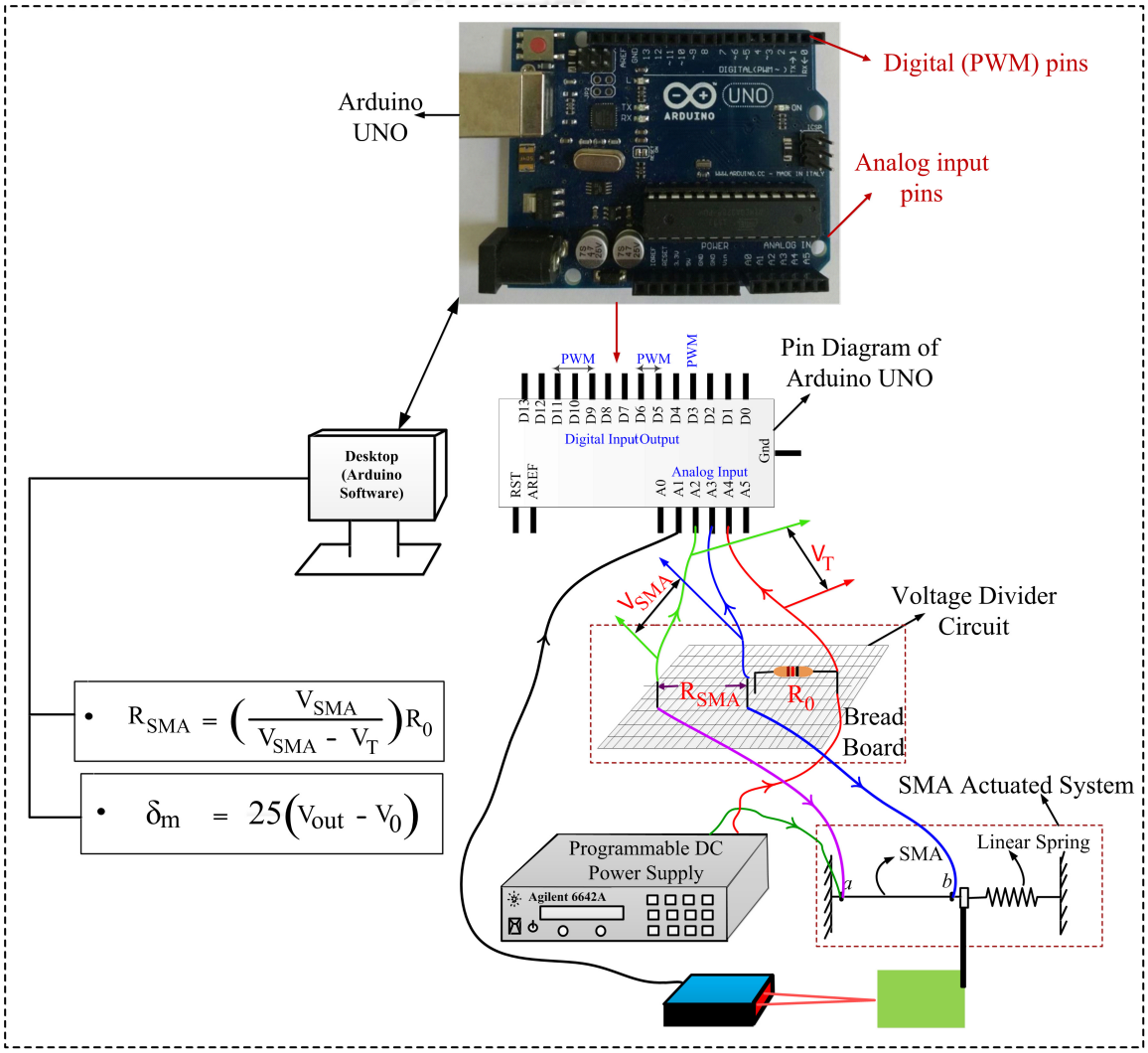

Figure 7.5: Voltage signal acquired from Arduino UNO for measuring the actual displacement of the system, and electrical resistance of SMA.

TH-1636_10610313

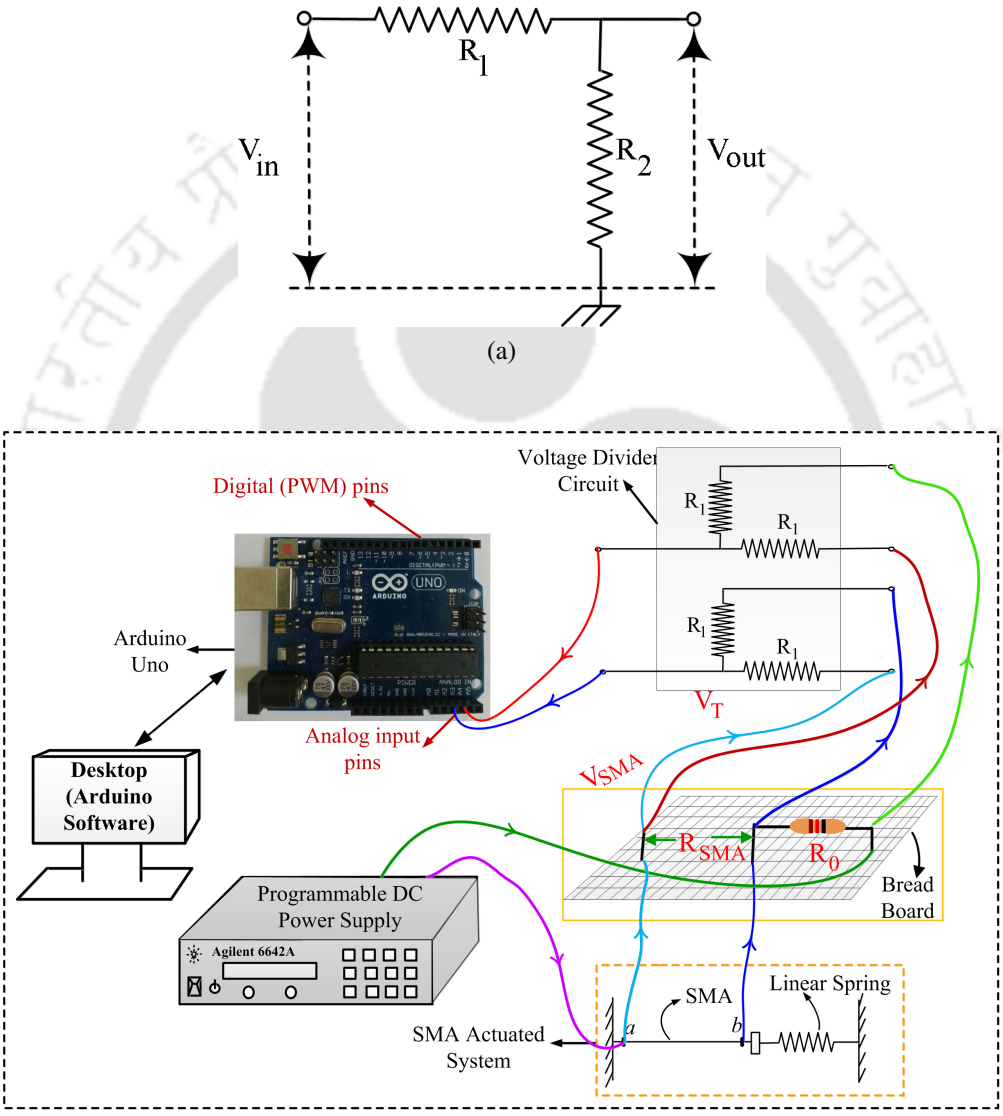

Figure 7.6: Schematic of (a) voltage divider circuit and (b) connection between voltage divider circuit with Arduino UNO.

TH-1636_10610313

This circuit divides the applied voltage by two, for $R_1 = R_2$, following Eqn. (7.4). Then the out voltage of the divider circuit is measured using the analog pin of the Arduino, depicted in Fig. 7.6b. However, this fact is taken care while computing the electrical resistance.

$$V_{out} = \frac{R_2}{R_1 + R_2} V_{in}. \tag{7.4}$$

7.3 Results and Discussion

It is observed in chapter 6, that with the help of dSPACE -DS1006, the developed EKF model can accurately track the response. However, since the dSPACE is very costly and bulky, it will be convenient if the developed algorithm can be implemented in small and cheap hardware. For this purpose, Arduino UNO has been chosen and the results are shown below. Figure 7.7 illustrates the estimated and measured response of the linear spring biased SMA actuator for both step, refer Fig. 7.7a, and continuous, refer Fig. 7.7b, input signals. These responses are obtained from realtime execution of the EKF model in Arduino UNO. These results clearly demonstrate that the developed EKF model is simple enough to work in low end harware like Arduino UNO.

TH-1636_10610313

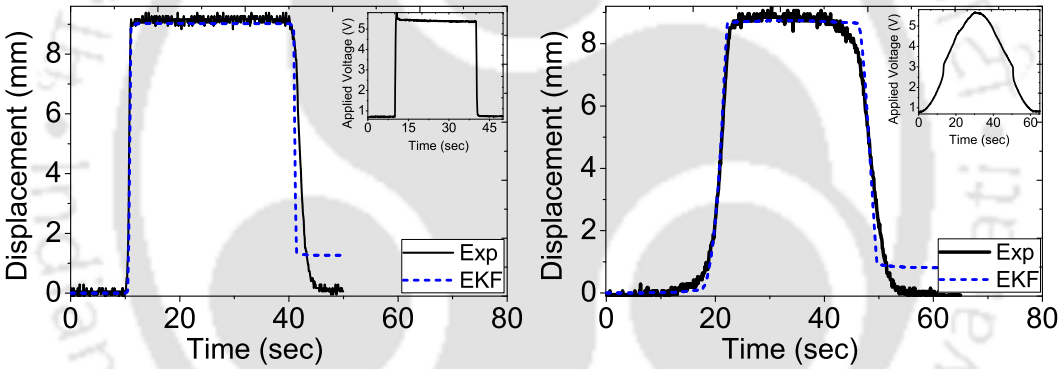

Figure 7.7: Comparison between EKF estimated and experimental response for (a) step and (b) continuous voltage signal .

TH-1636_10610313

7.4 Summary

EKF has be implemented in commercially available low end hardware. For EKF implementation using microcontroller the EKF code has been written in C language in the Arduino software. The electronics circuit has also been developed so as to acquire the experimental data. The real time comparisons between EKF estimation and experimental response, illustrates that EKF can be accurately estimates the states of the system using low cost hardware also, with the same level accuracy as EKF estimation using dSPACE. Therefore, EKF estimation using low cost hardware can be easily used in field application, where cost and space is a critical issue.

TH-1636_10610313

Chapter 8

Conclusions and Future Work

8.1 Contributions

The major contributions of the present work are as follows.

- A nonlinear estimator, called Extended Kalman Filter, is proposed and developed to estimate the state and the system response from the electrical resistance variation of the SMA wire, subjected to resistive heating. In this respect, a linear spring biased SMA wire actuator and a cantilever beam undergoing large displacement due to SMA actuation are considered. For both the systems, the state equations are derived following the basic laws of physics and are used in the respective EKF models.

- The a-priori state estimation is implemented following both explicit and implicit numerical schemes. From the convergence study, the time step of 0.01 sec is found to be suitable for both the schemes. Moreover, it has been found that the computational time of the EKF model following implicit scheme is almost 33% less as compared to the same of the EKF model using explicit scheme.

TH-1636_10610313

- The EKF models are verified by comparing the estimated responses with the simulated responses of an established model, for various possible extent of transformations.

- The process and measurement noise covariance, which affects the performance of a EKF model, are determined for the set-up and model, following heuristic and experimental techniques, respectively. The values of process and measurement noise covariance are found to be 10^{-6} and 8, respectively.

- An experimental set-up is developed to measure the electrical resistance of the SMA wire and the system response, i.e., the displacement of the spring, for different voltage signals. The measured electrical resistance is used in the developed EKF model to estimate the system response for the same input. The estimated responses are compared with the corresponding measured responses. The result shows a good qualitative agreement between the two. The maximum errors in estimation are found to be 0.5 mm and 3 mm for complete and partial transformations, respectively, in SMA.

- Another EKF model has been developed for a cantilever beam undergoing large displacement due to the constrained recovery of a SMA wire fixed to it at a discrete offset. The displacement of the free end of the beam is estimated from the measured resistance variation of the SMA wire and is compared with the corresponding measured displacement. In this case as well, the estimation follows the actual displacement only qualitatively. The maximum estimation error is found to be 25% of the maximum displacement.

- Drastic improvement in the estimation accuracy is achieved by proper choice of the convective heat transfer coefficient following an optimization technique. The maximum inaccuracy is found to decrease from 25% to 5% of the maximum displacement.

- An Unscented Kalman filter has been develop to explore the self-sensing capability of

TH-1636_10610313

SMA wire actuator. The state and output equations are derived and is implemented offline using the measured electrical resistance data and voltage signal for a linear spring biased SMA wire.

- For the linear spring biased SMA wire actuator, the estimated displacement obtained using the EKF and UKF models are compared with the corresponding measured displacement. The performance of the UKF model is found to be as accurate as that of the EKF model. However, in terms of computational effort, UKF model is superior; as the computational time of the UKF model is found to be almost 50% as that of the EKF model.

- Differential Scanning Calorimetry has been conducted to determine the phase transformation temperature of the SMA wire at zero stress. It is found that the forward and reverse transformation zones are partially overlapped. A modified algorithm has been proposed to implement the present phase kinetics model and in this case, only the explicit numerical scheme is suggested.

- The performance of an ANN model trained using the EKF estimated data is developed and compared with another ANN model trained solely using measured data. It has been observed that for the same configuration, EKF based ANN is performing better compared the other ANN model, even for higher frequencies.

- To reduce the quantitative difference between estimation and experimental response, a modified EKF with varying process noise covariance is developed and implemented. The process noise covariance matrix ($\mathbf{Q}$), is determined numerically from additional set of equations involving sensitivity matrix. However, this approach failed to improve the estimation accuracy.

- The electrical resistance of the SMA wire is found to increase at a faster rate at the

TH-1636_10610313

beginning of forward transformation as compared to the existing model. A modified model for electrical resistivity is proposed, which is found to simulate the electrical resistance variation of the SMA wire satisfactorily.

- Two constant parameters are introduced in the expressions of convective heat transfer coefficient and specific heat of SMA, respectively. The parameters are then appended to the state of the system so as to estimate the same along with the state of the system. This approach is found to yield significant accuracy for different input voltages as well as different frequencies. The maximum estimation error is found to be less than 0.8 mm.
- Finally, the effectiveness of the developed EKF model is demonstrated from the real-time implementation of the same in a less resourceful hardware, Arduino UNO.

8.2 List-of-Publications

(i) **Journals:**

- Gurung, H., and Banerjee, A. "Development of an extended Kalman filter for the self-sensing application of a spring-biased shape memory alloy wire actuator". Smart Materials and Structures-IOP Science, 25 (2016): 025012.
- Gurung, H., and Banerjee, A. "Self-sensing SMA actuator using extended Kalman filter and Artificial Neural Network". Procedia Engineering 144 (2016): 629-634.
- Gurung, H., and Banerjee, A. "Development of Unscented Kalman Filter for Self-sensing Application of Shape Memory Alloy Wire Actuator". Sensors and Actuators A: Physical 251 (2016): 258-265.

TH-1636_10610313

(ii) **International Conference:**

- Gurung, H., Karmakar, S., and Banerjee, A. "Development of an Extended Kalman Filter for Self-Sensing Application of Shape Memory Alloy Wire Actuator". ASME 2015 Conference on Smart Materials, Adaptive Structures and Intelligent Systems. September 21-23, 2015, Colorado Springs, Colorado, USA

(iii) **National Conference:**

- Gurung, H., and Banerjee, A. "Improved extended Kalman filter for self-sensing shape memory alloy wire actuator". ISSS National Conference on MEMS, Smart Materials, Structures and Systems. September 28-30, 2016, Kanpur, India.

8.3 Scope of Future Works

- In both the models, the noises are assumed to white Gaussian. Whereas, in the current system, in presence of structural as well as parametric uncertainties the choice of colored noise may be more realistic. This aspect needs to be looked into.
- In the present work, the developed EKF or UKF models have not be used in feedback control applications, i.e., to control the position of the system using the estimated displacement as feedback. This has to be explored.
- To explore more advanced estimators, e.g., Particle filter, to estimate the system response exploiting the self-sensing property of the SMA wire actuator.
- Following the technique of parameter estimation using Kalman Filters, some of the unknown properties of the SMA wire can be estimated. This has to be explored.

TH-1636_10610313

Appendices

TH-1636_10610313

Appendix A

Arbitary Thermomechanical Loading

Forward Transformation

The phase kinetics of SMA in forward transformation zone can be represented by Fig. A.1, following, which one can derive the expression as,

$$Z^M = \frac{P^M - P_j^M}{P_0^M - P_j^M}. \tag{A.1}$$

Here, $P_j^M = \sigma_j \cos\phi^M + (M_s - T_j)\sin\phi^M$, $P^M = \sigma\cos\phi^M + (M_s - T)\sin\phi^M$ and $P_0^M = (M_s - M_f)\sin\phi^M$.

Therefore, the normalized distance along the transformation domain can be given as,

$$Z^M = \frac{\sigma\cos\phi^M + (T_j - T)\sin\phi^M - \sigma_j\cos\phi^M}{\left(T_j - M_f\right)\sin\phi^M - \sigma_j\cos\phi^M}. \tag{A.2}$$

The rate form of Eqn. (A.2) can be written as,

$$\frac{dZ^M}{dt} = \frac{\cos\phi^M\left(\frac{d\sigma}{dt}\right) + \left\{-\sin\phi^M\right\}\left(\frac{dT}{dt}\right)}{\left(T_j - M_f\right)\sin\phi^M - \sigma_j\cos\phi^M}. \tag{A.3}$$

TH-1636_10610313

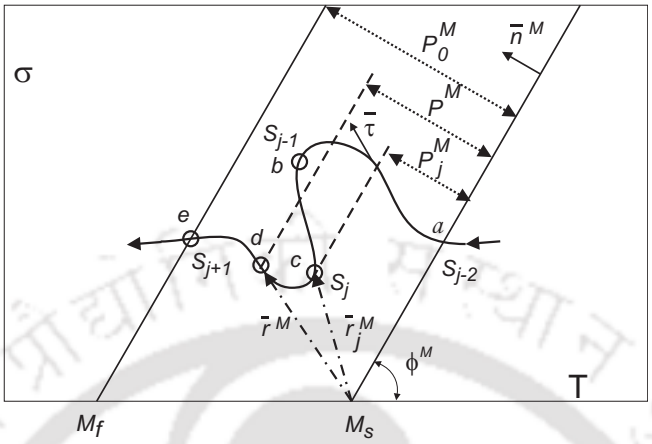

Figure A.1: Arbitrary thermo-mechanical loading path in forward transformation zone.

Following the phase kinetics proposed by Brinson [29], the martensite volume fraction can be written as,

$$\xi = \xi_j + 0.5\left(1-\xi_j\right)\left(1-\cos\left(\pi Z^M\right)\right). \tag{A.4}$$

The rate form of Eqn. (A.4), can be expressed as,

$$\begin{aligned}
\frac{d\xi}{dt} &= 0.5\left(1-\xi_j\right)\pi\sin\left(\pi Z^M\right)\frac{dZ^M}{dt}, \\
\text{or,} \quad &= 0.5\left(1-\xi_j\right)\pi\sin\left(\pi Z^M\right)\left\{\frac{\cos\phi^M\left(\frac{d\sigma}{dt}\right)+\left\{-\sin\phi^M\left(\frac{dT}{dt}\right)\right\}}{\left(T_j-M_f\right)\sin\phi^M-\sigma_j\cos\phi^M}\right\}, \\
\text{or,} \quad &= \frac{0.5(1-\xi_j)\pi\sin\left(\pi Z^M\right)\cos\phi^M}{\left(T_j-M_f\right)\sin\phi^M-\sigma_j\cos\phi^M}\frac{d\sigma}{dt}+\left\{\frac{-0.5(1-\xi_j)\pi\sin\left(\pi Z^M\right)\sin\phi^M}{\left(T_j-M_f\right)\sin\phi^M-\sigma_j\cos\phi^M}\right\}\frac{dT}{dt}.
\end{aligned} \tag{A.5}$$

Equation Eqn. (A.5) can be written as,

$$\frac{d\xi}{dt} = \psi_1\frac{d\sigma}{dt}+\psi_2\frac{dT}{dt}. \tag{A.6}$$

TH-1636_10610313

Following the phase kinetics proposed by Brinson [29], the stress induced martensite volume fraction can be written as,

$$\xi_S = \xi_{S_j} + 0.5\left(\xi^{'} - \xi_{S_j}\right)\left(1 - \cos\left(\pi Z^M\right)\right), \tag{A.7}$$

Here, $\xi^{'} = 0.5\left(1 + \tanh\left(\pi Z^{\sigma}\right)\right)$ and $Z^{\sigma} = \frac{\sigma - \sigma_s^{cr}}{\sigma_f^{cr} - \sigma_s^{cr}}$. The rate form of $\xi^{'}$ and Z^{σ} is obtained as,

$$\frac{dZ^{\sigma}}{dt} = \frac{1}{\sigma_f^{cr} - \sigma_s^{cr}}\frac{d\sigma}{dt}. \tag{A.8}$$

and,

$$\begin{aligned} \frac{d\xi^{'}}{dt} &= 0.5\pi \sec h^2\left(\pi Z^{\sigma}\right)\frac{dZ^{\sigma}}{dt}, \\ \text{or,} \qquad &= \frac{0.5\pi \sec h^2(\pi Z^{\sigma})}{\sigma_f^{cr} - \sigma_s^{cr}}\frac{d\sigma}{dt}. \end{aligned} \tag{A.9}$$

The rate form of Eqn. (A.7), can be expressed as,

$$\frac{d\xi_s}{dt} = 0.5\left(1 - \cos\left(\pi Z^M\right)\right)\frac{d\xi^{'}}{dt} + 0.5\pi\left(\xi^{'} - \xi_{S_j}\right)\sin\left(\pi Z^M\right)\frac{dZ^M}{dt}. \tag{A.10}$$

Thus Eqn. (A.10) becomes,

$$\begin{aligned} \frac{d\xi_s}{dt} &= 0.5\left(1 - \cos\left(\pi Z^M\right)\right)\frac{d\xi^{'}}{dt} + 0.5\pi\left(\xi^{'} - \xi_{s_j}\right)\sin\left(\pi Z^M\right)\frac{dZ^M}{dt}, \\ &= \frac{0.5\pi \sec h^2(\pi Z^{\sigma})}{\sigma_f^{cr} - \sigma_s^{cr}}\frac{d\sigma}{dt} + \frac{0.5\pi\left(\xi^{'} - \xi_{s_j}\right)\sin\left(\pi Z^M\right)\cos\phi^M}{\left(T_j - M_f\right)\sin\phi^M - \sigma_j\cos\phi^M}\frac{d\sigma}{dt} \\ &\quad + \left\{\frac{-0.5\pi\left(\xi^{'} - \xi_{s_j}\right)\sin\left(\pi Z^M\right)\sin\phi^M}{\left(T_j - M_f\right)\sin\phi^M - \sigma_j\cos\phi^M}\right\}\frac{dT}{dt}, \\ &= \left\{\frac{0.5\pi \sec h^2(\pi Z^{\sigma})}{\sigma_f^{cr} - \sigma_s^{cr}} + \frac{0.5\pi\left(\xi^{'} - \xi_{s_j}\right)\sin\left(\pi Z^M\right)\cos\phi^M}{\left(T_j - M_f\right)\sin\phi^M - \sigma_j\cos\phi^M}\right\}\frac{d\sigma}{dt} \\ &\quad + \left\{\frac{-0.5\pi\left(\xi^{'} - \xi_{s_j}\right)\sin\left(\pi Z^M\right)\sin\phi^M}{\left(T_j - M_f\right)\sin\phi^M - \sigma_j\cos\phi^M}\right\}\frac{dT}{dt}. \end{aligned} \tag{A.11}$$

TH-1636_10610313

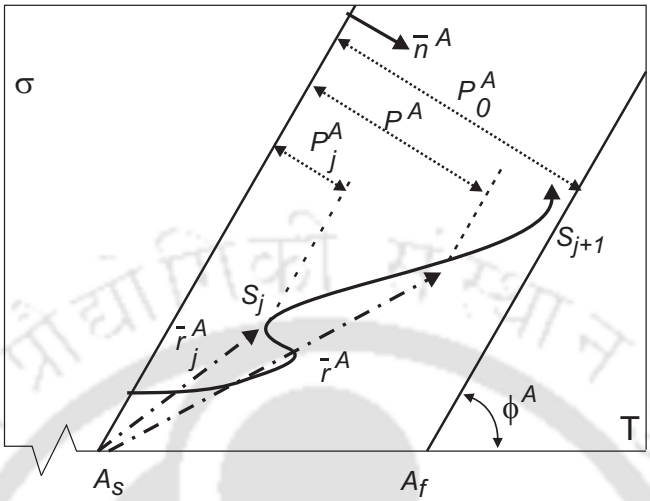

Figure A.2: Arbitrary thermo-mechanical loading path in reverse transformation zone.

Equation Eqn. (A.11) can be expressed as,

$$\frac{d\xi_s}{dt} = \psi_3 \frac{d\sigma}{dt} + \psi_4 \frac{dT}{dt}. \tag{A.12}$$

Reverse Transformation

The phase kinetics of SMA in reverse transformation zone can be represented by Fig. A.2. From the figure one can derive the following expressions,

$$Z^A = \frac{P^A - P_j^A}{P_0^A - P_j^A}. \tag{A.13}$$

Here, $P_j^A = -\sigma_j \cos\phi^A + (T_j - A_s)\sin\phi^A$, $P^A = -\sigma\cos\phi^A + (T - A_s)\sin\phi^A$, and $P_0^A = (A_s - A_f)\sin\phi^A$.

Thus the normalized distance can be derived as,

$$Z^A = \frac{(T - T_j)\sin\phi^A + (\sigma_j - \sigma)\cos\phi^A}{\left(A_f - T_j\right)\sin\phi^A + \sigma_j\cos\phi^A}. \tag{A.14}$$

TH-1636_10610313

The rate form of the normalized distance is,

$$\frac{dZ^A}{dt} = \frac{-\cos\phi^A\left(\frac{d\sigma}{dt}\right)+\sin\phi^A\left(\frac{dT}{dt}\right)}{\left(A_f-T_j\right)\sin\phi^A+\sigma_j\cos\phi^A},$$
$$= \frac{-\cos\phi^A}{\left(A_f-T_j\right)\sin\phi^A+\sigma_j\cos\phi^A}\frac{d\sigma}{dt} + \frac{\sin\phi^A}{\left(A_f-T_j\right)\sin\phi^A+\sigma_j\cos\phi^A}\frac{dT}{dt}. \tag{A.15}$$

Following the phase kinetics in reverse transformation zone [29],

$$\xi = 0.5\xi_j\left(1+\cos\left(\pi Z^A\right)\right). \tag{A.16}$$

The rate form of Eqn. (A.16) is found to be,

$$\frac{d\xi}{dt} = -0.5\xi_j\pi\sin\left(\pi Z^A\right)\frac{dZ^A}{dt},$$
$$= -0.5\xi_j\pi\sin\left(\pi Z^A\right)\left\{\begin{array}{l}\frac{-\cos\phi^A}{\left(A_f-T_j\right)\sin\phi^A+\sigma_j\cos\phi^A}\frac{d\sigma}{dt}\\ +\frac{\sin\phi^A}{\left(A_f-T_j\right)\sin\phi^A+\sigma_j\cos\phi^A}\frac{dT}{dt}\end{array}\right\}, \tag{A.17}$$
$$= \frac{0.5\xi_j\pi\sin\left(\pi Z^A\right)\cos\phi^A}{\left(A_f-T_j\right)\sin\phi^A+\sigma_j\cos\phi^A}\frac{d\sigma}{dt} + \left\{\frac{-0.5\xi_j\pi\sin\left(\pi Z^A\right)\sin\phi^A}{\left(A_f-T_j\right)\sin\phi^A+\sigma_j\cos\phi^A}\right\}\frac{dT}{dt}.$$

Equation (A.17) can be expressed as,

$$\frac{d\xi}{dt} = \psi_1\frac{d\sigma}{dt} + \psi_2\frac{dT}{dt}. \tag{A.18}$$

Similarly, the stress induced martensite volume fraction changes in the reverse transformation zone as [29],

$$\xi_S = 0.5\xi_{S_j}\left(1+\cos\left(\pi Z^A\right)\right). \tag{A.19}$$

TH-1636_10610313

The rate form is obtained as,

$$\frac{d\xi_s}{dt} = -0.5\xi_{s_j}\pi \sin\left(\pi Z^A\right) \frac{dZ^A}{dt}. \tag{A.20}$$

or,

$$\frac{d\xi_s}{dt} = -0.5\xi_{s_j}\pi \sin\left(\pi Z^A\right) \left\{ \begin{array}{l} \frac{-\cos\phi^A}{\left(A_f - T_j\right)\sin\phi^A + \sigma_j \cos\phi^A} \frac{d\sigma}{dt}, \\ + \frac{\sin\phi^A}{\left(A_f - T_j\right)\sin\phi^A + \sigma_j \cos\phi^A} \frac{dT}{dt} \end{array} \right\},$$

or,
$$= \frac{0.5\xi_{s_j}\pi \sin\left(\pi Z^A\right)\cos\phi^A}{\left(A_f - T_j\right)\sin\phi^A + \sigma_j \cos\phi^A} \frac{d\sigma}{dt} + \left\{ \frac{-0.5\xi_{s_j}\pi \sin\left(\pi Z^A\right)\sin\phi^A}{\left(A_f - T_j\right)\sin\phi^A + \sigma_j \cos\phi^A} \right\} \frac{dT}{dt}. \tag{A.21}$$

Equation (A.21) can be expressed in desired form as,

$$\frac{d\xi_S}{dt} = \psi_3 \frac{d\sigma}{dt} + \psi_4 \frac{dT}{dt}. \tag{A.22}$$

TH-1636_10610313

Appendix B

Derivation of the State Equations

The differential form of the constitutive relation of a SMA wire [31] is rewritten as,

$$\frac{d\sigma}{dt} = D\frac{d\epsilon}{dt} - \epsilon_l D\frac{d\xi_s}{dt} + (\epsilon - \epsilon_l \xi_S)(D_M - D_A)\frac{d\xi}{dt} + \Theta\frac{dT}{dt}. \tag{B.1}$$

The difference form of Eqn. (B.1) can be obtained as,

$$\Delta\sigma = D\Delta\epsilon - \epsilon_l D\Delta\xi_s + (\epsilon - \epsilon_l \xi_S)(D_M - D_A)\Delta\xi + \Theta\Delta T. \tag{B.2}$$

The phase kinetics of SMA in difference form can be expressed as,

$$\Delta\xi = \psi_1\Delta\sigma + \psi_2\Delta T. \tag{B.3}$$

$$\Delta\xi_s = \psi_3\Delta\sigma + \psi_4\Delta T. \tag{B.4}$$

TH-1636_10610313

Substituting Eqns. (B.3) and (B.4) in Eqn. (B.2), one gets,

$$\begin{aligned}\Delta\sigma &= D\Delta\epsilon - \epsilon_l D\left(\psi_3\Delta\sigma + \psi_4\Delta T\right) + \left(\epsilon - \epsilon_l\xi_{_S}\right)\left(D_M - D_A\right)\left(\psi_1\Delta\sigma + \psi_2\Delta T\right) + \Theta\Delta T,\\ &= D\Delta\epsilon + \left\{\left(\epsilon - \epsilon_l\xi_{_S}\right)\left(D_M - D_A\right)\psi_1 - \epsilon_l D\psi_3\right\}\Delta\sigma + \left\{\begin{array}{l}\left(\epsilon - \epsilon_l\xi_{_S}\right)\left(D_M - D_A\right)\psi_2\\ -\epsilon_l D\psi_4 + \Theta\end{array}\right\}\Delta T.\end{aligned} \tag{B.5}$$

Seperating ΔT and $\Delta\sigma$ term, one obtains,

$$\begin{aligned}\left[1 - \left\{\left(\epsilon - \epsilon_l\xi_{_S}\right)\left(D_M - D_A\right)\psi_1 - \epsilon_l D\psi_3\right\}\right]\Delta\sigma = D\Delta\epsilon +\\ \left\{\left(\epsilon - \epsilon_l\xi_{_S}\right)\left(D_M - D_A\right)\psi_2 - \epsilon_l D\psi_4 + \Theta\right\}\Delta T.\end{aligned} \tag{B.6}$$

Equation (B.6) can be expressed as,

$$X_a\Delta\sigma = D\Delta\epsilon + Y_a\Delta T. \tag{B.7}$$

Here, $X_a = \left[1 - \left\{\left(\epsilon - \epsilon_l\xi_s\right)\left(D_M - D_A\right)\psi_1 - \epsilon_l D\psi_3\right\}\right]$ and
$Y_a = \left\{\left(\epsilon - \epsilon_l\xi_{_S}\right)\left(D_M - D_A\right)\psi_2 - \epsilon_l D\psi_4 + \Theta\right\}$.

SMA Actuated Linear System

From geometry and force equilibrium, one gets,

$$\epsilon = \epsilon_0 - \frac{\sigma A}{K_s L_0}. \tag{B.8}$$

The rate form of Eqns. (B.8) is obtained as,

$$\frac{d\epsilon}{dt} = -\frac{A}{K_s L_0}\frac{d\sigma}{dt}. \tag{B.9}$$

TH-1636_10610313

The difference form Eqn. (B.9) is as follows.

$$\Delta\epsilon = -\frac{A}{K_s L_0}\Delta\sigma. \tag{B.10}$$

Using Eqn. (B.10) in Eqn. (B.5), one can write,

$$\begin{aligned}&\left[1 - \left\{\left(\epsilon - \epsilon_l\xi_s\right)\left(D_M - D_A\right)\psi_1 - \epsilon_l D\psi_3\right\} + \tfrac{A}{K_s L_0}\right]\Delta\sigma \\ &= \left[\left(\epsilon - \epsilon_l\xi_s\right)\left(D_M - D_A\right)\psi_2 - \epsilon_l D\psi_4 + \Theta\right]\Delta T.\end{aligned} \tag{B.11}$$

Equation Eqn. (B.11) can be rewritten as,

$$\Delta\sigma = F_5\Delta T. \tag{B.12}$$

where,

$$F_5 = \left[\frac{(\epsilon-\epsilon_l\xi_s)(D_M-D_A)\varphi_2-\epsilon_l D\varphi_4+\Theta}{1-\{(\epsilon-\epsilon_l\xi_s)(D_M-D_A)\varphi_1-\epsilon_l D\varphi_3\}+\frac{A}{K_s L_0}}\right]. \tag{B.13}$$

SMA Actuated NonLinear System

From the analysis of the beam, following [83], one gets the relation between stress and strain of the SMA wire as,

$$\epsilon = \Psi(\sigma). \tag{B.14}$$

The rate form of Eqn. (B.14) can be written as,

$$\frac{d\epsilon}{dt} = A_1(\sigma)\frac{d\sigma}{dt}. \tag{B.15}$$

TH-1636_10610313

where,

$$A_1 = \frac{d\psi}{d\sigma}. \tag{B.16}$$

Difference form of Eqn. (B.15) is obtained as,

$$\Delta\epsilon = A_1 \Delta\sigma. \tag{B.17}$$

Using Eqn. (B.5) in Eqn. (B.17), one claims,

$$\left[1 - \left\{\left(\epsilon - \epsilon_l \xi_s\right)\left(D_M - D_A\right)\psi_1 - \epsilon_l D\psi_3\right\} - DA_1\right]\Delta\sigma = \begin{bmatrix} \left(\epsilon - \epsilon_l \xi_s\right)\left(D_M - D_A\right)\psi_2 \\ -\epsilon_l D\psi_4 + \Theta \end{bmatrix} \Delta T. \tag{B.18}$$

Equation (B.18) can be expressed as,

$$\Delta\sigma = F_5 \Delta T. \tag{B.19}$$

where,

$$F_5 = \frac{(\epsilon - \epsilon_l \xi_s)(D_M - D_A)\varphi_2 - \epsilon_l D\varphi_4 + \Theta}{1 - \{(\epsilon - \epsilon_l \xi_s)(D_M - D_A)\varphi_1 - \epsilon_l D\varphi_3\} - DA_1}. \tag{B.20}$$

Heat Balance Equation

The heat balance equation for the SMA wire is rewritten as,

$$C_v \frac{dT}{dt} = \frac{1}{V_m}\left(\frac{V^2}{R} - hA_{surf}\left(T - T_0\right)\right) + \lambda\frac{d\xi}{dt} \tag{B.21}$$

The difference form of Eqn. (B.21) is obtained as,

$$C_v \Delta T = \frac{1}{V_m}\left(\frac{V^2}{R} - hA_{surf}\left(T - T_0\right)\right)\Delta t + \lambda\Delta\xi. \tag{B.22}$$

TH-1636_10610313

Using Eqn. (B.3) the above equation can be written as,

$$\begin{aligned} C_v \Delta T &= \tfrac{1}{V_m}\left(\tfrac{V^2}{R} - hA_{surf}\left(T - T_0\right)\right)\Delta t + \lambda\left(\phi_1 \Delta\sigma + \psi_2 \Delta T\right). \\ &= \tfrac{1}{V_m}\left(\tfrac{V^2}{R} - hA_{surf}\left(T - T_0\right)\right)\Delta t + \lambda\psi_1 \Delta\sigma + \lambda\psi_2 \Delta T. \end{aligned} \tag{B.23}$$

Rearranging ΔT and $\Delta\sigma$ terms, Eqn. (B.23) takes the form as, equation.

$$\left(C_v - \lambda\psi_2\right)\Delta T = \tfrac{1}{V_m}\left(\tfrac{V^2}{R} - hA_{surf}\left(T - T_0\right)\right)\Delta t + \lambda\psi_1 \Delta\sigma. \tag{B.24}$$

This can be rewritten as,

$$\begin{aligned} &\Delta T = \tfrac{1}{V_m\left(C_v - \lambda\psi_2\right)}\left(\tfrac{V^2}{R} - hA_{surf}\left(T - T_0\right)\right)\Delta t + \tfrac{\lambda\psi_1}{\left(C_v - \lambda\psi_2\right)}\Delta\sigma. \\ &\text{or,} \\ &\Delta T = X_b \Delta t + Y_b \Delta\sigma. \end{aligned} \tag{B.25}$$

Here, $X_b = \tfrac{1}{V_m\left(C_v - \lambda\psi_2\right)}\left(\tfrac{V^2}{R} - hA_{surf}\left(T - T_0\right)\right)$, and, $Y_b = \tfrac{\lambda\psi_1}{\left(C_v - \lambda\psi_2\right)}$.

Following Eqns. (B.12) and (B.25), one may write,

$$\begin{aligned} &\left(C_v - \lambda\psi_2\right)\Delta T = \tfrac{1}{V_m}\left(\tfrac{V^2}{R} - hA_{surf}\left(T - T_0\right)\right)\Delta t + \lambda\psi_1 F_5 \Delta T, \\ &\text{or,} \quad \left(\mathrm{C_v} - \lambda\psi_2 - \lambda\psi_1 \mathrm{F_5}\right)\Delta \mathrm{T} = \tfrac{1}{\mathrm{V_m}}\left(\tfrac{\mathrm{V^2}}{\mathrm{R}} - \mathrm{hA_{surf}}\left(\mathrm{T} - \mathrm{T_0}\right)\right)\Delta \mathrm{t} \end{aligned} \tag{B.26}$$

Equation (B.26) can be expressed as,

$$\Delta T = \frac{\tfrac{1}{V_m}\left(\tfrac{V^2}{R} - hA_{surf}\left(T - T_0\right)\right)}{C_v - \lambda\varphi_2 - \lambda\varphi_1 F_5}. \tag{B.27}$$

TH-1636_10610313

Bibliography

[1] D. C. Lagoudas. Shape memory alloys: Modeling and engineering applications, 2008.

[2] A. Banerjee. Simulation of shape memory alloy wire actuator behavior under arbitrary thermo-mechanical loading. *Smart Materials and Structures*, 21(12):125018, 2012.

[3] A. Banerjee, B. Bhattacharya, and A.K. Mallik. Forward and inverse analyses of an SMA actuated compliant link. *Journal of Mechanisms and Robotics*, 3(2):021003–1–10, 2011.

[4] A. Ölander. An electrochemical investigation of solid cadmiumgold alloys. *Journal of the American Chemical Society*, 54:3819–3833, 1932.

[5] A. B. Greninger and V. G. Mooradian. Strain transformation in metastable beta copper-zinc and beta copper-tin alloys. *Transactions of the Metallurgical Society of AIME*, 128:337–368, 1938.

[6] L.C. Chang and T.A. Read. *Trans. AIME*, 191:47, 1951.

[7] W. J. Büehler, J. V. Gilfrich, and R. C. Wiley. Effect of low-temperature phase changes on the mechanical properties of alloys near composition TiNi. *Journal of Applied Physics*, 34(5):1475–1477, 1961.

[8] D. Stoeckel and T. Waram. Use of Ni-Ti shape memory alloys for thermal sensor-actuators. In *San Diego-DL tentative*, pages 382–387, 1992.

[9] T. W. Duerig. Applications of shape memory, martensitic transformations II. *Materials Science Forum*, 56-58:679–692, 1990.

[10] J. V. Humbeeck. Non-medical applications of shape memory alloys. *Materials Science and Engineering: A*, 273:134–148, 1999.

[11] M. H. Wu and L. M. Schetky. Industrial applications for shape memory alloys. *Proceedings of the International Conference on Shape Memory and Superelastic Technologies*, pages 171–182, 2000.

[12] K. Otsuka and T. Kakeshita. Science and technology of shape-memory alloys: new developments. *Mrs Bulletin*, 27(02):91–100, 2002.

TH-1636_10610313

[13] Y. Nakamura, K. Onuma, H. Kawakami, and T. Nakamura. *Active forceps for endoscopic surgery*. Springer, 1998.

[14] N. B. Morgan. Medical shape memory alloy applicationsthe market and its products. *Materials Science and Engineering: A*, 378(1):16–23, 2004.

[15] L. G. Machado and M. A. Savi. Medical applications of shape memory alloys. *Brazilian Journal of Medical and Biological Research*, 36(6):683–691, 2003.

[16] Y. Haga, T. Mineta, W. Makishi, T. Matsunaga, and M. Esashi. Active bending catheter and endoscope using shape memory alloy actuators. *Shape memory alloys*, pages 107–126, 2010.

[17] H. Adldoost, B. R. Jouibary, and A. Zabihollah. Design of sma micro-gripper for minimally invasive surgery. In *Biomedical Engineering (ICBME), 2012 19th Iranian Conference of*, pages 97–100, 2012.

[18] M. Hashimoto, T. Tabata, and T. Yuki. Development of electrically heated sma active forceps for laparoscopic surgery. In *Robotics and Automation, 1999. Proceedings. 1999 IEEE International Conference on*, volume 3, pages 2372–2377, 1999.

[19] D. Amariei, C. Miclosina, D. Vela, M. Tufoi, and I. C. Mituletu. Contributions to design of systems actuated by shape memory active elements. *International Journal of Mechanical, Aerospace, Industrial, Mechatronic and Manufacturing Engineering*, 4(11):1178–1183, 2010.

[20] K. J. D. Laurentis and C. Mavroidis. Mechanical design of a shape memory alloy actuated prosthetic hand. *Technology and Health Care*, 10(2):91–106, 2002.

[21] G. Song and N. Ma. Robust control of a shape memory alloy wire actuated flap. *Smart Materials and Structures*, 16(6):N51, 2007.

[22] Y. Fu, H. Du, W. Huang, S. Zhang, and M. Hu. TiNi-based thin films in MEMS applications: a review. *Sensors and Actuators A: Physical*, 112(2):395–408, 2004.

[23] K. Manfred. *Shape memory microactuators*. Springer Science & Business Media, 2013.

[24] Y. Bellouard, R. Clavel, J. E. Bidaux, R. Gotthardt, and T. Sidler. A concept for monolithic shape memory alloy micro-devices. *Le Journal de Physique IV*, 7(C5):C5–603, 1997.

[25] V. Shankar, G. N. Dayananda, P. S. Kumar, M. S. Rao, and R. Balasubramaniam. In *Smart Materials, Structures, and Systems*, pages 914–921. International Society for Optics and Photonics, 2003.

[26] G. Song, N. Ma, and H. N. Li. Applications of shape memory alloys in civil structures. *Engineering Structures*, 28(9):1266–1274, 2006.

[27] K. Tanaka. A thermomechnical sketch for shape memory effect: One-dimensional tensile behavior. *Res Mechanica*, 18:251–263, 1986.

TH-1636_10610313

[28] C. Liang and C. A. Roger. One-dimensional thermomechanical constitutive relations for shape memory materials. *Journal of Intelligent Material Systems and Structures*, 1(2):207–234, 1990.

[29] L. C. Brinson. One-dimensional constitutive behavior of shape memory alloys: Thermomechanical derivation with non-constant material functions and redefined martensite internal variable. *Journal of Intelligent Material Systems and Structures*, 4(2):229–242, 1993.

[30] A. Khandelwal and V. R. Buravalla. A correction to the Brinson's evolution kinetics for shape memory alloys. *Journal of Intelligent Material Systems and Structures*, 19:43–46, 2007.

[31] V. R. Buravalla and A. Khandelwal. Differential and integrated form consistency in 1-D phenomenological models for shape memory alloy constitutive behavior. *International Journal of Solids and Structures*, 44(13):4369–4381, 2007.

[32] A. Bekker and L. C. Brinson. Temperature induced phase transformation in a shape memory alloy: Phase diagram based kinetics approach. *Journal of the Mechanics and Physics of Solids*, 45(6):949–988, 1997.

[33] V. Buravalla and A. Khandelwal. Evolution kinetics in shape memory alloys under arbitrary loading: Experiments and modeling. *Mechanics of Materials*, 43(12):807–823, 2011.

[34] L. Li, Q. Li, and F. Zhang. One-dimensional constitutive model of shape memory alloy with an empirical kinetics equation. *Journal of Metallurgy*, 2011, 2011.

[35] M. H. Elahinia and M. Ahmadian. An enhanced SMA phenomenological model: I. the shortcomings of the existing models. *Smart Materials and Structures*, 14(6):1297–1308, 2005.

[36] M. H. Elahinia and M. Ahmadian. An enhanced SMA phenomenological model: II. the experimental study. *Smart Materials and Structures*, 14(6):1309–1319, 2005.

[37] A. A. Likhachev and Yu. N. Koval. The model of hysteretic behavior of SMA based on the high order approximation of differential equation method. *Le Journal de Physique IV*, 7(C5):C5–77, 1997.

[38] A. Khandelwal and V. Buravalla. Models for shape memory alloy behavior: an overview of modeling approaches. *The International Journal of Structural Changes in Solids*, 1(1):111–148, 2009.

[39] G. Song, V. Chaudhry, and C. Batur. Precision tracking control of shape memory alloy actuators using neural networks and a sliding-mode based robust controller. *Smart Materials and Structure*, 12:223–231, 2003.

[40] N. Ma and G. Song. Control of shape memory alloy actuator using pulse width modulation. *Smart Materials and Structures*, 12(5):712–719, 2003.

[41] M. H. Elahinia and H. Ashrafiuon. Non-linear control of a shape memory alloy actuated manipulator. *Journal of Vibration and Acoustics*, 124(4):566–575, 2002.

TH-1636_10610313

[42] D. Grant and V. Hayward. Variable structure control of shape memory actuators. *IEEE Control Systems*, 17(3):80–88, 1997.

[43] Y. H. Teh and R. Featherstone. Frequency response analysis of shape memory alloy actuators. In *International Conference on Smart Materials and Nanotechnology in Engineering*, pages 64232J–. International Society for Optics and Photonics, 2007.

[44] G. Song, B. Kelly, and B. N. Agrawal. Active position control of a shape memory alloy wire actuated composite beam. *Smart Materials and Structures*, 9(5):711–716, 2000.

[45] H. J. Lee and J. J. Lee. Time delay control of a shape memory alloy actuator. *Smart Materials and Structures*, 13(1):227–239, 2004.

[46] Y. H. Teh and R. Featherstone. An architecture for fast and accurate control of shape memory alloy actuators. *The International Journal of Robotics Research*, 27(5):595–611, 2008.

[47] R. A. Russell and R. B. Gorbet. Improving the response of SMA actuators. In *Robotics and Automation, 1995. Proceedings., 1995 IEEE International Conference on*, volume 3, pages 2299–2304. IEEE, 1995.

[48] N. T. Tai and K. K. Ahn. Adaptive proportional–integral–derivative tuning sliding mode control for a shape memory alloy actuator. *Smart Materials and Structures*, 20(5):055010, 2011.

[49] J. Jayender, R. V. Patel, S. Nikumb, and M. Ostojic. Modelling and gain scheduled control of shape memory alloy actuators. In *Proceedings of 2005 IEEE Conference on Control Applications, 2005. CCA 2005*, pages 767–772. IEEE, 2005.

[50] A. Visioli. Fuzzy logic based set-point weight tuning of PID controllers. *IEEE Transactions on Systems, Man, and Cybernetics-Part A: Systems and Humans*, 29(6):587–592, 1999.

[51] A. Visioli. Tuning PID controllers with fuzzy logic. *IEE Proceedings-Control Theory and Applications*, 148(1):1–8, 2001.

[52] A. Khodayari, M. Talari, and M. M. Kheirikhah. Fuzzy PID controller design for artificial finger based SMA actuators. In *Fuzzy Systems (FUZZ), 2011 IEEE International Conference on*, pages 727–732. IEEE, 2011.

[53] A. Khodayari, B. Zarefar, M. M. Kheirikhah, and E. Mirsadeghi. Force control of a SMA actuated gripper by using self tuning fuzzy PID controller. In *Control System, Computing and Engineering (ICCSCE), 2011 IEEE International Conference on*, pages 312–316. IEEE, 2011.

[54] D. J. S. Ruth, S. S. Nakshatharan, and K. Dhanalakshmi. Auto-adaptive control of a one-joint arm direct driven by antagonistic shape memory alloy. *International Journal on Smart Sensing and Intelligent Systems*, 6(3), 2013.

[55] K. Ikuta, M. Tsukamoto, and S. Hirose. Shape memory alloy servo actuator system with electric resistance feedback and application for active endoscope. *IEEE International Conference on Robotics and automation*, 1:427–430, 1988.

TH-1636_10610313

[56] Z. He, K. R. Gall, and L. C. Brinson. Use of electrical resistance testing to redefine the transformation kinetics and phase diagram for shape-memory alloys. *Metallurgical and Materials Transactions A*, 37(3):579–587, 2006.

[57] V. Novak, P. Sittner, G. N. Dayananda, F. M. B. Fernandes, and K. K. Mahesh. Electric resistance variation of NiTi shape memory alloy wires in thermomechanical tests: Experiments and simulation. *Materials Science and Engineering: A*, 481:127–133, 2008.

[58] R. Brammajyosula, V. Buravalla, and A.Khandelwal. Model for resistance evolution in shape memory alloys including R-phase. *Smart Materials and Structures*, 20(3):035015, 2011.

[59] N. Ma, G. Song, and H. J. Lee. Position control of shape memory alloy actuators with internal electrical resistance feedback using neural networks. *Smart Materials and Structures*, 13(4):777–783, 2004.

[60] C.C. Lan and C.H.Fan. An accurate self-sensing method for the control of shape memory alloy actuated flexures. *Sensors and Actuators A: physical*, 163(1):323–332, 2010.

[61] C. C. Lan and C. H. Fan. Investigation on pretensioned shape memory alloy actuators for force and displacement self-sensing. In *Intelligent Robots and Systems (IROS), 2010 IEEE/RSJ International Conference on*, pages 3043–3048, 2010.

[62] C. C. Lan, C. M. Lin, and C. H. Fan. A self-sensing microgripper module with wide handling ranges. *IEEE/ASME Transactions On Mechatronics*, 16(1):141–150, 2011.

[63] S. H. Liu, T. S. Huang, and J. Y. Yen. Tracking control of shape-memory alloy actuators based on self-sensing feedback and inverse hystersis compensation. *Sensors*, 10(1):112–127, 2009.

[64] S. J. Furst, R. Hangekar, and S. Seeleck. Practical implementation of resistance feedback measurement for position control of a flexible smart inhaler nozzle. In *ASME 2010 Conference on Smart Materials, Adaptive Structures and Intelligent Systems.*, pages 205–213. American Society of Mechanical Engineers, 2010.

[65] J. Zhang and Y. Yin. SMA-based bionic integration design of self-sensor–actuator-structure for artificial skeletal muscle. *Sensors and Actuators A: Physical*, 181:94–102, 2012.

[66] Z. Q. Liu, H. Li, W. L. Chen, and J. P. Ou. Study on strain-sense property of TiNi and TiNiCu shape memory alloys. *Advances in Structural Engineering*, 8(6):637–644, 2005.

[67] R. Kratz, M. M. Stelzer, and S. O. Von. Design, measurement experiments and application of a macroscopic shape memory alloy actuator system. *Proc. Actuator 2006*, pages 14–16, 2006.

[68] A. T. Tung, B. H. Park, D. H. Liang, and G. Niemeyer. Laser-machined shape memory alloy sensors for position feedback in active catheters. *Sensors and Actuators A: Physical*, 147(1):83–92, 2008.

TH-1636_10610313

[69] R. Dunlop and A. C. Garcia. A nitinol wire actuated stewart platform. In *Australasian Conference on Robotics and Automation*, pages 122–127, 2002.

[70] H. Li, C. X. Mao, and J. P. Ou. Strain self-sensing property and strain rate dependent constitutive model of austenitic shape memory alloy: experiment and theory. *Journal of Materials in Civil Engineering*, 17(6):676–685, 2005.

[71] D. Cui, G. Song, and H. Li. Modeling of the electrical resistance of shape memory alloy wires. *Smart Materials and Structures*, 19(5):055019, 2010.

[72] K. Malukhin and K. F. Ehmann. An experimental investigation of the feasibility of "self-sensing" shape memory alloy based actuators.

[73] S. M. Dutta and F. H. Ghorbel. Differential hysteresis modeling of a shape memory alloy wire actuator. *IEEE/ASME Transactions on Mechatronics*, 10(2):189–197, 2005.

[74] D. Simon and D. L. Simon. Kalman filter constraint tuning for turbofan engine health estimation. 2005.

[75] D. Simon and D. L. Simon. Constrained kalman filtering via density function truncation for turbofan engine health estimation. *International Journal of Systems Science*, 41(2):159–171, 2010.

[76] M. H. Elahinia, M. Ahmadian, and H. Asfrafiuon. Design of a Kalman filter for rotary shape memory alloy actuators. *Smart Materials and Structures*, 13(4):691–697, 2004.

[77] M. H. Elahinia, T. M. Seigler, D. J. Leo, and M. Ahmadian. Nonlinear stress-based control of a rotary SMA-actuated manipulator. *Journal of Intelligent Material Systems and Structures*, 15:495–508, 2004.

[78] M. H. Elahinia and M. Ahmadian. Application of the extended Kalman filter to control of a shape memory alloy arm. *Smart Materials and Structures*, 15(5):1370–1384, 2006.

[79] I. Hassanzadeh, N. Nikdel, N. T. Motlagh, and M. A. Badamchizadeh. Design of augmented EKF for shape memory alloy actated manipulator. *International Journal of Engineering Science and Technology*, 2(7):3188–3198, 2010.

[80] W. J. Sinchina. DSC characterization of shape memory metal alloys. *Perkin Elmer Instruments*, 2000.

[81] T. Waram. *Actuator design using shape memory alloys*. Perkin Elmer Instruments, 1993.

[82] C. Liang and C. A. Rogers. One-dimensional thermomechanical constitutive relations for shape memory materials. *Journal of Intelligent Material Systems and Structures*, 1(2):207–234, 1990.

[83] A. Banerjee, B. Bhattacharya, and A.K. Mallik. Optimum discrete location of shape memory alloy wire for enhanced actuation of a compliant link. *Journal of Mechanical Design*, 132(2):021001, 2010.

[84] S. Bhowmik and C. Roy. Application of extended Kalman filter to tactical ballistic missile re-entry problem. *arXiv preprint arXiv:0707.1918*, 2007.

TH-1636_10610313

[85] V. Y. V Chandan and V. M. J Rao. Application of extended Kalman filter for a free falling body towards earth. *IJACSA Editorial*, 2011.

[86] M. A. Myers and R. H. Luecke. Process control applications of an extended Kalman filter algorithm. *Computers & chemical engineering*, 15(12):853–857, 1991.

[87] L. Loron and G. Laliberte. Application of the extended Kalman filter to parameters estimation of induction motors. In *Power Electronics and Applications, 1993., Fifth European Conference on*, pages 85–90. IET, 1993.

[88] D. Simon. *Optimal state estimation: Kalman, H infinity, and nonlinear approaches*. John Wiley & Sons, 2006.

[89] N. R. Conn, N.I. M. Gould, and P. Toint. Trust-region methods mps/siam series on optimization. Philadelphia, PA: SIAM, 2000.

[90] J. R. Dormand and P. J. Prince. A family of embedded Runge-Kutta formulae. *Journal of Computational and Applied Mathematics*, 6(1):19–26, 1980.

[91] J. J. Amalraj, A. Bhattacharya, and M. G. Faulkner. Finite-element modeling of phase transformation in shape memory alloy wires with variable material properties. *Smart Materials and Structures*, 9(5):22, 2000.

[92] M. G. Faulkner, J. J. Amalraj, and A. Bhattacharya. Experimental determination of thermal and electrical properties of Ni-Ti shape memory wires. *Smart Materials and Structures*, 9(5):632–639, 2000.

[93] K. Deb. *Optimization for engineering design: Algorithms and examples*. Prentice-Hall of India, 20012.

[94] P. Kim and L. Huh. *Kalman Filter for Beginners with MATLAB Examples*, volume 4. CreateSpace, 2011.

[95] S. J. Julier and J. K. Uhlmann. New extension of the Kalman filter to nonlinear systems. In *AeroSense'97*, pages 182–193. International Society for Optics and Photonics, 1997.

[96] J. Valappil and C. Georgakis. Systematic estimation of state noise statistics for extended Kalman filters. *AIChE Journal*, 46(2):292–308, 2000.

[97] N. P. G. Salau, J. O. Trierweiler, A. R. Seechi, and W. Marquardt. A new process noise covariance matrix tuning algorithm for Kalman based state estimators. *IFAC Proceedings Volumes.*, 42(11):572–577, 2009.

[98] A. R. Secchi, N. S. M. Cardozo, E. A. Neto, and T. F. Finkler. An algorithm for automatic selection and estimation of model parameters. *IFAC Proceedings Volumes*, 39(2):789–794, 2006.

[99] `http://www.arduino.org/products/boards/arduino-uno`.

[100] `https://www.arduino.cc/en/Guide/Environment`.

TH-1636_10610313